

Copyright

by

Rachel Marie Sammons

2018

The Dissertation Committee for Rachel Marie Sammons Certifies that this is the approved version of the following Dissertation:

Unconventional Approaches to Kinase Inhibition: Covalent Inhibitors and Docking Site Inhibitors of Mitogen-Activated Protein Kinases

Committee:

Kevin N. Dalby, Supervisor

Pengyu Ren

Amy Brock

Aaron B. Baker

Walter L. Fast

**Unconventional Approaches to Kinase Inhibition: Covalent Inhibitors
and Docking Site Inhibitors of Mitogen-Activated Protein Kinases**

by

Rachel Marie Sammons

Dissertation

Presented to the Faculty of the Graduate School of
The University of Texas at Austin
in Partial Fulfillment
of the Requirements
for the Degree of

Doctor of Philosophy

The University of Texas at Austin

May 2018

Dedication

This dissertation is dedicated to my family for their constant love and support.

Acknowledgements

I would first like to thank my supervisor Dr. Kevin Dalby. Thank you for teaching me how to think like a scientist. Thank you for believing in me and guiding me while also helping me find stronger confidence in myself and my abilities. I am proud to be a member of your lab, and grateful that you saw potential in me and gave me this chance.

I would also like to thank the other members of my committee, Dr. Ren, Dr. Brock, Dr. Baker, and Dr. Fast, for your time and guidance.

I am especially grateful for Tamer Kaoud. I am thankful for the time and energy that you devoted to teaching me, from the moment that I first arrived at UT Austin. I will always appreciate your support, advice, and unwavering kindness throughout the years. You are a truly great role model, as both a scientist and friend.

Additionally, I would like to thank Juliana Taliaferro, David Giles, Gabriel Stancu, and Catrina Chitjian for your help and friendship. I also appreciate all of the other past and current Dalby lab members, for your work, positive influence, and your advice.

Finally, I would like to thank the collaborators that have trained me and helped contribute to my research: Naoto Ueno, Chandra Bartholomeusz, Mary Kathryn Pitner, and Xuemei Xie of MD Anderson Cancer Center; Eun Jeong Cho and John Veloria of the Targeted Therapeutic Drug Discovery and Development Program at UT Austin; Nicole Perry and Tina Iverson of Vanderbilt University; Andrea Piserchio and Ranajeet Ghose of The City College of New York; Diana Zamora-Olivares; the Nathanael Gray Lab at Harvard University; and the Torrey Pines Institute for Molecular Studies. Thank you to

the Biomedical Engineering Department at UT Austin for allowing me this opportunity and providing me with an Imaging Sciences T32 Traineeship, and to CPRIT for providing me with a Cancer Prevention Research Traineeship.

Abstract

Unconventional Approaches to Kinase Inhibition: Covalent Inhibitors and Docking Site Inhibitors of Mitogen-Activated Protein Kinases

Rachel Marie Sammons, PhD

The University of Texas at Austin, 2018

Supervisor: Kevin N. Dalby

The body of work that follows is a description of biochemical screening methods to identify non-ATP competitive and covalent ERK inhibitors, as well as assay design for characterizing covalent inhibitors of JNK in an isoform-specific manner. A covalent ERK inhibitor is presented, as well as a novel class of non-covalent ERK docking site inhibitors. An assay to elucidate the kinetic parameters of covalent JNK inhibitors is described, and the kinetic parameters for the inhibitor JNK-IN-8 are illustrated as a case study. Additionally, a series of JNK-IN-8 analogues were tested in a PyVMT breast cancer cell model for their ability to preferentially inhibit either JNK1 or JNK2. The rationale behind targeting MAPKs at docking sites and focusing on covalent inhibitors is centered on several key elements. First, the proximity-based mechanism of MAPK catalysis depends on docking site interactions to direct substrate consensus sequences to the vicinity of the MAPK active site. MAPK activators, phosphatases, scaffolding proteins, and other molecules also engage docking sites. Therefore, targeting docking sites with inhibitors can not only directly or indirectly block substrate phosphorylation or enzyme activation, but the mechanisms of catalysis themselves can be altered. Secondly,

the signal dynamics of MAPKs, such as their switch-like behavior, intra-pathway feedback, and inter-pathway crosstalk makes complete inhibition of MAPKs necessary to stop signaling in a therapeutic context. Covalent, irreversible MAPK inhibitors can induce complete inhibition by being effectively immune to substrate competition, and by forcing recovery of signaling to be fully dependent on either MAPK mutations, protein synthesis, or pathway bypass. Targeting a MAPK at multiple interaction sites can further promote a full blockade of signaling. The collective goal of the work presented in this dissertation is to contribute to the breadth of targeted kinase inhibitors that can be used against cancers, such as BRAF-V600E melanoma. These inhibitors and methods of inhibitor development can be used as tools to probe the functionality of individual protein-protein interaction sites on ERK and JNK, and the principles described here can be adapted to apply to other kinases and binding sites as needed in future studies.

Table of Contents

List of Tables	xv
List of Figures	xvi
Chapter 1: Introduction	1
MAPK Overview	1
ERK Pathway.....	2
JNK Pathway	3
Targeting MAPKs in Cancer	4
Overview of Docking Interactions.....	7
D-Recruitment Site	8
ERK Inhibitors	10
JNK Inhibitors.....	11
F-Recruitment Site.....	13
ERK Inhibitors	14
Other Interaction Sites	15
Dimerization Interface	15
P-Loop Binding Pocket.....	16
DARPinS	16
FRS-Like Site for JNK1.....	18
Covalent Inhibitors	18
ERK Inhibitors.....	19
JNK Inhibitors.....	20
Multiple MAPK Targets as Cancer Treatment	20

JNK and ERK Pathway Cross-Talk.....	21
Adaptive Resistance to ERK Pathway Inhibition.....	22
Summary of Work	23
Chapter 2: Identification of Auranofin as a Bivalent, Irreversible ERK Inhibitor Using a High-Throughput Screening	34
Abstract.....	34
Introduction.....	35
Materials and Methods.....	37
Proteins, Peptides, and Buffers	37
Primary Fluorescence Anisotropy Screening	38
Secondary Activity-Based Screening	39
Selection of Hit Compounds.....	40
Anisotropy Dose-Response Assays	40
³² P Dose-Response Assays	41
Fluorescence Dose-Response Assays	41
Assays for Recovery of ERK2 Activity.....	42
Preparation of Cell Lysates.....	42
Western Blots.....	43
Results and Discussion	44
Anisotropy Assay Detected Small Molecules That Bind to the DRS.....	44
Screening Hits Inhibited Phosphorylation of Peptide Substrate by ERK2 ...	46
Screening Preferentially Detected Reactive Small Molecules	47
Auranofin Inhibits ERK2 via Cys159 and Cys164.....	49
Other Effects of Auranofin in Cells.....	51

Proposed Models for ERK Inhibition by Auranofin.....	52
Conclusions.....	53
Chapter 3: A Novel Class of Common Docking Domain Inhibitors That Prevent ERK2 Activation and Substrate Phosphorylation	62
Abstract.....	62
Introduction.....	63
Materials and Methods.....	66
Proteins, Peptides, and Buffers	66
DMF Tolerance.....	66
Validation Set	67
Combinatorial Library Screening	67
Synthesis of 2408 Libraries and Individual Compounds.....	68
Dose-Response Assays with Fluorescent Reporter	68
Anisotropy Dose-Response Assays	68
Quantifying Inhibition of ERK2 Activation In Vitro	69
³² P Assay for Evaluating 2507-1 Selectivity	70
NMR Spectroscopy.....	70
Expression and Purification of ERK2 for Crystallization	71
Crystallization, Structure Determination, and Analysis	72
Results and Discussion	73
Screening Identified Cyclic Guanidine Scaffolds as DRS Inhibitors	73
Hit Compounds Inhibit DRS Interactions in a Dose-Dependent Manner	75
Characterization of 2507-1 Selectivity	76
2507-1 Inhibited ERK2 Activation by Constitutively Active MEK1.....	77

Confirmation of DRS Binding by Structural Data.....	78
Conclusions.....	80
Chapter 4: Characterization of Kinetic Parameters and Isoform-Selectivity of Covalent JNK Inhibitors	92
Abstract.....	92
Introduction.....	92
Materials and Methods.....	95
Proteins, Peptides, and Small Molecules	95
Kinase Activity Assays	95
Steady State Kinetics: K_m and k_{cat} for Sox-NFAT4.....	96
Steady State Kinetics: K_m and k_{cat} for ATP	97
JNK-IN-8 Assays.....	97
Cell Lines and Treatments	100
Western Blots.....	101
Results and Discussion	102
Kinetic Parameters for Inactivation of JNK1/2 by JNK-IN-8.....	102
Comparing JNK-IN-8 Kinetic Parameters to Other Covalent Kinase Inhibitors.....	103
Limitations of the Reaction Progress Curve Assay	105
Evaluating Selectivity of Inhibitors for JNK Isoforms in Cells.....	105
Conclusions.....	108
Appendices.....	127
Appendix A: Peptides	127
Peptide Sequences.....	127

Sox-Alkylation of Peptide Substrates	127
Deprotection of Cys(Mmt).....	127
Cysteine Labeling	128
Cleaving and Deprotection of Peptides.....	128
Purification of Peptides.....	129
Appendix B: Supplementary Information for Chapter 2	130
Anisotropy Screening Optimization	130
Library Compound Aggregation Test.....	132
Primary Anisotropy Screening Validation.....	132
Top Compounds Ranked from the Primary and Secondary Screenings	133
Dose-Response Curves	134
Model for Fitting Anisotropy Dose-Response Curves	139
Evaluation of Inhibitor Reversibility	142
Compound Reactivity Test	142
ESI-MS for ERK2 with Aurano-fin	143
Phenotype Assays in HEK293T Cells	147
Viability Assay (MTS).....	147
Colony Formation Assays.....	147
Appendix C: Supplementary Information for Chapter 3	149
Combinatorial Library Screening Optimization	149
Dose-Response Curves	158
Structural Studies.....	165
Chemical Synthesis and Purification	169

Synthesis of Compounds.....	169
Synthesis of the Mixture-Based Tris-(2-(2-iminoimidazolidin-1-yl)ethyl)amine Library.....	172
Compound 2507-1	173
Compound 2507-8	174
Appendix D: Supplementary Information for Chapter 4	176
Michaelis-Menten Kinetics.....	176
Global Fitting of JNK1/2 Inactivation in GraphPad Prism.....	178
Kinetics of THZ-3-60-1 Inhibition	179
Evaluation of IC ₅₀ Values for THZ-3-60-1.....	179
References	181

List of Tables

Table 2.1.	IC ₅₀ and K _i * values for the top 9 screening hits.	56
Table 3.1.	Top mixtures that exhibited highest displacement of fluorescent probe in scaffold screening	82
Table 3.2.	Top individual compounds resulting from positional scanning of library 2408.....	84
Table 3.3.	Binding affinities of top 10 compounds.....	85
Table 4.1.	JNK-IN-8 kinetic parameters.	112
Table 4.2.	Kinetic parameters of covalent kinase inhibitors.....	114
Table B1.	Assay validation measurements to determine Z-factor.....	132
Table B2.	List of top ranking compounds from the screening.	133
Table B3.	GraphPad Prism input parameters, initial values, and constraints.	141
Table B4.	Initial conditions used in reactivity test.	143
Table C1.	Validation of manual screening plate preparation.	150
Table C2.	Top mixtures derived from scaffold 2408 in screening Phase II.	154
Table C3.	Chemical shift perturbations for ERK2 residues in the presence of compound 2507-8.	165
Table C4.	Crystallographic data collection and refinement statistics.....	168

List of Figures

Figure 1.1.	Basic components of the ERK and JNK signaling pathways.	25
Figure 1.2.	Types of kinase inhibitors.	26
Figure 1.3.	Scheme of potential outcomes of docking site inhibition.	27
Figure 1.4.	The structural elements of the DRS.	28
Figure 1.5.	DRS inhibitors.	29
Figure 1.6.	The FRS and putative dimerization interface of ERK2.	30
Figure 1.7.	Non-ATP competitive inhibitors of ERK and JNK.	31
Figure 1.8.	ERK and JNK signaling pathway crosstalk.	32
Figure 1.9.	Models of acquired resistance to melanoma treatments.	33
Figure 2.1.	Fluorescence anisotropy screening and secondary screening.	55
Figure 2.2.	<i>In vitro</i> ERK2 mutant activity in the presence of auranofin.	58
Figure 2.3.	C159A/C164A mutant ERK2 overexpression in HEK293T cells recovers ERK activity in presence of 5 μ M auranofin.	59
Figure 2.4.	Selectivity of auranofin in HEK293T cells against JNK and p38 α	60
Figure 2.5.	Scheme of possible influences of DRS inhibition on ERK signaling.	61
Figure 3.1.	Deconvolution of cyclic guanidine libraries.	81
Figure 3.2.	Potency and selectivity of 2507-1.	86
Figure 3.3.	2507-1 inhibits MKK1G7B phosphorylation of ERK2 <i>in vitro</i>	87
Figure 3.4.	Docking of 2507-8 at the DRS via NMR.	88
Figure 3.5.	The 1.9Å structure of ERK2 in complex with inhibitor 2507-8.	89
Figure 3.6.	Electrostatic interactions of Fragment A with the DRS of ERK2.	91
Figure 4.1.	Reaction progress curves for JNK-IN-8 inhibition of JNK1.	110
Figure 4.2.	Reaction progress curves for JNK-IN-8 inhibition of JNK2.	111
Figure 4.3.	Average values of kinetic parameters for JNK-IN-8.	113

Figure 4.4. Reactive functional groups associated with selected covalent kinase inhibitors.	116
Figure 4.5. THZ-3-60-1.	117
Figure 4.6. JNK-In-B.	118
Figure 4.7. JNK-In-C.	119
Figure 4.8. YL-01-035-1.	120
Figure 4.9. YL-02-053-1.	121
Figure 4.10. YL-01-042-1.	122
Figure 4.11. YL-02-057-1.	123
Figure 4.12. YL-02-079-1.	124
Figure 4.13. YL-02-048-1.	125
Figure 4.14. YL-02-056-1.	126
Figure B1. Optimization of FITC-X-Lig-D and ERK2 concentrations for anisotropy screening.	131
Figure B2. Effects of DMSO concentration on anisotropy signal.	131
Figure B3. Dose-response curves for the top 9 compounds.	134
Figure B4. Anisotropy dose-response curves for compounds 3, 4, and 5 against WT and C159S ERK2.	135
Figure B5. Anisotropy dose-response curves for compounds 12, 13, and 16 against WT and C159S ERK2.	136
Figure B6. Anisotropy dose-response curves for compounds 18, 21, and 23 against WT and C159S ERK2.	137
Figure B7. Dose-response curves for JNK2 inhibition.	138
Figure B8. K_d curve for C159S ERK2 binding to FITC-X-Lig-D.	141
Figure B9. Covalent modification test for top 9 compounds.	142

Figure B10. ESI-MS data for inactive ERK2.	145
Figure B11. ESI-MS data for ERK2 with auranofin.....	146
Figure B12. Auranofin inhibits proliferation and survival in HEK293T cells.	148
Figure C1. Dependence of maximum anisotropy signal on DMF % (v/v).	149
Figure C2. Screening Phase I – scaffold mixtures at 50 $\mu\text{g/mL}$	151
Figure C3. Screening Phase I – scaffold mixtures at 25 $\mu\text{g/mL}$	152
Figure C4. Positional scanning of library 2408 mixtures at 25 and 50 $\mu\text{g/mL}$	153
Figure C5. Screening of crude individual compounds at 12.5 and 25 μM	156
Figure C6. Screening of crude individual compounds at 12.5, 6.25, and 3.125 μM	157
Figure C7. Binding affinities of FITC-X-Lig-D for active and inactive ERK2.	158
Figure C8. K_i curves for inactive ERK2 inhibition, part 1.....	159
Figure C9. K_i curves for inactive ERK2 inhibition, part 2.	160
Figure C10. K_i curves for active ERK2 inhibition, part 1.....	161
Figure C11. K_i curves for active ERK2 inhibition, part 2.	162
Figure C12. IC_{50} curves for top 10 compounds, part 1.	163
Figure C13. IC_{50} curves for top 10 compounds, part 2.	164
Figure C14. Synthetic approach for tris-(2-(2-iminoimidazolidin-1-yl)ethyl)amines. ...	171
Figure C15. LC-MS results for compound 2507-1 purification.	173
Figure C16. LC-MS results for compound 2507-8 purification.	174
Figure D1. Michaelis-Menten kinetics for JNK phosphorylation of sox-NFAT4.	176
Figure D2. Michaelis-Menten kinetics for JNK with respect to ATP.....	177
Figure D3. Characterization of THZ-3-60-1.	179

Chapter 1: Introduction

MAPK OVERVIEW

The mitogen-activated protein kinase (MAPK) signal transduction cascades are highly studied due to their roles in critical cellular processes and disease development and progression. Over 500 (518) genes have been identified that encode protein kinases, accounting for approximately 1.7% of the human genome [1]. There are four core MAPK signaling pathway subgroups: ERK1/2, p38, JNK, and ERK5. Each of these pathways consists of a central 3-tiered signaling module of MAP3K, MAP2K, and MAPK [2, 3]. Here, extracellular stimuli such as stress, mitogens, and cytokines result in the activation of these modules, where subsequently MAP3Ks phosphorylate MAP2Ks, which in turn phosphorylate MAPKs (Figure 1.1). The MAPKs go on to phosphorylate hundreds of substrates that govern important cellular processes such as survival, apoptosis, gene expression, and proliferation. In each phosphorylation event, the acting kinase transfers the γ -phosphate of ATP to a hydroxyl group of the downstream effector. This process is reversed by appropriate phosphatases. These basic three-tiered kinase cascades are flanked by a wide variety of stimuli and outputs. Extensive pathway cross-talk, feedback and feed-forward signaling regulation, subcellular compartmentalization, and scaffolding interactions all create additional levels of signaling complexity. Here we discuss the basic components and functions of the ERK1/2 and JNK pathways and explore different protein-protein interacting (PPI) sites on the MAPK level of these cascades, as a layer of signaling regulation and potential target for drug therapies.

ERK Pathway

The two main extracellular signal-regulated kinase (ERK) isoforms, ERK1 and ERK2, are the final components of the Ras/Raf/MEK/ERK signaling cascade [4]. This pathway is activated by a variety of mitogens and other extracellular sources, such as growth factors, insulin, osmotic stress, and cytokines [5, 6]. These ligands and stimuli trigger receptor-tyrosine kinase (RTK) dimerization and activation at the cell membrane, which in turn leads to recruitment of Ras-GDP to the receptor. Ras-GDP is converted to Ras-GTP with facilitation from the guanine-nucleotide exchange factors Sos-1/2 (son of sevenless (*drosophila*) -1 and -2) [7], which are recruited to the receptor via several adaptor proteins (Shc, Grb2) [5]. Ras-GTP then leads to the activation of the Raf family (A-Raf, B-Raf, C-Raf) which culminates in Raf dimerization [8]. Raf serves as the primary member of the MAP3K tier in the core ERK signaling pathway. Activated Raf then phosphorylates and activates MEK1/2, which phosphorylate a threonine and tyrosine on ERK1 (T202/Y204) and ERK2 (T185/Y187) to activate them [5].

ERK1 and ERK2 are serine/threonine protein kinases that phosphorylate over 175 known substrates [9]. The functional redundancy of the two isoforms appears to be dependent on cell type and context. For example, ERK2, but not ERK1, was reported to be essential for mouse trophoblast development [10]. The substrates that ERK1/2 phosphorylate include transcription factors (e.g. Ets-1, Elk1, c-Fos, c-Jun), the RSK family of kinases, phosphatases, apoptotic proteins, and cytoskeletal proteins [5]. This wide array of substrates governs cellular processes such as proliferation, gene transcription, cell cycle progression, migration, adhesion, survival, and chromatin remodeling [3]. Since the cellular functions that depend on ERK signaling are so critical, dysregulation of the ERK pathway is a common driving factor in a variety of diseases. Particularly, the pathway is activated in numerous cancers. Ras activation is present in

over 30% of cancers [11], and activating BRAF mutations occur in 40-60% of melanomas (BRAF-V600E in over 50% of metastatic melanomas) [12, 13]. Aberrant ERK signaling is also implicated in neurodegenerative diseases, cardiac hypertrophy, diabetes, and kidney diseases [14-17].

JNK Pathway

Mammalian c-Jun N-terminal kinases (JNKs) are encoded by three genes, *jnk1*, *jnk2*, and *jnk3*, where *jnk1* and *jnk2* are ubiquitously expressed, and *jnk3* is expressed in the heart, brain, and testes [18, 19]. These genes encode the three isoforms JNK1-3 which encompass a total of 10 different splice variants [18]. Due to their ubiquity, JNK1/2 will be the main focus of this discussion. JNKs were originally identified as ‘stress-activated protein kinases’ (SAPKs) that phosphorylate a canonical substrate c-Jun, part of the AP-1 transcription factor complex [20-22]. Numerous other mechanisms of JNK pathway activation have been identified since its discovery, including pro-inflammatory cytokines (TNF- α , interleukin-1 β), growth factors, pathogens, ER stress, and toll-like receptor activation [23]. Pathway stimulation leads to activation of a large pool of MAP3Ks, such as the mixed-lineage protein kinase group members (MLK1-3), the MEKK family (MEKK1-4), and ASK1/2 [19]. These MAP3Ks phosphorylate and activate the dual-specificity kinases MKK4 and MKK7, which are responsible for JNK1/2 activation by phosphorylation of Thr183 and Tyr185 in the activation loop (Thr-Xxx-Tyr motif). Though they are dual-specificity kinases, MKK4 preferentially phosphorylates Tyr on JNK, while MKK7 conversely targets Thr, and both can be activated by different mechanisms [19].

Once activated, JNK1/2 phosphorylate a variety of substrates, including transcription factor activator protein complex -1 (AP-1) components (Jun and Fos

proteins), activating transcription factor -2 (ATF-2), NFAT, the Bcl-2 family, and numerous others [23]. These effectors regulate cellular processes like proliferation, survival, morphology, apoptosis, and differentiation. As with the ERK pathway, disturbances in JNK pathway signaling are a hallmark of a number of different pathologies, including neurodegenerative diseases like Alzheimer's [23-25], diabetes [26], inflammatory disorders [24, 27], and cardiovascular disease [14]. JNK1 and JNK2 also play critical roles in tumorigenesis and tumor suppression, in an isoform- and cell-type- specific manner that remains controversial [28, 29]. For example, JNK has been shown to promote the cancer stem cell (CSC) phenotype in TNBC models [30], while it acts as a tumor suppressor in mouse models of prostate cancer [31]. In tumorigenesis, the JNK2 isoform drives migration in PyVMT mouse models of breast cancer [32] and is the major active isoform in glioblastoma [33]. Conversely, JNK1 has been shown to be the primary JNK isoform driving proliferation in gastric and hepatocellular carcinoma models [34-37]. The substantial conflicting evidence suggests non-redundant roles for the two isoforms that depend on a complex variety of environmental factors and signaling events.

TARGETING MAPKS IN CANCER

Due to the prevalence of MAPK signaling in development and progression of diseases like cancer, the components of these pathways are ideal drug targets. There are numerous inhibitors of the ERK MAPK pathway in clinical use or pre-clinical development for cancer therapy, particularly for BRAF-V600E melanoma. Vemurafenib and dabrafenib (B-Raf inhibitors) are approved for treatment of BRAF-V600E melanoma, but often result in acquired resistance with a median time of 6-8 months [38, 39]. MEK inhibitors, such as trametinib, have been used alone or in combination with

mutant B-Raf inhibitors to combat this resistance, with limited efficacy [40-42]. ERK inhibition has emerged as a possible method of overcoming these resistance mechanisms, but relatively few ERK inhibitors have been clinically investigated. Currently a trial of the ERK inhibitor LY3214996 is recruiting for treatment of advanced cancers (NCT02857270), and the inhibitor ulixertinib (BVD-523) is also being clinically studied for various forms of cancer (NCT02296242). Another ERK inhibitor, ravoxertinib (GDC-0994), has completed a phase I trial for advanced and metastatic solid tumors (NCT01875705). A dual Akt/ERK inhibitor, ONC201, is the subject of 15 past, current, and recruiting clinical trials for different forms of cancer (clinicaltrials.gov). Phase I study recruitment is currently underway for several newer ERK inhibitors: LTT462, KO-947, and MK-8353 (clinicaltrials.gov). Similarly to the ERK pathway, JNK inhibition in cancer may target a signaling bottleneck that could overcome issues with upstream pathway inhibition. JNK signaling is also crucially linked to ERK signaling in melanoma [43, 44], indicating the utility of targeting multiple pathways. This pathway crosstalk is discussed in more detail later in this chapter. In 2002, Celgene advanced the JNK inhibitor CC-401 into a phase I clinical trial for cancers and inflammation though this trial was terminated (NCT00126893). As with ERK, many inhibitors of JNK have been developed, though none have been approved for cancer treatment so far.

There are four main classes of kinase inhibitors that must be considered in drug design (Figure 1.2) [45-47]. Type I inhibitors bind to the ATP-binding pocket of the kinase in the active DFG-in conformation, where the aspartate residue on the kinase activation loop faces into the pocket. Type II inhibitors bind to the same ATP-binding pocket while the kinase is in the inactive DFG-out conformation. In this conformation, the aspartate residue of the activation loop is flipped outward from the binding site. Type III-IV inhibitors are allosteric; they inhibit the kinase without blocking the ATP-site or

substrate binding sites [48, 49]. Additional types of kinase inhibitors include protein-protein interaction (PPI) inhibitors, also referred to as docking site or substrate-competitive inhibitors, and covalent inhibitors. Most biochemical and computational methods for kinase inhibitor discovery utilize ATP competition as an inhibitor detection method [45]. Therefore, the majority of identified kinase inhibitors are ATP-competitive (Type I and II). Type III and IV inhibitors are often serendipitously identified during mechanistic evaluations of hit compounds from ATP-site –directed biochemical screenings. However, the design of ATP-competitive inhibitors has numerous shortcomings that limit their potency and selectivity. Kinases have high affinity for ATP, which is often present at millimolar-level concentrations in cells, thus ATP-competitive inhibitors must be extremely potent [50-52]. Additionally, ATP-binding sites have high structure and sequence homology among the kinase groups, so ATP-competitive inhibitors must be highly selective to avoid off-target effects and promiscuity [52].

Because of these issues, growing attention has been placed on development of kinase inhibitors that block substrate or other protein interactions, allowing for specificity and selectivity in signaling manipulation by avoiding ATP competition. Irreversible, covalent inhibitors are of particular interest in this context, as they can potentially overcome substrate competition at any interaction site, including the ATP site. PPI sites, or docking sites, serve at a regulatory level as a recognition mechanism to identify binding partners and direct signaling specificity within the hundreds of MAPK substrates. Here we will explore inhibitors of the docking sites of ERK and JNK that are distinct from the ATP-binding pocket, as well as covalent inhibitors, as pertaining to the future of targeted cancer therapy.

OVERVIEW OF DOCKING INTERACTIONS

MAPK-binding docking motifs are typically less than 20 amino acids in length and are linear, disordered regions that adopt defined structure upon binding [53]. There can often be multiple docking motifs on the same protein that target the same sites, or different sites, on one or more MAPK [54]. These docking motifs can bind their targets in different conformations. For example, D-motifs can bind to the D-recruitment site of JNK in either NFAT4-like or JIP-like classes of conformations [54]. These extensive layers of complexity liken a single MAPK to a telephone switchboard, where the cell acts as an operator to relay a single explicit interaction among hundreds or thousands of possible outcomes and connections. In fact, it has been predicted that while the size of docking motifs is generally around 10 amino acids in length, there are likely over 100,000 different docking motifs in the human proteome [55].

For MAPKs, there are two main docking sites: the D-recruitment site (DRS) and the F-recruitment site (FRS), which are discussed here in detail. Aside from these sites, there are numerous other postulated protein-protein interaction domains on JNK and ERK. These docking sites interact with upstream and downstream effectors, positive and negative regulatory elements, as well as structural and scaffolding proteins. We predict that targeting docking sites with small-molecule inhibitors can have a variety of different outcomes, as shown in Figure 1.3. Primarily, an inhibitor of a docking site could directly prevent the phosphorylation of the MAPK substrates or the phosphorylation/dephosphorylation of the MAPK itself, resulting in full competitive inhibition (Figure 1.3 A). A docking site inhibitor could also indirectly inhibit MAPK substrate phosphorylation or actions performed on the MAPK by other enzymes (Figure 1.3 B). This can be accomplished if the inhibitor causes allosteric effects at other distinct binding locations, or if the inhibitor blocks a scaffolding protein from binding to the MAPK that

is required for a specific reaction to occur. Substrate phosphorylation may only be partially blocked by a single docking site inhibitor, especially if the substrate employs multiple docking sites on the kinase. This can result in altered reaction mechanism, processivity, and efficiency, as docking sites are often utilized to bring phosphorylation consensus sequences into close proximity of the MAPK active site (Figure 1.3 E) [54, 56, 57]. Additionally, MAPKs have specific functions in different subcellular locations, and docking sites are known to be involved in regulation of subcellular location. Therefore, inhibition of docking sites may disrupt spatiotemporal MAPK signaling (Figure 1.3 C). It has also been shown that inhibition of MAPK signaling can have widespread effects on the kinome, where other pathways or upstream effectors can be upregulated to bypass or overcome MAPK inhibition in order to achieve the same signaling outcomes (Figure 1.3 D) [40, 58]. There are likely to be more functions of docking sites and inhibitors that have yet to be explored. In the following sections, the details of specific docking sites on ERK and JNK are discussed, along with descriptions of their known functions and examples of existing targeted inhibitors.

D-Recruitment Site

The D-recruitment site (DRS) can be found on all MAPKs (p38, JNK, ERK1/2, ERK5) (Figure 1.4) in a location distal to the ATP-site on the protein surface [59]. The DRS binds to proteins with complementary D-site, or D-motif, sequences that are linear regions of varying lengths. The general consensus sequence of these D-motifs is $\psi_{1-3}X_{3-7}\Phi X\Phi$ where ψ , X, and Φ , indicate positively charged, hydrophobic, and any residue, respectively [53]. The DRS on all MAPKs includes a charged region and a hydrophobic groove. The charged region is a conserved acidic patch consisting of Asp or Glu residues, referred to as the common docking (CD) domain (Figure 1.4 B). The

hydrophobic groove region of the DRS is flanked by the CD domain and another motif, the ED domain, which consists of two variable residues (ED in p38, SD in JNK, TT in ERK1/2, and EN in ERK5). The ED domain helps convey specificity among the different MAPK D-recruitment sites (Figure 1.4 B) [60, 61]. The hydrophobic docking grooves are different for p38, ERK1/2 and JNK, making this region an ideal target for design of selective inhibitors [53]. The hydrophobic groove also contains a solvent-exposed cysteine residue, adjacent to the ED domain, that is conserved among all MAPKs. These cysteines can be targeted by covalent inhibitors. Additionally, binding at the DRS results in different conformational changes for each type of MAPK that mainly impact the kinase activation loop [59]. This kinase-specific effect offers an additional avenue of selectively targeting a given MAPK.

Blocking the DRS of ERK can result in direct inhibition of interactions with substrates (RSK-1 [62, 63] and MAPKAPK2 (MK2) [64], and caspase-9 [65]), phosphatases (MKP-5 and HePTP [64]), activators (MEK1/2 [66]), and scaffolding proteins such as PEA-15 [67]. Many of these interactions influence subcellular localization of ERK, such as binding to PEA-15 and MEK1/2 which both sequester ERK in the cytoplasm [67-72]. Similarly, the DRS of JNK interacts directly with substrates such as c-Jun and ATF-2, the upstream activators MKK4 and MKK7, phosphatases like PPM1J, as well as numerous cytoskeletal proteins, receptors, scaffolds and adaptor proteins that are listed in further detail in a review by Zeke, *et al.* (2016) [73]. These examples illustrate that a wide array of different ERK and JNK functions are influenced by the DRS. Therefore, it is expected that targeting the DRS of each kinase with small molecules will significantly alter signaling events.

ERK Inhibitors

Numerous inhibitors of the ERK DRS have been identified, namely through computer aided drug design (CADD) and virtual screening. In 2005, Hancock, *et al.* used CADD to detect small molecules that bind to the hydrophobic groove between the CD and ED domains of the DRS of unphosphorylated ERK2 [74]. This groove is known to be the interaction location of the phosphatase HePTP by crystal structure, so it is often used as a starting point for DRS inhibitor development [5, 75]. Five hit compounds were found to inhibit proliferation and colony formation of multiple cancer cell lines. Two of those compounds, 1.1 and 1.2 (Figure 1.5), were shown to bind ERK2 by a fluorescence quenching assay with dissociation constants near 5 μM *in vitro*. In 2006, the same group (Chen, *et al.*) published findings for a CADD screening for inhibitors that target active, phosphorylated ERK2 [76]. The activation of the enzyme induces conformational changes in various regions of ERK2, though this study indicated that changes in the DRS are minimal. Of the biologically active compounds, compounds 1.3, 1.4, and 1.5 were found to bind ERK2 with dissociation constants of 13-20 μM (Figure 1.5). Compound 1.1 was further optimized by virtual screening of analogues (Boston, *et al.*) [77] and synthetic chemistry to evaluate structure-activity relationship (Li, *et al.*) [78]. The inhibitors identified by Boston, *et al.* activated the intrinsic apoptosis pathway in cells, inhibiting proliferation and p90RSK-1 and Bad phosphorylation [77]. The compounds also showed the potential to preferentially target transformed cells over non-transformed cells. In addition to these inhibitors, Kinoshita, *et al.* identified small-molecule DRS inhibitors by *in silico* methods, which they validated by displacement of a peptide (PEP) designed based on the STAT3-ERK2 interaction [79]. Interestingly, these compounds did not interact with the DRS hydrophobic pocket, but rather the charged acidic region denoted by the CD domain. The hit compounds that met the criteria of $\text{IC}_{50} < 100 \mu\text{M}$ had

IC₅₀ values ranging from 11-82 μM by ELISA assay (Figure 1.5, compounds 1.6 and 1.7). These reported small-molecule inhibitors have shown great potential for ERK pathway inhibition, though there is still further room for development of inhibitors with drug-like biological activities. It is also notable that, to our knowledge, no biochemical high-throughput screenings have been developed to date that target the DRS of ERK.

JNK Inhibitors

Early work on JNK inhibitors that target the DRS began with peptides modeled after the JNK-JIP protein interaction (Figure 1.5). JIP (JNK Interacting Protein) scaffolds include the four isoforms JIP1-JIP4, which bind to JNK and MKK7 to facilitate JNK activation. The peptide pepJIP1 was first developed as an 11-mer D-site sequence of JIP1 that acts as an allosteric inhibitor of JNK [80]. It exhibited high selectivity for JNK over the other MAPKs and blocked JNK phosphorylation of numerous downstream substrates *in vitro*. PepJIP1 was modified with the addition of an HIV-TAT sequence to increase cell permeability (L-JNKI-1), and further modified to the *D-retro-inverso* peptide D-JNKI-1 (XG-102) to prevent cellular degradation [81, 82]. XG-102 has been studied in multiple clinical trials for treatment of inflammation and is a neuroprotective agent in animal models of stroke and Alzheimer's disease [81, 83]. It is also effective in animal models of insulin resistance and Type II diabetes, as well as numerous other disease models, which are reviewed further in Bogoyevitch, *et al.* (2010) [83]. However, our group has shown that XG-102 is not an inhibitor of JNK in kinase assays *in vitro*, suggesting that its effectiveness in these models and clinical trials is due to mechanisms outside of the JNK pathway [32]. L-JNKI-1, on the other hand, does inhibit JNK in kinase assays with an IC₅₀ of 0.45 μM for JNK2, 0.33 μM for JNK1, and 0.06 μM for JNK3 [32]. Our group has further developed this peptide into a 10-mer fused to either

inverted HIV-TAT (JIP¹⁰- Δ -TATⁱ) or polyarginine (JIP¹⁰- Δ -R₉) cell-penetrating sequences via an aminohexanoyl linker (Figure 1.5) [32]. These peptides potently inhibited cell migration in PyVMT mouse mammary tumor models and showed a 10-fold selectivity for the JNK2 isoform (IC₅₀ ~90 nM) over JNK1 and JNK3. Ngoei, *et al.* have also identified a peptide that binds the DRS of JNK, D-PYC98, from yeast two-hybrid screenings [84]. The *retro-inverso* peptide was found to be five times more potent than L-PYC98 *in vitro*. When linked to the HIV-TAT sequence and tested in cells, the peptide inhibited c-Jun phosphorylation by JNK in a manner that did not affect JNK activation.

In addition to peptide inhibitors of the JNK DRS, several small-molecule inhibitors have also been discovered that target this site. The compound BI-78D3 (Figure 1.5) was identified by Stebbins, *et al.* in a high-throughput screening to detect displacement of pepJIP1 from the DRS of JNK1 [85], and several other thiadiazole analogues have since been developed by the same group [86-88]. BI-78D3 exhibited an IC₅₀ of 12.5 μ M against c-Jun phosphorylation in HeLa cells. It was speculated that BI-78D3 may react covalently to Cys163 in the DRS of JNK1/2 [89], however data by Stebbins' group and other experiments conducted by our lab have suggested that if such a covalent reaction takes place, it is reversible. We have found that BI-78D3 also potently and irreversibly targets the DRS of ERK2, suggesting that future work should focus on its development as an ERK inhibitor.

Our lab has also identified the lignan (-)-zuonin A (Figure 1.5) as a selective inhibitor of the JNK DRS. This compound was discovered by virtual screen using BI-78D3 as a starting point [90]. Both enantiomers of zuonin A bind the DRS of JNK2 with an IC₅₀ of approximately 2.5 μ M, while (-)-zuonin A can achieve 80% maximal inhibition of c-Jun phosphorylation compared to 15% for (+)-zuonin A [90, 91]. (-)-Zuonin A prevented JNK activation by MKK4 and MKK7 as well as downstream c-Jun

phosphorylation in cells [91]. It also inhibited migration of MDA-MB-231 breast cancer cells [91].

Though these potent and selective inhibitors of the JNK DRS have been developed, small-molecule inhibitors that are selective for individual JNK isoforms will be vital to understanding the roles of the different isoforms in disease. Isoform-specific non-ATP competitive inhibitors will also be crucial for tuning inhibition to target specific interactions while minimizing undesired effects.

F-Recruitment Site

ERK1/2 and p38 α are known to have an additional distinct docking site, called the F-recruitment site (FRS), which may be putatively found on p38 β and ERK5 as well [92-94]. This docking site is not canonically present in JNK2 or the other p38 isoforms [95]. The FRS binds to proteins containing the consensus sequence Phe-Xxx-Phe-Pro (FXFP), also known as the DEF motif (Docking site for ERK, FXFP) [96]. The FRS is located adjacent to the active site, and is comprised of a hydrophobic cavity that is exposed subsequent to the activation of the kinase (Figure 1.6) [95]. The key hydrophobic ERK2 residues that compose the FRS are Y231, L232, L235, Y261, M197, and L198 (*rat*) [95].

The FRS of ERK is known to interact with several ERK substrates including c-Fos, Elk-1, and Ets-1 and is suggested to interact with nucleoporins, indicating it may have a role in nuclear transport of ERK [57, 62, 63, 97]. The fact that it is exposed upon activation of ERK suggests that its function is only associated with ERK docking interactions post-activation, thus inhibitors of the FRS would inevitably target active ERK.

As mentioned above, no substrates of JNK have been identified that contain the FXFP consensus sequence [73, 98]. However, the surface of JNK that structurally

corresponds to the FRS of ERK may still be a functional docking site, as suggested by assays of artificial substrates containing docking motifs [73, 99]. More recently, a structural study by Liu, X., *et al.* (2016) showed that this FRS-like region of JNK1 mediated interactions with the phosphatase MKP7 [100]. The motif of MKP7 that bound JNK1 was the sequence FNFL rather than FXFP. The FRS-like region of human JNK1 responsible for MKP7 interaction was found to include the hydrophobic residues W234, I197, L198, V256, Y259, V260, adjacent to the MAPK insert. Charged and polar residues involved in the interaction included T255, Q253, N263, T228, and D229. As discussed later in this chapter, inhibitors have been found that target this region of JNK1, providing further evidence that this surface is biologically relevant for JNK signaling [101]. Going forward, we refer to the region as ‘FRS-like’ for JNK, while reserving ‘FRS’ as the notation for the sites on ERK and p38 isoforms that bind classical FXFP motifs.

ERK Inhibitors

Recently, a class of small molecules that targets the FRS of ERK2 was identified by Samadani, *et al.* (2015) using virtual database screening [102]. The core thienyl benzenesulfonate scaffold molecule (Figure 1.7, compound 1.8) was shown to interact with the FRS of ERK2 in a pocket exposed by Phe181 and Leu182 (rat residue numbering). Compound 1.8 and its analogs were found to selectively inhibit FRS-mediated phosphorylation of c-Fos and c-Myc proteins. Notably, the compounds selectively inhibited proliferation of BRAF-V600Q melanoma cell lines that exhibited constitutively active ERK signaling. A high-throughput biochemical assay to identify FRS inhibitors was recently reported by Miller, *et al.* (2017) [103]. The screening employed a proximity-based AlphaScreen (Perkin-Elmer) to detect displacement of a

DEF peptide by library compounds. Though no hit compounds have been reported by the authors, this screening method will likely be a useful tool for biochemical detection of FRS inhibitors. In addition to small molecules, numerous peptides containing the DEF consensus sequence have been generated in order to probe the FRS and its role in ERK catalysis and binding interactions [97, 104-106].

Other Interaction Sites

While the FRS and DRS are well-documented, there are likely to be other physiologically relevant surfaces on MAPKs that have not yet been identified or fully characterized. Here we describe some of these likely PPI sites as well as binding pockets that appear to be induced by inhibitors.

Dimerization Interface

ERK2 has been reported to dimerize upon activation in order to regulate its subcellular localization. The putative dimer interface was first identified using the crystal structure of rat ERK2 [107] and includes the residues E343, E339, K340, P337, L336, D335, L333, E332, F329, F181, and H176 [108, 109]. This region is adjacent to the FRS but they do not share common key residues (Figure 1.6). Many of the studies supporting dimerization utilized His₆-tagged ERK2, however, the His₆ tag is known to induce association of proteins under certain circumstances [110, 111]. Our lab has shown that active recombinant ERK2 with the His₆ tag removed does not dimerize under physiologically relevant conditions *in vitro* [112]. Recently, Herrero, *et al.* identified a compound, DEL-22379 (Figure 1.7, compound 1.9), as targeting this putative dimerization interface via a docking groove [109]. The compound was an effective inhibitor of proliferation in ERK pathway-driven tumor cells, even in models of MEK

and B-Raf inhibitor resistance. While this compound clearly showed an inhibitory effect on ERK signaling, its mechanism requires more investigation. Regardless of whether this interface region mediates dimerization or other protein-protein interactions, it is apparent that it is a physiologically important site.

P-Loop Binding Pocket

The discovery of the potent tight-binding ERK inhibitor SCH772984 (Figure 1.7, compound 1.14) led to the identification of another binding pocket on ERK, the P-loop binding pocket [113]. The interaction of this compound with ERK2 induces the formation of this binding pocket, which is not found on the unbound active or inactive forms of the kinases. The pocket is located adjacent to the ATP binding site, thus SCH772984 functions as a type II (DFG-out, ATP-competitive) inhibitor and a type III allosteric inhibitor at the same time [47]. It has been proposed that the P-loop binding pocket forms slowly and this conformational change is the rate-limiting step of SCH772984 binding, indicating a slow-binding kinetic mechanism [114]. This suggests that the P-loop pocket may be a beneficial target to produce ERK inhibitors with long drug residence times.

DARPin

Non-ATP competitive MAPK inhibitors need not be limited to small molecules or peptides. In 2012, Kummer, *et al.* identified two designed ankyrin repeat proteins (DARPins) that selectively bind either active (doubly phosphorylated) or inactive ERK2 [115]. These DARPins are small proteins of 33 amino acids each, with a fixed structural framework and an interaction interface of randomized residues, allowing for synthesis of combinatorial libraries. The identified DARPins are not ATP-competitive, but rather bind

to the activation loop of ERK2 and adjacent regions, recognizing the conformational changes that occur upon phosphorylation of T183/Y185. The DARPins interact with several key hydrophobic residues of the FRS, including Y231, L232, Y261, and L198 (rat residue numbering), and slightly overlap with the putative dimerization interface of ERK2 as well. The DARPins were found to inhibit ERK2 phosphorylation and were able to distinguish the phosphorylation state of ERK2 in cells.

DARPins that bind JNK have also been identified and are capable of differentiating between the JNK1 and JNK2 isoforms. Parizek, *et al.* (2012), the same group that developed the ERK-binding DARPins, described sets of DARPins that either target human JNK1 α 1, JNK2 α 1, or both, with low nanomolar affinities and little binding to other MAPKs [116]. These DARPins prevent JNK activation, but do not inhibit active JNK, and are therefore similar in mechanism to the DARPins that target ERK. Later, the group crystallized two of the DARPins with truncated JNK1, using a chaperone DARPIn (D12) to achieve crystallization [117]. As with ERK, the DARPins interact with the FRS-like region of JNK1 along with surrounding areas and the activation loop. The DARPIn referred to as 47 (or J1_4_7) interacts with an alpha helix of the MAPK insert region composed of residues 253-265. The activation loop residues 173-181 are forced to fold back into the ATP-binding pocket, which is likely how the DARPIn inhibits JNK1 activation. The DARPIn interacts with both lobes of JNK1, via hydrogen bonds with Arg59 and Arg150. Thr255 and Thr258 of JNK1 are buried in amphiphatic pockets of J1_4_7. The DARPins interact with JNK1 in a manner similar to that of MKP7 [100], indicating a key role for the FRS-like region in the activation state of JNK1. The differences in the residues of this region for JNK1 compared to JNK2 was proposed as the source of isoform-specific DARPins, and this may be a critical consideration for development of isoform-specific small molecules. These examples of designed proteins

for MAPK inhibition further illustrate the utility in identifying and targeting unique, biologically relevant surfaces on kinases.

FRS-Like Site for JNK1

Comess, *et al.* in 2010 developed a unique biochemical screening method for detection of p38 α and JNK1 inhibitors that bind at any exposed surface of the proteins without bias [101]. The proteins were exposed to small molecules, and any poorly bound compounds were removed by ultrafiltration. The remaining high affinity compounds were identified by mass spectrometry, and the binding sites of the active compounds were determined by NMR. The screen identified both ATP-competitive and non-ATP competitive inhibitors. Of interest, a non-ATP competitive inhibitor of JNK1 activation was found to bind in the region of JNK1 bordered by the activation loop and the MAPK insert region (Figure 1.7, compound 1.10). As mentioned, this region is analogous to the FRS of ERK2 [75, 97], though no such site has been characterized for JNK via conventional DEF-consensus sequences. This method offers an additional way to identify new high-affinity inhibitors and new interaction sites on MAPKs.

COVALENT INHIBITORS

Development of covalent inhibitors for therapeutic purposes has long been met with concern for a variety of reasons, including toxicity, off-target reactivity, and haptization [118, 119]. However, the benefits of covalent inhibition, including duration of action and high potency, can outweigh these risks with careful inhibitor design. This design must involve a balance of reactivity and selectivity [118]. Optimal covalent inhibitor design can potentially be achieved by targeting non-conserved nucleophilic residues that are located in functionally relevant regions of proteins [120].

Irreversible covalent inhibitors can be interpreted as non-ATP competitive regardless of target location, since they can inherently overcome high substrate concentrations and affinities over time [119, 121]. Covalent inhibitors can also potentially overcome issues with signaling pathway feedback mechanisms and acquired resistance in response to reversible targeted kinase inhibition [122-124]. Examples of covalent ERK and JNK inhibitors are discussed below.

ERK Inhibitors

Numerous covalent inhibitors have been identified that target a non-catalytic active site cysteine of ERK (Cys164 for rat ERK2). The natural product hypothemycin (Figure 1.7, compound 1.11) and its analog FR148083 (Figure 1.7, compound 1.12) were identified as covalent inhibitors of numerous ERK pathway components, including ERK1/2 [125, 126]. However, these compounds are not selective enough to overcome covalent drug reactivity issues without further optimization, considering that they target multiple kinases outside of the MAPK pathway at the conserved active site cysteine. Ward, *et al.* took a different approach to discovering covalent ERK inhibitors [127]. They identified non-covalent inhibitors that selectively target the ATP-site of ERK using both high-throughput screening results and published literature. They then modified these inhibitors to incorporate reactive warheads in proximity to Cys164 of ERK2 by structure-aided drug design. Ultimately, they identified a covalent class of pyrimidine-based inhibitors that showed great potential for *in vivo* efficacy (Figure 1.7, scaffold compound 1.13).

Our lab has focused on identifying covalent inhibitors of ERK that target the solvent-exposed DRS cysteine (Cys159 of rat ERK2) rather than targeting the ATP-site. As mentioned, we have found that the reversible JNK inhibitor BI-78D3 covalently binds

the DRS of ERK2 at this residue (Kaoud, *et al.*, in preparation). Much of this dissertation is devoted to describing a biochemical high-throughput screening method to identify covalent DRS inhibitors, and the results of this screen.

JNK Inhibitors

Zhang, *et al.* developed the first class of covalent JNK inhibitors that target the active site cysteine residue (Cys116 for JNK1/2, Cys154 for JNK3) [128]. The small molecules contain a phenylamino-pyrimidine core scaffold modified by addition of an acrylamide with a dimethylamino group. The core compound was initially intended as an imatinib-based inhibitor of c-Kit but was found to potently inhibit JNK1/2/3 in a kinome screening. Of the series of analogues that the group developed from these findings, JNK-IN-8 showed high potency and selectivity for JNK, potential for studying JNK inhibition in cells and *in vivo*, and possibility for further development into isoform-selective inhibitors (Figure 1.7, compound 1.15). In the work described within this dissertation, we sought to develop methods to characterize the *in vitro* kinetic parameters and cellular effects of JNK-IN-8 and its analogues to pave the way for development of isoform-specific covalent inhibitors.

MULTIPLE MAPK TARGETS AS CANCER TREATMENT

The numerous protein-interaction sites on MAPKs that direct signaling events in unique ways indicate the possibility of targeting ERK and JNK signaling by multiple direct mechanisms. There is growing evidence that targeting multiple MAPK signaling components in cancer may be advantageous. This includes drug combinations that act within a single kinase pathway, multiple sites of a single kinase, parallel pathways, or upon kinases and alternative targets that converge on a common cancer phenotype [129-

132]. For example, bivalent ERK and JNK inhibitors have been developed to target both the DRS and the ATP-binding site of each kinase [133-137]. As a case study here, we discuss the crosstalk between JNK and ERK pathways in cancers, as well as the barriers to effective targeted kinase inhibition in BRAF-V600E melanoma that may be overcome by multivalent inhibition of the two pathways.

JNK and ERK Pathway Cross-Talk

ERK and JNK signaling pathways exhibit crosstalk at a multitude of levels that are not yet fully understood, and much of this crosstalk results in tumorigenic signaling (Figure 1.8). For example, numerous extracellular stimuli can activate both JNK and ERK signaling, and ERK and JNK share common downstream substrates, namely c-Jun, c-Myc, and Elk-1 [23]. Additionally, DUSP4 is a known phosphatase for both ERK1/2 and JNK1/2. Loss of DUSP4 drives ERK and JNK activation in cancers, and this promotes the cancer stem cell (CSC) phenotype in basal-like breast cancer (BLBC) [138]. Thus, it has been proposed that under these conditions, inhibition of both JNK and ERK would be of therapeutic benefit [138]. The protein BPGAP1 mediates another crosstalk node between the pathways in cancer. BPGAP1 scaffolds MP1 and MEK at the late endosome to facilitate ERK activation, leading to nuclear translocation of ERK to phosphorylate substrates that drive tumor development. JNK phosphorylation of BPGAP1 is required for this process, showing how ERK/JNK pathways can merge to facilitate cellular proliferation [139].

ERK and JNK pathways can also interact to antagonize their respective signaling in cancer as well. For example, ERK1 (but not ERK2) has been found to directly interact with JNK1 to suppress its activity and Ras/JNK/c-Jun –mediated transformation [140]. Conversely, JNK pathway activation has been shown to inhibit ERK signaling by

inducing hyper-phosphorylation of Sos-1 and the Raf isoforms, leading to their phospho-inhibition and unresponsiveness to upstream signals [141]. Additionally, in melanoma driven by constitutive ERK activity, it has been found that ERK signaling upregulates JNK and c-Jun activity, leading to cyclin D1 transcription and tumor progression [44]. It is clear from these examples that the nature of interactions between the ERK and JNK pathways in cancer is dependent on numerous factors like cell type, cancer type, subcellular context, and possible feedback signaling. The examples of ERK/JNK pathway interactions discussed here are summarized in Figure 1.8. It is also important to note that these examples include JNK/ERK pathway interactions alone, so this does not exclude the possible involvement of other additional pathways, such as p38 and PI3K/Akt/mTOR.

Adaptive Resistance to ERK Pathway Inhibition

Given that ERK and JNK pathways positively regulate one another in melanoma, we focus on melanoma here as a case where dual-pathway inhibition could be therapeutically beneficial. This is an especially critical future directive when considering adaptive resistance to clinically developed ERK pathway inhibitors. It has in fact been shown that c-Jun activity is upregulated in response to Raf inhibition in BRAF-V600E melanoma, and Raf and JNK inhibitors can synergize to cause melanoma cell death [43]. As previously mentioned, Raf inhibitors (vemurafenib and dabrafenib) and MEK inhibitors (trametinib, selumetinib, and cobimetinib) have been clinically used to treat BRAF-V600E melanoma either alone or in combination [42, 142], though these treatment methods are commonly met with acquired resistance [40, 41]. Targeted kinase inhibitor resistance can arise by a variety of mechanisms, such as mutations of the target kinase itself or mutations within the kinase pathway [40, 143, 144], pathway bypass via

alternative signaling routes [40, 145, 146], epigenetic changes [147-150], and adaptation of cellular processes such as drug transport [147]. Some examples of these acquired resistance mechanisms are illustrated in Figure 1.9. ERK pathway reactivation is observed in 50-70% of melanoma tumors that have been treated with a single B-Raf inhibitor [151-153]. Upregulation of receptor tyrosine kinases at the cell surface can drive other pathways such as PI3K/Akt signaling to overcome ERK pathway inhibition, and this is a critical result of the entire kinome remodeling in response to inhibitor treatment [154, 155]. These factors indicate that targeting ERK and other MAPKs positioned at the bottleneck of their respective signaling pathways may be a method of overcoming resistance; often BRAF-V600E melanoma cell lines that become resistant to Raf inhibitors and exhibit pathway reactivation maintain sensitivity to ERK inhibitors [113, 156]. However, considering that ERK pathway reactivation can be observed in as little as 24 hours post- B-Raf inhibitor exposure [157], combination therapies will likely be a necessary approach for clinical treatment of melanoma.

SUMMARY OF WORK

The goal of the work presented in the following chapters is to expand the arsenal of targeted MAPK inhibitors that can be used in cancer therapies, particularly BRAF-V600E melanoma. We focused on targeting ERK and JNK because these signaling pathways interact in cancers to lead to pro-tumorigenic phenotypes, and current clinical inhibitors upstream of ERK in melanoma are often met with acquired resistance. Therefore, inhibiting multiple pathways, kinases, and binding sites on individual kinases may be therapeutically beneficial. A covalent ERK DRS inhibitor is presented in Chapter 2, and a novel class of non-covalent ERK DRS inhibitors is described in Chapter 3. In Chapter 4, an assay to elucidate the kinetic parameters of covalent JNK inhibitors is

described, and the kinetic parameters for JNK-IN-8 are illustrated as a case study. Fluorescence-based methods for identifying and characterizing inhibitors are at the core of these projects.

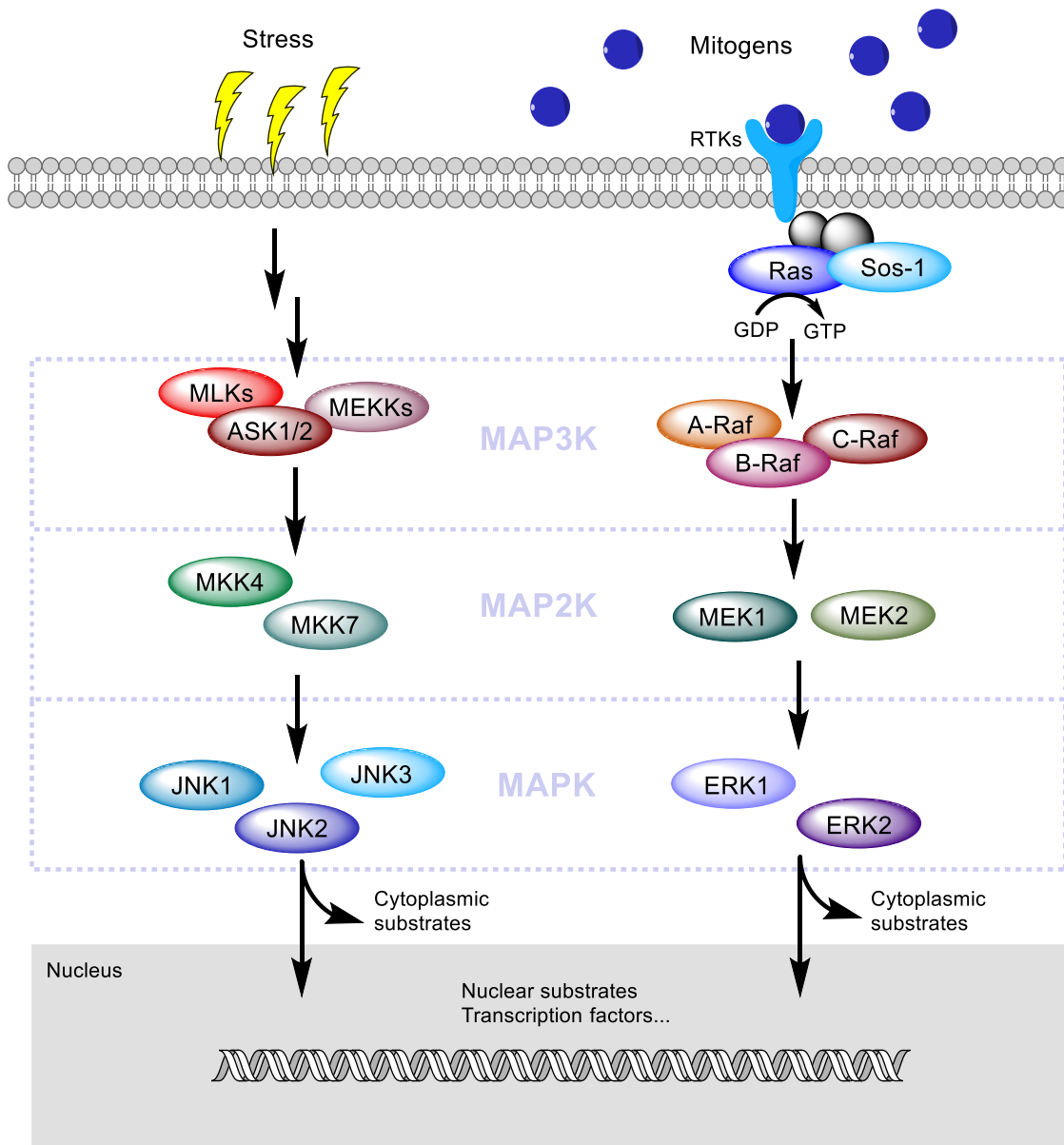


Figure 1.1. Basic components of the ERK and JNK signaling pathways.

The JNK and ERK pathway phosphorylation cascades consist of three core tiers: MAP3K, MAP2K, and MAPK. Examples of each tier are represented. Pathways are activated by extracellular stresses, ligand-receptor interactions, and a variety of other stimuli, and in each case the signaling pathways culminate in phosphorylation of nuclear and cytoplasmic substrates that govern critical cellular processes like apoptosis, proliferation, and differentiation. (Sources: [5, 28])

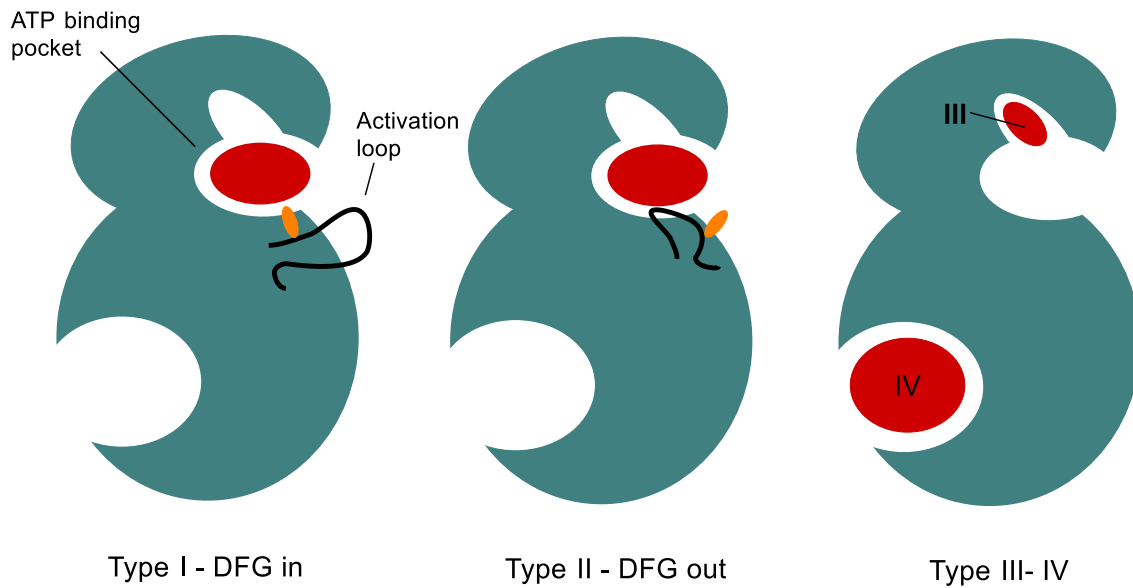


Figure 1.2. Types of kinase inhibitors.

A kinase, depicted with an ATP-binding site and distal protein-binding site, can be inhibited in a variety of ways (inhibitor is shown in red). Type I inhibitors target the ATP site when the kinase is active and in the DFG-in conformation, where the DFG-motif (orange) of the activation loop is facing into the pocket. Type II inhibitors target the ATP site of the inactive kinase conformation, when the DFG-motif is facing out from the pocket. Type III and IV inhibitors are allosteric, targeting sites adjacent and distant from the ATP site, respectively. These inhibitors do not block the binding of ATP. (Sources: [45, 47, 114])

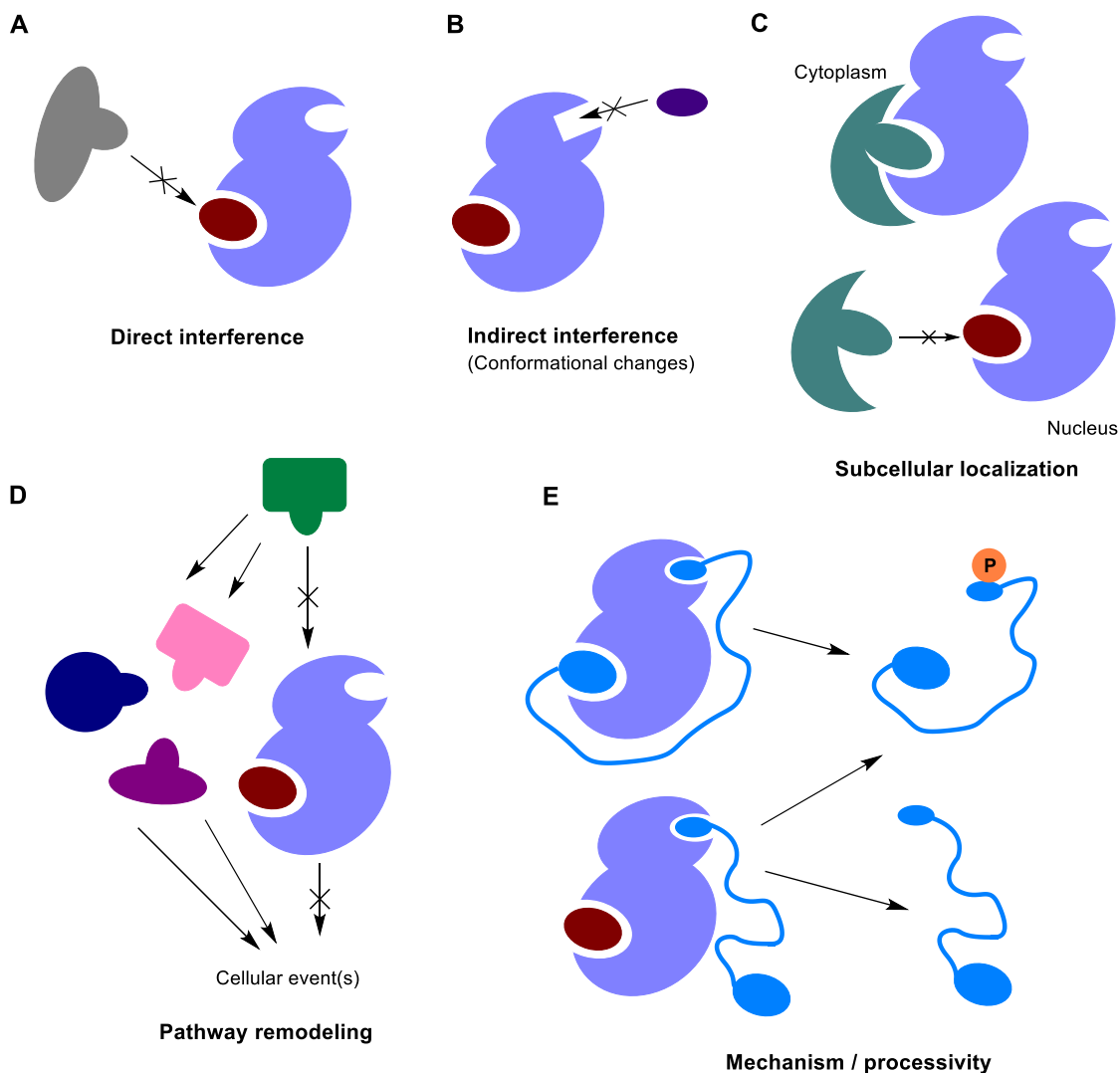


Figure 1.3. Scheme of potential outcomes of docking site inhibition.

A docking site inhibitor (red) bound to a MAPK (light blue) can result in: (A) direct inhibition of substrate phosphorylation or MAPK phosphorylation, (B) indirect inhibition of substrate phosphorylation through conformational changes or inhibition of scaffold protein binding, (C) inhibition of MAPK translocation or sequestration in subcellular compartments, (D) kinome remodeling or signaling pathway bypass in response to MAPK inhibition, and (E) altered reaction mechanisms or processivity due to the involvement of docking sites in bringing substrate S/T-P consensus sequences within proximity of the MAPK active site.

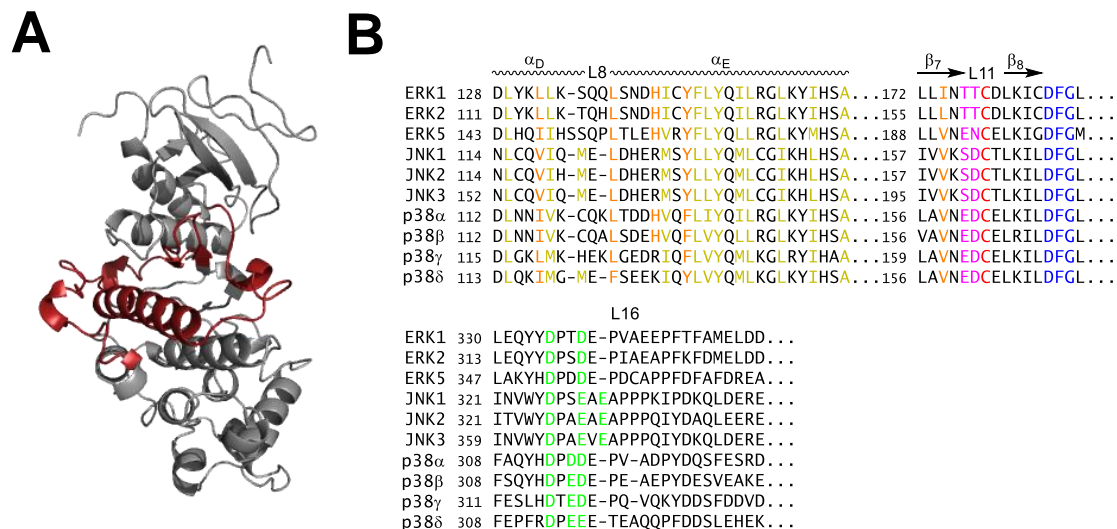


Figure 1.4. The structural elements of the DRS.

(A) The structure of ERK2 is shown (gray, PDB ID: 2ERK) depicting the secondary structural elements of the DRS (red). (B) The sequence alignment of the major domains of the DRS for all major MAPKs is shown. The DRS is composed of three major elements: (1) a groove formed by the hydrophobic residues of the α_D and α_E helices that is bordered by (2) the β_7 - β_8 reverse turn containing the ED domain, and (3) the L16 loop containing the CD domain. Key hydrophobic residues identified via ERK2 are shown in orange, while other conserved hydrophobic residues are highlighted in gold. The ED domain is shown in pink, adjacent to the conserved DRS cysteine residue (red). The DFG motif of the activation segment is shown in blue, and residues of the CD domain are shown in green. All MAPK sequences are human, obtained from UniProt database and aligned using Clustal Omega.

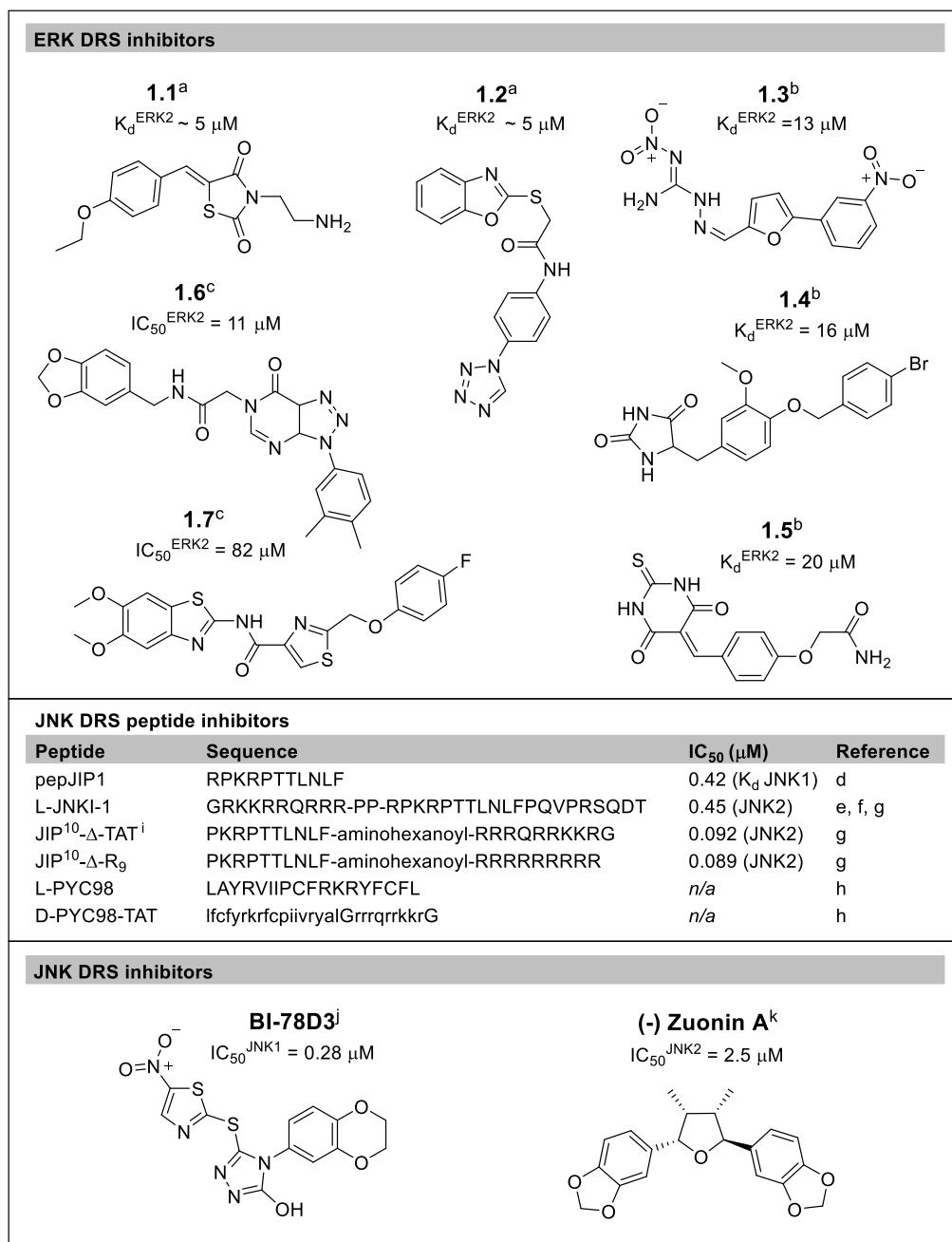


Figure 1.5. DRS inhibitors.

Structures of small-molecule inhibitors of the ERK and JNK DRS are shown, along with sequences of selected peptides that target the JNK DRS. (Superscripts indicate sources: a [74], b [76], c [79], d [80], e [81], f [82], g [32], h [84], j [85], k [90], “i” superscript indicates inverted peptide sequence, lowercase amino acid codes indicate D-amino acids). IC_{50} values for specified isoforms are provided unless they are unreported.

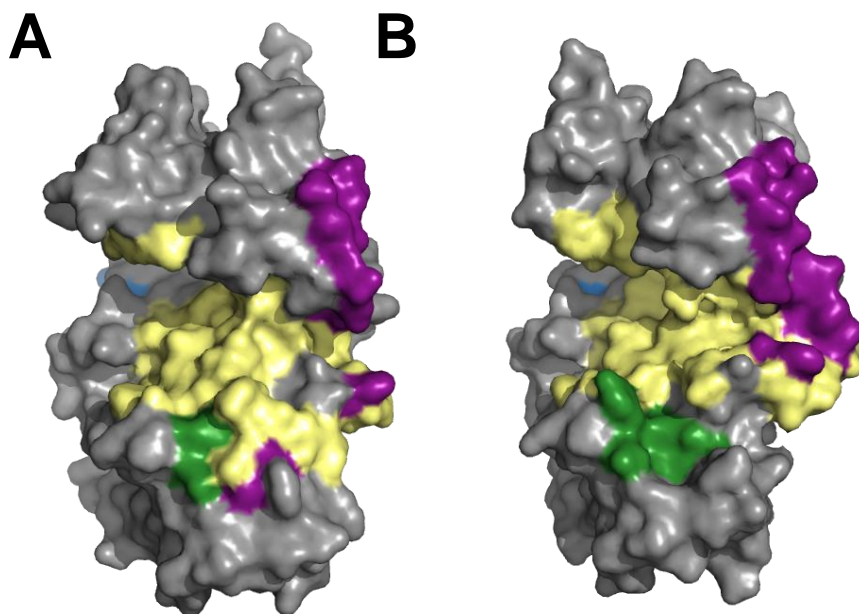


Figure 1.6. The FRS and putative dimerization interface of ERK2.

ERK2 is shown in gray, with the FRS in green, interface residues in purple, and the catalytic site in light yellow. The FRS and interface are both adjacent to the catalytic region. The inactive conformation of ERK2 (PDB ID: 1ERK) is shown in (A) while (B) depicts the active conformation (PDB ID: 2ERK), showing the changes in the organization of the domains. Namely, the hydrophobic FRS pocket opens upon activation, and the interface residues become more ordered and clustered, separated more distinctly from the FRS. (Sources: [95, 108, 109])

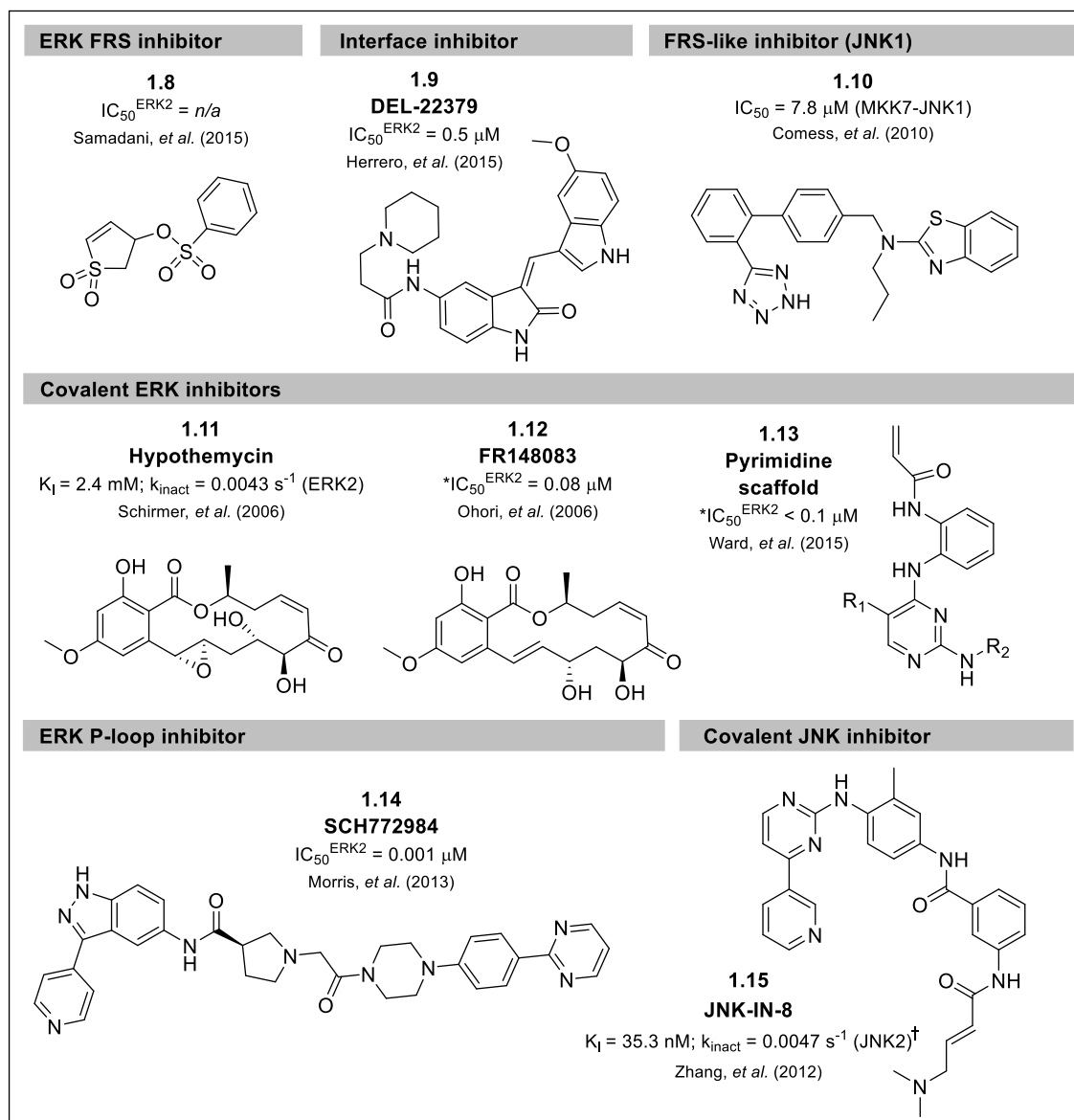


Figure 1.7. Non-ATP competitive inhibitors of ERK and JNK.

Structures are shown for selected inhibitors that target the ERK FRS, P-loop, and putative dimerization interface, along with covalent inhibitors that target ERK and JNK, and an inhibitor that targets the MAPK insert domain of JNK1 in an FRS-like site. IC_{50} values are given (when provided) for reversible inhibitors and are used as estimates (*) for covalent inhibitors when parameters (K_I and k_{inact}) are not determined. † Publication in preparation. (Sources: [101, 102, 109, 113, 125-128])

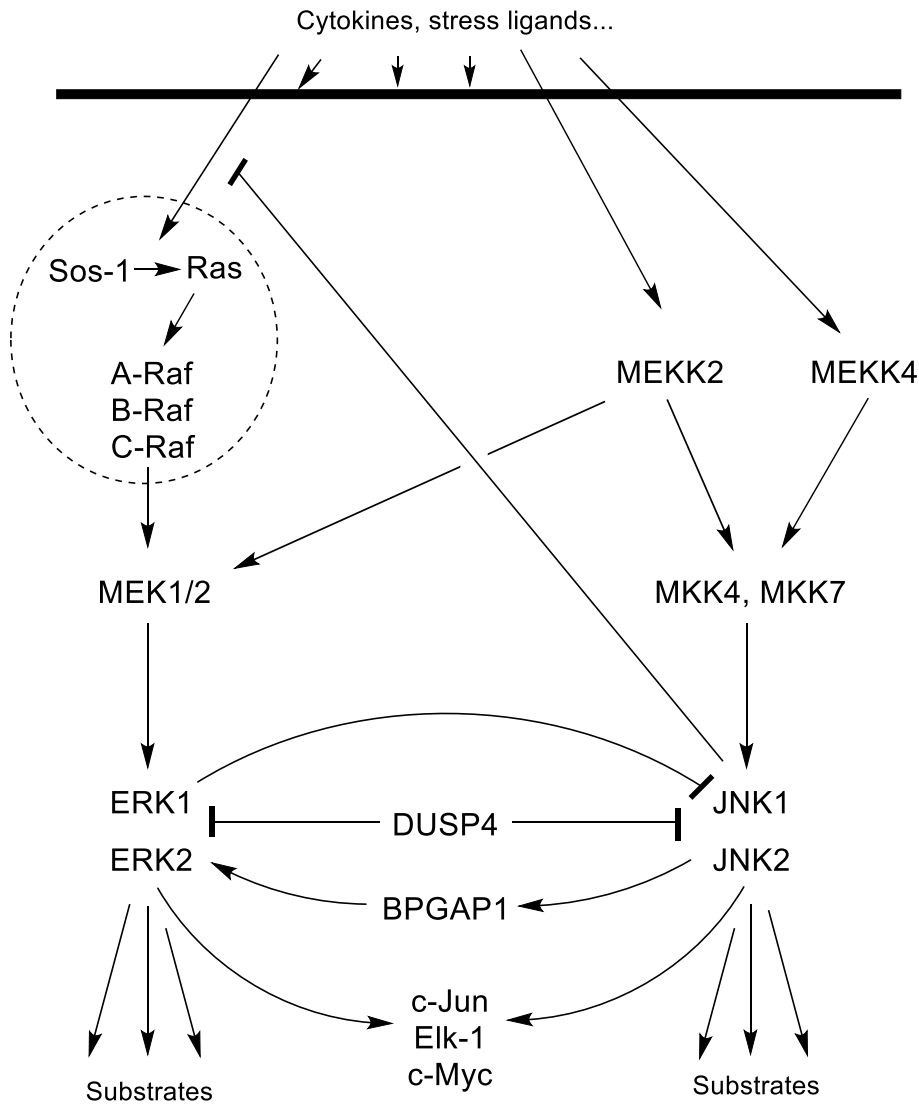


Figure 1.8. ERK and JNK signaling pathway crosstalk.

ERK and JNK signaling can be stimulated by common stresses or ligand-receptor interactions, and both ERK and JNK can phosphorylate common substrates such as c-Jun, Elk-1, and c-Myc. DUSP4 is a phosphatase that acts on both JNK and ERK. In cancer, ERK1 can directly suppress JNK1 activity, while at the late endosome JNK can activate ERK via BPGAP1. In melanoma, ERK signaling is known to upregulate JNK and c-Jun activity. Conversely, JNK signaling can suppress ERK pathway activity by hyperphosphorylation of Sos-1 and the Raf isoforms. (Sources: [23, 43, 44, 138-141, 158, 159])

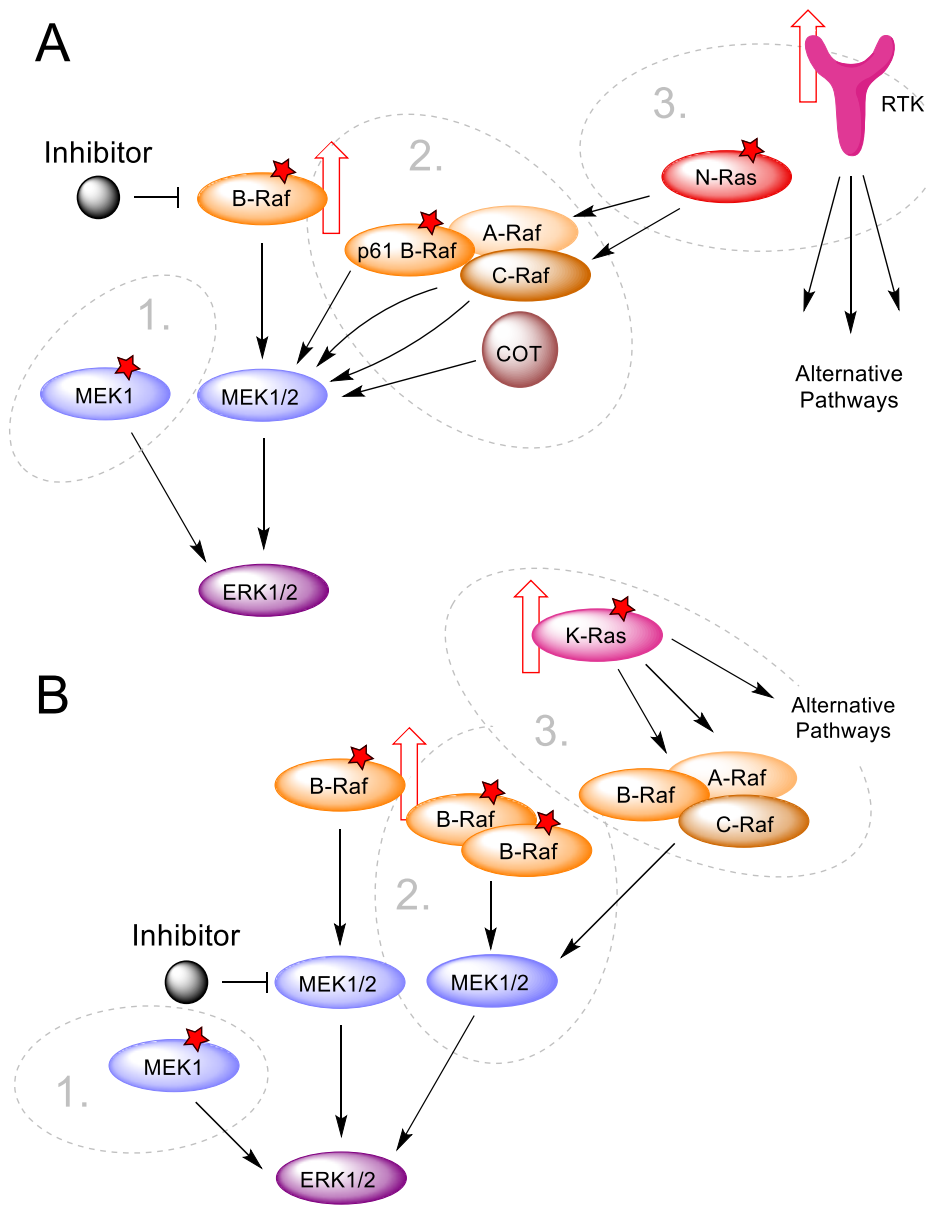


Figure 1.9. Models of acquired resistance to melanoma treatments.

(A) Acquired resistance to mutant B-Raf inhibitors resulting from (1) MEK mutation, (2) alternative activators of MEK, including BRAF-V600E spliceforms (p61 B-Raf), other Rafs, and MAP3Ks, and (3) signaling through alternative pathways driven by events such as upstream NRAS mutations and upregulated RTKs. (B) Acquired resistance to MEK inhibition arising from (1) MEK1 mutation, (2) upregulation of mutant B-Raf, and (3) mutant K-Ras to drive signaling through the remaining active population of MEK. Upregulated mutant K-Ras (3) can also drive signaling through alternate pathways (like PI3K) to overcome resistance. (Figure adapted from [40])

Chapter 2: Identification of Auranofin as a Bivalent, Irreversible ERK Inhibitor Using a High-Throughput Screening

ABSTRACT

Docking sites on mitogen-activated protein kinases (MAPKs) facilitate protein complex formation and help generate signaling specificity. Therapeutically targeting these sites offers a way to potentially overcome many issues associated with ATP-competitive MAPK inhibitor design. Extracellular signal-regulated kinases 1/2 (ERK1/2) are MAPKs that are up-regulated to drive numerous cancers. ERKs possess two protein docking sites that are distinct from the active site: the D-recruitment site (DRS) and the F-recruitment site (FRS). In this study, we have developed a novel high-throughput fluorescence anisotropy screen to identify small molecules that target the DRS of ERK2. The screen promotes identification of compounds that covalently target this region via Cys159. Over 23,000 molecules were screened for the ability to competitively displace a fluorescent peptide from the DRS. From the screen, we identified auranofin, an FDA-approved anti-rheumatic agent, as an inhibitor of ERK signaling that covalently targets the DRS of ERK2 at Cys159, in addition to the active site at Cys164. Both *in vitro* and in transfected HEK293T cells, mutating Cys159 and Cys164 together prevented inhibition of ERK by auranofin. The results here indicate the utility of targeting the DRS as a method for ERK inhibition and support the notion that the DRS cysteine is a viable target for covalent inhibition of ERK. Auranofin as a hit molecule shows that this covalent inhibition can be achieved by gold (I) -thiol bond formation, illustrating the potential to utilize the gold (I)-triisopropylphosphine electrophile of auranofin as a functional group in future ERK inhibitor design.

INTRODUCTION

Extracellular signal-regulated kinases (ERKs) are positioned at a critical location in the Ras/Raf/MEK/ERK signaling pathway. ERK transduces signals through this mitogen-activated protein kinase (MAPK) pathway as two classical isoforms: ERK1 and ERK2. Upon activation by upstream kinases, ERK1/2 can phosphorylate over 175 cytosolic and nuclear substrates, including transcription factors and other kinases [5, 160]. These phosphorylation events result in tightly controlled transcription of genes that facilitate processes such as cellular proliferation, differentiation, survival, and motility [5, 160]. Abnormal ERK signaling is a driving factor in many forms of cancer, where constitutive activation of ERK arises from alterations in the upstream pathway. These alterations include mutations in the three RAS genes (KRAS, NRAS, HRAS), MEK, and BRAF, with KRAS mutations present in 30% of human cancers [161]. These factors make the ERK pathway an attractive therapeutic target. However, there are numerous barriers to developing effective inhibitors of ERK signaling in cancer.

Traditional MAPK inhibitors are ATP-competitive, targeting a binding site that is highly conserved among the 518-member kinase family, which can lead to poor selectivity [5, 51, 52, 162]. An additional issue is that these direct inhibitors of kinases must out-compete ATP, which is present in cells at millimolar concentrations and binds to MAPKs with high affinity [50, 51]. This makes the design of potent ATP-competitive ERK inhibitors difficult. However, there are several known ATP-competitive inhibitors of ERK1/2 that inhibit at nanomolar-level IC_{50} s, such as VTX-11e [163], SCH772984 [113, 114], and the covalent inhibitor FR180204 [126]. Though these potent inhibitors exist, it is important to explore alternative avenues of inhibiting ERK signaling to combat drug resistance mechanisms and target particular signaling events in a tunable manner. In cancer, resistance-causing mutations within MAPK active sites are known to arise from

targeted ATP-competitive kinase inhibitors [40, 113, 164-166]. Furthermore, recent studies indicate that kinome remodeling in response to targeted kinase inhibitors results in rapid adaptive resistance in cancers [154, 155]. For all of these reasons, it is critical to explore inhibition of the known binding sites on ERK that facilitate substrate recognition and protein complex formation. These docking sites, the D-recruitment site (DRS) and F-recruitment site (FRS), are distinct from the active site of ERK. Thereby, they offer a method of ERK inhibition that is not ATP-competitive.

This study focuses on finding inhibitors of the DRS, an extended protein-binding site located opposite of the active site on the surface of ERK. It consists of a hydrophobic groove, a polar surface known as the ED domain, as well as a common docking domain of two aspartate residues [5]. Due to its size and varied chemical properties, potently inhibiting interactions at the DRS with a single small molecule is difficult. Numerous small-molecule inhibitors of the ERK DRS have been identified by computer-aided drug design (CADD) and *in silico* screening methods. These inhibitors have affinities for ERK ranging from approximately 5-20 μM [74, 76, 77], with some inhibitors showing *in vitro* IC_{50} values as high as 82 μM [79]. Current DRS inhibitors show significant cellular activity against ERK signaling at concentrations exceeding 50 μM [77, 78]. Highly potent inhibitors that target the DRS are therefore difficult to detect. We hypothesized that covalently targeting the DRS via a solvent-exposed cysteine residue located within its hydrophobic region (Cys159 for ERK2) could overcome these difficulties. Covalent kinase inhibitors offer potential for increased potency and selectivity when targeted to unique residues in comparison to reversible inhibitors. Therapeutically, they often require lower and less frequent doses than reversible inhibitors, have a longer duration of action, and have potential to effectively target shallow, solvent-exposed sites that are difficult to drug, like the DRS [167]. Once

bound, irreversible covalent inhibitors are not susceptible to increased substrate concentrations. Due to their permanent modification of enzymes, irreversible inhibitors also have potential to overcome acquired resistance mechanisms that are often observed in cancer [123, 124, 168].

To our knowledge, there are currently no reported biochemical high-throughput screening methods to specifically discover ERK DRS inhibitors, though one has been developed for the FRS [169]. Biochemical screening methods are typically designed to favor ATP-competitive kinase inhibitors, where inhibitors are identified by measured reduction of kinase activity. Non-ATP competitive inhibitors can only potentially be identified from kinase activity-based screens after extensive kinetic characterization of hit molecules. Here, we report a fluorescence anisotropy assay to detect small molecules that bind to the DRS by competitively displacing a fluorescent peptide probe. The screen was designed to preferentially identify covalent modifiers of Cys159 in the DRS of ERK2 by eliminating use of reducing agents and allowing sufficient time for covalent molecules to react and achieve maximum potency. We ultimately show that covalently targeting Cys159 is a viable method of ERK2 inhibition by example of auranofin, one of the top inhibitors identified from the screen.

MATERIALS AND METHODS

Proteins, Peptides, and Buffers

Proteins: Tag-less ERK2 was expressed, purified, and activated essentially as described in [112]. Erk2 DNA (NM_053842) was ligated into a pet28a (+) vector that was modified to include a TEV cleavage site for His₆-tag removal. Vector modification and cleavage of the His₆-tag with TEV protease were performed as described in [170]. ERK2 was activated using the constitutively active MKK1G7B mutant [171]. Active

ERK2 mutants (C159S, C164A, Cys-less, -Cys+C159) were expressed and purified essentially as described in [172] and activated in the same manner as WT ERK2. GST-c-Jun and active JNK2 were prepared as previously reported [170, 173].

Peptides: The ERK substrate peptide Sub-D was prepared as described in [105]. The control peptide Lig-D(Dap) was synthesized in the same manner as the DRS ligand Lig-D in [97], with the exception that diaminopropionic acid (Dap, or, Fmoc-Dap(MTT)-OH from Chem-Impex International) was substituted for Gly-13 in the peptide sequence. Sox-labeled Sub-D (sox-Sub-D) was synthesized by alkylation of sox-Br (2-bromomethyl-8-tertbutyldiphenylsilyloxy-5- (N, N-dimethyl) sulfonamide quinolone) to Sub-D on resin [174, 175]. Sox-Br was provided by William H. Johnson at the University of Texas at Austin. FITC-labeled Lig-D (FITC-X-Lig-D) was prepared by labeling the C-terminus of Lig-D with FITC via a 6-aminohexanoic acid linker on a cysteine residue [32]. For peptide sequences and synthesis of sox-labeled peptides, see Appendix A.

Buffers: The following buffers were used for all *in vitro* ERK2 assays: anisotropy buffer (25 mM HEPES pH 7.5, 50 mM KCl, 0.1 mM EDTA, 0.1 μ M EGTA, 1.3% glycerol), kinase assay buffer (50 mM HEPES pH 7.5, 100 mM KCl, 0.1 mM EDTA, 0.1 mM EGTA, 10 mM MgCl₂, 10 μ g/mL BSA), and fluorescence assay buffer (25 mM HEPES pH 7.5, 50 mM KCl, 0.1 mM EDTA, 0.1 μ M EGTA, 10 mM MgCl₂, 10 μ g/mL BSA, 0.01% (v/v) Triton X-100).

Primary Fluorescence Anisotropy Screening

All fluorescence anisotropy measurements were collected at room temperature on a Synergy H4 plate reader using a 480 nm excitation filter and a 512 nm emission filter. Assays were performed at room temperature in 30 μ L reaction volumes in anisotropy

buffer with 10 $\mu\text{g}/\text{mL}$ BSA. Samples contained 10 nM FITC-X-Lig-D and 1 μM ERK2 (inactive, His₆-cleaved), with or without library compounds. Compounds were diluted in anisotropy buffer from 10 mM DMSO stocks to reach a final assay concentration of 50 μM and 0.5% DMSO. Positive controls included 50 μM Lig-D(Dap) with 10 nM FITC-X-Lig-D and 1 μM ERK2, and 10 nM FITC-X-Lig-D alone in anisotropy buffer with 10 $\mu\text{g}/\text{mL}$ BSA. Compounds or DMSO controls were allowed to incubate with the enzyme-peptide mixture for 1 hour before data collection. Details of the screening process and assay optimization can be found in Appendix B.

Secondary Activity-Based Screening

The ability of 2 nM ERK2 (active, His₆-cleaved) to phosphorylate 10 μM Sub-D in the presence of 10 and 50 μM compounds (0.1 and 0.5% (v/v) final DMSO) and saturating [γ -³²P] MgATP (1 mM) was assessed in kinase assay buffer with 0.01% Triton X-100. Positive controls were (1) background (kinase assay buffer) and (2) assay mixture with either 10 or 50 μM of Lig-D(Dap) as a known inhibitor of the DRS. Negative controls were (1) assay mixture with no compounds present and (2) selected non-binding compounds from the primary screening. The assay was performed in 96-well plate format at room temperature, with total reaction volumes of 50 μL . 10 μL of each compound at 5X their final concentration were added to 35 μL of assay mixture, following dilution in assay buffer. After 30 minutes of incubation at room temperature, reactions were initiated by addition of 5 μL of 10 mM [γ -³²P] MgATP. The reactions were quenched after 10 minutes by transfer of 35 $\mu\text{L}/\text{well}$ reaction mixture to 96-well plates containing P-81 filter paper (Whatman) and 50 mM phosphoric acid (approx. 200 μL per well). The plates were washed 10X, or until flow-through reached background CPM levels, with 50 mM phosphoric acid and 1X with acetone using a MultiScreen^{HTS}

Vacuum Manifold system (EMD Millipore). After fully drying the P-81 paper, the plate bottoms were sealed with MutliScreen Sealing Tape (EMD Millipore). Each well was filled with 20 μ L of OptiPhaseTM SuperMix liquid scintillation cocktail (Perkin Elmer), and the plate tops were sealed in the same manner as the bottoms. The counts in each sample were read using a MicroBeta[®]TriLux microplate scintillation counter (Perkin Elmer). Hits were ranked by their relative % inhibition of ERK2 at each concentration.

Selection of Hit Compounds

The top 100 compounds were ranked from 0 to 99 based on their percent inhibition (secondary screening) or % displacement (primary screening validation) with 99 being the most effective inhibitor. A weighted average of each validation assay result was used to find the best hits. Each ranking was normalized by the respective compound concentration used, and these values were averaged as follows.

Equation 2.1:

$$score = \frac{1}{5} \left(\frac{A}{5.5} + \frac{B}{16.7} + \frac{C}{50} + \frac{D}{10} + \frac{E}{50} \right)$$

Here A, B, and C are the rankings for the anisotropy validation assays at 5.5, 16.7, and 50 μ M of each compound, and D and E are the rankings for the secondary screening assays at 10 and 50 μ M of each compound, respectively.

Anisotropy Dose-Response Assays

1 μ M ERK2 (inactive, His₆-cleaved) was pre-incubated with 10 nM FITC-X-Lig-D and 0, 1, 2.5, 5, 10, 25, 50, 100, and 200 μ M of each compound at room temperature for 45 minutes prior to anisotropy measurements as described for the primary screening. For inactive C159S mutant ERK2, 5 μ M enzyme and 50 nM FITC-X-Lig-D were used to

account for their weaker binding affinity and resulting lower anisotropy signal. K_d for C159S ERK2 binding to FITC-X-Lig-D was determined in the same manner as for WT ERK2. Each sample contained 0.01% Triton X-100, 10 $\mu\text{g/mL}$ BSA, and a final concentration of 2% DMSO in anisotropy buffer. Anisotropy values were corrected for compound intrinsic fluorescence as described in the screening validation procedure. The anisotropy dose-response curves were fit to an equilibrium binding model for conditions where the FITC-X-Lig-D substrate concentration is much less than the concentration of ERK2 [67, 68]. Curve fitting was performed in GraphPad Prism software (see Appendix B).

³²P Dose-Response Assays

ERK2 DRS inhibition: 2 nM ERK2 was pre-incubated with 0-200 μM of each compound for 20 minutes at room temperature prior to reaction initiation by the addition of 10 μM Sub-D and 1 mM [γ -³²P] MgATP. Reactions were initiated by addition of 2 nM ERK2 and performed at 28°C. *JNK2 inhibition:* 25 nM JNK2 was pre-incubated with 0 – 50 μM inhibitor (compounds 3, 4, 5, 18, 21) for 20 minutes at room temperature. Reactions were initiated by addition of 2 μM GST-c-Jun and 0.5 mM [γ -³²P] MgATP. All reactions were carried out at 28°C in kinase assay buffer with 0.01% Triton X-100. Phosphorylated substrate was quantified at 0.5, 1, 1.5, 2, and 4 minute time points as previously described (³²P protocol) [176] on a MicroBeta®TriLux scintillation counter (Perkin Elmer).

Fluorescence Dose-Response Assays

Assays and data analysis were performed essentially as previously described [177]. 2 nM ERK2 was pre-incubated with 0 – 50 μM inhibitor for 20 minutes at room

temperature in fluorescence assay buffer, prior to addition of 2 μM sox-Sub-D and 1 mM MgATP. Data were collected on a Perkin Elmer 1420 multilabel counter with a 355/40 nm excitation filter and 460/25 nm emission filter and integration time of 0.1 s. Fluorescence intensity was measured at room temperature every 40 seconds for 1 hour.

Assays for Recovery of ERK2 Activity

Auranofin (0 or 50 μM) was pre-incubated in fluorescence assay buffer with 1 nM ERK2 variants (WT, C159S, C164A, Cys-less, -Cys+C159) for 10 minutes at room temperature prior to addition of 10 μM sox-Sub-D and 1 mM MgATP. Alternatively, ERK2 variants were pre-incubated with 1 mM MgATP for 5 minutes prior to addition of auranofin or DMSO and sox-Sub-D. Initial rates were collected at 26°C for 300s on a Horiba Jobin-Yvon Fluorolog-3 spectrofluorometer.

Preparation of Cell Lysates

HEK293T cells were maintained in DMEM with 10% (v/v) FBS, 2 mM L-glutamine, 100 U mL⁻¹ penicillin, and 100 g mL⁻¹ streptomycin. All cell culture reagents were from Sigma-Aldrich or Thermo Fisher Scientific. Cells were cultured at 37°C in a humidified incubator with 5% CO₂.

For transfection experiments, HEK293T cells were plated into poly-D-lysine - coated 12-well plates at 600,000 cells per well in antibiotic-free media. After reaching 50-60% confluence, the cells were transfected with the following DNA by Lipofectamine®3000 protocol: WT ERK2, C164A ERK2, C159A ERK2, C159A/C164A ERK2, pcDNA3 (empty vector). Transfections were performed in antibiotic-free media, using 1 μg DNA and 1.5 μL Lipofectamine reagent per well. Non-transfected cells were included as an additional control. After 30 hours, the media was removed and transfected

(and non-transfected) cells were treated with 5 or 10 μM auranofin or 1% (v/v) DMSO in serum-free media for 12 hours. The cells were then treated with/without 0.1 μM EGF (Invitrogen) for 25-30 minutes to stimulate ERK signaling and immediately washed with PBS (Thermo Fisher Scientific). The cells were lysed on ice for 10-15 minutes in M-PER™ Mammalian Protein Extraction Reagent (Thermo Scientific) supplemented with 10 $\mu\text{L}/\text{mL}$ Halt™ Protease and Phosphatase Inhibitor Single-use Cocktail (Thermo Scientific). Lysates were flash-frozen in liquid N_2 and stored at -80°C .

Western Blots

Thawed lysates were cleared by centrifugation and protein concentrations were evaluated by Bradford assay (Bio-Rad). A total of 40 μg protein per sample was resolved on 10% SDS polyacrylamide gels and transferred to Immobilon®-FL PVDF membranes (EMD Millipore). Membranes were blocked for 1 hour at room temperature with 4X diluted Odyssey® Blocking Buffer (PBS) (LI-COR). Membranes were incubated with primary antibodies overnight at 4°C in 5% BSA or non-fat dry milk in Tris-buffered saline/Tween® 20 (TBST) according to manufacturer protocols. The membranes were then washed in TBST and incubated with appropriate secondary antibodies for 1 hour at room temperature. After washing again with TBST and Tris-buffered saline, fluorescence was detected on an Odyssey® Sa imaging system (LI-COR) and quantified.

All primary antibodies are from Cell Signaling Technology unless otherwise noted: 1:2000 antiphospho-p44/42 MAPK (Erk1/2) (Thr202/Tyr204) (D13.14.4E) XP® rabbit mAb; 1:1000 anti-p44/42 MAPK (Erk1/2) (137F5) rabbit mAb; 1:2000 antiphospho-SAPK/JNK (Thr183/Tyr185) (G9) mouse mAb, antiphospho-p38 α (Thr180/Tyr182) clone 8.78.8 rabbit mAb (EMD Millipore); 1:6000 anti-actin (clone C4) mouse mAb (EMD Millipore); 1:3000 anti-vinculin (E1E9V) XP® rabbit mAb.

Secondary antibodies: 1:15000 IRDye® 800CW Goat (polyclonal) anti-rabbit IgG or IRDye® 680RD Goat (polyclonal) anti-mouse IgG (LI-COR).

RESULTS AND DISCUSSION

Anisotropy Assay Detected Small Molecules That Bind to the DRS

In order to develop a method to screen for DRS inhibitors, we reasoned that we could design a competitive displacement assay using a previously identified peptide, Lig-D, that binds to the DRS of ERK2 [97]. By linking the fluorophore FITC to this peptide and allowing it to bind to ERK2, small molecules that target the DRS can be identified by change in anisotropy signal upon displacement of the peptide (FITC-X-Lig-D). To test this concept, we first incubated FITC-X-Lig-D (10, 60 or 100 nM) with varied concentrations of ERK2 (inactive, His₆-cleaved) from 0-12 μ M. Anisotropy values were measured at equilibrium after 10-20 minutes of incubation. Apparent dissociation constants were estimated at each FITC-X-Lig-D concentration using a basic single step binding model (Supplementary Figure B1). FITC-X-Lig-D concentration was minimized at 10 nM without loss of signal. The observed dissociation constant ($K_{d,obs}$) for this condition was then calculated to be $0.57 \pm 0.12 \mu$ M by fitting the binding data to a previously established anisotropy model [67] (Figure 2.1 A). Using the binding curve, we fixed ERK2 concentration at 1 μ M for the competition assay in order to achieve a robust anisotropy signal for the negative control (no displacement of fluorescent peptide). To test competitive displacement of the fluorescent probe, we incubated a non-fluorescent DRS-binding peptide (Lig-D(Dap)) at 0-200 μ M with 10 nM FITC-X-Lig-D and 1 μ M ERK2 and measured resulting anisotropy. The observed IC₅₀ for the non-fluorescent peptide was measured at $0.83 \pm 0.15 \mu$ M (Figure 2.1 B). Lig-D(Dap) fully displaced the fluorophore from ERK2 at 50 μ M by comparison to background anisotropy

measurements, so this concentration was selected for use as a positive control in the high-throughput screening.

To prepare the assay format for high-throughput screening, we first tested the tolerance of the control signals to increasing amounts of DMSO. All stocks of library compounds used in the screen were dissolved in DMSO. We selected a final concentration of 0.5% (v/v) DMSO for the screening assay to maximize compound concentration while minimizing effects on anisotropy signal (Supplementary Figure B2). In high-throughput assay development, the Z-factor is a statistical parameter often used to assess assay quality [178]. A 384-well validation plate consisting of positive and negative controls, representing maximum and minimum fluorophore binding, yielded a test Z-factor of 0.80. This value indicated that the screening design was of sufficient quality to identify DRS inhibitors (Supplementary Table B1).

We then applied the displacement assay to 23,534 compounds at 50 μ M, allowing them to incubate with ERK2-bound FITC-X-Lig-D for approximately 1 hour prior to data collection. Hit compounds were identified as causing over 50% change in anisotropy signal from the negative controls (Figure 2.1 C). This yielded 204 compounds, indicating a hit rate of 0.87% with an overall average Z-factor of 0.86. Figure 2.1 D shows a selection of data from the screen that illustrates library compound results compared to each control group and the hit threshold of 50% signal change. If it is initially assumed that the FITC-X-Lig-D binding state is the only influence on anisotropy and the binding state does not affect FITC emission intensity, a library compound inducing a 50% signal change indicates that 50% of bound FITC-X-Lig-D has been displaced from the DRS. However, several factors aside from the relative amounts of free and bound FITC-X-Lig-D can affect anisotropy. Intrinsic fluorescence of compounds at the emission wavelength of FITC-X-Lig-D as well as scattered light from aggregated compounds can generate

false positives and negatives. The most obvious of these false positives and negatives in the screening data were compounds that generated percent signal changes over 100% or under 0%. In order to account for potential aggregate inhibition, the 204 compounds were assessed at varied concentrations by anisotropy assays incorporating 0.01% Triton X-100 [179, 180]. Additionally, the anisotropy measurements were corrected for any intrinsic compound fluorescence. To further rule out false hits, we tested the resulting top 100 compounds in a secondary validation assay, measuring their ability to prevent ERK2 phosphorylation of a D-site substrate peptide (Sub-D) [105] at both 10 and 50 μM (Figure 2.1 E). We ultimately selected the top 30 compounds arising from the aggregation test and secondary assay using a concentration-weighted score (equation (2.1)) and narrowed this to 21 based on compound safety and availability (Supplementary Table B2).

Screening Hits Inhibited Phosphorylation of Peptide Substrate by ERK2

We evaluated the top 9 inhibitors (compounds 3, 4, 5, 12, 13, 16, 18, 21, and 23) by a fluorescence-based dose-response assay. The ERK2 substrate used here was the Sub-D peptide modified to include a chelation-enhanced sox moiety. Sox fluorescence increases in the presence of 10 mM Mg^{2+} when the peptide is phosphorylated by active ERK2 [174]. As seen in Table 2.1 and Supplementary Figure B3, all of the 9 compounds show IC_{50} values of less than approximately 12 μM . The compounds were also evaluated in anisotropy dose-response assays to determine their observed dissociation constants, or K_i^* values (Table 2.1, Supplementary Figures B4, B5, and B6). K_i^* values were defined as the observed compound binding affinity (K_i) after approximately 45 minutes of incubation of 0-200 μM compound with ERK2 and FITC-X-Lig-D. The values were fit according to a previously established binding model that accounts for the high

concentration of ERK2 compared to the fluorescent probe (see Appendix B). This model also corrects for differing fluorescence intensities of free and bound fluorophore. However, the model only describes an apparent K_i value in this study because it assumes reversible equilibrium binding with 1:1 stoichiometry. As discussed later, this is not the case for many of the hit compounds. K_i^* , like the IC_{50} here, is used as a method of comparing the top hits to one another. It can be considered a complimentary method to validate the order of magnitude of potency of the compounds as determined by IC_{50} , and, like the IC_{50} values, is not intended to be absolute.

Screening Preferentially Detected Reactive Small Molecules

We then sought to determine if the compounds interacted at Cys159 in the DRS of ERK2. When the cysteine residue in the DRS (Cys159) was mutated to serine, the compounds showed no quantifiable binding in the anisotropy dose-response assays (Table 2.1 and Supplementary Figures B4, B5, and B6). This implies that Cys159 forms critical interactions with all 9 of the compounds. When selected compounds (3, 4, 5, 18, 21) were tested for inhibition of JNK2 phosphorylation of c-Jun, they showed similar magnitude IC_{50} values to ERK2 (Table 2.1 and Supplementary Figure B7). This suggests that they likely target the kinase DRS motif non-specifically, or they target other additional locations on the proteins. Based on the potentially reactive chemical moieties found on the top 9 compounds, we predicted that they likely covalently modify Cys159. To evaluate this, the compounds were incubated with ERK2, and all unreacted compounds were removed by size-exclusion column and dilution. The ability of ERK2 to phosphorylate Sub-D was then measured, and only compound 5 showed recovery of activity similar to controls (Table 2.1, Supplementary Figure B9 and Table B4). This coincides with the structure of compound 5 showing no notably reactive functional

groups (Table 2.1). These results indicate that all of the compounds are likely reactive with ERK2, potentially excluding compound 5.

Compound reactivity is required in order to covalently target Cys159, however, reaction promiscuity is generally undesirable. Highly reactive covalent inhibitors can generate off-target effects and toxicities. The top hits, other than compound 5, likely meet the criteria of being both reactive and targeting numerous cellular proteins according to definitions of assay interference compounds (PAINs) [181, 182]. Ideal covalent inhibitors must balance selectivity and reactivity to maximize potential therapeutic index. However, deprioritizing hits based on the use of PAINs filters for substructural features has been found to overlook potential drug candidates [183, 184]. It has also been shown that compounds with substructures that match criteria for PAINs do not actually reflect increased activity trends in a broad study of different screenings [185]. We cross-referenced the 9 hit compounds from this screening with 4 other screenings that we have performed in the absence of reducing agents, against the proteins ENL, NDM-1, Aldolase A, and TRIM24. We found that compounds 3, 5, and 21 were not hits in any of these screenings, but the other 6 compounds were hits for one or more of the proteins. Hits here were defined as having a minimum of 50% inhibition under screening conditions. This assessment indicates that while some hit compounds may match PAINs criteria, they are not necessarily promiscuous inhibitors. Rather than using PAINs definitions as a filter, we looked for other indicators to warrant further investigation of the hit compounds. Compound 3 was selected as a promising hit for several reasons. Compound 3 is auranofin (AF), an FDA-approved anti-rheumatic drug that is under investigation for its antimicrobial properties (NCT02089048, NCT02736968) and also for treatment of HIV/AIDS (NCT02961829), several cancers (NCT01747798, NCT01419691, NCT01737502, NCT02770378), and neurodegenerative disorders [186].

Its pharmacology profile is well-evaluated [187] and it shows potential for drug-repurposing. Therefore, we chose to further evaluate AF inhibition of ERK2.

Auranofin Inhibits ERK2 via Cys159 and Cys164

AF is known to be a covalent inhibitor, so in order to confirm interaction of AF at the DRS, we studied its effects on different cysteine mutants of ERK2 *in vitro*. Here, we tested the ability of ERK2 variants to phosphorylate a fluorescent peptide (sox-Sub-D) in the presence of AF. Mutating all ERK2 cysteine residues to alanine (Cys-less ERK2) completely recovered activity of AF-treated ERK2 to DMSO-treated control levels, but individual cysteine mutations in the active site (C164A) or DRS (C159S) did not (Figure 2.2 A). In fact, C159S ERK2 showed no noticeable recovery of activity compared to WT ERK2, and C164A ERK2 showed partial recovery, suggesting that AF may inhibit with greater potency at the active site. Together, these data indicate that AF activity against ERK2 is fully dependent on cysteine interactions. Additionally, protecting the active site with 1 mM ATP prior to treatment with AF gave full recovery of activity, with respect to DMSO controls, to C159S ERK2 but not WT ERK2 (Figure 2.2 B). This again suggests that AF interacts in the active site as well as the DRS. For mutant ERK2 with a single intact cysteine in the DRS (-Cys+Cys159), ATP protection of the active site did not affect activity in response to AF treatment when compared to C164A ERK2. This indicates that inhibition of the -Cys+C159 and C164A mutants of ERK2 arises solely from interactions at C159. All together, these results signify that AF interacts with two cysteine residues on ERK2: Cys164 and Cys159, located in the active site and DRS, respectively. It is also apparent from these data that binding of AF at each site contributes to the inhibition of ERK2. We further validated that AF covalently interacts with ERK2 at two locations by mass spectrometry (Supplementary Figures B10 and B11).

We then tested whether AF targets both the active site and DRS cysteines of ERK in HEK293T cells. In this case, we looked at effects of AF on activation of ERK, as MEK is known to interact at the ERK DRS [66]. Different ERK2 variants (wildtype (WT), C159A, C164A, and C159A/C164A) were overexpressed in these cells, and ERK pathway activation was stimulated with EGF. Upon pathway stimulation, auranofin inhibited ERK phosphorylation at 5 μ M in all cases after 12 hours of treatment except for the double mutant C159A/C164A ERK2 (Figure 2.3). This indicates that mutation of these two residues prevents AF effects on ERK activation.

It is expected that AF would block ERK activation by MEK for the C164A ERK2 mutant in cells and have no effect on C159A ERK2 activation, given that MEK is known to bind at the DRS in order to phosphorylate Thr/Tyr of the ERK activation loop. It has been shown that docking at the DRS can induce an alternate conformation of the activation loop of ERK, such that the Thr/Tyr residues become solvent exposed and primed for phosphorylation [188, 189]. This conformation does not match the fully active or inactive conformations of ERK but is possibly an intermediate conformation that prepares ERK for phosphorylation by MEK or dephosphorylation by phosphatases. As shown in this study, auranofin can inhibit ERK2 activation by MEK in cells by either disrupting the DRS interaction at Cys159 or by targeting the ATP-binding site via Cys164 (Figure 2.3). Blocking the DRS interaction should theoretically be enough to prevent MEK phosphorylation of ERK, given that this docking interaction influences the activation loop [189]. It is possible that auranofin binding in the active site can alter the conformation of the activation loop in such a way that phosphorylation of ERK is prevented, as has been observed with the ERK inhibitor SCH772984 [114]. Inhibition of ERK activation by AF in C159A ERK2 cells can also potentially be explained by other factors. For example, MEK1/2 activation of ERK may be impaired to a greater degree

than phosphatase activity, causing a net dephosphorylation of ERK in these cells. Also, AF binding in the active site could cause conformational changes that alter the scaffolding and subcellular localization interactions that are necessary for ERK phosphorylation. These mechanisms can potentially explain why both mutation of Cys159 and Cys164 are necessary to prevent ERK inhibition by AF in cells. In contrast, for downstream inhibition, the *in vitro* Sub-D –based peptide substrate utilizes both the DRS and the ATP-site of ERK2 in order to be phosphorylated, so blockage at either site by auranofin explains inhibition of Sub-D phosphorylation. This inhibition can only be rescued *in vitro* by mutation of both Cys159 and Cys164.

Other Effects of Auranofin in Cells

In these same transfected HEK293T cells, no inhibition of JNK or p38 α phosphorylation was observed at 5 μ M AF (Figure 2.4). Rather, JNK and p38 α phosphorylation exhibited an overall dose-dependent activation in response to AF treatment. For JNK, this stimulated phosphorylation subsided by 10 μ M doses of AF, while conversely for p38 α , activation was most notable at 10 μ M AF (Figure 2.4). This activation of other MAPK pathways can be potentially explained by the known stress-inducing effects of AF in cells. AF has been shown to inhibit thioredoxin reductase and is also a broad-spectrum deubiquitinase inhibitor, thereby inducing oxidative stress and intrinsic apoptosis that can culminate in the activation of the JNK and p38 MAPK pathways [190-193].

AF also inhibited HEK293T cell proliferation in a dose dependent manner, with $EC_{50} = 0.7 \pm 0.2 \mu$ M after 3 days of treatment (Supplementary Figure B12 C). In 2-D clonogenic assays, AF inhibited HEK293T colony size at 0.5 μ M as seen in Supplementary Figure B12 A. In analogous anchorage-independent growth assays, AF

significantly reduced the number of colonies per well at 0.5 μ M (Supplementary Figure B12 B). However, it is unclear whether the results of these phenotypic assays are due to ERK pathway inhibition or other effects of auranofin, such as ROS generation and intrinsic apoptosis.

In addition to its involvement in oxidative stress, auranofin has been observed to down-regulate JAK/STAT signaling [194], antiapoptotic protein Mcl-1, NF- κ B transactivated anti-apoptotic proteins [195], PKC activity [191, 196] and proinflammatory cytokines [197]. To date, the observed effects of AF on ERK signaling appear to be cell type- and dose-dependent [198]. The off-pathway effects of AF, in addition to ERK inhibition, can potentially be of therapeutic benefit. Increasingly, inhibitors with polypharmacological behavior have been recognized as possible drug candidates. It is apparent that auranofin's versatility is the source of its clinical and pre-clinical success in such a broad range of disease states. Therefore, the possible off-target effects of auranofin here could be an advantage in cancer therapy.

Proposed Models for ERK Inhibition by Auranofin

Figure 2.5 illustrates a scheme of potential outcomes of inhibiting the DRS of ERK. Blocking the DRS can result in direct inhibition of ERK interactions with substrates (like the kinases RSK-1 [62, 63] and MAPKAPK2 (MK2) [64], caspase-9 [65]), phosphatases (such as MKP-5 and HePTP [64]), and activators (MEK1/2 [66]). Binding at the DRS can also influence the conformation of ERK2 as discussed earlier, which can result in allosteric inhibition at other locations on the kinase [189]. Disruption of particular protein interactions with ERK can result in altered subcellular location. For example, the MEK/ERK interaction is involved in sequestration of ERK in the cytoplasm [71, 72]. Additionally, the protein PEA-15 directly interacts at both the DRS and FRS of

ERK and is known to retain ERK in the cytoplasm as well [67-70]. Blocking the DRS can also affect the mechanism of phosphorylation of ERK substrates that utilize multiple docking sites. For example, the transcription factor Ets-1 undergoes bipartite binding to the DRS and FRS in order to place its phosphorylation site in close proximity to the ERK active site for efficient phosphorylation [56]. Blocking the DRS with small molecules can result in partial inhibition of Ets-1 phosphorylation (data not shown), as the proximity-mediated mechanism is disrupted. Thus, phosphorylation of specific substrates may still be possible with inhibitors present at the DRS but may occur by different methods or at different efficiencies. Blocking the ERK signaling pathway can also result in upregulation of alternative signaling pathways and kinome remodeling to achieve the same signaling outcomes [58, 154, 199]. In many of these examples, the off-target effects of auranofin or its bivalent inhibition of ERK may be more beneficial for preventing ERK signaling outcomes than an inhibitor that targets the DRS alone. This is especially true when considering that the cellular pool of ERK can retain its full signaling capacity when only 10% of ERK is activated [200]. In therapeutic contexts where full pathway inhibition is desired, auranofin irreversibly targets two key locations on ERK so it may be more effective than reversible or single-site inhibitors. In contrast, selectively targeting the DRS may further reveal its roles in ERK signaling or allow particular ERK interactions to be targeted discretely. This can be accomplished by functionalizing the gold (I)-triisopropylphosphine electrophile of auranofin with DRS-selective inhibitors in future studies.

CONCLUSIONS

Though it is clear that further structural optimization of auranofin is necessary to improve specificity and potency, its ability to target ERK2 at both Cys159 and Cys164

could be beneficial in treatment of cancer via ERK pathway inhibition. Fundamentally, the screening method developed here successfully identified compounds that covalently target the DRS of ERK2 through Cys159. Further iterations of the screen could potentially generate other types of novel ERK inhibitors. For example, using a high concentration of ATP in the screening to protect the active site of ERK could yield hits that exclusively target the DRS, whereas auranofin targets both the DRS and active site. Inclusion of reducing agents in the assay would facilitate finding reversible inhibitors. Different inhibitors could also be identified by using active rather than inactive ERK2 in the screen, or a fluorescent peptide ligand that binds the active site or FRS. Thus, the screening method presented here is a valuable and versatile tool for identifying molecules that interact with ERK. These molecules can be used to probe ERK signaling events that are mediated by specific binding sites and can be further optimized to yield highly selective ERK inhibitors with potential therapeutic value. This is illustrated by the top hit from the screen, auranofin. Overall, the findings here suggest that covalently targeting the DRS is a viable approach to ERK inhibition that warrants further investigation.

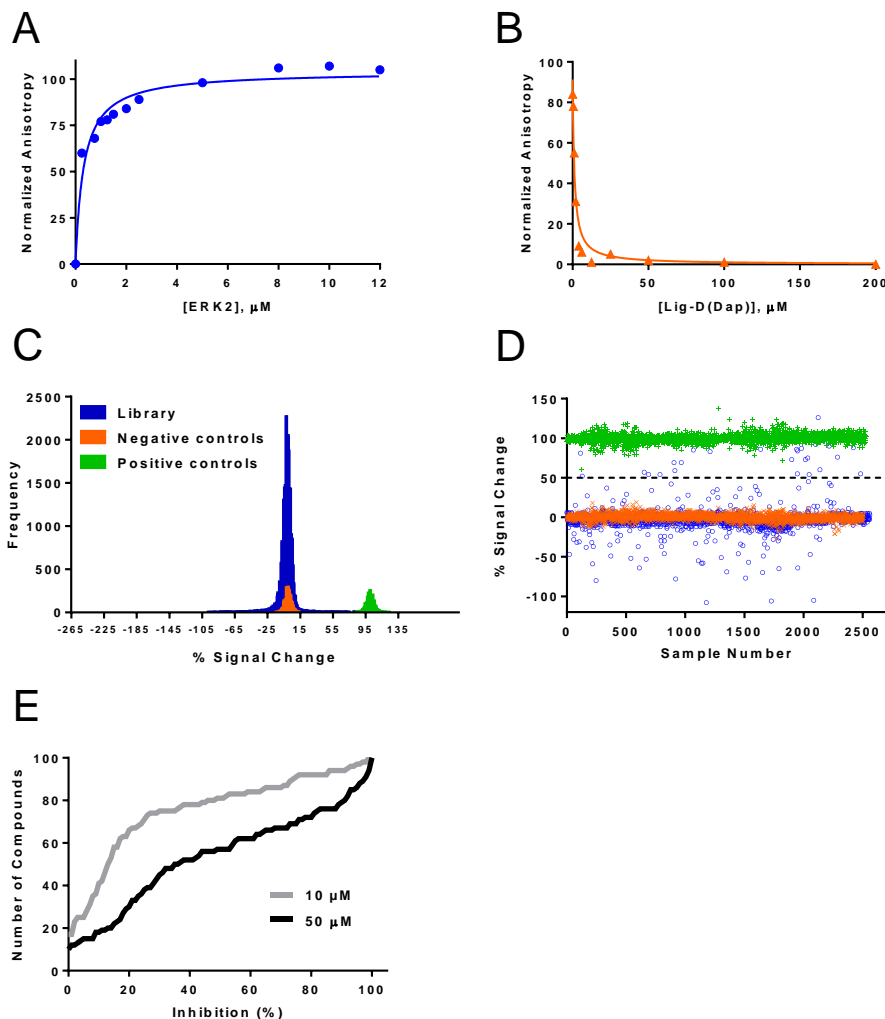


Figure 2.1. Fluorescence anisotropy screening and secondary screening.

(A) The dissociation constant for ERK2 binding to FITC-X-Lig-D was determined by incubating varied concentrations of ERK2 with 10 nM FITC-X-Lig-D for 10-20 min prior to anisotropy measurements. (B) To test competitive displacement of FITC-X-Lig-D, Lig-D(Dap) at 0-200 μM was incubated with 10 nM FITC-X-Lig-D and 1 μM ERK2 prior to anisotropy measurements. (C) Histogram of all primary screening data: positive controls (green), negative controls (orange), and samples (blue). (D) Plot of representative data from the primary screening: 2506 negative controls (orange x's), 2528 positive controls (green crosses) and 2561 samples (blue circles). The dashed line indicates the hit threshold of $\geq 50\%$ signal change. (E) Cumulative frequency distribution of secondary screening percent inhibition data for both 10 and 50 μM compound concentrations. Normalized anisotropy is with respect to positive controls. % Signal change is defined in methods as a function of positive and negative controls.

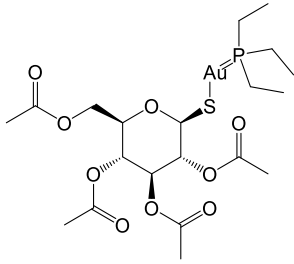
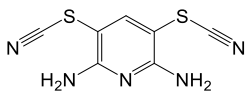
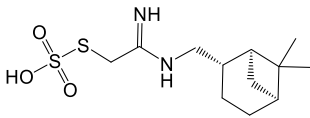
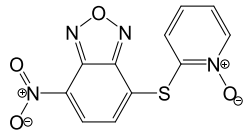
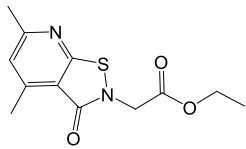
Compound #	Structure	WT ERK2 IC ₅₀ , μM	WT ERK2 K _i [*] , μM	C159S ERK2 K _i [*] , μM	JNK2 IC ₅₀ , μM	Reactivity/ (% residual activity)
3		1.6 ± 0.3	1.4 ± 0.2	> 1900	3.6 ± 0.4	Yes/ (28)
4		0.38 ± 0.06	0.19 ± 0.04	> 900	1.0 ± 0.3	Yes/ (12)
5		1.5 ± 0.3	0.50 ± 0.13	NI	2.2 ± 0.6	Potentially/ (62)
12		0.93 ± 0.21	4.5 ± 1.0	NI	NC	Yes/ (none)
13		1.3 ± 0.2	3.2 ± 1.6	NI	NC	Yes/ (19)

Table 2.1. IC₅₀ and K_i^{*} values for the top 9 screening hits.

The top compound structures and IDs are listed. For IC₅₀ measurements, the compounds were tested for inhibition of ERK2 (2 nM) phosphorylation of sox-Sub-D (2 μM) or for inhibition of JNK2 (25 nM) phosphorylation of GST-c-Jun (2 μM) after 20 min pre-incubation. For determination of K_i^{*} values by anisotropy, 1 μM WT ERK2 (or 5 μM C159S ERK2) was incubated with the compounds and 10 nM (or 50 nM) FITC-X-Lig-D for 45 minutes prior to anisotropy measurements. Reactivity of the compounds was assessed by structural analysis, and percent residual activity was determined by a covalent test (Appendix B): compounds were incubated with ERK2 and excess compound was then removed by dilution and dialysis, prior to testing ERK2 activity. NI = no observed inhibition; NC = not tested.

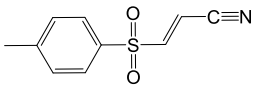
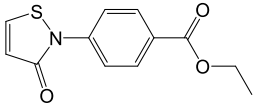
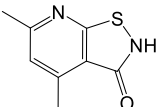
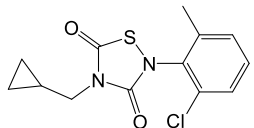
Compound #	Structure	WT ERK2 IC ₅₀ , μM	WT ERK2 K _i [*] , μM	C159S ERK2 K _i [*] , μM	JNK2 IC ₅₀ , μM	Reactivity/ (% residual activity)
16		11 ± 5.2	6.6 ± 2.2	NI	NC	Yes/ (none)
18		0.27 ± 0.02	8.9 ± 3.6	NI	0.06 ± 0.02	Yes/ (26)
21		12 ± 1.6	4.5 ± 1.4	> 1000	0.77 ± 0.23	Yes/ (16)
23		0.97 ± 0.14	6.4 ± 3.3	NI	NC	Yes/ (11)

Table 2.1, continued.

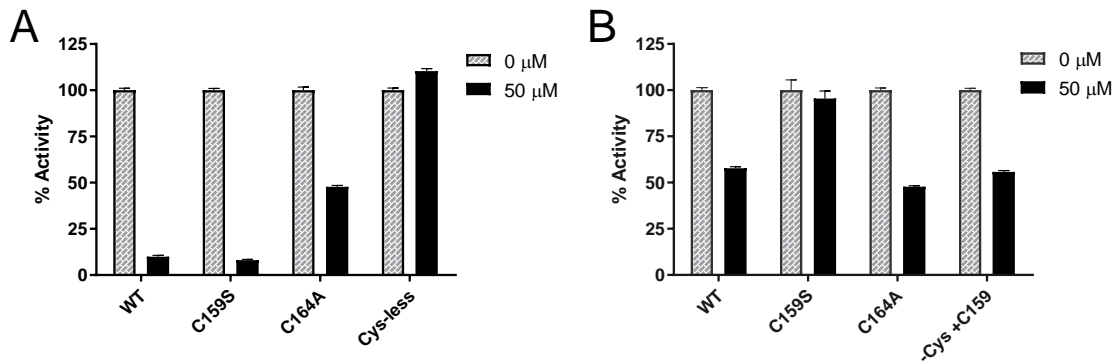


Figure 2.2. *In vitro* ERK2 mutant activity in the presence of auranofin.

(A) 1 nM ERK2 (WT, C159S, C164A, and Cys-less) was incubated with 0 or 50 μ M auranofin (2% DMSO final) for 10 min at 26°C. Reactions were initiated by addition of 10 μ M sox-Sub-D and 1 mM MgATP (final concentrations). Cys-less ERK2 results in full recovery of ERK2 activity. (B) 1 nM ERK2 (WT, C159S, C164A, or -Cys+C159) was pre-incubated with 1 mM MgATP for 5 min at 26°C to protect the active site from auranofin. Reactions were initiated by 0 or 50 μ M auranofin and 10 μ M sox-Sub-D and monitored for 240s. Only mutation of C159 in combination with ATP-protection of the active site results in full recovery of ERK2 activity.

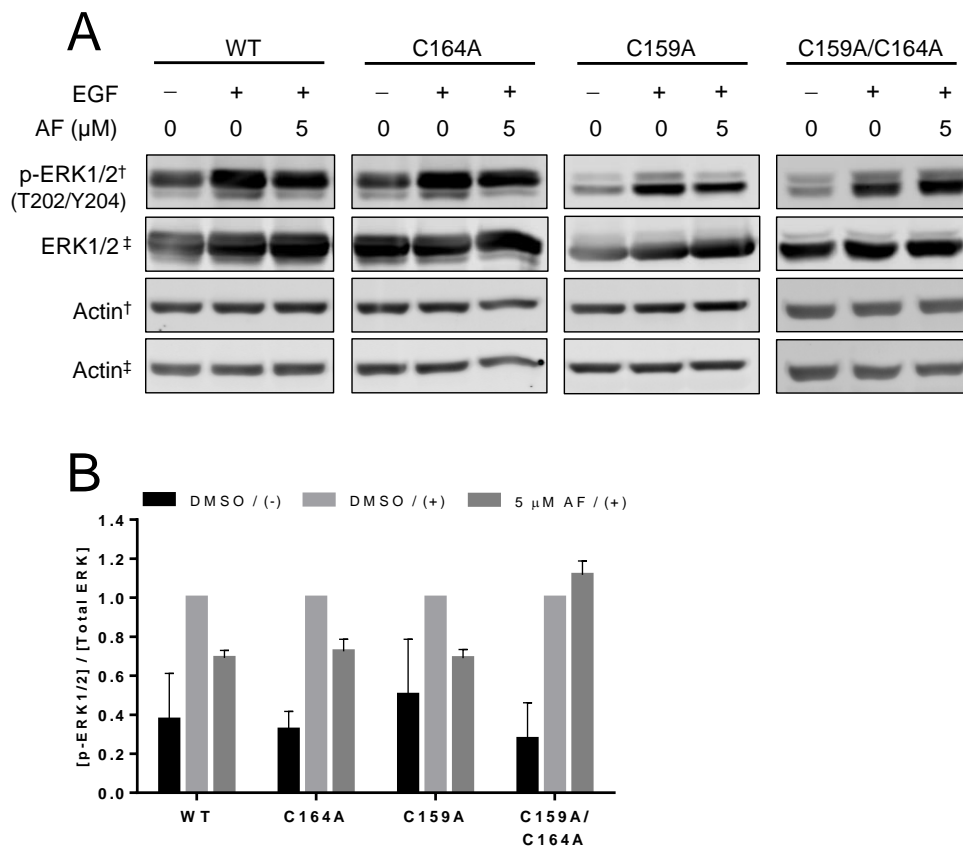


Figure 2.3. C159A/C164A mutant ERK2 overexpression in HEK293T cells recovers ERK activity in presence of 5 μ M auranofin.

HEK293T cells were transfected with WT ERK2 or mutants of ERK2 (C159A, C164A, C159A/C164A). Cells were treated with DMSO or 5 or 10 μ M auranofin for 12 hours followed by stimulation with 0.1 μ M EGF (+) (or no stimulation for control (-)). (A) Representative Western blots showing ERK phosphorylation changes in response to auranofin treatment. [†] and [‡] denote loading controls used for corresponding band quantification. (B) Densitometry of phosphorylated ERK normalized to total ERK fluorescence signal. *n*=4 for each treatment condition.

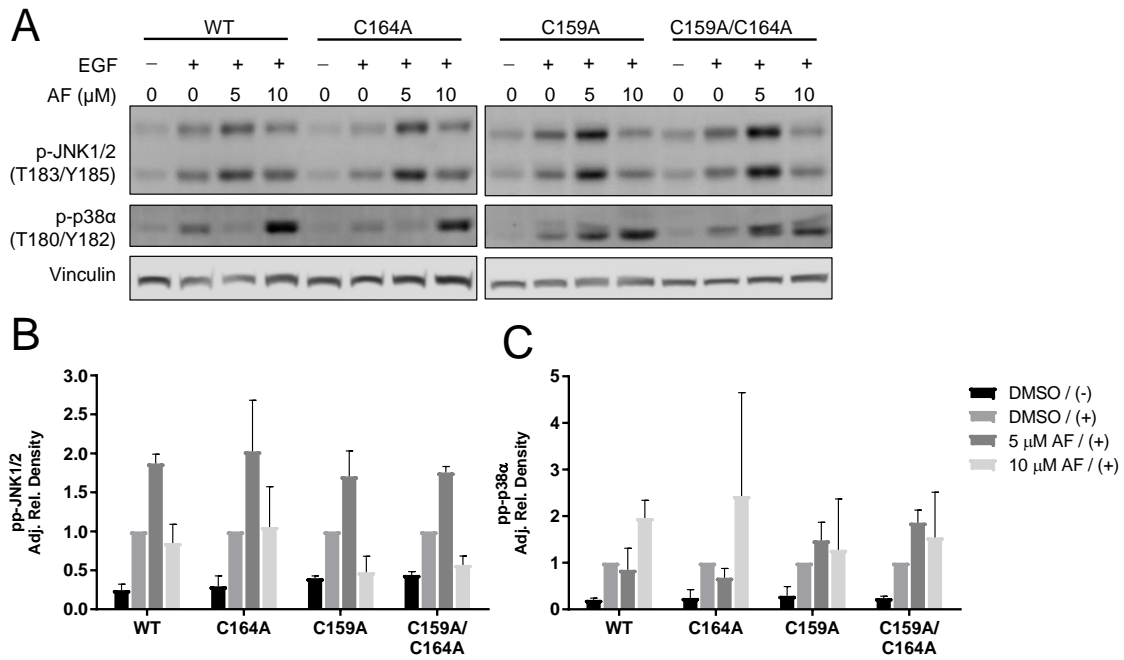


Figure 2.4. Selectivity of auranofin in HEK293T cells against JNK and p38 α .

JNK1/2 and p38 α phosphorylation are not significantly inhibited at 5 μ M auranofin treatment for any of the ERK2-transfection cases. (A) Representative Western blot showing JNK1/2 and p38 α phosphorylation. Transfected HEK293T cells were treated with 0, 5, or 10 μ M auranofin for 12 hours followed by stimulation with 0.1 μ M EGF (+) or no stimulation (-). Densitometry for (B) phospho- JNK1/2 and (C) phospho- p38 α are shown, along with the legend for both on the lower right. $n=2$.

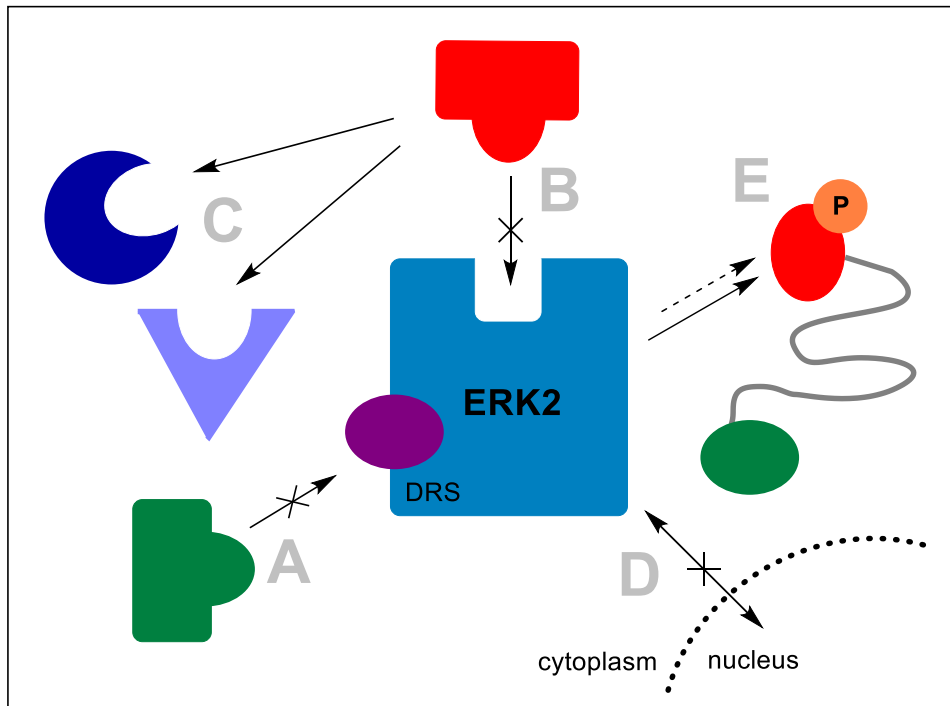


Figure 2.5. Scheme of possible influences of DRS inhibition on ERK signaling.

The results of targeting the DRS of ERK1/2 with a small molecule could include (A) direct inhibition of binding at the DRS, (B) indirect inhibition at other binding sites such as the active site via conformational changes (allosteric inhibition), (C) MAPK pathway remodeling where inhibited ERK is bypassed to achieve the same signaling outcomes, (D) altered subcellular localization such as inhibited nuclear translocation, and (E) altered substrate phosphorylation mechanisms or reaction processivity for substrates that dock at the DRS.

Chapter 3: A Novel Class of Common Docking Domain Inhibitors That Prevent ERK2 Activation and Substrate Phosphorylation

ABSTRACT

Extracellular signal-regulated kinases 1/2 (ERK1/2) are mitogen activated protein kinases (MAPKs) that have a pro-tumorigenic role in numerous cancers. ERK1/2 possess two protein-docking sites that are distinct from the active site: the D-recruitment site (DRS) and the F-recruitment site (FRS). Protein-docking sites on mitogen-activated protein kinases facilitate substrate recognition, intracellular localization, signal specificity, and protein complex assembly. Targeting these sites on ERK in a therapeutic context may overcome numerous problems that are associated with traditional ATP-competitive inhibitors. Here, we identified a new class of inhibitors of the ERK DRS by screening a synthetic combinatorial library of over 30 million compounds. The screen that we employed detects the competitive displacement of a fluorescent peptide from the DRS of ERK2. The top molecular scaffolds from the screen were optimized for structure-activity relationships by positional scanning of different functional groups. The core structure of the resulting 10 compounds consists of a central tertiary amine hub from which three functionalized cyclic guanidine branches extend. We found that the compound 2507-1 inhibited ERK2 from phosphorylating substrates that bind to the DRS and prevented the activation of ERK2. Direct interaction between an analogue, 2507-8, and the DRS of ERK2 was confirmed by both NMR spectroscopy and macromolecular X-ray crystallography, which yielded a 1.9 Å -resolution structure. 2507-8 forms critical interactions at the common docking domain residue D319 via an arginine-like moiety that is shared among all 10 hits, suggesting a common binding motif.

INTRODUCTION

The protein kinome consists of 518 members, representing 1.7% of the human genome [5]. Of these kinases, 385 are known Ser/Thr kinases that are directed to phosphorylate motifs consisting of only two residues (Ser/Thr-Pro) [5]. ERK1/2 alone have over 175 known cellular substrates [9]. Additionally, MAPKs like ERK1/2 have highly conserved active sites, so despite their structural and mechanistic similarities, they must each take part in specialized interactions in order to control critical cellular processes. As a result, extensive regulation of these MAPK signaling networks is required to reliably orchestrate specific events. One level of MAPK signaling specificity is achieved through protein docking sites. Docking sites are interfaces of protein-protein interaction that are distinct from catalytic sites. In the case of MAPKs, docking sites can bind substrates in a position that orients specific S/T-P sequences into proximity of the active site in order to facilitate catalysis [98, 201]. For example, the transcription factor Ets-1 weakly engages both the FRS and DRS of ERK2 in order to position Thr38 near the ERK2 active site for efficient phosphorylation [56, 202, 203]. In comparison, the substrate Elk-1 binds the FRS to direct ERK2 to phosphorylate Ser383, but different residues are phosphorylated when Elk-1 binds the DRS [201]. The number of protein docking sites, the order in which they are engaged, as well as their positions and arrangement on an enzyme can all influence binding interactions and substrate phosphorylation. Therefore, inhibitors that block these sites can potentially disrupt particular MAPK binding interactions and signaling events, while leaving others unaffected. An additional advantage to targeting these docking sites is that inhibitors do not have to compete with ATP, which is present in cells at millimolar concentrations and binds to MAPKs with high affinity [50, 51]. Instead, kinase substrates that utilize these docking sites are typically present in cells at or below their K_m values, so high affinity

inhibitors may not be required to block interactions [204, 205]. Consequently, protein-docking sites on MAPKs offer an alternative approach to classical kinase inhibition that could improve selectivity and block specific signaling events in a tunable manner.

ERK phosphorylates substrates in a signaling cascade that controls cellular processes such as proliferation and survival. Thus, ERK plays a critical role in the development of diseases associated with excessive cell proliferation, like cancer [206, 207]. ERK is also implicated in cardiac hypertrophy, neurodegenerative diseases, and diabetes [14-17]. Consequently, ERK inhibitors are potentially of significant therapeutic value. Here, we focus on identification of ERK inhibitors that target the D-recruitment site (DRS), a protein-protein interaction surface that is distal from the active site of ERK. Classically, linear regions of proteins that bind to the DRS consist of the D-site sequence $\psi_{1-3}X_{3-7}\phi X\phi$, where ψ , ϕ , and X are positively charged, hydrophobic, and any residue, respectively. The DRS is composed of a hydrophobic groove located between an ED domain (T157/T158 on ERK2) and an acidic common docking domain (D316 and D319 on ERK2). Though MAPK sequences are highly conserved among the ERK1/2, p38, and JNK subfamilies [75] and all of these subfamily members possess a DRS, it has been shown that kinase-specific DRS inhibitors can be designed [53] and that differences among the D-recruitment sites, particularly in the ED domain, can help confer substrate specificity [60]. Though protein-protein interaction sites like the DRS are large and shallow compared to standard druggable features, small-molecule inhibitors have been shown to successfully disrupt expansive protein binding interfaces much larger than the inhibitors themselves [77, 208-210].

The ERK DRS mediates numerous specific interactions, including binding of the upstream activators MEK1/2 [211-213], certain phosphatases like MKP3 [211, 214], and the substrates MNK1[211], caspase-9 [65], p90Rsk-1 [63, 208, 215], and Ets-1[56, 203].

In cancer, several mutations in the ERK DRS confer resistance to upstream Raf/MEK inhibition by preserving ERK activity. For example, the sevenmaker mutant D319N of ERK2 is known to significantly decrease MEK1 binding, while in cells, it is a gain-of-function mutation due to pathway feedback signaling and probable decrease in phosphatase binding [216]. DRS mutations are observed in cervical, head, and neck cancers and can be found in the COSMIC database (E322 and D321 alterations in human ERK2 correspond to E320 and D319 in rat ERK2) [217]. Distinct DRS mutations have been observed for ERK1 and ERK2 isoforms, suggesting non-redundant functions associated with the DRS between the two isoforms [217]. Therefore, the DRS is likely of biological importance in these cancers, so targeting it with inhibitors could be beneficial. In addition, ERK DRS inhibitors could be valuable tools for understanding signaling events that are mediated by the DRS, both in cancerous and in normal cells.

Several small-molecule ERK DRS inhibitors have been discovered using computer-aided drug design (CADD) [74, 208] or *in silico* screening methods [79]. This pool of inhibitors was expanded by further *in silico* screening and computational searches for similar compounds, and by synthesis of analogues for SAR studies [76-78]. CADD and *in silico* screenings have also been used to identify inhibitors of the other known docking site of ERK2, the F-recruitment site (FRS) [102]. Biochemical screenings for non-ATP competitive kinase inhibitors are difficult, given there are multiple mechanisms of kinase inhibition, and high-throughput screenings typically rely on kinase activity assays that focus on the active site. Assays against ERK docking sites must be biased against discovery of ATP-competitive inhibitors. For example, a high-throughput AlphaScreen assay has previously been designed to identify ERK2 FRS inhibitors, utilizing a high ATP concentration to prevent ATP-competitive inhibitors from binding [169]. Here, we describe a competition-based screen to identify inhibitors that displace a

fluorescent peptide from the DRS of ERK2. The compounds identified from this screening method are a new structural class of ERK inhibitors. NMR spectroscopy and x-ray crystallography data confirmed that these compounds bind to the DRS of ERK2, which opens avenues for the future chemical optimization of ERK DRS inhibitors.

MATERIALS AND METHODS

Proteins, Peptides, and Buffers

Proteins: Tag-less ERK2 was expressed, purified, and activated essentially as described in [112] (see Chapter 1, Materials and Methods). The ERK substrate Ets-1 (residues 1-138) (Ets Δ 138) was expressed and purified as previously described [218]. GST-c-Jun and active JNK2 were prepared as previously reported [170, 173].

Peptides: The ERK substrate peptides Sub-F and Sub-D were prepared as described in [105] and Lig-D was synthesized in the same manner, as described [97]. Sox-labeled Sub-D (sox-Sub-D) [174, 175] and FITC-labeled Lig-D (FITC-X-Lig-D) [32] were prepared as previously described (see Chapter 1, Materials and Methods). See Appendix A for peptide sequences and synthesis protocols for sox-labeled peptides.

Buffers: The following buffers were used for all *in vitro* ERK2 assays: Buffer A (25 mM HEPES pH 7.5, 50 mM KCl, 0.1 mM EDTA, 0.1 μ M EGTA, 1.3% glycerol, 2 mM DTT, 10 μ g/mL BSA, and 0.1% w/v Triton X-100), and Buffer B (25 mM HEPES pH 7.5, 50 mM KCl, 0.1 mM EDTA, 0.1 μ M EGTA, 10 mM MgCl₂, 2 mM DTT, 10 μ g/mL BSA, 0.01% (v/v) Triton X-100, 2% (v/v) DMSO).

DMF Tolerance

To assess effects of DMF on anisotropy signal, DMF was varied from 0-4% (v/v) in the presence of 1 μ M ERK2 and 10 nM FITC-X-Lig-D in Buffer A. Anisotropy of

free FITC-X-Lig-D in Buffer A with no ERK2 or DMF was measured as a background control. All samples were prepared in triplicate and incubated at room temperature for 1 hour prior to data collection on a Synergy H4 plate reader. Library compounds were dissolved in water with 5% (v/v) DMF for a final concentration of 0.5% (v/v) DMF in the screening. All library compounds were obtained from Richard A. Houghten, Marc Guilianotti, and Yangmei Li at Torrey Pines Institute for Molecular Studies (Port St. Lucie, FL).

Validation Set

To validate the screening procedure, we measured fluorescence intensities for one full 384-well plate of manually pipetted controls with and without FITC-X-Lig-D in Buffer A (no ERK2 present). %CV values for parallel and perpendicular fluorescence intensities were confirmed to be under 5%, and Z-factors exceeded 0.9.

Combinatorial Library Screening

All screening samples were prepared in 384-well low-volume black polystyrene plates (Corning) with final volumes of 30 μ L per well. Compounds were tested in Buffer A with 1 μ M ERK2 and 10 nM FITC-X-Lig-D with 0.5% (v/v) DMF. All anisotropy readings were conducted at room temperature after 1 hour of incubation. Controls included maximal anisotropy signal (full binding of 10 nM FITC-X-Lig-D to 1 μ M ERK2 with no inhibitor present), and minimum signal (free 10 nM FITC-X-Lig-D with no ERK2 present). Phase I of the screening tested 78 scaffolds at 50 μ g/mL and 25 μ g/mL in duplicate. The compounds were also tested for intrinsic fluorescence in Buffer A. The top two scaffolds, 2408 and 2157, were selected for the second phase of the screening: positional scanning of the scaffold R-groups. The 2408 library contained 125

mixtures (9,765,625 compounds) and the 2157 library contained 110 mixtures (45,864 compounds). The samples were screened at 50 $\mu\text{g}/\text{mL}$ and 25 $\mu\text{g}/\text{mL}$ in duplicate, with original hit mixtures from Phase I as additional controls. The top 50 compounds were selected for individual synthesis (purity $\geq 70\%$) and screened at 12.5, and 25 μM , and the top 31 compounds from those results were rescreened at 3.125, 6.25, and 12.5 μM . The top 10 compounds were selected for additional purification and further characterization.

Synthesis of 2408 Libraries and Individual Compounds

The synthesis methods for creating the 2408 scaffold and the details for the synthesis and purification of 2507-8 are described in Appendix C (Figure C14).

Dose-Response Assays with Fluorescent Reporter

Compounds at concentrations of 0-100 μM were pre-incubated with 0.5 nM ERK2 at room temperature for 20 minutes. The ability of ERK2 to phosphorylate 2 μM sox-Sub-D in the presence of 1 mM MgATP was then assessed in Buffer B. Reactions were initiated by addition of MgATP and sox-Sub-D and carried out at room temperature in a Synergy H4 plate reader for 10 minutes. Data collection and analysis was conducted as previously described [177].

Anisotropy Dose-Response Assays

1 μM active or inactive ERK2 was pre-incubated with 10 nM FITC-X-Lig-D and 0, 1, 2.5, 5, 10, 25, 50, 100, and 200 μM of each compound at room temperature for 45 minutes prior to anisotropy measurements as described for the primary screening. The anisotropy dose-response curves were fit to an equilibrium binding model for conditions where the ERK2 concentration is in excess of FITC-X-Lig-D concentration (see Appendix B for basic curve fitting protocol) [68]. The affinities of active and inactive

ERK2 for FITC-X-Lig-D were evaluated for use in the anisotropy binding model (Supplementary Figure C7).

Quantifying Inhibition of ERK2 Activation *In Vitro*

The ability of 20 nM MKK1G7B to phosphorylate and activate 1 μ M ERK2 was tested in the presence of 0, 50, 100, and 200 μ M compound 2507-1 with 10 mM MgATP in Buffer B (with MgCl₂ at 0.5 mM). ERK2 was incubated with 2507-1 for 10 minutes at 28°C prior to initiation with MKK1G7B and MgATP. Reactions were quenched in SDS loading buffer at time points ranging from 0-30 minutes. All quenched samples were loaded into 10% SDS polyacrylamide gels at 52 ng/lane ERK2. Fully active and inactive ERK2 at 52 ng/lane were used as controls. The gels were transferred to Immobilon-FL membranes overnight at 4°C. Membranes were then blocked in 4X diluted Odyssey® Blocking Buffer (PBS) (LI-COR) for 1 hour at room temperature. Membranes were incubated in TBST (5% milk) with 1:2000 antiphospho-p44/42 MAPK (Erk1/2) (Thr202/Tyr204) (E10) mouse mAb (Cell Signaling Technology), or TBST (5% BSA) with 1:1000 anti-p44/42 MAPK (Erk1/2) (137F5) rabbit mAb (Cell Signaling Technology) for 1 hour at room temperature and washed with TBST. The membranes were incubated with appropriate secondary antibodies (1:15000 IRDye® 800CW Goat (polyclonal) anti-rabbit IgG or IRDye® 680RD Goat (polyclonal) anti-mouse IgG (LI-COR)) for 30 minutes at room temperature. After washing again with TBST and Tris-buffered saline, fluorescence was detected on an Odyssey® Sa imaging system (LI-COR).

³²P Assay for Evaluating 2507-1 Selectivity

2507-1 was tested for its ability to inhibit ERK2 (2 nM) phosphorylation of Ets-1 (10 μM), Sub-D (10 μM), or Sub-F (30 μM), and JNK2 (25 nM) phosphorylation of c-Jun (2 μM). Enzymes were pre-incubated with 0-200 μM 2507-1 at room temperature for 30 minutes prior to reaction initiation by addition of substrate and [γ -³²P] MgATP (1 mM for ERK2 reactions and 500 μM for JNK2 reactions). All reactions were carried out at 28°C in Buffer B with reduced MgCl₂ (0.5 mM). Sub-F phosphorylation reactions contained final DMSO concentration of 3.2% (v/v) DMSO. Phosphorylated substrate was quantified at 0.5, 1, 1.5, 2, and 4 minute time points as previously described (³²P protocol) [176] on a Tri-Carb® 2910TR liquid scintillation analyzer (Perkin Elmer).

NMR Spectroscopy

NMR spectroscopy was performed by Andrea Piserchio at City College of New York, NY. The protocol for producing uniformly labeled ²H,¹³C,¹⁵N kinase has been described elsewhere [188]. The NMR data were collected at 25 °C on a 300 μl sample containing 100 μM inactive ERK2, 20 mM potassium phosphate, pH 6.8, 150 mM KCl, 200 μM EDTA and 5.0 mM DTT (10 % ²H₂O) using a 700 MHz Bruker Avance III spectrometer equipped with a triple resonance cryogenic probe and capable of applying pulsed field gradients along the z-axis. ¹H-¹⁵N TROSY [219] experiments with 128 transients, a 1.5 s recycling delay and a digital resolution of 8.9 and 18.3 Hz/point in the direct and indirect dimension, respectively, were collected in the absence and presence of a two-fold excess (200 μM) of the ligand (compound 2507-1, 2507-8, or 2507-26). Data were processed using NMRPipe [220] and analyzed using Sparky [221]. Chemical shift perturbations based on the previously published partial assignment of ERK2 [188] were calculated as previously described [56].

Expression and Purification of ERK2 for Crystallization

ERK2 for crystallization was expressed and purified by Nicole Perry at Vanderbilt University, TN. The ERK2 plasmid Npt7-5H6ERK2 was transformed into BL21 *DEM* Gold cells and a single colony was used to inoculate a 100 mL overnight culture in Luria Broth at 37°C. The next morning, 20 mL of culture was added to 1 L of LB supplemented with ampicillin (100 µg/mL) and incubated to an OD of 0.6 at 37°C and 205 rpm. The cells were induced with IPTG (0.5 mM) and grown for 4-5 hours at 30°C before harvesting (6000 rpm, 4°C, 10 minutes). Pellets were frozen in liquid nitrogen and kept at -80°C until purification.

Cells were resuspended in 30 mL lysis buffer (40 mM Tris-HCl pH 7.0, 1% Triton X-100, 750 mM NaCl, 5 mM imidazole, 0.1 mM PMSF, 2 mM TCEP, 1X protease inhibitor cocktail powder (Sigma)) per 1 L culture. The suspension was sonicated for 3 minutes (model FB505 (Fisher Scientific), 75% maximum amplitude, in cycles of 5 seconds on and 10 seconds off) at 4°C. The crude lysate was then centrifuged (18,000 rpm, 4°C, 45 min) and the supernatant loaded onto a nickel column (HisTrap HP 5 mL, GE Healthcare Life Sciences), which was then washed in equilibration buffer (40 mM Tris HCl pH 7.5, 10 mM Imidazole, 0.1 mM PMSF, 2 mM TCEP). The eluate was collected over a 30 mL gradient (0-100%) of elution buffer (40 mM Tris-HCl pH 7.5, 200 mM Imidazole, 0.1 mM PMSF, 2 mM TCEP) and loaded directly onto a Source Q column for anion exchange (20 mM Tris HCl pH 8.0, 0.1 mM EDTA, 0.1 mM EGTA, 2 mM TCEP). After elution with an upper gradient of 250 mM NaCl (0-100%), all fractions containing ERK2 were dialyzed overnight into the final storage buffer (20 mM Tris HCl pH 8.0, 0.1 mM EDTA, 0.1 mM EGTA, 200 mM NaCl, 10% glycerol).

Crystallization, Structure Determination, and Analysis

The following protein crystallization protocols and data analysis were performed by Nicole Perry and Tina Iverson at Vanderbilt University, TN. Crystals were grown using the hanging-drop vapor diffusion method with droplets containing 1 μ L protein solution (8-10 mg/ml ERK2 in 20 mM Tris HCl, pH 8.0, with 0.1 mM EDTA, 0.1 mM EGTA, 200 mM NaCl, 10% glycerol) and 1 μ L of the reservoir solution (33% PEG 5,000 MME, 0.25 M ammonium sulfate, 0.1 M MES, pH 6.5) in the presence of an arrestin-3 peptide (CH₃CO-AVPETDAPVDTNLIEFE-NH₂) at a molar ratio of 1:2. Droplets were allowed to equilibrate over the reservoir solution at room temperature (approximately 22°C). The 2507-8 inhibitor was soaked into the crystals at a molar ratio of 1:3 (ERK2:2507-8) for 24 hours prior to flash cooling. Crystals were cryo-protected with a solution comprised of the reservoir solution and 15% glycerol.

X-ray diffraction data were collected at the Advance Photon Source (APS) beamline 21-ID-F at -173°C using a wavelength of 0.9798 Å and a MarMosaic225 CCD detector. Data were processed and scaled using HKL2000 [222]. The structure was determined using molecular replacement in the program Phaser-MR [223] through the Phenix interface [224], with wild-type ERK2 (PDB entry 1ERK [225]) as the search model. As 1ERK was reported prior to the widespread use of the R_{free} for cross-validation, R_{free} reflections were randomly selected for ERK2. However, because the original model (1ERK) was refined against these reflections, the free-R is of limited utility in this case. Model building was performed in Coot [226] and refinement was conducted using Phenix [224]. Residues 328-332 are not included in the final model as the electron density corresponding to these residues was not readily interpretable. Protein-inhibitor interactions were analyzed using the program LigPlot [227], which builds schematic diagrams of protein-ligand interactions using PDB files. All structural

figures were made using PyMOL Molecular Graphics System (version 1.5.04, Schrodinger, LLC, New York) unless otherwise indicated. Data collection and refinement statistics are summarized in Supplementary Table C4.

RESULTS AND DISCUSSION

Screening Identified Cyclic Guanidine Scaffolds as DRS Inhibitors

To identify reversible inhibitors that bind the DRS of ERK2, we first designed and optimized a screening method suitable for combinatorial ligand libraries. This library format allows high-throughput screening with low resource consumption, i.e. less than 100 samples are needed to screen millions of compounds [228, 229]. We previously designed a high-throughput screening method to preferentially detect covalent inhibitors of the ERK2 DRS that react with Cys159 (Chapter 2). In that method, a FITC-tagged peptide (FITC-X-Lig-D) was competitively displaced from the DRS by library compounds, generating a change in fluorescence anisotropy. We modified this protocol to avoid the detection of covalent cysteine-reactive inhibitors by including a reducing agent (2 mM DTT) in each sample. Since the combinatorial libraries contained the solvent DMF, we then tested the effects of DMF concentration on the anisotropy signal for fully bound FITC-X-Lig-D (Supplementary Figure C1). Concentrations of DMF exceeding 0.5 % (v/v) significantly reduced the anisotropy, so this concentration was chosen as a maximum functional limit for the screening. Additionally, we determined the Z-factor for manual 384-well plate preparation by measuring the fluorescence signal for FITC-X-Lig-D samples in a 384-well plate (Supplementary Table C1). The Z-factor was ≥ 0.90 for all fluorescence intensity readings, which indicated that plate preparation was consistent [178].

The screening then proceeded in three phases that allowed for inherent optimization of the structure-activity relationship (Figure 3.1). In Phase I, a library of scaffolds, each with randomly varied functional groups, was screened at 50 and 25 $\mu\text{g}/\text{mL}$ to measure displacement of FITC-X-Lig-D from the DRS (Supplementary Figures C2 and C3). The top 5 scaffolds that caused the greatest displacement of the fluorescent peptide all contained cyclic guanidine moieties (Table 3.1). 2408 was the most potent hit by at least two-fold, so it was selected for the second screening phase. It qualitatively has an additional plane of symmetry compared to the other hits, which could increase its productive binding modes and account for its higher potency. 2157, 2353, and 2354 differ only by stereochemistry. 2157 was selected to continue to Phase II two of the screening, as it encompasses the basic bicyclic guanidine core found in 4 out of the 5 hit scaffolds and includes both (*S*) and (*R*) stereocenters. In Phase II of the screening, 5 functional groups on 2408 and 3 functional groups on 2157 were varied in mixture format and re-screened at 50 and 25 $\mu\text{g}/\text{mL}$. In each sample mixture, a single R-group was held constant while the remaining groups were randomly varied. The 2408 scaffold was selected for continued study, due to its larger number of variable groups that could potentially increase structural diversity of hits in the subsequent screening phase. The hit functional groups for each location on the scaffold, based on the results shown in Supplementary Figure C4 and Table C2, were combined to generate structures of 48 single-compound hits. The individual structurally optimized hits were then rescreened in Phase III (Supplementary Figure C5 and C6) and the resulting top 10 hit compounds were selected and purified for further characterization (Table 3.2).

Hit Compounds Inhibit DRS Interactions in a Dose-Dependent Manner

Next, we measured the dose-dependent change in anisotropy signal for each of the top 10 compounds upon competitive displacement of FITC-X-Lig-D from the DRS of ERK2. Both inactive (unphosphorylated) and active (bis-phosphorylated) forms of ERK2 were tested to evaluate if the conformational changes of ERK2 upon its activation have any effect on DRS binding. The resulting apparent affinities (K_i values) of the compounds for ERK2 ranged from approximately 0.24 – 1.5 μM for each enzyme activation state (Table 3.3, Supplementary Figures C8, C9, C10, and C11). The activation state of ERK2 did not appear to have a dramatic effect on the inhibitor binding affinities; the largest observed difference between inhibitor affinity values for active and inactive forms of ERK2 was 2.4-fold. These results indicated that while there are minor differences between the affinities of each compound for active and inactive ERK2, the compounds all effectively bind to both forms of the enzyme under the assay conditions.

The compounds were also tested for their ability to prevent active ERK2 from phosphorylating sox-Sub-D, a fluorescent reporter substrate peptide (Table 3.2, Supplementary Figures C12 and C13). This peptide sequence included the same core sequence of FITC-X-Lig-D without the FITC tag and 6-aminohexanoic acid linker (X). The peptide also contained a phosphorylation consensus sequence such that it can bind to both the DRS and active site of ERK2. The peptide was labeled with the sox moiety, which fluoresces upon chelation with magnesium and peptide phosphorylation. Dose-response curves were obtained for each compound against ERK2 phosphorylation of sox-Sub-D. The resulting IC_{50} values indicated that the relative potency among the 10 compounds was similar to the observed K_i measurements; however, the IC_{50} values for each compound were larger than their respective K_i values by approximately 2 orders of magnitude. This large difference is not expected, though it could be attributed to a

number of factors. First, the substrate/ligand peptides and experimental conditions are distinctly different for the two assays that were employed to determine K_i and IC_{50} . The activation state of a kinase can affect substrate binding affinity, as suggested by the anisotropy dose-response data for the compounds binding to active and inactive ERK2. Also, the presence of MgATP which binds the kinase can influence substrate binding and phosphorylation [230, 231]. Specifically, bound ATP can induce communication to other binding sites [79, 189]. Here, the IC_{50} assay required MgATP with large excess of free magnesium (Mg^{2+}) in order to chelate with sox-Sub-D, while the anisotropy dose-response assay did not include MgATP or Mg^{2+} . Combined, these factors could account for the differences in measurements between the two assays.

Characterization of 2507-1 Selectivity

Compound 2507-1 (Figure 3.2 A, Supplementary Figure C15) showed the most potent IC_{50} at $28.5 \pm 4.4 \mu M$, so we selected it for further mechanistic evaluation. In [γ - ^{32}P] ATP-based dose-response assays, we found that 2507-1 more potently inhibited ERK2 phosphorylation of the substrate Ets-1 compared to the non-fluorescent Sub-D peptide, with an IC_{50} of $5.62 \pm 0.96 \mu M$ (Figure 3.2 B). Meanwhile, the IC_{50} against the Sub-D peptide phosphorylation was measured at $46 \pm 14 \mu M$, which is within error of the IC_{50} against sox-Sub-D. Interestingly, 2507-1 was found to be a partial inhibitor of Ets-1 phosphorylation (~77% maximum inhibition), which is consistent with Ets-1 docking at the FRS of ERK2, in addition to the DRS and active site. To validate that 2507-1 does not interact at the FRS, we tested it as an inhibitor of ERK2 phosphorylation of Sub-F, a peptide that only docks at the FRS. The IC_{50} of 2507-1 in this case was not accurately measurable due to solubility limits of the compound, so we concluded that 2507-1 does not effectively target the FRS. Knowing that other kinases like p38 α and JNK1/2 share

similar DRS regions to ERK2, we tested the ability of 2507-1 to inhibit JNK2 phosphorylation of GST-c-Jun *in vitro* (Figure 3.2 B). This IC₅₀ was measured at 43 ± 6 μM, which indicated that 2507-1 has similar selectivity for JNK2 when compared to ERK2 phosphorylation of Sub-D, but much less selectivity for JNK2 when compared to ERK2 phosphorylation of the more physiologically relevant substrate Ets-1. It is possible that the difference in IC₅₀s observed for 2507-1 inhibition of Ets-1 and Sub-D phosphorylation could be explained by multiple modes of inhibitor binding that occur with different affinities.

2507-1 Inhibited ERK2 Activation by Constitutively Active MEK1

Because MEK1 is known to interact at the DRS of ERK2 [211-213], we tested whether 2507-1 would prevent activation of ERK2 by the constitutively active MEK1 mutant, MKK1G7B. We found that 2507-1 blocks ERK2 activation *in vitro* in a dose-dependent manner, with an IC₅₀ of 9.9 ± 1.9 μM (Figure 3.3). Thus, this small molecule can potently block ERK2 protein-protein interactions *in vitro*. D-site sequences frequently contain basic residues, such as arginine, that are important for engaging the common docking region of the DRS, which consists of D316 and D319. As mentioned, the sevenmaker mutation D319N causes significant decrease in MEK1 binding to ERK2, and in cells, and acts as a gain-of-function mutation due to signaling pathway feedback and other effects [216]. Thus, only small interferences in this region can disrupt protein docking. All 10 hit compounds have at least one arginine-like functional group and 2507-1 significantly blocked MKK1G7B activation of ERK2. This indicates that the compounds may function in a similar manner as the D319N mutant by neutralizing the acidic environment of the common docking region.

Confirmation of DRS Binding by Structural Data

To confirm the binding mode of the hit compounds, we used a combination of NMR and macromolecular X-ray crystallography. For the NMR experiments, inhibitor interactions at particular residues of ERK2 were detected by measuring chemical shift perturbations in response to addition of inhibitor [188]. We tested three of the top 10 hit compounds, 2507-1, 2507-8, and 2507-26, by this method in order to observe binding interactions for different R-groups on the 2507 scaffold. As shown in Figure 3.4 for compound 2507-8, most perturbations were localized to the DRS region of ERK2, as was also the case for 2507-1 and 2507-26 (not shown). All three compounds induced chemical shift perturbations above two standard deviations for the following key DRS residues: both common docking domain residues (D316 and D319), either T157 or T158 of the ED domain, the hydrophobic residues L119, L155, H123, Y126, and a solvent-exposed cysteine residue C159 (Supplementary Table C3). These results indicated that the compounds likely bind the DRS in the same manner, regardless of their differing R-groups.

To ensure that the chemical shift perturbations detected by NMR were not caused by allosteric effects, conformational changes of the protein, or nonspecific binding of the inhibitor, we crystallized compound 2507-8 (Figure 3.5 A) in complex with inactive ERK2 and determined the structure with 1.9 Å resolution (Figure 3.5 B, Supplementary Table C4). We observed the appearance of new density near ERK2 residues 311-318. This electron density was not fully contiguous and was difficult to model with a single molecule of 2507-8 (Figure 3.5 C, D). Instead, our best interpretation of this electron density used two fragments of 2507-8, termed Fragment A and Fragment B. When considering this model, one possibility is that one or both of the fragments are portions of two intact inhibitor molecules, but only part of each molecule is resolvable. A second

possibility is that one or both of the fragments are impurities or degradation products of 2507-8. This may be likely for Fragment B, given that LC-MS analysis of the 2507-8 inhibitor identified Fragment B ((*S*)-4-benzylimidazolidin-2-imine) as an impurity (Appendix C, Supplementary Figure C16). Finally, although it is unlikely given the distance between the two regions, it remains possible that this density is attributed to a single inhibitor molecule, where the structural elements of the inhibitor that link the regions are too flexible for visualization. Nevertheless, both modeled 2507-8 fragments indicate that binding is localized at the DRS and does not occur at the active site of ERK2 (Figure 3.5 B).

As predicted, the arginine-like group on Fragment A is located sufficiently close to form ionic interactions with the common docking domain residue D319, in addition to Y129 and Y314 (Figure 3.5 E, Figure 3.6). These interactions may stabilize the binding position of this functional group, which is consistent with the observation of clear electron density for Fragment A. Additional hydrophobic interactions engage Fragment A with D316 of the common docking domain, as well as E312, Y315, and P317. In contrast, Fragment B is bound in the hydrophobic groove between the common docking and ED domains. It forms hydrophobic interactions at the key DRS residues H123 and Y126, as well as with D122 and Y314 (Figure 3.5 F). Both Fragment A and Fragment B appear to participate in similar binding interactions to those of a peptide derived from the phosphatase HePTP, which has previously been crystallized in complex with ERK2 and is known to bind to the DRS [189]. This peptide has been used as a basis for identifying inhibitors of the DRS via computer-aided drug design [74, 76]. Thus, the HePTP peptide provides further context for the mechanism and binding mode of 2507-8. Interestingly, the phenyl carbon at the meta- position of Fragment B is approximately 4.5 Å from the C159 sidechain, which we have shown to be a suitable target for covalent inhibition of

ERK2 (Chapter 2). Functionalization of the phenyl ring with a cysteine-reactive substituent could generate future covalent ERK inhibitors with greater potency than the reversible inhibitors identified here.

CONCLUSIONS

From the binding interactions of 2507-8 and the ability of the hit compounds to inhibit ERK2 activity and activation, it is clear that this class of small molecule is effective at inhibiting ERK2 through the DRS. The structural data showed that small-molecule interactions at the acidic common docking region and the hydrophobic residues adjacent to the ED domain of the DRS are likely the basis of this inhibition. Further structural modifications of these compounds could improve selectivity for ERK or promote covalent inhibition of the solvent-exposed cysteine residue of the DRS. The continued development of these inhibitors can potentially lead to ERK-targeted drugs that do not compete with ATP but rather function by disrupting critical protein-protein interactions.

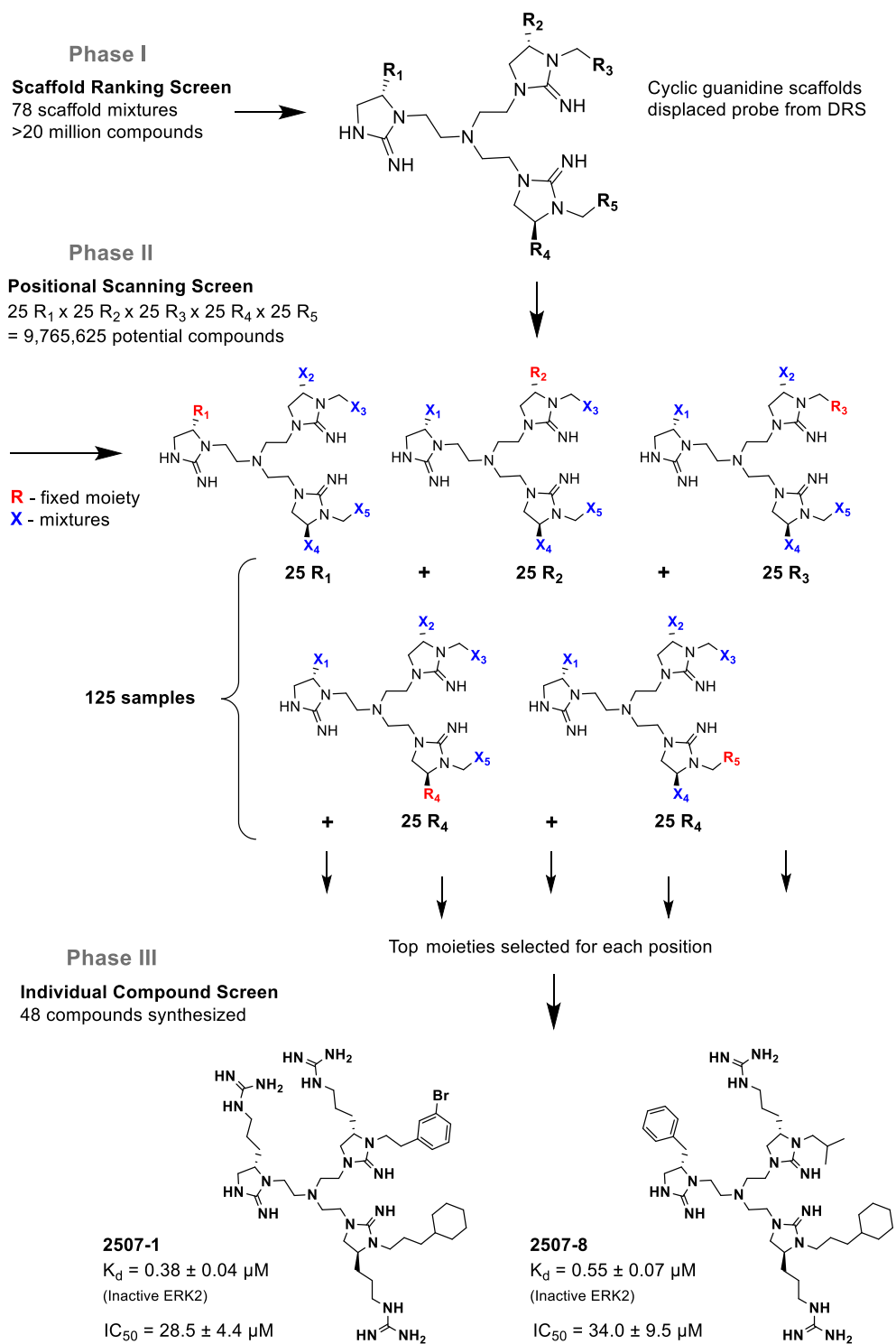


Figure 3.1. Deconvolution of cyclic guanidine libraries.

Mixture Sample #	Structure	Percent (%) signal change
2408		55.7
2407		21.2
2353		19.5
2157		19.4
2354		16.3

Table 3.1. Top mixtures that exhibited highest displacement of fluorescent probe in scaffold screening

Table 3.1. Top mixtures that exhibited highest displacement of fluorescent probe in scaffold screening

Screening results for scaffold ranking library at 25 $\mu\text{g}/\text{mL}$. Scaffold mixtures were ranked by their average % displacement of the FITC-X-Lig-D probe from the D-recruitment site of ERK2. The anisotropy screening is described in Materials and Methods, and Appendix C. Data reported as average of 2 replicate samples at mixture dose of 25 $\mu\text{g}/\text{mL}$.

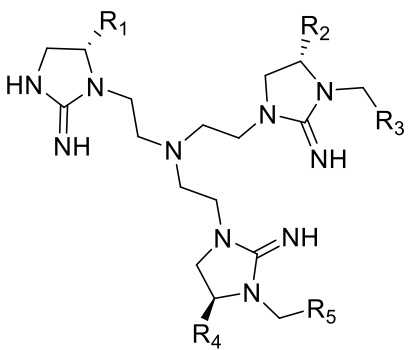
Compound #						Dose-response data	
	R1	R2	R3	R4	R5	IC ₅₀ , μM	
8	Phe	Arg	isobutyric acid	Arg	cyclohexanepropionic acid	34.0 ± 9.5	
2			3-bromophenylacetic acid		p-tolylacetic acid	41.2 ± 4.5	
26					Phe(4-F)	cyclohexanepropionic acid	54.8 ± 15.3
14						Arg	p-tolylacetic acid
1	Arg	Met		Phe(4-F)	cyclohexanepropionic acid	41.8 ± 4.0	
25			p-tolylacetic acid		68.7 ± 15.9		
13			cyclohexanepropionic acid		ND ^A		
37			p-tolylacetic acid		60.8 ± 13.4		
16							
40							

Table 3.2. Top individual compounds resulting from positional scanning of library 2408

Structure-activity relationship and potency of the top 10 individual hit compounds from the 2408 scaffold library. IC₅₀s were evaluated by fluorescence assay. ERK2 at 2 nM was incubated with 0-50 μM compounds for 20 minutes prior to reaction with 2 μM sox-Sub-D and 1 mM MgATP. Values shown indicate IC₅₀ ± standard error. Compounds are organized according to structural similarities. ^AIC₅₀ was too large to be accurately measured.

ID	Inactive ERK2 K _i , μM	Active ERK2 K _i , μM	Approx. K _i ratio (Active/Inactive)
2507-1	0.383 ± 0.042	0.567 ± 0.122	1.48
2507-2	0.247 ± 0.026	0.584 ± 0.104	2.36
2507-8	0.549 ± 0.066	0.384 ± 0.048	0.70
2507-13	0.351 ± 0.045	0.598 ± 0.085	1.70
2507-14	0.933 ± 0.110	0.660 ± 0.112	0.71
2507-16	1.48 ± 0.11	1.273 ± 0.203	0.86
2507-25	0.611 ± 0.064	0.861 ± 0.138	1.41
2507-26	0.501 ± 0.075	0.404 ± 0.061	0.81
2507-37	0.567 ± 0.066	0.564 ± 0.078	0.99
2507-40	0.938 ± 0.109	0.783 ± 0.092	0.83

Table 3.3. Binding affinities of top 10 compounds.

Potency of top inhibitors against ERK2. K_i values were determined by anisotropy assay in the same manner as the original screening. Active or inactive ERK2 at 1 μM was incubated with 0-200 μM compounds for 45 minutes at room temperature prior to anisotropy measurements as conducted in the main screening. K_i values were calculated in GraphPad Prism as described in Appendix B. Values shown indicate K_i ± standard error of the fit.

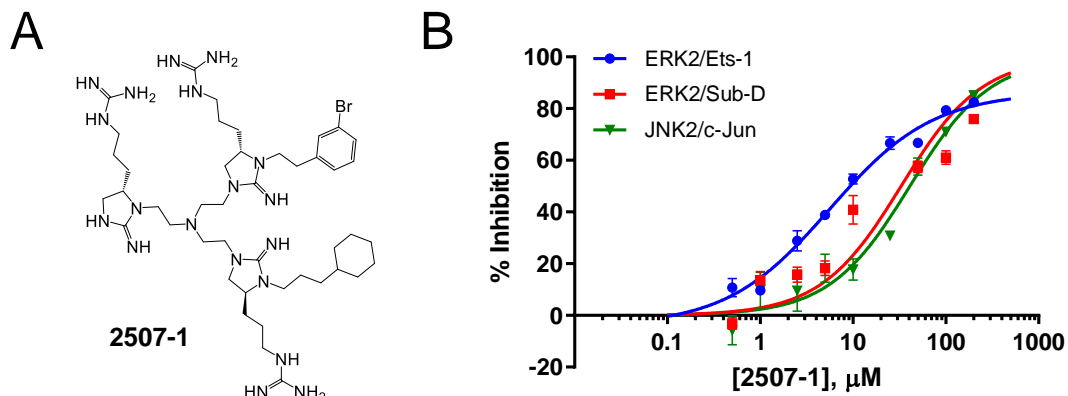


Figure 3.2. Potency and selectivity of 2507-1.

(A) Structure of lead compound 2507-1. (B) The ability of 2507-1 to inhibit 2 nM ERK2 phosphorylation of 10 μM Ets-1 and 10 μM Sub-D, as well as 25 nM JNK2 phosphorylation of 2 μM c-Jun, was assessed by ^{32}P assay as described in Materials and Methods. Enzymes were incubated with 0-200 μM 2507-1 for 30 minutes prior to reaction initiation by addition of MgATP and substrate. Initial rates \pm standard errors are shown fit to standard IC_{50} models.

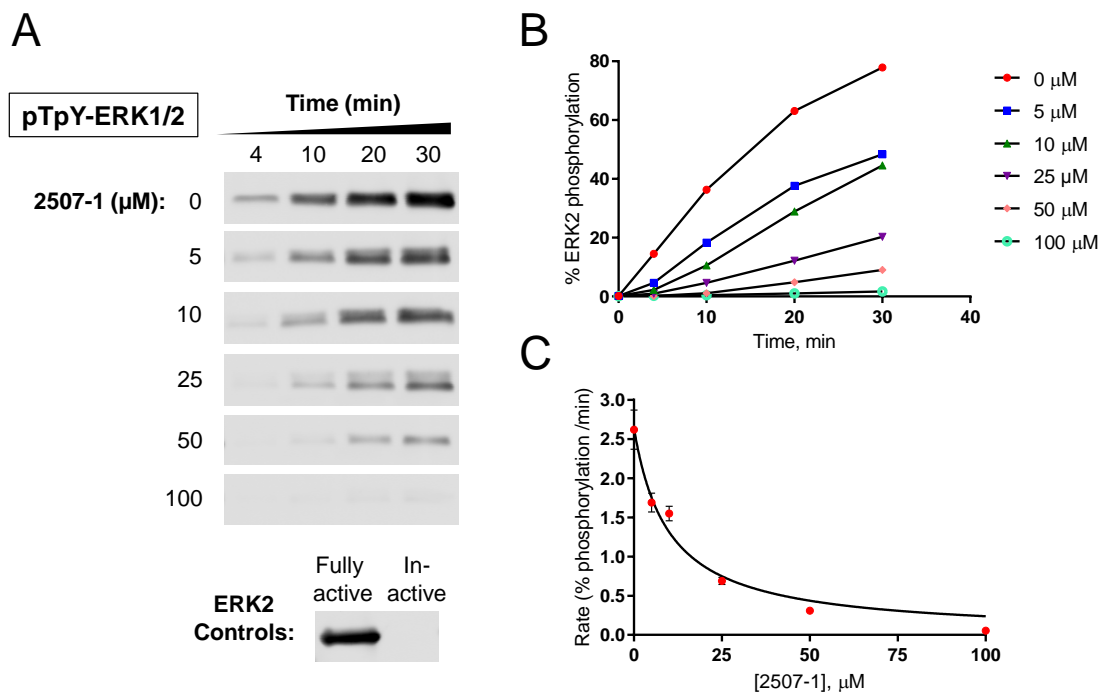


Figure 3.3. 2507-1 inhibits MKK1G7B phosphorylation of ERK2 *in vitro*.

Recombinant ERK2 was incubated with varied concentrations of 2507-1 (0-100 μM) for 10 minutes prior to reaction with MKK1G7B and MgATP as described in Methods. (A) Resulting ERK2 phosphorylation was measured by Western blot. Controls include fully phosphorylated active ERK2 and unphosphorylated inactive ERK2. (B) Densitometry of Western blot, where phospho-ERK signal is normalized to total ERK signal. (C) IC₅₀ curve was generated from initial rate measurements of % ERK2 phosphorylation.

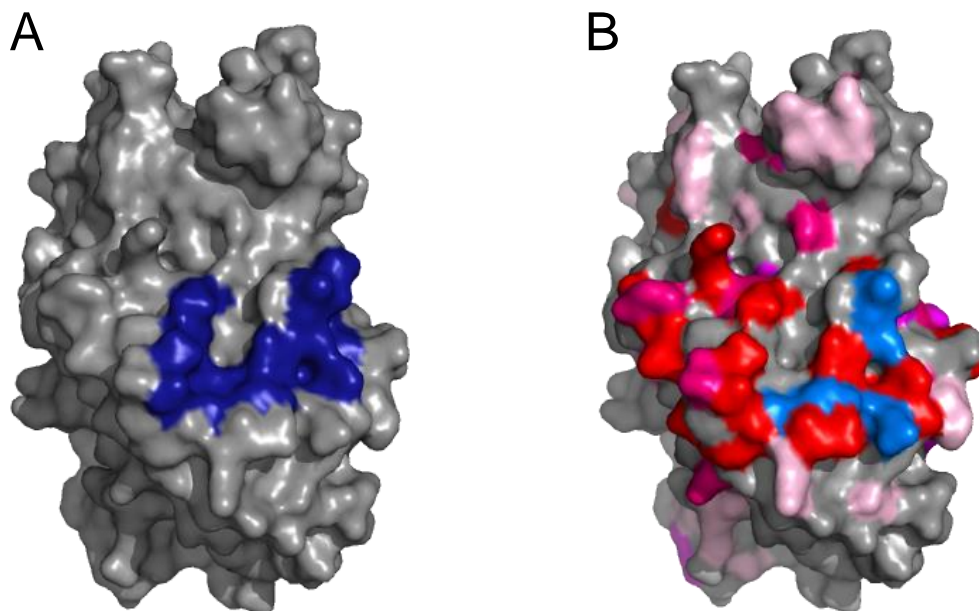


Figure 3.4. Docking of 2507-8 at the DRS via NMR.

2507-8 binding to ERK2 was analyzed by NMR. (A) Structure of ERK2 (PDB ID: 3ERK, grey) showing key DRS residues (dark blue). (B) Solution NMR results showing ERK2 (PDB ID 3ERK) residues affected by 2507-8 binding. Colors indicate chemical shift perturbations: 1-1.5 S.D.: light pink, 1.5-2 S.D.: magenta, 2-3 S.D.: hot pink, >3 S.D.: red, and perturbations beyond detectable limits: marine. (S.D. = standard deviation).

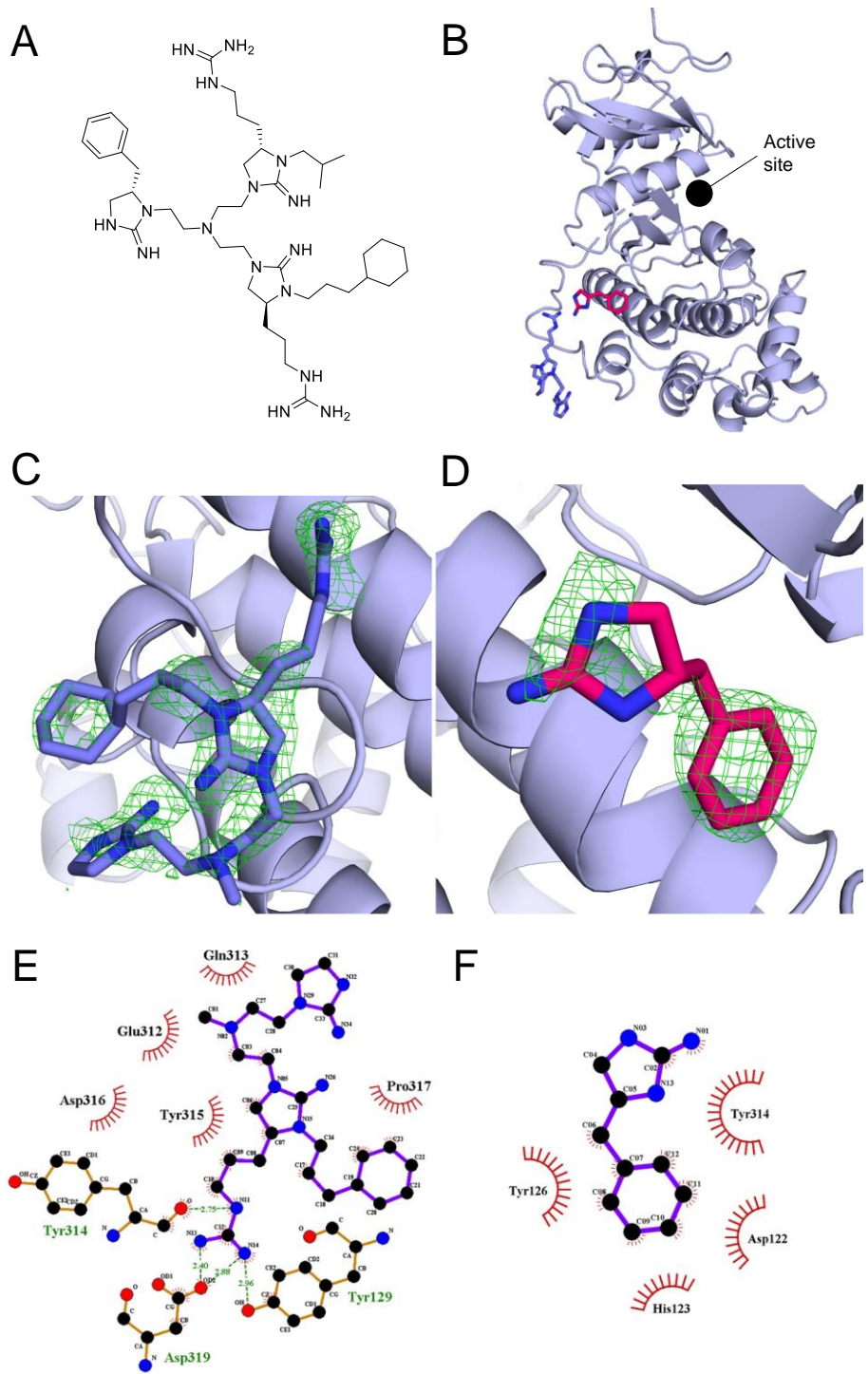


Figure 3.5. The 1.9Å structure of ERK2 in complex with inhibitor 2507-8.

Figure 3.5. The 1.9Å structure of ERK2 in complex with inhibitor 2507-8.

(A) Chemical structure of inhibitor 2507-8 (B) ERK2 (light blue) in complex with inhibitor 2507-8, which was resolved as two fragments termed A and B, that are labeled in blue and red respectively. The OMIT map is shown for the crystallized inhibitor (C) Fragment A and (D) Fragment B with a sigma of 2.5. LigPlot projections of hydrophobic and ionic interactions are shown for (E) Fragment A and (F) Fragment B. Ionic interactions are shown using green dashed lines. Hydrophobic interactions are shown using circular red bursts. Residues are listed using the three-letter code followed by the residue number. (Crystallographic and LigPlot data provided by Nicole Perry and Tina Iverson at Vanderbilt University.)

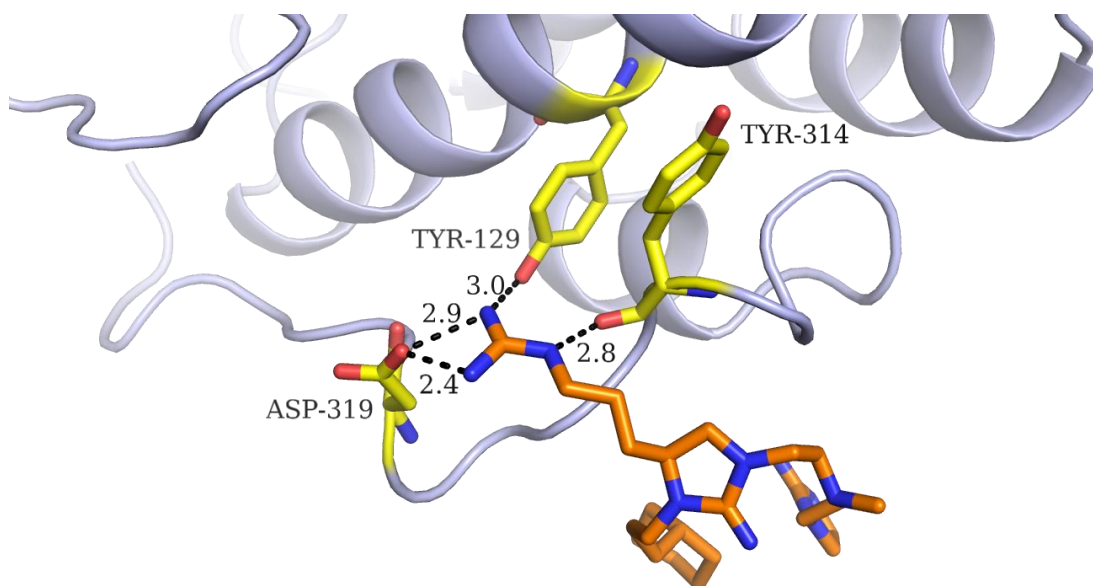


Figure 3.6. Electrostatic interactions of Fragment A with the DRS of ERK2.

Ionic and hydrogen-bonding interactions between ERK2 and Fragment A of inhibitor 2507-8. Interactions were measured using the free available software LigPlot. Three nitrogen atoms in inhibitor 2507-8 interact with residues Tyr129, Tyr314, and Asp319 in ERK2. (Crystallographic and LigPlot data provided by Nicole Perry and Tina Iverson at Vanderbilt University.)

Chapter 4: Characterization of Kinetic Parameters and Isoform-Selectivity of Covalent JNK Inhibitors

ABSTRACT

c-Jun N-terminal kinases (JNKs) are an extensively studied subfamily of mitogen-activated protein kinases. The three isoforms of JNK, JNK1/2/3, have been observed performing different context-dependent roles in tumorigenesis. These isoform-specific functions are difficult to study due to lack of inhibitors that are selective for individual isoforms. JNK-IN-8, a potent inhibitor that selectively targets JNK through a covalent mechanism, has recently been discovered. This inhibitor can potentially be structurally optimized to target specific isoforms. In order to properly characterize the mechanism of JNK-IN-8 and its analogs, we explored different methodologies to determine isoform selectivity. We developed a fluorescence-based assay to monitor the time-dependent reaction of JNK-IN-8 with JNK1 and JNK2. This assay allows the direct quantification of the kinetic parameters K_I and k_{inact} for two-step covalent inhibition by JNK-IN-8. We found that for JNK1, K_I is 23.8 ± 1.8 nM and k_{inact} is $(12 \pm 4) \times 10^{-3} \text{ s}^{-1}$, while for JNK2, K_I is 35.3 ± 12.2 nM and k_{inact} is $(4.7 \pm 1.5) \times 10^{-3} \text{ s}^{-1}$. Additionally, we tested 10 analogs of JNK-IN-8 in *jnk1*^{-/-} and *jnk2*^{-/-} PyVMT cells and found that four of the compounds showed selectivity for JNK2 with little effects on JNK1 activity. The methods described here are essential tools for the continued development of isoform-specific JNK inhibitors.

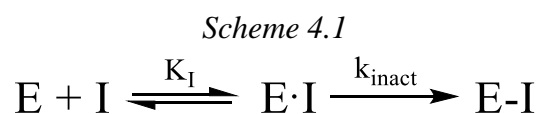
INTRODUCTION

c-Jun N-terminal kinases (JNKs) belong to the mitogen-activated protein kinase (MAPK) family. The JNK pathway transduces cellular signals via a kinase phosphorylation cascade that is stimulated by a variety of sources, such as external stresses, cytokines, and growth factors [232, 233]. JNK is expressed as three isoforms,

JNK1/2/3, where JNK1 and JNK2 are ubiquitous, and JNK3 expression seems to be localized to the brain, heart, and testes [18, 234]. Activation of JNK leads to its phosphorylation of numerous substrates such as c-Jun and ATF-2, members of the AP-1 group of transcription factors [19, 233]. JNK substrates govern critical cellular processes such as proliferation, migration, and apoptosis [19]. Accordingly, JNK signaling has been implicated as a therapeutic target in diseases such as diabetes, CNS disorders, cancer, and inflammation [232, 235-237]. The role of JNK in cancer has been controversial, with evidence supporting both pro- and anti- tumorigenic effects of its signaling that are likely due in part to non-redundant isoform functions [29]. Probing JNK signaling with isoform-specific inhibitors would allow the crucial clarification of these functions. However, no isoform-specific small-molecule inhibitors have been reported to date.

Recently, Zhang, *et al.* (2012) discovered covalent inhibitors of JNK that show potential for development into isoform-specific inhibitors [128]. Of the identified inhibitors, JNK-IN-8 has ~5-fold selectivity for JNK3 over JNK1, ~20-fold selectivity for JNK3 over JNK2, and exhibits no off-pathway activity in cellular pathway profiling experiments [128]. Although this slight isoform-selectivity is observed, JNK-IN-8 is not discrete enough to act on only one isoform, especially given its high potency. Covalent inhibitors as drugs have long been regarded with concern due to potential off-target effects and toxicities. Despite this concern, as of 2005, approximately 30% of marketed drugs acted by irreversible mechanisms [118]. In recent years the benefits of covalent drugs have received renewed attention, with particular applications as kinase inhibitors in cancer that can overcome resistance mechanisms [122, 238, 239]. Therefore, JNK-IN-8 and its derivatives could be of additional therapeutic value due to their covalent nature and minimal off-target reactivity.

IC₅₀ values are often used to describe and compare the ability of different inhibitors to prevent a kinase from phosphorylating a substrate *in vitro*. However, this parameter cannot reliably describe covalent inhibitors because of their time-dependent reactivity. Incubation of inhibitor and enzyme can be done for an arbitrary duration of time in these dose-response experiments, so IC₅₀ values for time-dependent inhibitors are therefore variable and can often obscure critical attributes of inhibitors. For example, given sufficient time to react, any irreversible inhibitor will inactivate an enzyme with 1:1 stoichiometry, thus rendering them indistinguishable from one another at such time points. Therefore, it is necessary to characterize covalent inhibitors in terms of the kinetic parameters K_I and k_{inact}. The parameter k_{inact} is the maximal rate constant for inactivation of enzyme by the inhibitor. K_I describes the inhibitor binding step and is the inhibitor concentration that results in half-maximal k_{inact}. These terms are independent of reaction conditions and apply in the general case of two-step covalent inhibition, as shown in the reaction scheme below (Scheme 4.1), where enzyme (E) reacts with inhibitor (I).



For JNK-IN-8, reaction occurs at C116 (JNK1/2) or C154 (JNK3), a cysteine residing in the active site that is not directly involved in catalysis. Therefore, it doesn't function as a typical mechanism-based inhibitor that is modified by the catalytic residues of JNK, but rather blocks the binding of ATP in the same pocket.

MATERIALS AND METHODS

Proteins, Peptides, and Small Molecules

Full-length human tag-less JNK1 α 1 (GenBank accession number NM_002750) and human JNK2 α 2 (GenBank accession number NM_002752) were expressed, purified, and activated as previously described by Tamer Kaoud at the University of Texas at Austin [32]. GST-tagged ATF-2 was expressed and purified as described by Szafranska, *et al.* [240]. Sox-NFAT4 peptide (Ac-LERPSRDHLYLPLSGRYRES(C-Sox)LSPSPA) was synthesized and purified as described previously (see Appendix A) [174]. JNK-IN-8, JNK-In-B, JNK-In-C, and THZ-3-60-1 were synthesized by Ramakrishna Edupuganti from the Targeted Therapeutic Drug Discovery and Development Program at the University of Texas based on the synthesis methods described by Zhang, *et al.* (2012) [128]. All other JNK-IN-8 analogues were provided by Nathanael Gray at Harvard University.

Kinase Activity Assays

Catalytic parameters for JNK1 and JNK2 substrate phosphorylation, as well as covalent inhibition, were determined by continuous fluorometric assay. The peptide reporter sox-NFAT4 is phosphorylated by JNK1 or JNK2 on Ser-23 in the presence of MgATP. Fluorescence assay buffer (pH 7.4) contained 25 mM HEPES, 50 mM KCl, 0.1 mM EDTA, 0.1 mM EGTA, 10 μ g/mL BSA, 2 mM DTT, and 10 mM MgCl₂. Assays were performed at 25°C, pH 7.4 in 384-well plates with 70 μ L sample volumes. Fluorescence measurements, in relative fluorescence units (RFU), were collected using a Synergy H4 plate reader at $\lambda_{\text{ex}}/\lambda_{\text{em}}$ of 360 nm/482 nm.

Steady State Kinetics: K_m and k_{cat} for Sox-NFAT4

Michaelis-Menten parameters were determined for sox-NFAT4 phosphorylation to validate the fluorometric assay. JNK1 or JNK2 (25 nM) phosphorylated sox-NFAT4 (0-35 μM) in the presence of 500 μM MgATP. Reactions were initiated by addition of MgATP and fluorescence measurements were taken every 30 seconds for 1 hour. Reaction progress curves were normalized by background subtraction of unphosphorylated sox-NFAT4 signal for each concentration. Curves were fit to the single-exponential equation (4.1) [177].

Equation 4.1:

$$F(t) = F_0 + (F_\infty - F_0)(1 - e^{-k_{obs}t})$$

To evaluate linearity of the fluorescence signal as a function of phosphorylated peptide concentration, the maximal signal (F_∞) from equation (4.1) was plotted against sox-NFAT4 concentration for each condition (Supplementary Figure D1 A). The resulting curve was fit by linear regression to evaluate the conversion factor, Q (1027 ± 27 RFU/ μM for JNK1 and 1095 ± 14 RFU/ μM for JNK2). Q is a proportionality constant used to convert fluorescence units to reaction product concentration. Strong linearity ($r > 0.99$) was confirmed, so in all subsequent assays the peptide concentration was treated as directly proportional to the fluorescence output by the conversion factor (Q), and Q was re-evaluated for each experiment as validation. To evaluate K_m and k_{cat} for sox-NFAT4 phosphorylation ($K_{m,S}$ and $k_{cat,S}$) for JNK1 and JNK2, the initial rates of each reaction were defined over the range of 0-600 s, and this subset of the data was fit by linear regression (Supplementary Figure D1, parts B and D). The initial rates for each reaction were then expressed in units of $\mu\text{M/s}$ by normalizing the fluorescence rates by the appropriate conversion factor (Q). Steady state kinetic parameters were then

evaluated by fitting the rate data to the Michaelis-Menten equation (Supplementary Figure D1, parts C and E).

The $K_{m,S}$ values for JNK1 and JNK2 were evaluated to be $1.2 \pm 0.2 \mu\text{M}$ and $2.3 \pm 0.5 \mu\text{M}$, respectively (Supplementary Figure D1). This provided a starting estimate for concentration of sox-NFAT4 in the optimization of JNK-IN-8 assays. Similarly the $k_{cat,S}$ was measured at $0.21 \pm 0.01 \text{ s}^{-1}$ for JNK1 and $0.32 \pm 0.02 \text{ s}^{-1}$ for JNK2.

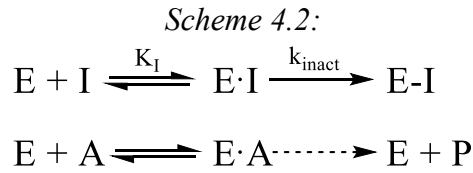
Steady State Kinetics: K_m and k_{cat} for ATP

To determine K_m and k_{cat} for ATP substrate under the reaction conditions for covalent inhibition of JNK, we tested phosphorylation $4 \mu\text{M}$ sox-NFAT4 by 2.5 nM JNK1 or 5 nM JNK2 in the presence of varied MgATP ($0.5\text{-}100 \mu\text{M}$). Fluorescence measurements were collected every 5 s for 600 s (Supplementary Figure D2, parts A and C). The Michaelis constants with respect to ATP ($K_{m,A}$) were determined in the same manner as described for sox-NFAT4, resulting in $K_{m,A}$ for JNK1 of $7.0 \pm 0.8 \mu\text{M}$ and $K_{m,A}$ for JNK2 of $6.4 \pm 0.6 \mu\text{M}$ (Supplementary Figure D2, parts B and D). These parameters were used in evaluation of the constant K_I for JNK-IN-8.

JNK-IN-8 Assays

Reaction progress curves were measured for 2.5 nM JNK1 (or 5 nM JNK2) phosphorylation of sox-NFAT4 ($4 \mu\text{M}$) in the presence of varied amounts of JNK-IN-8 ($0\text{-}5 \mu\text{M}$). This assay was repeated at varied concentrations of MgATP for each JNK isoform. ATP concentrations were determined by measuring the absorbance of 7X concentrated MgATP stock solutions at $\lambda = 259 \text{ nm}$. Fluorescence data were collected every 5 s for a minimum of 600 s .

To model the mechanism of time-dependent inhibition of JNK by JNK-IN-8, we assumed a model of enzyme affinity labeling that is equivalent to mechanism-based inactivation. This model is characterized by two steps: JNK-IN-8 binding in the active site, followed by irreversible covalent reaction at C116. The enzyme mechanism in the presence of JNK-IN-8 is shown in Scheme 4.2. The enzyme is assumed to follow Michaelis-Menten kinetics over the time-course of the experiment.



Here E (enzyme) can either react covalently with inhibitor (I) and become inactivated, or it can react with ATP substrate (A) to yield ADP product (P). The substrate in this model is depicted as ATP rather than sox-NFAT4 since JNK-IN-8 directly competes with ATP for the same binding site. Negligible depletion of unphosphorylated sox-NFAT4 is assumed over the time-course of the experiment, as discussed further below.

Data sets were fit globally in GraphPad Prism to the system of equations below [241]. The Prism equation and parameter inputs are further described in Appendix D.

Equation 4.2:

$$[P] = \begin{cases} v_s t & \text{if } [I] = 0 (k_{obs} = 0) \\
 \left(\frac{v_o - v_s}{k_{obs}} \right) (1 - e^{-k_{obs}t}) & \text{if } [I] \neq 0 (k_{obs} \neq 0) \end{cases}$$

Equation 4.3:

$$k_{obs} = \frac{k_{\text{inact}}[I]}{K_I^* + [I]}$$

Equation 4.4:

$$K_I^* = K_I \left(1 + \frac{[A]}{K_{m,A}} \right)$$

In equation (4.2), [P] is the concentration of the phosphorylated sox-NFAT4, which is directly measured as the fluorescence signal normalized by the conversion factor Q. (Note that the concentration of phosphorylated sox-NFAT4 is equivalent to that of ADP due to reaction stoichiometry.) The rates v_s and v_0 are the steady state and initial rates of reaction, respectively, and k_{obs} is the apparent first-order rate constant for conversion from v_0 to v_s . This change in the reaction rate is attributable to the rate of inactivation of JNK by the inhibitor, assuming the following assumptions are valid:

- (1) There is no substrate depletion for the duration of measurement of the control reaction ($[I] = 0 \mu\text{M}$); i.e. for $[I] \neq 0 \mu\text{M}$, the only possible source of measured change in reaction rate is due to enzyme inactivation by inhibitor. In order for this assumption to be valid, the reaction progress curve for this case must be linear.
- (2) There is no tight-binding inhibition, or initial enzyme concentration $[E]_0 \ll K_I^*$ and inhibitor concentration is not depleted over the course of the reaction ($[I] \gg [E]_0$).

Assumption (1) above was validated by analyzing the linearity of the control (0 μM JNK-IN-8) progress curves. Assumption (2) was confirmed by using inhibitor concentrations at least 20X the initial enzyme concentration of 2.5 nM, and by using substrate (ATP) protection at the active site to raise the observed K_I^* . Therefore, it can be assumed that k_{obs} is also the apparent first order rate constant for inactivation of JNK. From the enzyme reaction model, k_{obs} is described by equation (4.3) where K_I^* is the

apparent concentration of inhibitor required to reach half-maximal enzyme inactivation and k_{inact} is the maximum rate of enzyme inactivation.

Since JNK-IN-8 is a competitive inhibitor of the ATP binding site, K_I^* is a function of ATP concentration, as given by equation (4.4). Here, ATP concentration was assumed to be saturating with negligible depletion over the course of each reaction, so it was quantified by absorbance measurements of initial MgATP stocks. The K_m for ATP, $K_{m,A}$, was determined from steady state substrate kinetics assays. Equation (4.4) allows evaluation of the observed K_I by extrapolating to the theoretical absence of ATP.

Cell Lines and Treatments

PyVMT *jnk1*^{-/-} and PyVMT *jnk2*^{-/-} cell lines were provided by the Van den Berg laboratory at the UT Austin Institute for Cellular and Molecular Biology [242]. Cells were plated in 10 cm dishes at 1.5 million cells per plate (PyVMT *jnk1*^{-/-}) or 750,000 cells per plate (PyVMT *jnk2*^{-/-}) and cultured in DMEM-F:12 media containing 10% FBS, 25 $\mu\text{g}/\text{mL}$ EGF, and 10 $\mu\text{g}/\text{mL}$ insulin for approximately 24 hours. The cells were washed 2X with warm PBS and serum-starved overnight in DMEM-F:12 media containing 1X MEM amino acids and 10 mM HEPES. Then the cells were treated with 0-5 μM inhibitor (final concentration of 0.1% (v/v) DMSO) for a total of 4 hours in serum –free media. During the last 45 minutes of this treatment, the cells were stimulated with 8 μM anisomycin. Stimulated and un-stimulated DMSO controls were included in each experiment. After 45 minutes, the plates were placed on ice and the media was replaced with ice-cold PBS. The cells were collected by manual scraping in 100 μL ice-cold PBS and were centrifuged at 400 rcf for 5 minutes at 4°C. The remaining cell pellets were resuspended in 60 μL MPER lysis buffer containing 1X

Halt™ protease and phosphatase inhibitor cocktail (Thermo Scientific) and were flash-frozen in liquid nitrogen.

Western Blots

Thawed lysates were cleared by centrifugation and protein concentrations were evaluated by Bradford protein assay (Bio-Rad). Sample lysates were run on SDS-PAGE gels (10% acrylamide gel) at 40 µg protein/lane, and the gel contents were transferred to Immobilon®-FL PVDF membranes (EMD Millipore) overnight at 4°C (30 V). The membranes were blocked in 4X diluted Odyssey® blocking buffer (LI-COR) in PBS for 1 hour at room temperature. Primary antibodies were applied at 4°C overnight according to the following conditions: 1:500 phospho-c-Jun (Ser63) II rabbit antibody (5% BSA in TBST), 1:1000 phospho-SAPK/JNK (Thr183/Tyr185) (G9) mouse mAb (5% milk in TBST), 1:1000 c-Jun (60A8) rabbit mAb (5% milk in TBST), and 1:1000 JNK1 (2C6) mouse mAb or JNK2 (56G8) rabbit mAb (5% BSA in TBST). All primary antibodies were obtained from Cell Signaling Technology. The membranes were washed 3 times for 5 minutes each in TBST. Then they were incubated with appropriate secondary antibodies at 1:15,000 in 5% milk/TBST for 30 minutes at room temperature. Secondary antibodies included IRDye® 800CW Goat (polyclonal) anti-rabbit IgG and/or IRDye® 680RD Goat (polyclonal) anti-mouse IgG (LI-COR). The membranes were washed and scanned on an Odyssey® Sa imaging system (LI-COR) and fluorescence was quantified. The membranes were saved and incubated with 1:3000 vinculin (E1E9V) XP® rabbit mAb for 1 hour at room temperature to provide a loading control. The secondary antibody was applied and the membranes were imaged again as described.

RESULTS AND DISCUSSION

Kinetic Parameters for Inactivation of JNK1/2 by JNK-IN-8

In order to characterize the mechanism of JNK-IN-8, we developed a method to determine K_I and k_{inact} for JNK1 and JNK2 inhibition. There are several types of experiments that can be used to evaluate these parameters. Directly solving differential equations to evaluate rate constants is possible if assay conditions can be used to simplify the reaction mechanism [243]. It is also possible to evaluate K_I and k_{inact} from IC_{50} measurements taken at different inhibitor incubation times, however this method can become too mathematically intensive and strongly depends on k_{inact} to allow a broad measurement window [244]. A more common method of evaluating these parameters involves incubation of enzyme with inhibitor, followed by dilution of the mixture and measurement of residual enzyme activity [245]. However, this method is not appropriate for very potent inhibitors like JNK-IN-8 that still exhibit reactivity at nanomolar concentrations. For JNK-IN-8, we instead chose to directly measure product formation over time via a fluorescent peptide substrate, sox-NFAT4. The resulting reaction progress curves allowed simple evaluation of K_I and k_{inact} .

For JNK1 and JNK2, reaction progress curves were evaluated for a range of JNK-IN-8 concentrations at different saturating ATP concentrations, as shown in Figures 4.1 and 4.2, respectively. Saturating both substrates was necessary for the duration of each experiment, so any observed decreases in the rate of product formation could be attributed solely to inactivation of the enzyme by JNK-IN-8 rather than substrate depletion. Substrate saturation was confirmed by linearity of the reaction progress curves for the controls (0 μ M JNK-IN-8), and ATP concentrations themselves were confirmed by absorbance measurements at 259 nm wavelength. The calculated apparent K_I^* is

dependent on ATP concentration as described in Materials and Methods, due to competition of ATP and JNK-IN-8 for the same binding site. The known ATP concentration [A] and the Michaelis constant for JNK1 or JNK2 phosphorylation of ATP ($K_{m,A}$) were used to determine the ATP-independent parameter K_I (equation (4.4)). Values of K_I and k_{inact} for each experiment, along with calculated K_I^* and ATP concentration, are shown in Table 4.1. The resulting average K_I and k_{inact} values for JNK-IN-8 inactivation of each JNK isoform are shown in Figure 4.3. For JNK1, $K_I = 23.8 \pm 1.8$ nM and $k_{inact} = (12 \pm 4) \times 10^{-3} \text{ s}^{-1}$. Similarly, for JNK2, $K_I = 35.3 \pm 12.2$ nM and $k_{inact} = (4.7 \pm 1.5) \times 10^{-3} \text{ s}^{-1}$. The ratio of k_{inact}/K_I is a second-order rate constant of enzyme inactivation and is used as an indicator of inhibitor potency. The value of k_{inact}/K_I is $5.0 \times 10^5 \text{ M}^{-1}\text{s}^{-1}$ for JNK1 and $1.3 \times 10^5 \text{ M}^{-1}\text{s}^{-1}$ for JNK2, which reveals a 4-fold selectivity of JNK-IN-8 for JNK1 over JNK2. These values are consistent with the trend shown by previously reported IC_{50} values of 4.7 nM for JNK1 and 18.7 nM for JNK2, which also indicate that the inhibitor has approximately 4-fold selectivity for JNK1 over JNK2 [128]. This suggests that it is possible to use IC_{50} experiments as an initial test for isoform selectivity in the future development of JNK-IN-8 analogs.

Comparing JNK-IN-8 Kinetic Parameters to Other Covalent Kinase Inhibitors

Table 4.2 shows the values of K_I and k_{inact} as well as k_{inact}/K_I for examples of other covalent kinase inhibitors in comparison to JNK-IN-8. The values of k_{inact}/K_I for JNK-IN-8 are very high for both isoforms of JNK. Its potency is similar to those of CL-387785 and WZ-4002, which are in pre-clinical development for EGFR tyrosine kinase inhibition. JNK-IN-8 has much more potent k_{inact}/K_I ratios than 2'-thioadenosine, a weak EGFR inhibitor, and hypothemycin, a natural product that is a promiscuous kinase inhibitor. However, K_I and k_{inact} must also be considered individually when evaluating

covalent inhibitors, not just as a ratio. The value of K_I is a metric of binding affinity while k_{inact} indicates reactivity of an inhibitor, but their numerical values do not always directly correspond to favorable characteristics. For example, an increase in an inhibitor's k_{inact} might result in off-target promiscuity, though it will positively increase the metric k_{inact}/K_I . Sometimes a high k_{inact} is a result of a moderately reactive inhibitor that binds in a position that strongly facilitates its reaction. This favorable, highly selective binding would be reflected by a low K_I (high affinity). This balance of parameters is illustrated by the EGFR- L858R/T790M inhibitors listed in Table 4.2. In contrast, 2'-thioadenosine is a much less potent example, with a high K_I and a moderate k_{inact} . JNK-IN-8 falls well within the broad range of these kinetic parameters for known covalent kinase inhibitors, and it is additionally highly selective for JNK isoforms over other kinases [128].

The reactive functional groups of the inhibitors listed in Table 4.2 are displayed in Figure 4.4. Other inhibitors with the same reactive group as JNK-IN-8 include afatinib, neratinib, and compound III, all of which target the active site of EGFR-L858R/T790M (Figure 4.4) [243]. Though the reactive functional groups of these inhibitors are the same, their kinetic parameters significantly vary, illustrating the importance of binding mode in determining potency. When compared to the FDA-approved covalent drugs afatinib and neratinib, JNK-IN-8 has a weaker K_I value by over 100-fold, while k_{inact} values are all relatively similar. Thus, JNK-IN-8 can likely be improved through development of analogues that focus on the inhibitor binding step of the covalent reaction instead of on altering reactivity. These data together show the utility of addressing covalent inhibitors in terms of K_I and k_{inact} rather than IC_{50} . In addition to being independent of experimental conditions, these parameters contain more information about a covalent inhibitor than the IC_{50} , though IC_{50} values can be a good indicator of an individual inhibitor's relative potency against multiple enzyme targets.

Limitations of the Reaction Progress Curve Assay

To test the versatility of the described reaction progress curve assay, it was applied to a derivative of JNK-IN-8, THZ-3-60-1, in order to evaluate its potential selectivity for JNK2 over JNK1. However, this inhibitor was found to absorb UV light at the wavelength of the fluorescent probe excitation (Supplementary Figure D3) and subsequently degraded into fragments as confirmed by TLC (data not shown). Thus, this assay is not applicable to all potential derivatives of JNK-IN-8. Additionally, the assay described here can only determine K_I and k_{inact} for covalent inhibitors of the active enzyme, as phosphorylation of the fluorescent probe is required to obtain the reaction progress curves. Potential inhibitors that selectively target the inactive form of JNK1 or JNK2 must be detected and characterized by other methods.

It is possible that some of the analogues tested in this study may have a different binding mode than JNK-IN-8 itself. This is especially likely given that THZ-3-60-1 was found to be non-covalent, as determined by dose-response experiments that did not utilize fluorescence detection methods (Appendix D). THZ-3-60-1 is also much less potent than JNK-IN-8 against JNK phosphorylation of ATF-2 *in vitro*, and it is highly selective for JNK2 with an IC_{50} of $4.0 \pm 1.1 \mu\text{M}$ as compared to $>100 \mu\text{M}$ for JNK1 (Supplementary Figure D3 A). Ideally, an isoform-specific JNK inhibitor would covalently target a single isoform with nanomolar potency, while leaving the other isoforms unaffected.

Evaluating Selectivity of Inhibitors for JNK Isoforms in Cells

Given the importance of evaluating the isoform-selectivity of different JNK inhibitors and the apparent limitations of the reaction progress curve assay when applied to inhibitors other than JNK-IN-8, we explored a different approach to inhibitor characterization. We tested 10 JNK-IN-8 analogues in PyVMT cells with either *jnk1* or

jnk2 knocked out, in order to determine if the compounds preferentially inhibit JNK1 or JNK2. The PyVMT model closely resembles human breast cancer, wherein JNK2 has been shown to play a major isoform-specific role in cell migration in comparison to JNK1 [32]. The *jnk1*^{-/-} and *jnk2*^{-/-} cell lines are derived from spontaneous mouse mammary tumors [246]. Testing these compounds in this model should not only indicate JNK isoform-specificity, but also therapeutic potential and SAR details that can be used to further modify and improve the compound structures.

Each cell line was treated with 0-5 μ M of each compound for 4 hours, including 45 minutes of anisomycin treatment for stimulation of JNK signaling (or unstimulated control) prior to harvesting cells. The levels of phosphorylated and total c-Jun, as well as phosphorylated and total JNK1 and JNK2, were detected and quantified by Western blot.

THZ-3-60-1 (Figure 4.5) showed preference for inhibition of JNK2 phosphorylation and c-Jun phosphorylation in *jnk1*^{-/-} cells. Additionally, JNK-In-B (Figure 4.6) and JNK-In-C (Figure 4.7) selectively inhibited JNK2 phosphorylation in *jnk1*^{-/-} cells. For all three compounds, however, JNK1 phosphorylation was also inhibited significantly in *jnk2*^{-/-} cells at slightly higher compound concentrations than required for JNK2 inhibition. Compound YL-01-035-1 showed similar inhibition of JNK1, JNK2, and c-Jun phosphorylation in each cell line, with a possible slight preference for inhibition of JNK2 phosphorylation of c-Jun in *jnk1*^{-/-} cells (Figure 4.8). Thus, these compounds all exhibited a minor selectivity for targeting JNK2 over JNK1. Conversely, YL-02-053-1 showed slight inhibition of JNK1 phosphorylation and c-Jun phosphorylation in *jnk2*^{-/-} cells, but it had little to no effect on JNK2 phosphorylation or activity (Figure 4.9).

YL-01-042-1, YL-02-057-1, and YL-02-079-1 all showed some inhibition of JNK2 phosphorylation but no significant effects on phosphorylation of JNK1 or c-Jun in

either cell line (Figures 4.10, 4.11, 4.12 respectively). YL-02-048-1 had the opposite effects, with most drastic inhibition of JNK1 phosphorylation in *jnk2*^{-/-} cells (Figure 4.13). YL-02-056-1 fully inhibits c-Jun phosphorylation in *jnk1*^{-/-} cells and has no effect on c-Jun phosphorylation in *jnk2*^{-/-} cells; however, it similarly inhibits JNK phosphorylation in both cell lines (Figure 4.14). Of the 10 tested compounds, these five showed the most evidence of isoform-specific effects.

Interestingly, the 10 compounds tested here inhibited JNK1 or JNK2 activation to at least some degree. Previously, JNK-IN-8 was also shown by our group to inhibit JNK activation in the PyVMT model with a preference for JNK2 inhibition [242]. However, when JNK-IN-8 and several of its analogs were tested by Zhang, *et al.* (2012) in HEK293-ILR1 cells, they did not inhibit JNK phosphorylation over a concentration range of 0-3 μ M and treatment duration of 18 hours [128].

It is possible that some of the analogues tested here may have a different binding mode than JNK-IN-8 itself. This is especially likely given that THZ-3-60-1 was found to be non-covalent, as determined by dose-response experiments (Appendix D) and lack of observed band shifts for JNK in Western blot analyses that would indicate covalent reaction. THZ-3-60-1 is also much less potent than JNK-IN-8 against JNK1 and JNK2 *in vitro*. The cell experiments conducted by Zhang, *et al.* (2012) suggest that JNK-IN-8 does not block or otherwise prevent the upstream kinases MKK4 and MKK7 from activating JNK. Unlike their cell experiments, ours utilize a different cell line which can result in different pathway interactions and protein expression levels between the two studies. Additionally, we measured JNK1 or JNK2 phosphorylation, rather than the two isoforms together. We believe that the drop in JNK2 phosphorylation that we have previously observed with JNK-IN-8 in PyVMT cells is likely due to inhibition of JNK2 autophosphorylation, something that would not necessarily be observed in other cell lines

if looking at cumulative JNK1 and JNK2 [242]. On the other hand, some of the THZ-3-60-1 analogues discussed here may bind in such a way as to induce a different activation loop conformation that prevents JNK phosphorylation. This would potentially account for the dose-dependent loss of JNK1 phosphorylation observed for THZ-3-60-1, JNK-IN-B, JNK-IN-C, YL-02-048-1, YL-01-035-1, YL-02-056-1, and YL-02-053-1 treatments. THZ-3-60-1 appears to be more potent in cells than *in vitro* experiments (Figure 4.5, Supplementary Figure D3 A), suggesting that it is a non-covalent inhibitor that preferentially targets the inactive form of JNK, preventing its activation by upstream kinases. This could imply a similar mechanism to other known kinase inhibitors like the MEK inhibitor PD098059 [247]. JNK-IN-8 analogues that potently block both activation of JNK by upstream kinases as well as phosphorylation of downstream substrates by active JNK may bear more resemblance to the ERK inhibitor SCH772984 that induces a conformational change in the activation loop of ERK [113].

CONCLUSIONS

Ideally, an isoform-specific JNK inhibitor would potently target one isoform while leaving the others unaffected. Based on the quantified Western blot data collected over the inhibitor concentration range of 0-5 μM , compounds YL-01-042-1, YL-02-056-1, YL-02-057-1, and YL-02-079-1 most closely meet these criteria for JNK2 inhibition. Importantly, JNK2 is a therapeutic target in breast cancer and the PyVMT mammary tumor model. These inhibitors must be tested over a larger concentration range to determine their fold-selectivity for JNK2 and could be further structurally optimized to increase their selectivity. Inhibition of JNK phosphorylation could indicate that the compounds selectively target the inactive enzyme, so it is also necessary to evaluate their potency against active and inactive JNK isoforms. Once potent small-molecule inhibitors

with isoform selectivity are developed, they will be a crucial tool to differentiate the roles of each isoform in different disease states and cellular processes.

Here we have presented two methods for evaluating JNK-IN-8 analogues: a reaction progress curve assay to evaluate kinetic parameters, and a cell-based assay for quantifying isoform-specific inhibition. This study has demonstrated the importance of fully characterizing the kinetic parameters of covalent inhibitors. From K_I and k_{inact} for JNK-IN-8, with respect to other covalent kinase inhibitors, it is clear that binding potency can be improved in future analogue design while reactivity is appropriate for minimizing off-target effects. This room to adjust binding affinity (K_I) can be utilized to design isoform-specific inhibitors, which can be evaluated in *jnk1*^{-/-} and *jnk2*^{-/-} cells as we have described in this study.

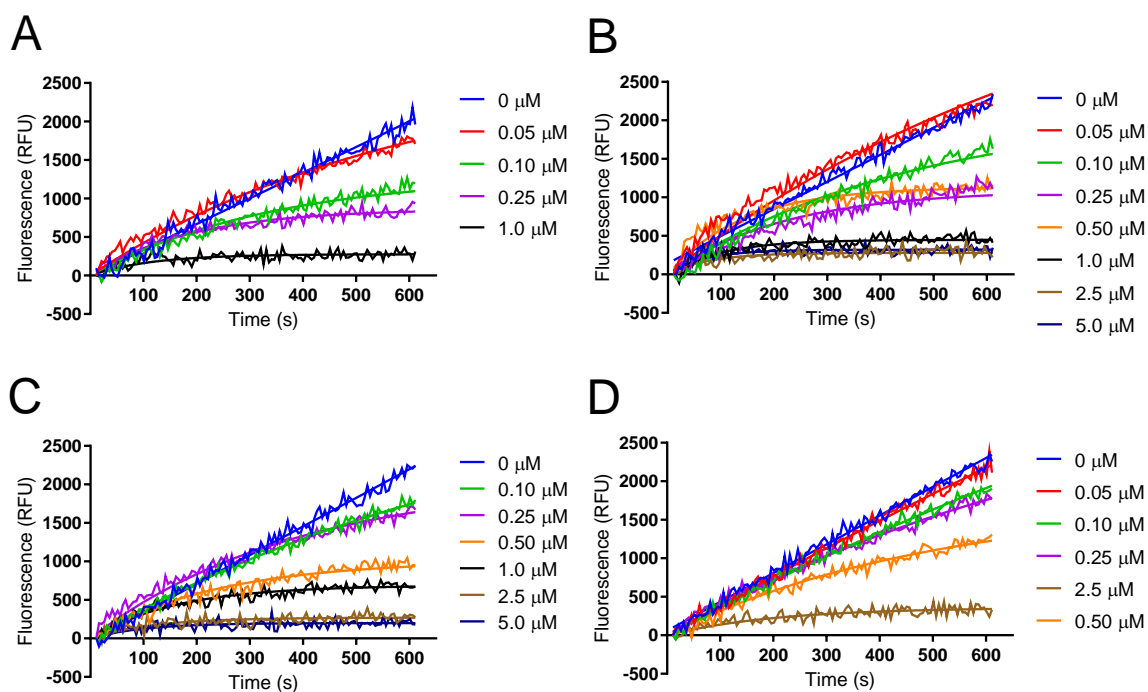


Figure 4.1. Reaction progress curves for JNK-IN-8 inhibition of JNK1.

The ability of JNK1 to phosphorylate the fluorescent reporter peptide sox-NFAT4 was measured in the presence of JNK-IN-8. ATP concentrations were fixed at (A) 83 μM, (B) 164 μM, (C) 251 μM, and (D) 402 μM. JNK-IN-8 concentrations were varied from 0-5 μM at each ATP concentration. Time ranges of measurements were set by linearity of the control (0 μM JNK-IN-8). Data were fit globally as described in Materials and Methods and Appendix D.

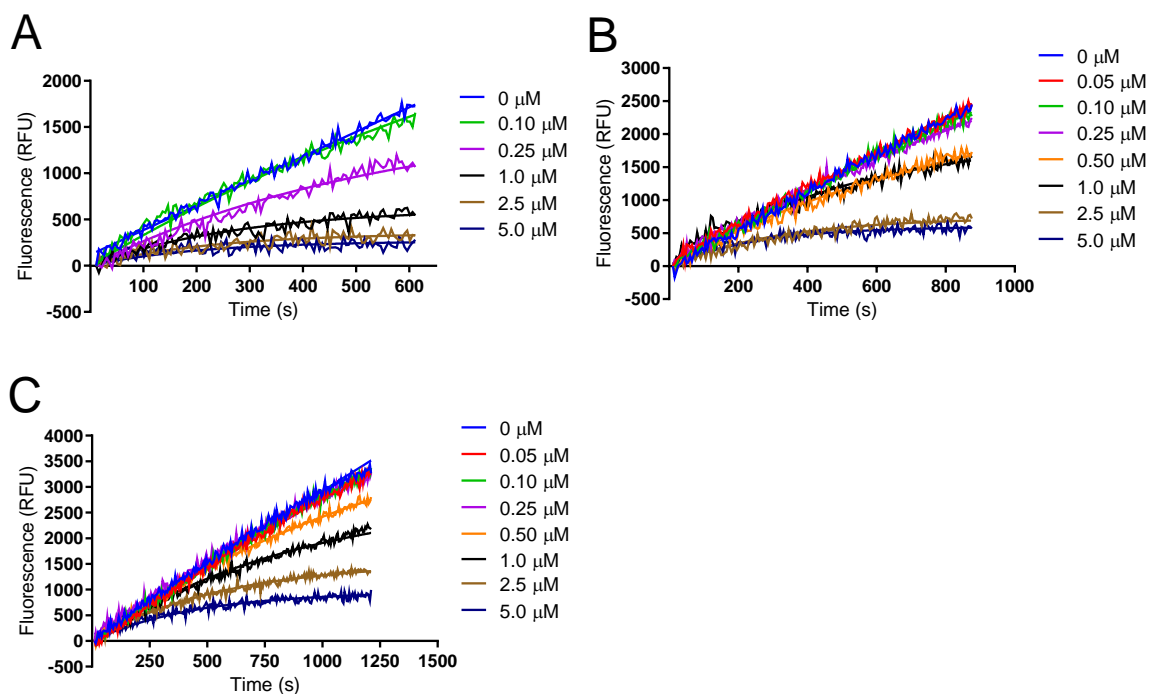


Figure 4.2. Reaction progress curves for JNK-IN-8 inhibition of JNK2.

The ability of JNK2 to phosphorylate the fluorescent reporter peptide sox-NFAT4 was measured in the presence of JNK-IN-8. ATP concentrations were fixed at (A) 92 μM , (B) 254 μM , and (C) 426 μM . JNK-IN-8 concentrations were varied from 0-5 μM at each ATP concentration. Time ranges of measurements were set by linearity of the control (0 μM JNK-IN-8). Data were fit globally as described in Materials and Methods and Appendix D.

JNK isoform	k_{inact} (10^{-3} s^{-1})	K_{I}^* (μM)	K_{I} (nM)	[ATP], μM
JNK1	11.3 ± 1.5	0.283 ± 0.054	22.0 ± 4.3	83
	16.3 ± 1.6	0.644 ± 0.088	26.2 ± 3.6	164
	11.7 ± 1.2	0.879 ± 0.126	23.9 ± 3.5	251
	7.5 ± 1.5	1.35 ± 0.35	23.1 ± 6.0	402
JNK2	5.3 ± 0.6	0.505 ± 0.097	32.9 ± 6.3	92
	5.6 ± 0.5	1.97 ± 0.25	48.5 ± 6.3	254
	3.0 ± 0.1	1.65 ± 0.13	24.4 ± 1.8	426

Table 4.1. JNK-IN-8 kinetic parameters.

For JNK-IN-8 inhibition of JNK1 and JNK2, the kinetic parameters k_{inact} and K_{I} are shown for each experimental condition. Each experiment was conducted at different saturating ATP concentrations, resulting in varying apparent K_{I}^* due to competition between ATP and JNK-IN-8.

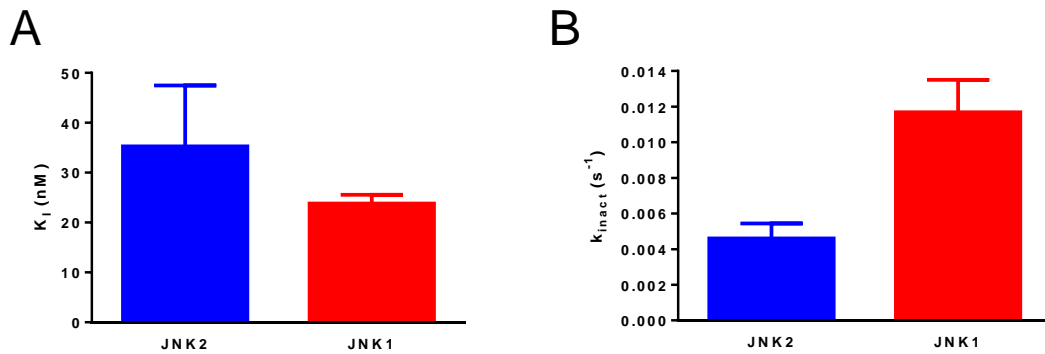


Figure 4.3. Average values of kinetic parameters for JNK-IN-8.

Average values of (A) K_I and (B) k_{inact} for each JNK isoform from all experiments (n=3 for JNK2, n=4 for JNK1). Error bars are standard error of global data fits for each parameter.

Inhibitor	Target	K _I (10 ⁻⁹ M)	k _{inact} (10 ⁻³ s ⁻¹)	Approx. k _{inact} /K _I (10 ⁶ M ⁻¹ s ⁻¹)	Source
CI-1033	EGFR-L858R/T790M	0.11 ± 0.03	11.0 ± 0.2	100	Schwartz, <i>et al.</i> , PNAS, 2014 [243]
Dacomitinib		0.63 ± 0.05	1.8 ± 0.1	2.9	
Afatinib*		0.16 ± 0.03	2.4 ± 0.3	15	
Neratinib*		0.14 ± 0.03	1.1 ± 0.2	7.9	
WZ-4002		13 ± 3	5.0 ± 0.1	0.38	
CL-387785		10 ± 2	2.0 ± 0.3	0.20	
I		0.14 ± 0.07	8.0 ± 0.4	57	
II		2.3 ± 0.3	3.5 ± 0.6	1.5	
III*		4.0 ± 1.0	1.8 ± 0.1	0.4	
IV		108 ± 20	0.15 ± 0.02	0.0014	
V		30 ± 3	1.1 ± 0.1	0.037	
hypothemycin	ERK1	8400	5.0	0.0006	Schirmer, <i>et al.</i> , PNAS, 2006 [125]
	ERK2	2400	4.3	0.0018	
	MEK1	17	2.0	0.12	
	MEK2	38	1.0	0.026	
2'-thioadenosine	EGFR	1000 ± 300	2.3 ± 0.2	0.0023	Singh, <i>et al.</i> , J. Med. Chem. 1997 [248]
VI	BTK	2.0 ± 1.4	2.3 ± 0.7	1.2	Wang, <i>et al.</i> , Eu. J. Med. Chem., 2017 [249]
VII		3.2 ± 0.06	2.5 ± 0.2	0.78	
VIII		14.2 ± 2.8	2.2 ± 0.8	0.15	
XVIII		97 ± 30	1.2 ± 0.5	0.012	
1a	PDK1	3700 ± 300	5.6 ± 0.3	0.0015	Liu, <i>et al.</i> , J. Med. Chem. 2017 [250]
1m		1800 ± 200	7.0 ± 0.5	0.0039	
2e		3300 ± 100	0.21 ± 0.01	0.00006	
2g		870 ± 70	0.47 ± 0.03	0.00054	
2h		4000 ± 700	0.32 ± 0.03	0.00007	
2k		110 ± 20	0.44 ± 0.02	0.0042	
2r		22000 ± 2500	0.69 ± 0.01	0.00003	
2s		120 ± 30	0.50 ± 0.02	0.0041	
3a		110 ± 10	0.55 ± 0.04	0.0051	
XVI		460 ± 50	0.88 ± 0.02	0.0019	
JNK-IN-8		JNK1	23.8 ± 1.8	12 ± 4	
	JNK2	35.3 ± 12.2	4.7 ± 1.5	0.13	

Table 4.2. Kinetic parameters of covalent kinase inhibitors.

Table 4.2. Kinetic parameters of covalent kinase inhibitors.

Selected covalent kinase inhibitors, their target kinases, and corresponding values of K_I , k_{inact} , and k_{inact}/K_I are shown. Inhibitors with the same reactive functional group as JNK-IN-8 are denoted with (*).

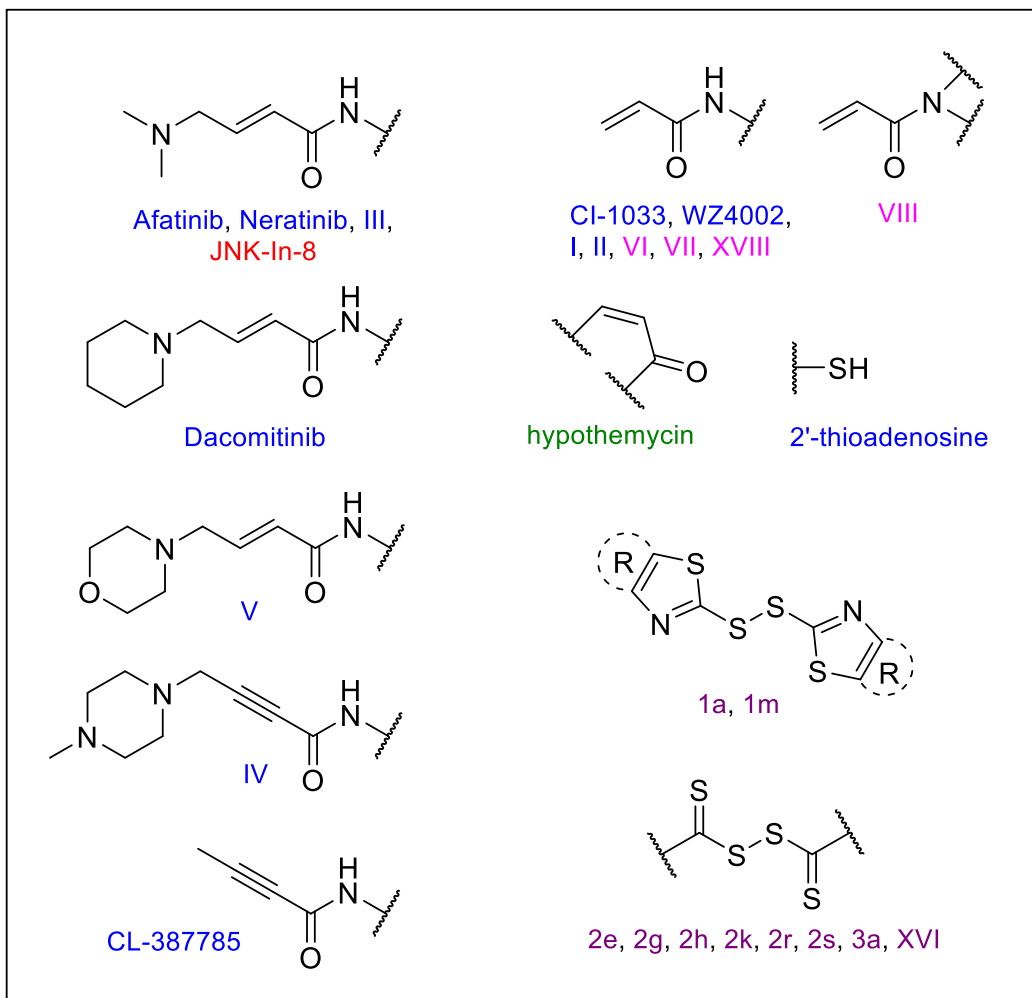


Figure 4.4. Reactive functional groups associated with selected covalent kinase inhibitors.

Reactive groups of the covalent inhibitors referenced in the table. Text color coded to indicate JNK inhibitors (red), EGFR inhibitors (blue), BTK inhibitors (pink), PDK1 inhibitors (purple), and ERK/MEK inhibitors (green). 'R' indicates variable functional groups.

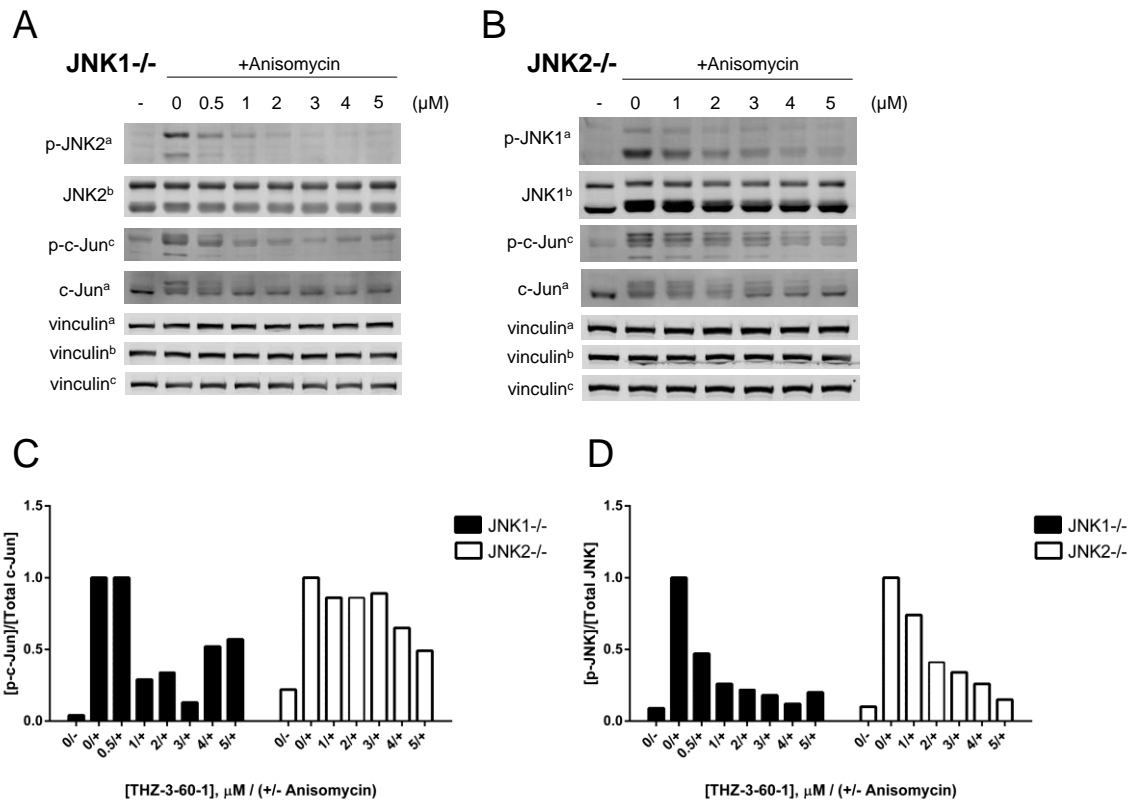


Figure 4.5. THZ-3-60-1.

Western blots for THZ-3-60-1 inhibition of (A) *jnk1*^{-/-} and (B) *jnk2*^{-/-} PyVMT cells. Phosphorylated and total levels of both c-Jun and JNK1 or JNK2 were measured for 4-hour treatment with 0-5 μM THZ-3-60-1, with or without stimulation of signaling with 8 μM anisomycin. Superscripts after protein labels indicate corresponding vinculin loading controls used for quantification. (C) Quantification of the ratio of phospho-c-Jun to total c-Jun for each sample. (D) Quantification of the ratio of phosphorylated JNK1/2 to total JNK1 or JNK2 for each cell line. All sample signals were normalized to appropriate vinculin loading controls prior to further data processing. Ratios of phospho- to total protein levels were normalized to the maximal signal control (DMSO + anisomycin treatment).

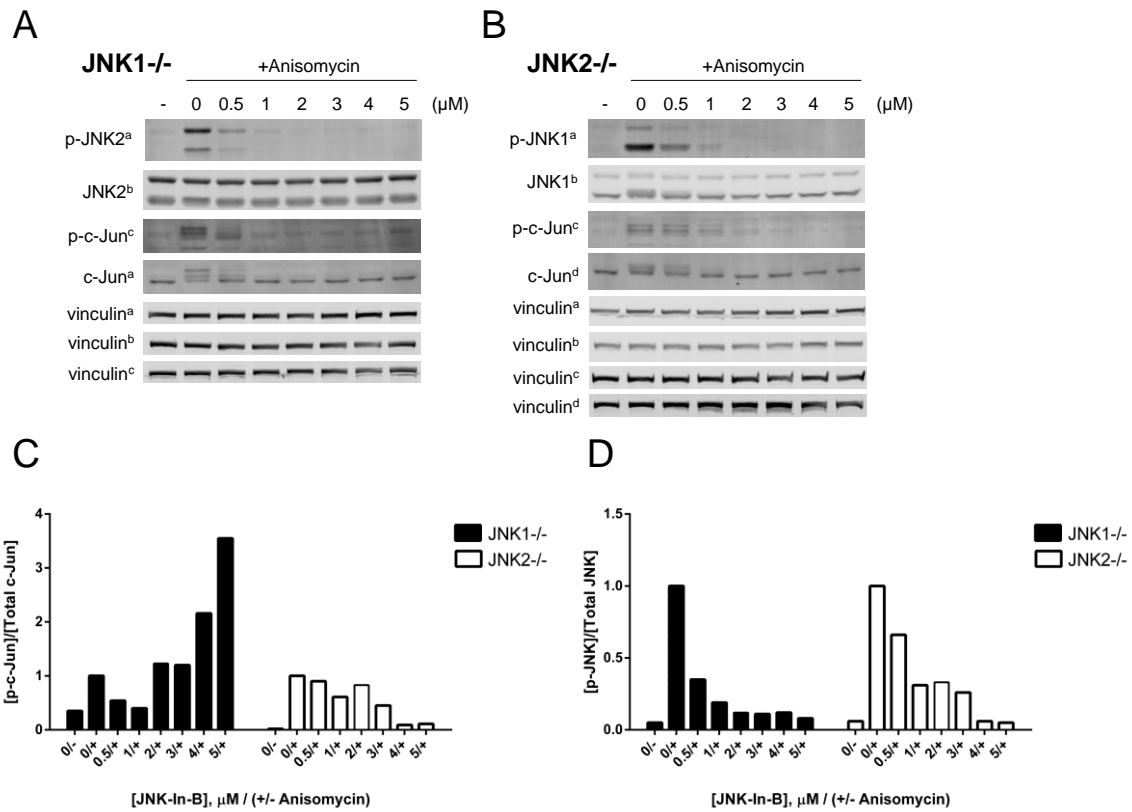


Figure 4.6. JNK-In-B.

Western blots for JNK-In-B inhibition of (A) *jnk1*^{-/-} and (B) *jnk2*^{-/-} PyVMT cells. Phosphorylated and total levels of both c-Jun and JNK1 or JNK2 were measured for 4-hour treatment with 0-5 μM JNK-In-B, with or without stimulation of signaling with 8 μM anisomycin. Superscripts after protein labels indicate corresponding vinculin loading controls used for quantification. (C) Quantification of the ratio of phospho-c-Jun to total c-Jun for each sample. (D) Quantification of the ratio of phosphorylated JNK1/2 to total JNK1 or JNK2 for each cell line. All sample signals were normalized to appropriate vinculin loading controls prior to further data processing. Ratios of phospho- to total protein levels were normalized to the maximal signal control (DMSO + anisomycin treatment).

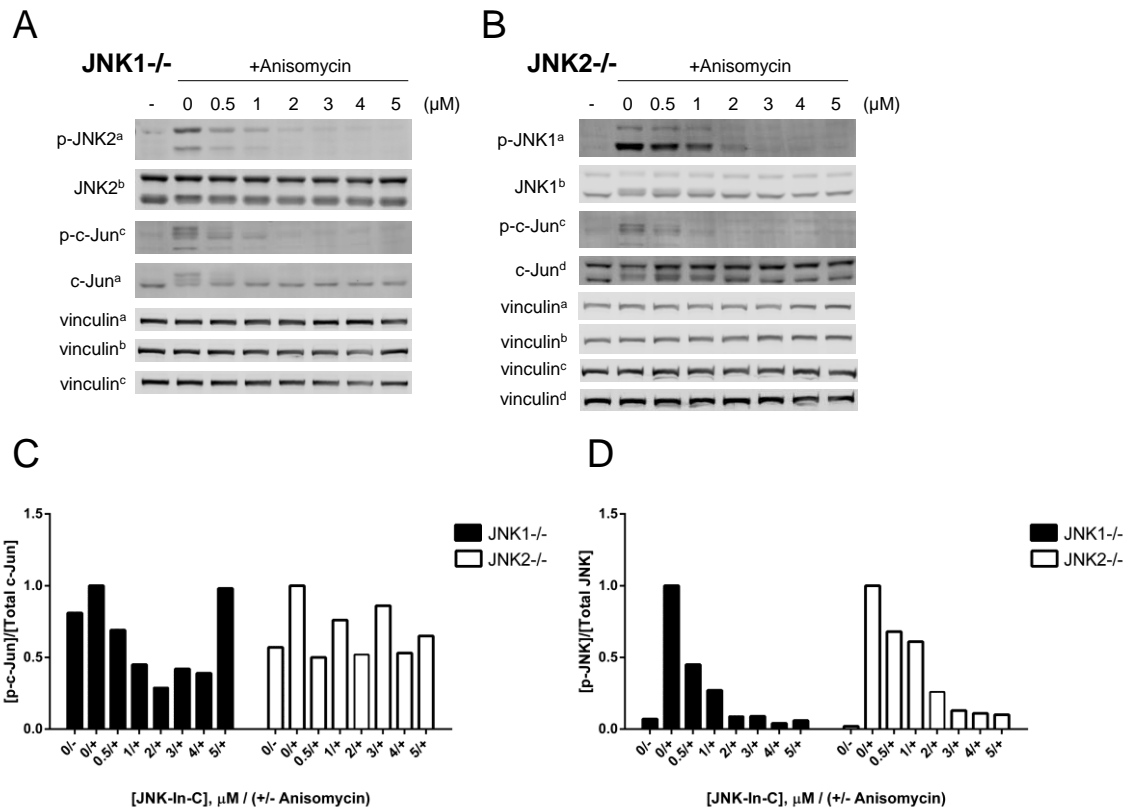


Figure 4.7. JNK-In-C.

Western blots for JNK-In-C inhibition of (A) *jnk1*^{-/-} and (B) *jnk2*^{-/-} PyVMT cells. Phosphorylated and total levels of both c-Jun and JNK1 or JNK2 were measured for 4-hour treatment with 0-5 μM JNK-In-C, with or without stimulation of signaling with 8 μM anisomycin. Superscripts after protein labels indicate corresponding vinculin loading controls used for quantification. (C) Quantification of the ratio of phospho-c-Jun to total c-Jun for each sample. (D) Quantification of the ratio of phosphorylated JNK1/2 to total JNK1 or JNK2 for each cell line. All sample signals were normalized to appropriate vinculin loading controls prior to further data processing. Ratios of phospho- to total protein levels were normalized to the maximal signal control (DMSO + anisomycin treatment).

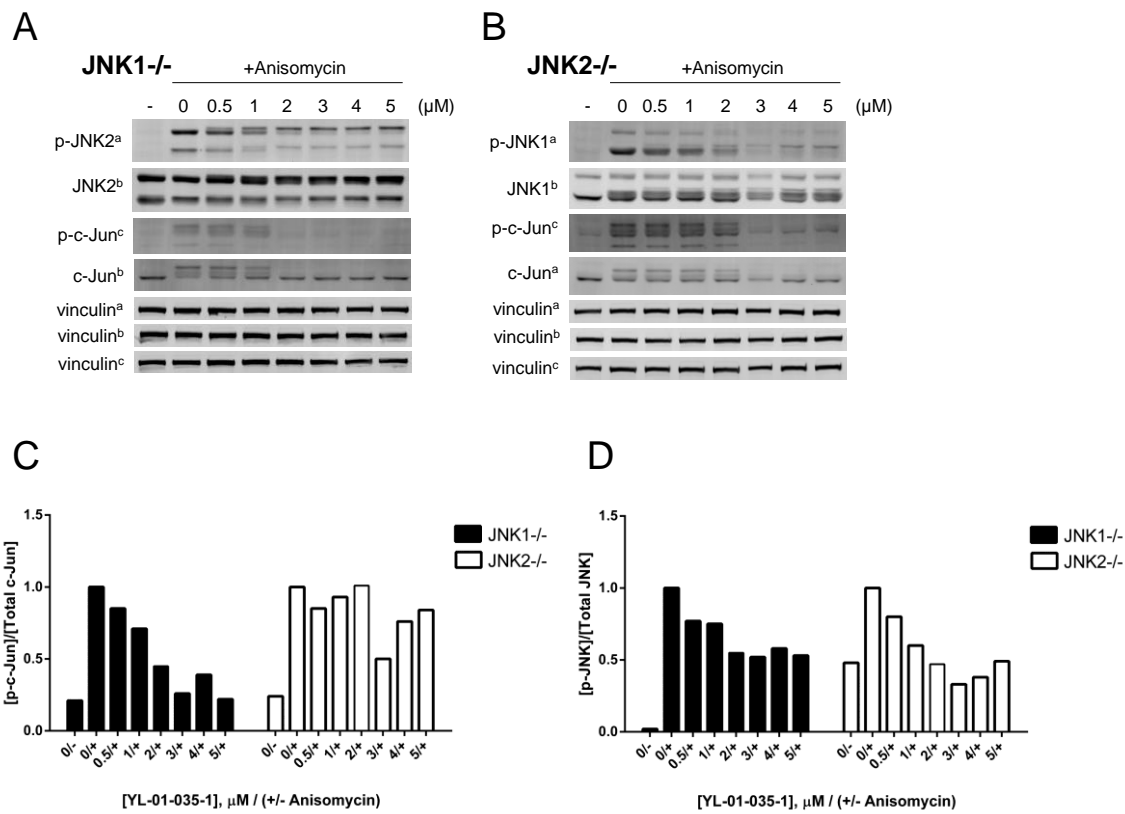


Figure 4.8. YL-01-035-1.

Western blots for YL-01-035-1 inhibition of (A) *jnk1*^{-/-} and (B) *jnk2*^{-/-} PyVMT cells. Phosphorylated and total levels of both c-Jun and JNK1 or JNK2 were measured for 4-hour treatment with 0-5 μM YL-01-035-1, with or without stimulation of signaling with 8 μM anisomycin. Superscripts after protein labels indicate corresponding vinculin loading controls used for quantification. (C) Quantification of the ratio of phospho-c-Jun to total c-Jun for each sample. (D) Quantification of the ratio of phosphorylated JNK1/2 to total JNK1 or JNK2 for each cell line. All sample signals were normalized to appropriate vinculin loading controls prior to further data processing. Ratios of phospho- to total protein levels were normalized to the maximal signal control (DMSO + anisomycin treatment).

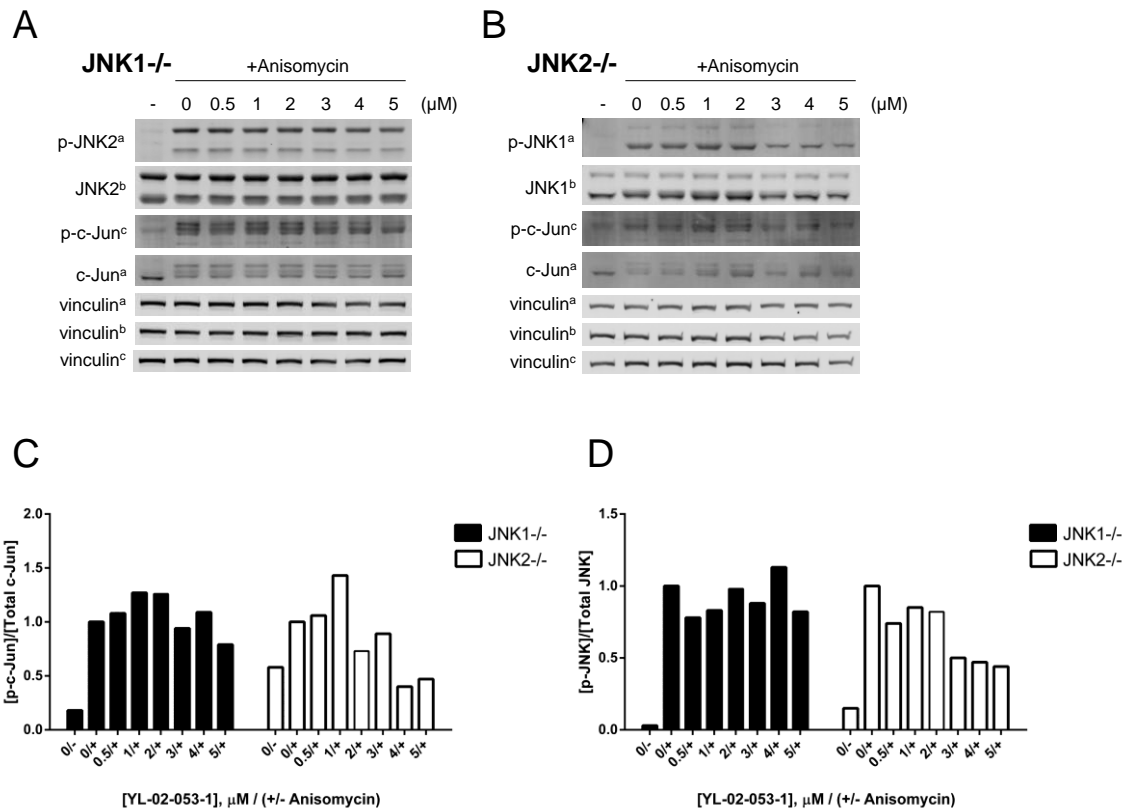


Figure 4.9. YL-02-053-1.

Western blots for YL-02-053-1 inhibition of (A) *jnk1*^{-/-} and (B) *jnk2*^{-/-} PyVMT cells. Phosphorylated and total levels of both c-Jun and JNK1 or JNK2 were measured for 4-hour treatment with 0-5 μM YL-02-053-1, with or without stimulation of signaling with 8 μM anisomycin. Superscripts after protein labels indicate corresponding vinculin loading controls used for quantification. (C) Quantification of the ratio of phospho-c-Jun to total c-Jun for each sample. (D) Quantification of the ratio of phosphorylated JNK1/2 to total JNK1 or JNK2 for each cell line. All sample signals were normalized to appropriate vinculin loading controls prior to further data processing. Ratios of phospho- to total protein levels were normalized to the maximal signal control (DMSO + anisomycin treatment).

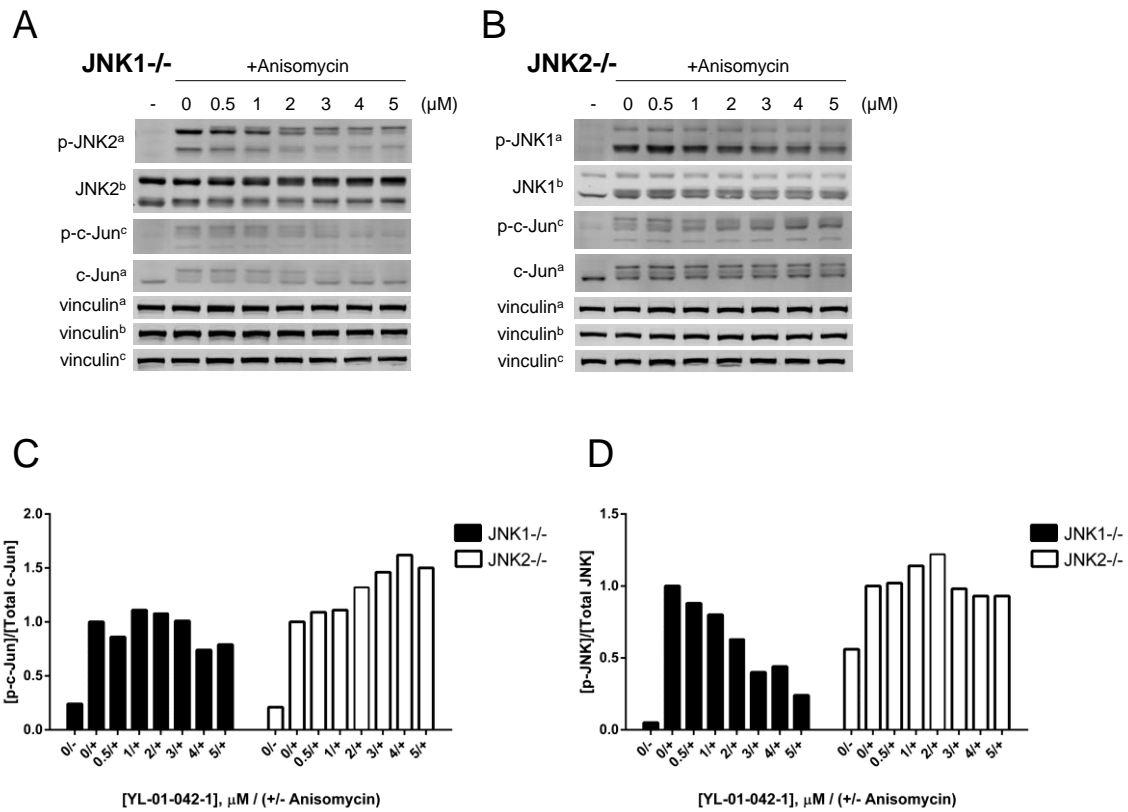


Figure 4.10. YL-01-042-1.

Western blots for YL-01-042-1 inhibition of (A) *jnk1*^{-/-} and (B) *jnk2*^{-/-} PyVMT cells. Phosphorylated and total levels of both c-Jun and JNK1 or JNK2 were measured for 4-hour treatment with 0-5 μM YL-01-042-1, with or without stimulation of signaling with 8 μM anisomycin. Superscripts after protein labels indicate corresponding vinculin loading controls used for quantification. (C) Quantification of the ratio of phospho-c-Jun to total c-Jun for each sample. (D) Quantification of the ratio of phosphorylated JNK1/2 to total JNK1 or JNK2 for each cell line. All sample signals were normalized to appropriate vinculin loading controls prior to further data processing. Ratios of phospho- to total protein levels were normalized to the maximal signal control (DMSO + anisomycin treatment).

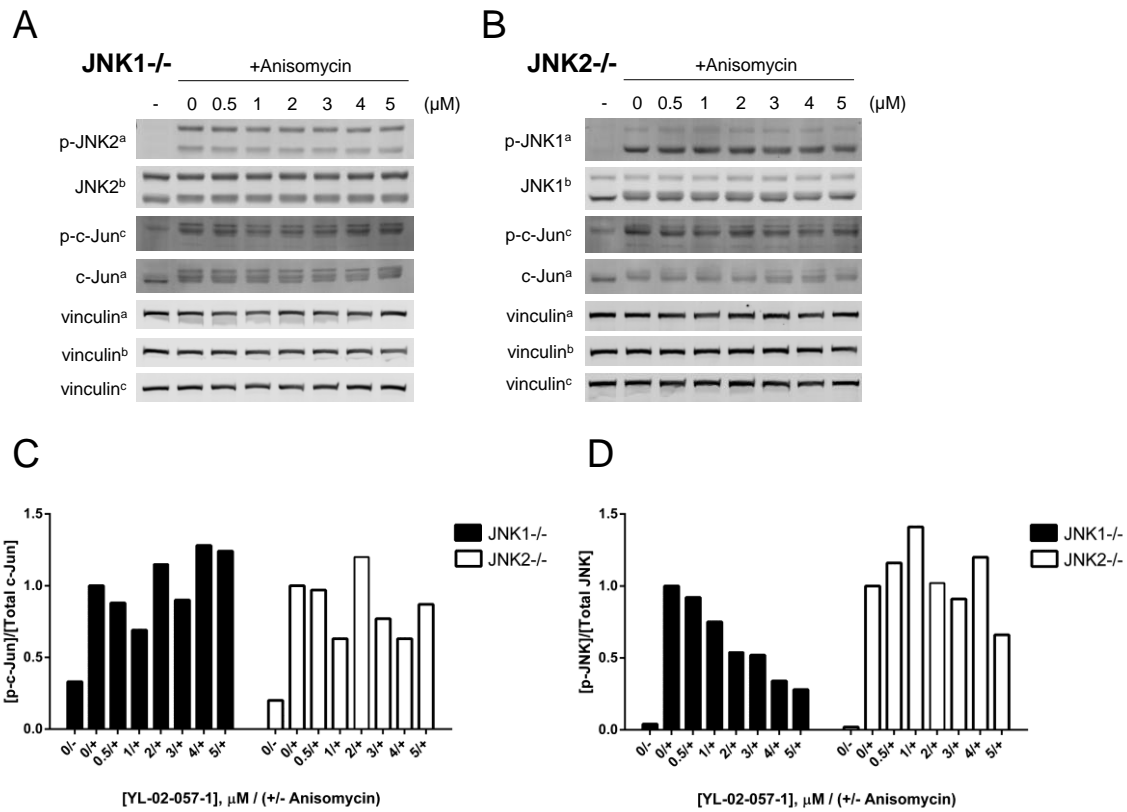


Figure 4.11. YL-02-057-1.

Western blots for YL-02-057-1 inhibition of (A) *jnk1*^{-/-} and (B) *jnk2*^{-/-} PyVMT cells. Phosphorylated and total levels of both c-Jun and JNK1 or JNK2 were measured for 4-hour treatment with 0-5 μM YL-02-057-1, with or without stimulation of signaling with 8 μM anisomycin. Superscripts after protein labels indicate corresponding vinculin loading controls used for quantification. (C) Quantification of the ratio of phospho-c-Jun to total c-Jun for each sample. (D) Quantification of the ratio of phosphorylated JNK1/2 to total JNK1 or JNK2 for each cell line. All sample signals were normalized to appropriate vinculin loading controls prior to further data processing. Ratios of phospho- to total protein levels were normalized to the maximal signal control (DMSO + anisomycin treatment).

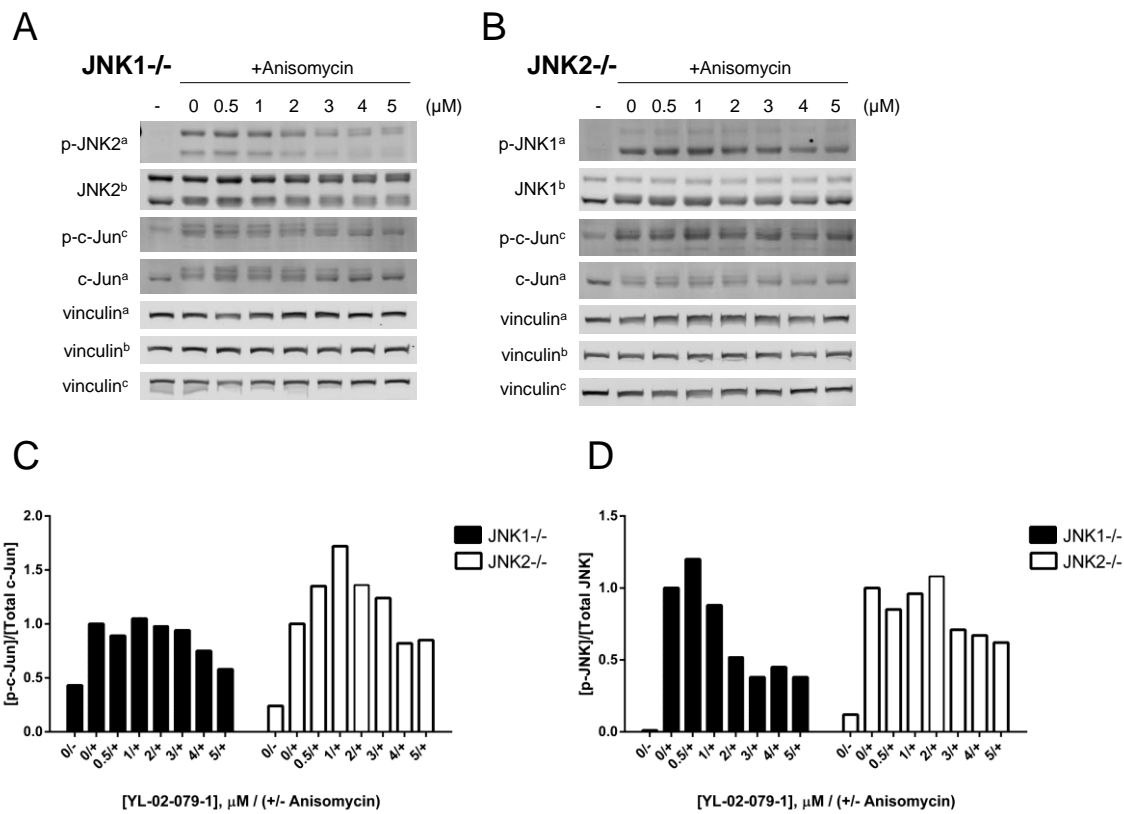


Figure 4.12. YL-02-079-1.

Western blots for YL-02-079-1 inhibition of (A) *jnk1*^{-/-} and (B) *jnk2*^{-/-} PyVMT cells. Phosphorylated and total levels of both c-Jun and JNK1 or JNK2 were measured for 4-hour treatment with 0-5 μM YL-02-079-1, with or without stimulation of signaling with 8 μM anisomycin. Superscripts after protein labels indicate corresponding vinculin loading controls used for quantification. (C) Quantification of the ratio of phospho-c-Jun to total c-Jun for each sample. (D) Quantification of the ratio of phosphorylated JNK1/2 to total JNK1 or JNK2 for each cell line. All sample signals were normalized to appropriate vinculin loading controls prior to further data processing. Ratios of phospho- to total protein levels were normalized to the maximal signal control (DMSO + anisomycin treatment).

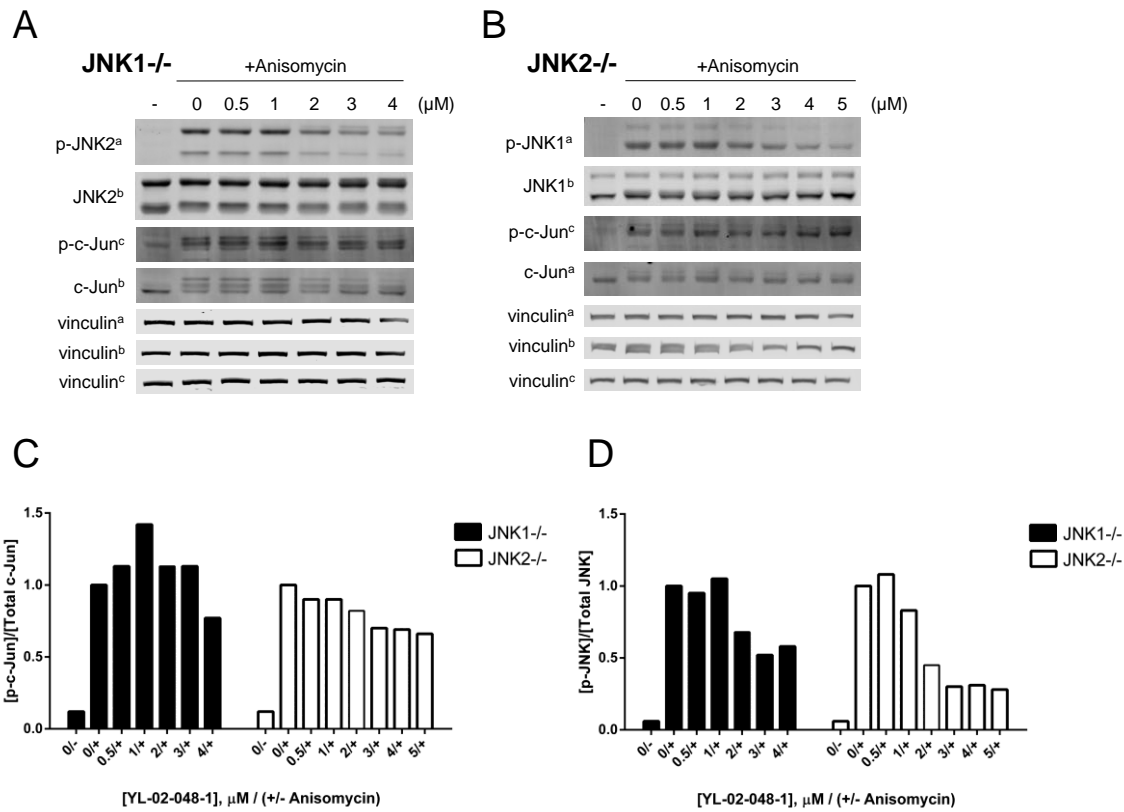


Figure 4.13. YL-02-048-1.

Western blots for YL-02-048-1 inhibition of (A) *jnk1*^{-/-} and (B) *jnk2*^{-/-} PyVMT cells. Phosphorylated and total levels of both c-Jun and JNK1 or JNK2 were measured for 4-hour treatment with 0-5 μM YL-02-048-1, with or without stimulation of signaling with 8 μM anisomycin. Superscripts after protein labels indicate corresponding vinculin loading controls used for quantification. (C) Quantification of the ratio of phospho-c-Jun to total c-Jun for each sample. (D) Quantification of the ratio of phosphorylated JNK1/2 to total JNK1 or JNK2 for each cell line. All sample signals were normalized to appropriate vinculin loading controls prior to further data processing. Ratios of phospho- to total protein levels were normalized to the maximal signal control (DMSO + anisomycin treatment).

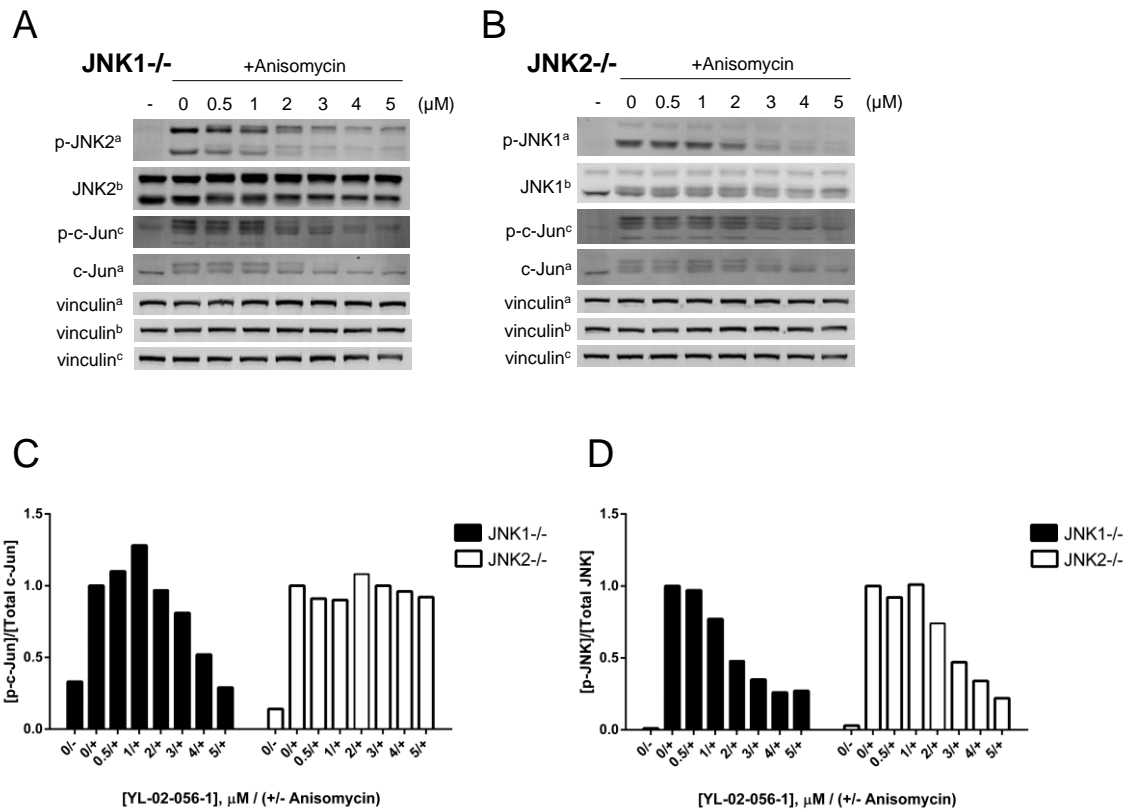


Figure 4.14. YL-02-056-1.

Western blots for YL-02-056-1 inhibition of (A) *jnk1*^{-/-} and (B) *jnk2*^{-/-} PyVMT cells. Phosphorylated and total levels of both c-Jun and JNK1 or JNK2 were measured for 4-hour treatment with 0-5 μM YL-02-056-1, with or without stimulation of signaling with 8 μM anisomycin. Superscripts after protein labels indicate corresponding vinculin loading controls used for quantification. (C) Quantification of the ratio of phospho-c-Jun to total c-Jun for each sample. (D) Quantification of the ratio of phosphorylated JNK1/2 to total JNK1 or JNK2 for each cell line. All sample signals were normalized to appropriate vinculin loading controls prior to further data processing. Ratios of phospho- to total protein levels were normalized to the maximal signal control (DMSO + anisomycin treatment).

Appendices

APPENDIX A: PEPTIDES

Peptide Sequences

Sub-D: FQRKTLQRRNLKGLNLNL-XXX-TGPLSPGPF

Sub-F: YAEPLTPRILAKWEWPA

Lig-D: FQRKTLQRRNLKGLNLNL (no acetylation)

Lig-D(Dap): FQRKTLQRRNLK(Dap)LNLNL-NH₂

FITC-X-Lig-D: FITC-X-FQRKTLQRRNLKGLNLNL

Sox-Sub-D: FQRKTLQRRNLKGLNLNL-XXX-TGPLSP-C(Sox)-PF

Sox-NFAT4: LERPSRDHLYLPLSGRYRES-C(Sox)-LSPSP

X= 6-aminohexanoic acid; all peptides N-acetylated and C-amidated unless noted.

Sox-Alkylation of Peptide Substrates

Peptides were purchased on-resin from Anaspec: sox-Sub-D (Ac-FQRKTLQRRNLKGLNLNL-X-X-X-TGPLSP-C(Mmt)-PF on Rink amide resin; X= 6-aminohexanoic acid) and sox-NFAT4 (Ac-LERPSRDHLYLPLSGRYRES-C(Mmt)-LSPSPA on Wang resin. The peptides were N-acetylated (Ac) and modified to include cysteine residues with Mmt protecting groups. The sox-alkylation procedure for these peptides was performed essentially as described by Zamora-Olivares, *et al.* (2014) [174].

Deprotection of Cys(Mmt)

A cleaving solution of 60 mL dry DCM with 0.5% TFA (0.3 mL) and 2.5% TIS (1.5 mL) was prepared under argon. 200 mg of each peptide on resin was allowed to swell in 20 mL DCM, added in 5 mL increments. The cleaving solution was then added

to the resin drop-wise in 5 mL increments. As Mmt is removed from cysteine, the solution changes from clear to a bright yellow-orange color. The cleavage is complete when color returns to clear. After cleavage was complete, the resin was washed in 20 mL DCM.

Cysteine Labeling

The sox-labeling reaction requires 2.2 mol.EQ sox-Br and 10 mol.EQ tetramethylguanidine as base. Sox-Br was synthesized by William H. Johnson (University of Texas at Austin). For each peptide, the resin loading from Anaspec was used in calculating the theoretical yield: Rink amide resin loading 0.43 mmol/g, Wang resin loading 0.82 mmol/g. Tetramethylguanidine base and ~4 mL DMF were added to the measured sox-Br and peptide resin. The activation of cysteine was confirmed by a bright yellow solution color. The reaction was allowed to proceed under argon overnight with shaking. Reaction completion was confirmed by the solution color changing to red, indicating free bromine. The resin was washed with 20 mL DMF, 20 mL DCM, followed by 20 mL methanol, and was allowed to dry under vacuum prior to storage at 4°C.

Cleaving and Deprotection of Peptides

A small sample of each peptide was cleaved to verify labeling was successful. Approximately 1-5 mg of resin was added to 1 mL of cleaving solution containing 95% TFA, 2.5% TIS, and 2.5% water. The mixture was vortexed and allowed to sit for 1 hour at room temperature. The cleaved peptide was drained from the resin and dried under a nitrogen flow. The dried peptide was then dissolved in 1:1 acetonitrile:water, filtered with a 0.45 µM PVDF membrane, and analyzed via LC-MS.

After LC-MS, the full 200 mg amount of resin was cleaved and deprotected with 15 mL cleaving solution for 4 hours at room temperature. The resin was filtered from the peptide solution, and the cleaving solution was evaporated by a nitrogen flow until 3-5 mL remained. The peptide was precipitated from the solution with 40 mL of ethyl ether at -20°C. The solution was centrifuged at 7000 rpm for 10 minutes at 10°C and the pellet of crude peptide was collected by decanting off the remaining ethyl ether. Crude peptides were stored at -20°C prior to purification.

Purification of Peptides

Crude peptides were purified via preparative reverse phase HPLC on an Alltima™ C18 5µm particle-size column. Each peptide was purified ~20 mg at a time after dissolution in 5 mL degassed DI water with 0.1% TFA using a gradient from solvent A (degassed DI water, 0.1% TFA) to solvent B (degassed acetonitrile, 0.1% TFA). A flow rate of 1.5 mL/min with fraction size of 1.5 mL was employed. Absorbance of the eluate was measured at wavelengths of 220 nm (peptide backbone) and 316 nm (sox) to detect labeled peptide. Fractions corresponding to all peaks were collected and analyzed via MALDI. The fractions corresponding to each labeled peptide were as follows: sox-Sub-D (observed mass 3757.95, calculated mass 3757.53), sox-NFAT4 (observed mass 3390.16, calculated mass 3408.67). Sox-NFAT4 peptide mass discrepancy was attributed to loss of water at Ser5 by LC-MS/MS analysis. This did not affect the ability of JNK1/2 to phosphorylate sox-NFAT4.

APPENDIX B: SUPPLEMENTARY INFORMATION FOR CHAPTER 2

Anisotropy Screening Optimization

Fluorescence anisotropy assays were optimized for 384-well, low-volume black polystyrene plates (Corning). To determine optimal ERK2 and FITC-X-Lig-D concentration, FITC-X-Lig-D was held at 10, 60 or 100 nM and ERK2 (inactive, His₆-cleaved) was varied from 0-12 μ M in anisotropy buffer with 10 μ g/mL BSA. Anisotropy values were measured at equilibrium after 10-20 minutes incubation. Observed dissociation constants ($K_{d,obs}$) were calculated at each FITC-X-Lig-D concentration assuming a single-step binding model. FITC-X-Lig-D was minimized at 10 nM without loss of signal (Figure B1), and $K_{d,obs}$ was measured as $0.57 \pm 0.12 \mu$ M. From the binding curve, ERK2 concentration was fixed at 1 μ M to achieve optimal signal. As a positive control, Lig-D(Dap) (0-200 μ M) was incubated with 10 nM FITC-X-Lig-D and 1 μ M ERK2. The observed IC_{50} was measured at $0.83 \pm 0.15 \mu$ M. At 50 μ M Lig-D(Dap) fully displaced the fluorophore from ERK2, so this was selected as a positive control for the screening.

All library compounds were dissolved in DMSO. To determine effects of DMSO on anisotropy signal, DMSO was varied from 0-10% (v/v) in the presence of 10 nM FITC-X-Lig-D and 0.5 μ M ERK2 (Figure B2). A maximum value of 5% (v/v) DMSO was chosen to ensure maximal anisotropy signal. Anisotropy was measured after 10-20 minutes of incubation to establish equilibrium. 0.5% (v/v) DMSO was selected for use in the screening.

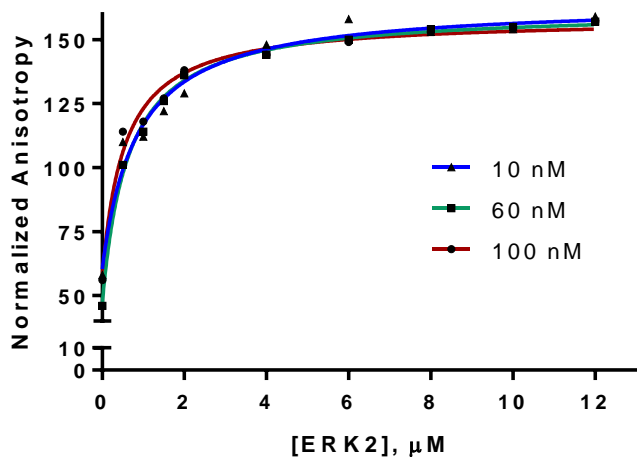


Figure B1. Optimization of FITC-X-Lig-D and ERK2 concentrations for anisotropy screening.

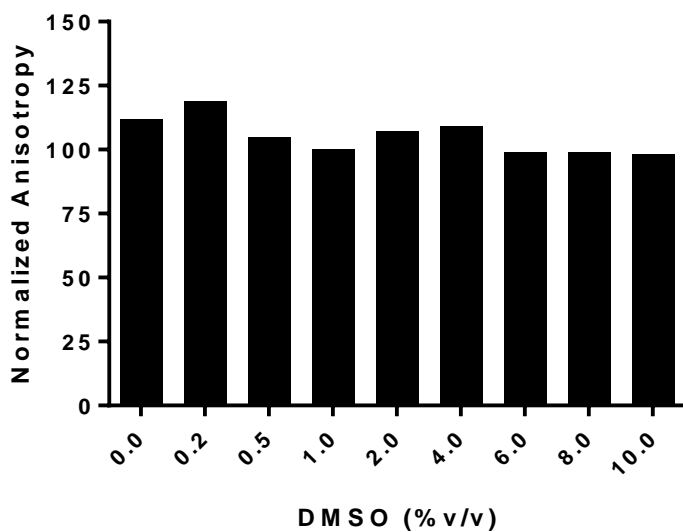


Figure B2. Effects of DMSO concentration on anisotropy signal.

DMSO was varied from 0-10% (v/v) in the presence of 0.5 μM ERK2 bound to 10 nM FITC-X-Lig-D. DMSO had very little effect on the observed anisotropy signal.

We then evaluated if the assay was suitable for high-throughput format by measuring the preliminary Z-factor [178]. A validation plate consisting of positive controls (10 nM FITC-X-Lig-D in anisotropy buffer with 10 μ g/mL BSA) and negative controls (10 nM FITC-X-Lig-D and 1 μ M ERK2 in anisotropy buffer with 10 μ g/mL BSA) with 0.5% (v/v) DMSO was prepared and anisotropy measurements were collected and averaged for each control (Table B1). The Z-factor was measured at 0.80, which is well above the acceptable threshold for a high-throughput assay.

	Mean anisotropy	Standard deviation
(+) control	120.6	2.0
(-) control	57.1	2.3

Table B1. Assay validation measurements to determine Z-factor.

Average anisotropy values for positive (+) controls (10 nM free FITC-X-Lig-D) and negative (-) controls (10 nM FITC-X-Lig-D fully bound to 1 μ M ERK2) were measured for a 384-well validation plate. Resulting mean and standard deviation for each control were used to calculate the Z-factor.

Library Compound Aggregation Test

The 204 hit compounds resulting from the primary anisotropy screening were tested for aggregate inhibition of ERK2 using the same primary screening protocol with added 0.01% Triton X-100 [179, 180]. The compounds were re-ranked based on % displacement of FITC-X-Lig-D, and the top 100 compounds were selected for dose-response validation.

Primary Anisotropy Screening Validation

The top 100 compounds were tested in dose-response assays at 5.5, 16.7, and 50 μ M concentrations using the primary screening protocol including 0.01% (v/v) Triton X-100. Additionally, the anisotropy measurements were corrected for intrinsic compound

fluorescence by blank-subtracting the parallel and perpendicular intensity components of each sample anisotropy by the intensity components of the compounds in anisotropy buffer alone.

Top Compounds Ranked from the Primary and Secondary Screenings

From the final ranking score, the top 30 compounds were chosen for further analysis. This number was reduced to 21 based on compound stability, availability, and toxicity or hazards. These 21 compounds are described in Table B2 below.

Score	ID	Name	CAS/Other*	Manufacturer	Part Number
6.43	1	Sennoside A	81-27-6	Sigma Aldrich	68909
5.28	3	Auranofin	34031-32-8	Enzo Life Sciences	BML-EI206
5.10	4	JFD 01947	2645-32-1	Calbiochem	662141
4.03	5	NSC 194308	90379-42-3	NCI	194308
3.59	9	JFD 00257	119-70-0	Sigma Aldrich	S572039
3.55	8	Menadione	58-27-5	Acros Organics	127180050
3.47	10	Sanguinarine chloride	5578-73-4	Tocris	2302
3.17	11	BTB 12919	BTB 12919	Maybridge	BTB 12919
3.16	12	NSC 228155	113104-25-9	NCI	228155
2.91	14	1215 (Stattic)	19983-44-9	Enzo Life Sciences	BML-EI368
2.74	13	HTS 12959	HTS 12959	Maybridge	HTS 12959
2.63	16	Bay 11-7082	19542-67-7	EMD Millipore	196870
2.54	18	KM 04416	KM 04416	Maybridge	KM 04416
2.50	17	S 11893	S 11893	Maybridge	S 11893
2.42	22	Protoporphyrin IX	553-12-8	Frontier Scientific	P562-9
2.36	23	HTS 01833	HTS 01833	Maybridge	HTS 01833
2.27	21	HTS 12963	HTS 12963	Maybridge	HTS 12963
2.07	26	Ethacrynic acid	58-54-8	Enzo Life Sciences	BML-EI128
1.78	30	S 11269	S 11269	Maybridge	S 11269
1.76	29	SEW 01906	SEW 01906	Maybridge	SEW 01906
1.71	28	NSC 48443	6641-18-5	NCI	48443

Table B2. List of top ranking compounds from the screening.

Compounds are identified by their library name, hit ID number, and CAS number or library ID if unavailable. Manufacturers and part numbers for purchased compounds are also listed. *Compounds from NCI and Maybridge are identified by their library IDs.

Dose-Response Curves

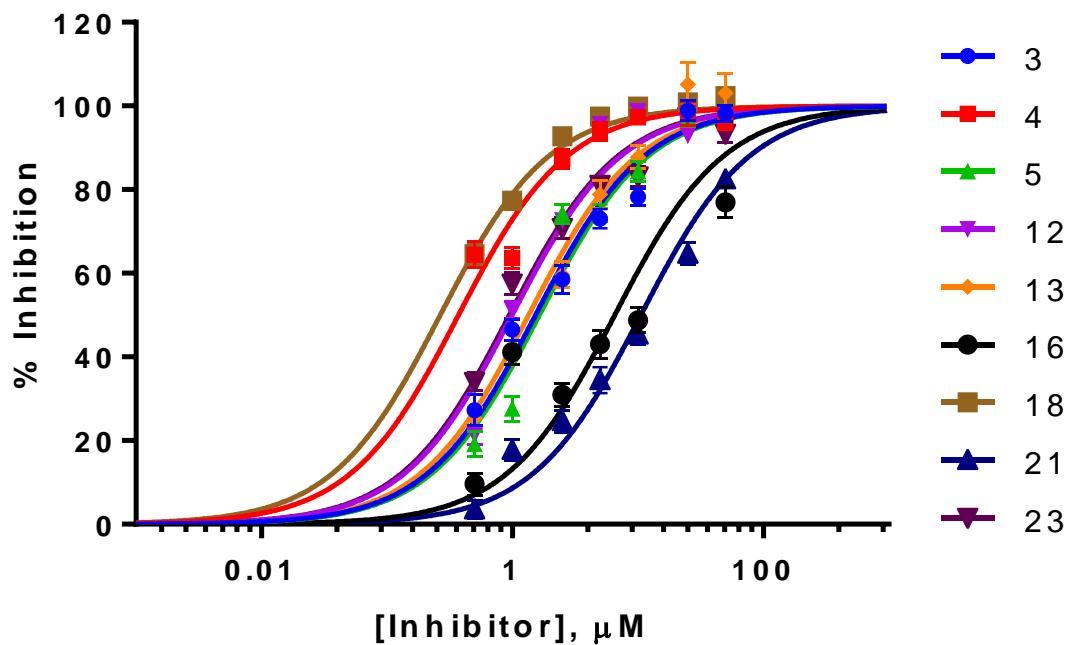


Figure B3. Dose-response curves for the top 9 compounds.

Dose-response curves showing the ability of the 9 hit compounds (3, 4, 5, 12, 13, 16, 18, 21, and 23) to inhibit ERK2 (2 nM) phosphorylation of sox-Sub-D (2 μM) after 20 min pre-incubation. Data were fit to IC_{50} equation.

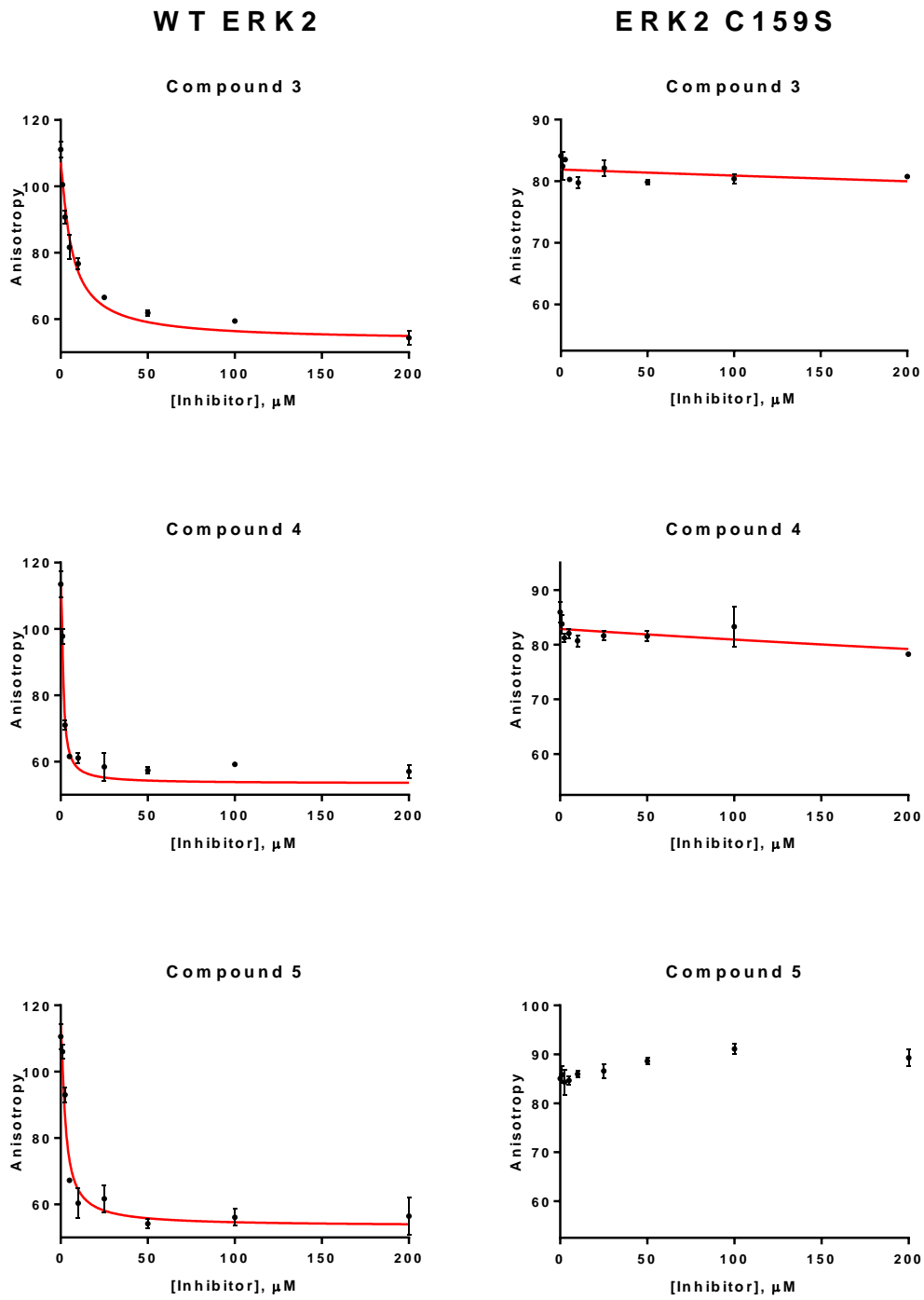


Figure B4. Anisotropy dose-response curves for compounds 3, 4, and 5 against WT and C159S ERK2.

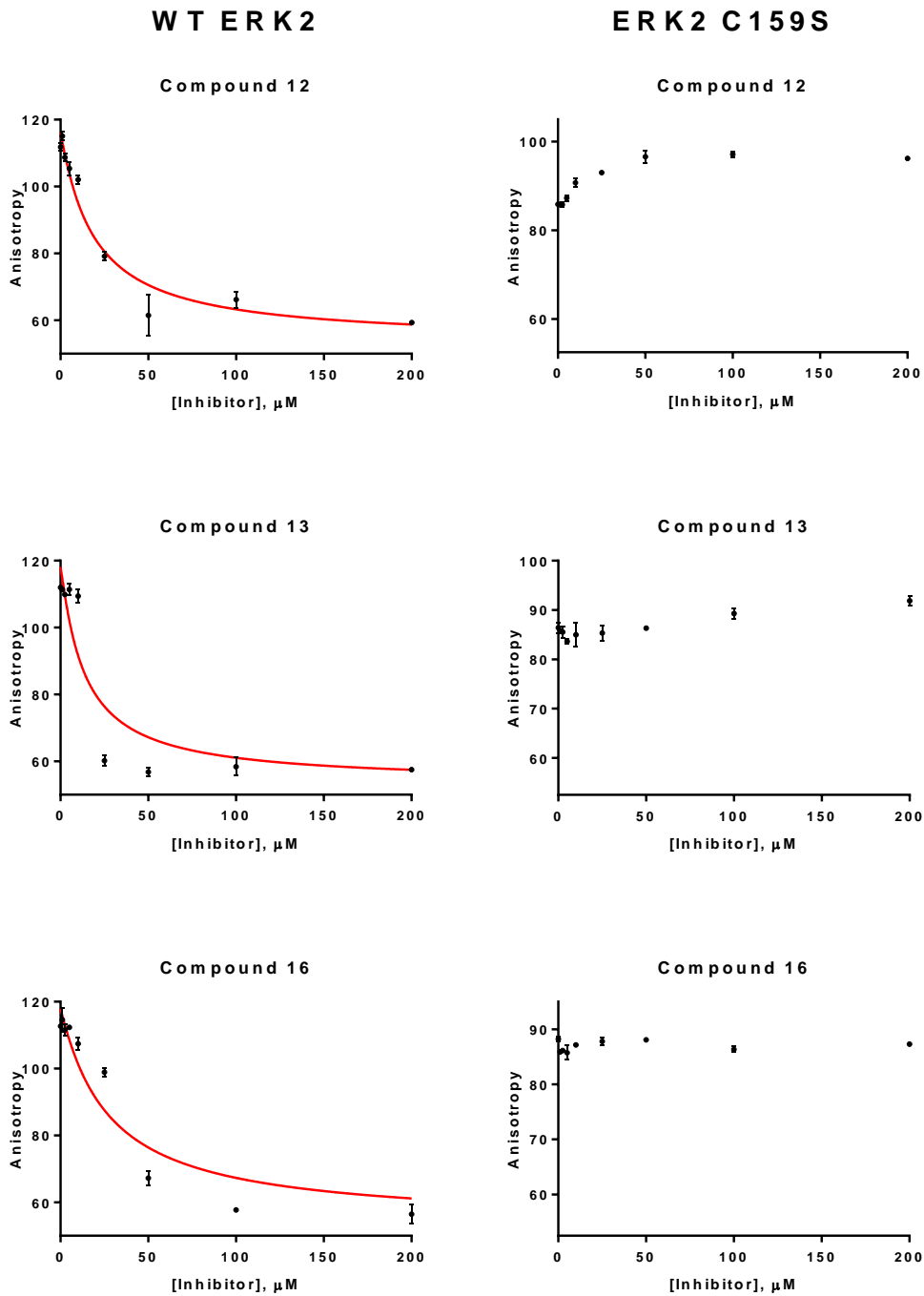


Figure B5. Anisotropy dose-response curves for compounds 12, 13, and 16 against WT and C159S ERK2.

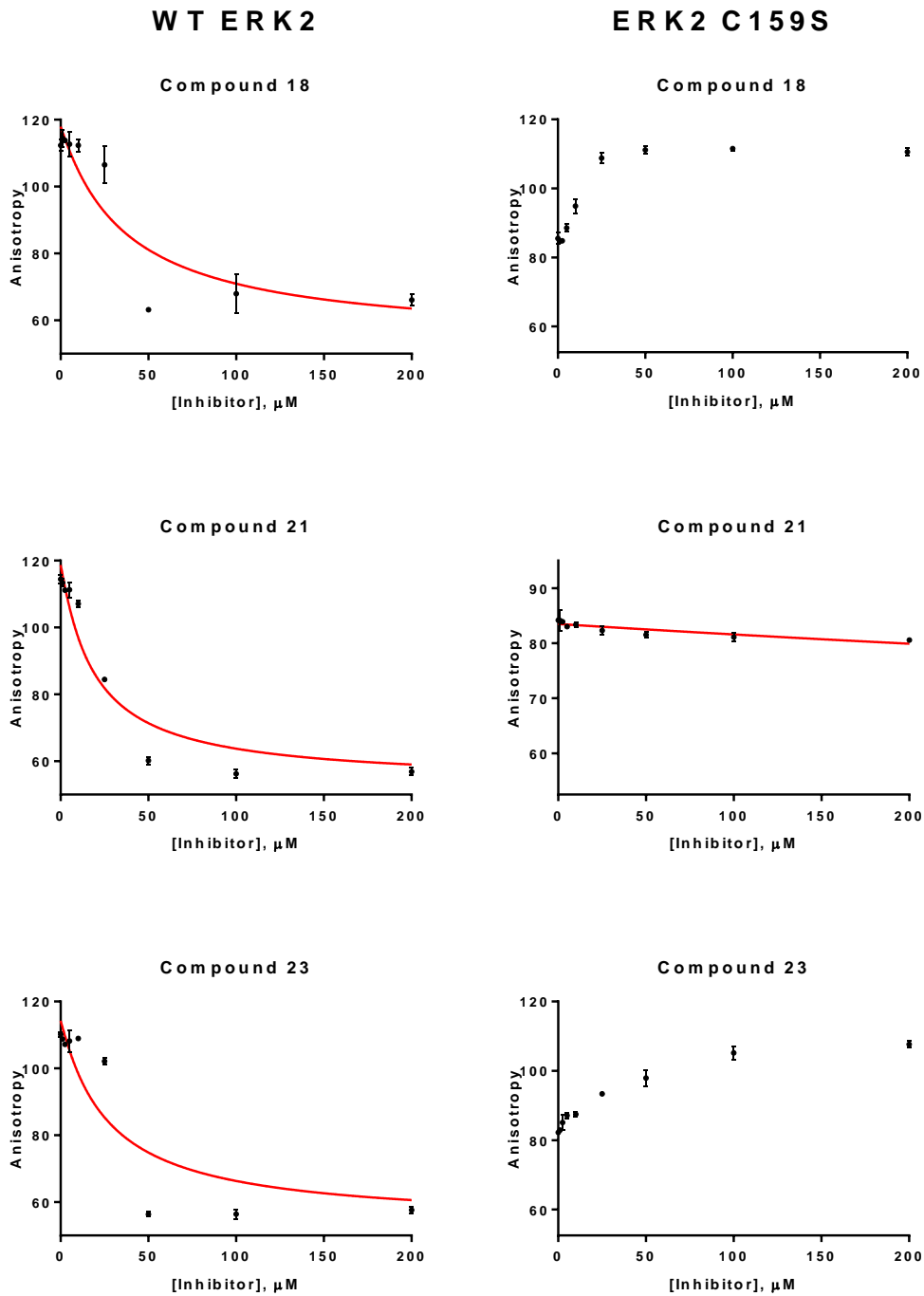


Figure B6. Anisotropy dose-response curves for compounds 18, 21, and 23 against WT and C159S ERK2.

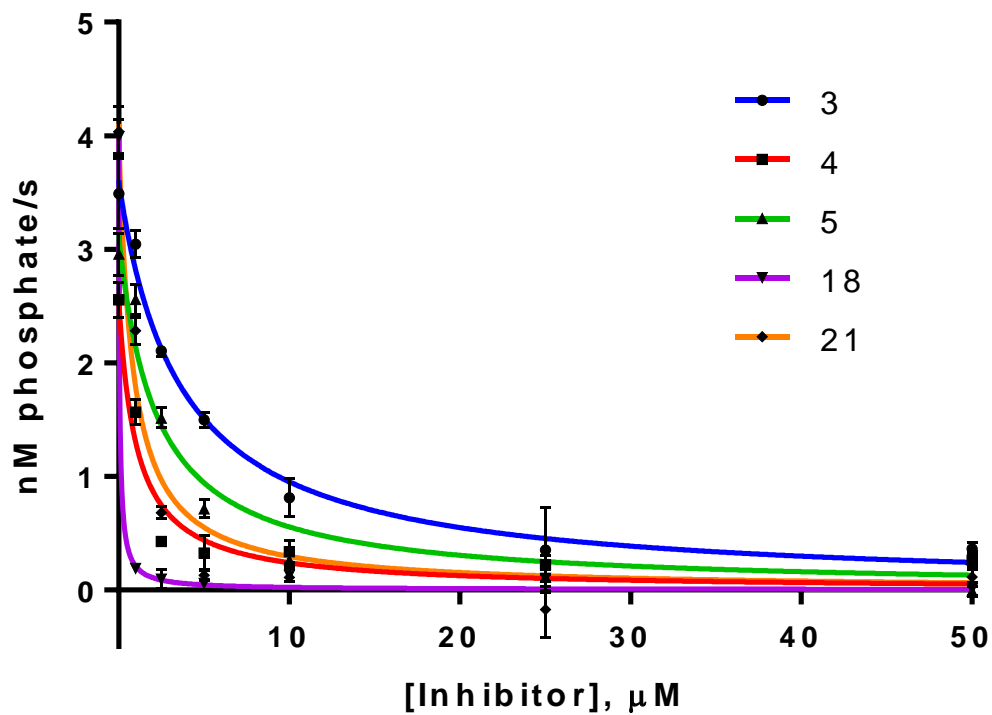


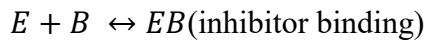
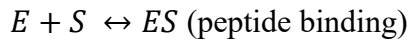
Figure B7. Dose-response curves for JNK2 inhibition.

Dose-response curves for inhibition of JNK2 (25 nM) phosphorylation of GST-c-Jun by selected compounds (3, 4, 5, 18, and 21).

Model for Fitting Anisotropy Dose-Response Curves

The anisotropy dose-response curves were fit to an equilibrium binding model for conditions where the FITC-X-Lig-D substrate concentration is much less than the concentration of ERK2 [67].

Equilibrium binding model:



Mass Balances:

$$E_t = ES + EB + E_f = EB + E_f \text{ since } S_t \ll E_t$$

$$B_t = B_f + EB$$

$$S_t = S_f + ES$$

Equations:

$$r = \frac{\frac{[ES]}{[S_t]} (r_b R - r_f) + r_f}{1 + \frac{[ES]}{[S_t]} (R - 1)}$$

$$[ES] = \frac{[E_f][S_t]}{K_d + [E_f]}$$

$$[EB] = \frac{[E_f][B_f]}{K_i}$$

Here, r is the anisotropy signal and r_b and r_f are the anisotropies of bound and free fluorophore, respectively. R is the ratio of fluorescence intensities of the bound to the free fluorophore, which was measured to be 1.8 using the average intensity values of the positive and negative controls. E , S , and B are concentrations of enzyme, fluorophore, and inhibitor, respectively. Subscripts t and f indicate ‘total’ and ‘free’ species

concentrations. EB denotes concentration of enzyme-inhibitor complexes, and ES is enzyme-fluorophore complex concentration. Dissociation constants for the inhibitor and the fluorophore are indicated by K_i and K_d , respectively.

Substituting the mass balances into the second two equations and algebraically rearranging them leads to the following equations that can be modeled in the GraphPad Prism software program.

$$[ES] = \frac{[S_t]([E_t] - [EB])}{K_d + [E_t] - [EB]}$$

$$[EB] = \frac{1}{2} \left[([E_t] + [B_t] + K_i) - \sqrt{([E_t] + [B_t] + K_i)^2 - 4[E_t][B_t]} \right]$$

Variable subscripts were converted to lowercase letters for software-compatible notation. X indicates total inhibitor concentration (independent variable) and Y indicates anisotropy (dependent variable). Total enzyme (Et) and substrate (St) concentrations, the dissociation constants for FITC-X-Lig-D (Kd), the ratio of intensities of bound to free fluorophore (R), and the anisotropy of the free fluorophore (rf) were fixed at their known values (Table B3).

Equation system input to Prism:

$$EB = ((Et + X + Ki) - \sqrt{(Et + X + Ki)^2 - 4 * Et * X}) / 2$$

$$ES = St * (Et - EB) / (Kd + Et - EB)$$

$$Y = ((ES / St * (rb * R - rf)) + rf) / (1 + (ES / St * (R - 1)))$$

For each parameter identified in the system of equations, initial values and constraints were specified in Prism (Table B3). Et was fixed at 1 μ M for WT ERK2 (or 5 μ M for C159S mutant), and St was fixed at 10 nM (or 50 nM for C159S mutant). Dissociation constants (Kd) for WT and C159S ERK2 were also fixed at their approximate measured values of 0.57 and 19.4 μ M, respectively (see Figure B8). The

anisotropy parameters of R and rf were set to 1.8 and 53, respectively, while maximum anisotropy rf was allowed to float with an initial guess value of the maximum anisotropy signal input (Y_{max}). The value of K_i was initially estimated at 50 nM and constrained to be greater than 0 for both WT and C159S ERK2.

Parameter	WT ERK2 Initial Value (units)	C159S ERK2 Initial Value (units)	Constraint
Et	1.0 (μM)	5.0 (μM)	Fixed
Ki	0.05 (μM)	0.05 (μM)	>0.0
St	0.01 (μM)	0.05 (μM)	Fixed
Kd	0.570 (μM)	19.4 (μM)	Fixed
rb	1.0*(Y_{max})	1.0*(Y_{max})	[none]
R	1.8	1.8	Fixed
rf	53.4	53.0	Fixed

Table B3. GraphPad Prism input parameters, initial values, and constraints.

Fixed parameters are indicated with their values and units (if applicable). Y_{max} indicates maximum anisotropy value for a given data set (Y).

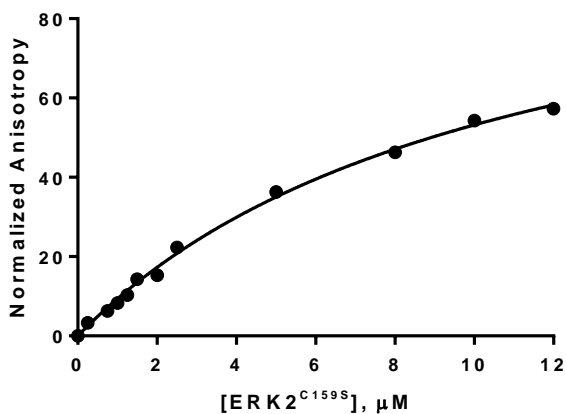


Figure B8. K_d curve for C159S ERK2 binding to FITC-X-Lig-D.

K_d is equal to $19.4 \pm 1.9 \mu\text{M}$ evaluated using anisotropy model with $R = 1.8$, with FITC-peptide concentration fixed at 50 nM. Value was approximated as 10 μM for K_i^* measurements with C159S ERK2.

Evaluation of Inhibitor Reversibility

Compound Reactivity Test

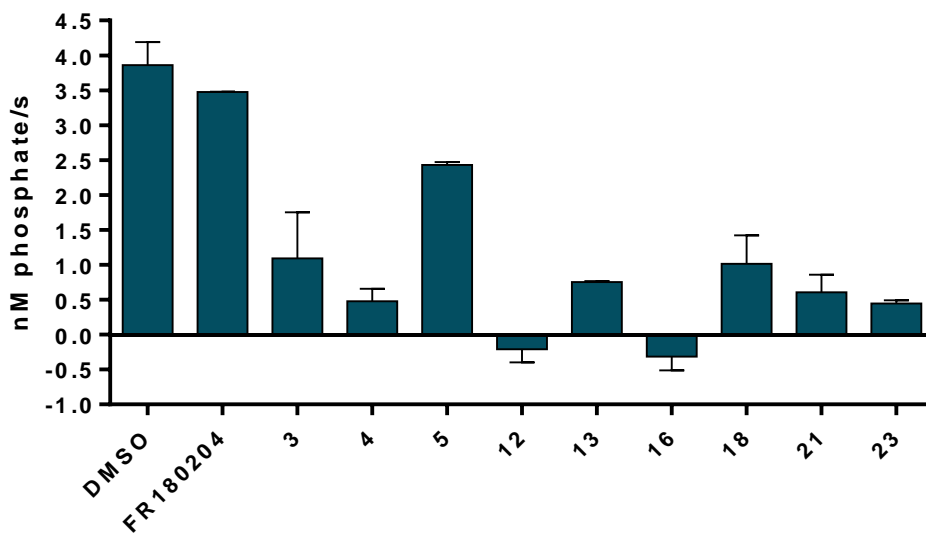


Figure B9. Covalent modification test for top 9 compounds.

3 μM active ERK2 was incubated with each compound for 2 hours at room temperature. Compound concentrations were chosen to be approximations of $10 \times [\text{ERK2} (\mu\text{M})] \times K_i^*$ but not allowed to exceed 200 μM or be less than 5X ERK2 concentration (Table B4). These thresholds were chosen in order to avoid aggregation of compounds or solubility limits while still ensuring saturation of ERK2 binding sites. After incubation, the samples were run through Bio-Spin® size exclusion columns (Bio-Rad) to remove all unbound inhibitor. ERK2 from each sample was diluted to 50 nM and kept on ice for 1 hour to allow any remaining reversible inhibitors to dissociate. The ERK2 from each sample was then diluted to 4 nM and assayed for phosphorylation of 10 μM Sub-D with 1 μM $[\gamma\text{-}^{32}\text{P}]\text{-MgATP}$ (Chapter 2 Materials and Methods). DMSO and

the reversible inhibitor FR180204 were used as controls for maximal remaining ERK2 activity.

ID #	Conc., μM
3	30
4	15
5	15
12	90
13	60
16	150
18	180
21	120
23	120
FR180204	15

Table B4. Initial conditions used in reactivity test.

Concentrations for each compound were chosen based on their affinities in order to ensure full binding or reaction of the compounds with ERK2 without exceeding solubility limits.

ESI-MS for ERK2 with Auranofin

Inactive ERK2 (5 μM) was incubated with 100 μM auranofin or 5 % (v/v) DMSO overnight at room temperature. The incubation was performed in 1 mL (total volume) of buffer: 50 mM HEPES pH 7.5, 100 mM KCl, 0.1 mM EDTA, and 0.1 mM EGTA. To remove unbound auranofin, the samples were then washed 3 times in the buffer using 10 kDa MWCO centrifugal concentrator tubes at 5000xg for 10 minutes. The protein was then washed in 30 mL of 50 mM ammonium bicarbonate, pH 7.5, in PD-10 columns to exchange buffer and continue removal of auranofin. The eluate from the column was

collected in 200-500 μL aliquots, and each aliquot was tested by Bradford Assay for presence of protein. The fractions of eluate containing protein were combined and concentrated in 10 kDa MWCO microcentrifuge concentrator tubes at 10,000 rpm. The collected protein was evaluated to be approximately 20 μM and 60 μL volume for each sample. The protein samples were flash-frozen in liquid N_2 and sent to the Laboratory for Biological Mass Spectrometry at Texas A&M University for analysis by ESI-MS (Yohannes H. Rezenom).

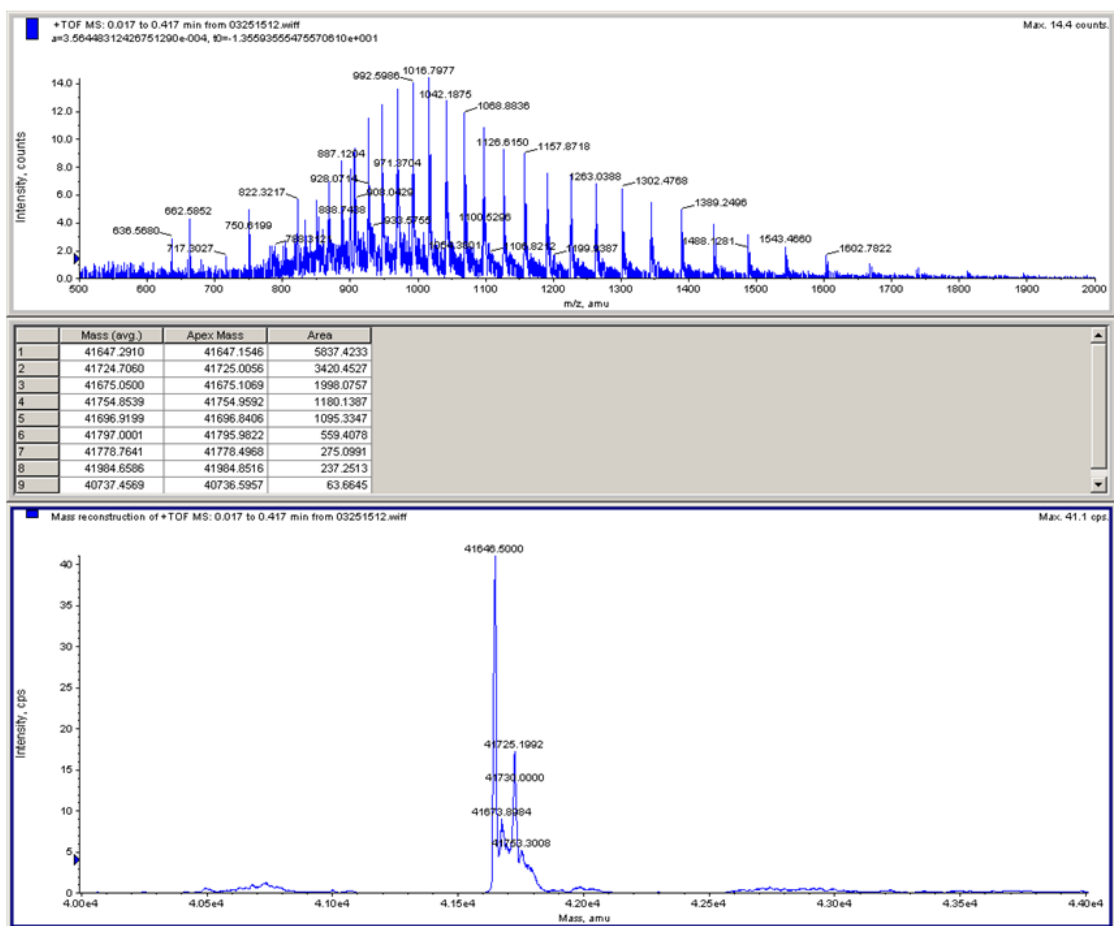


Figure B10. ESI-MS data for inactive ERK2.

Data shown for inactive ERK2 incubated without inhibitor (control). The main peak for inactive ERK2 appears at 41647 amu. Spectrum obtained by Yohannes H. Rezenom, Texas A&M University – Laboratory for Biological Mass Spectrometry.

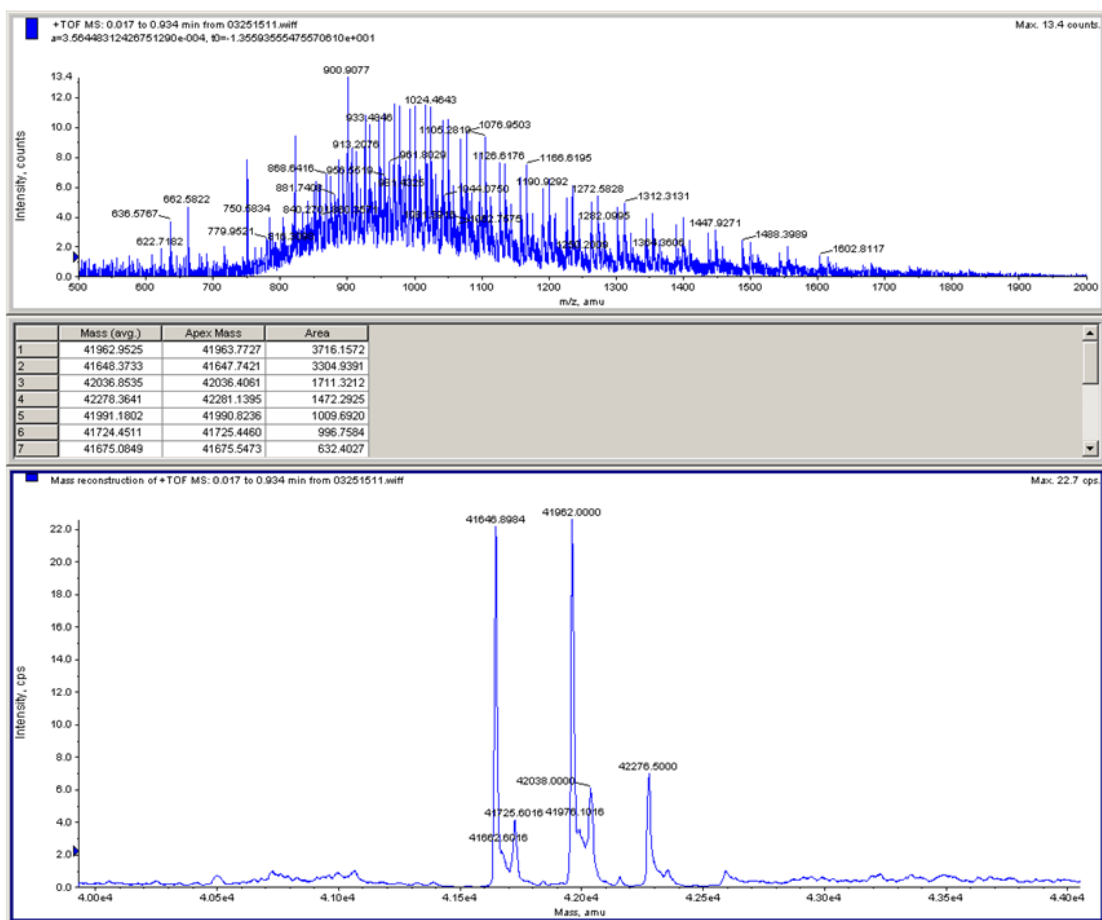


Figure B11. ESI-MS data for ERK2 with auranofin.

The main peak for inactive ERK2 appears at 41647 amu. Two additional peaks are observed at 41962 and 42277 amu, corresponding to two covalent modifications of 315 amu each that are attributed to the gold(I) triisopropylphosphine of auranofin appended to both C159 and C164 [251]. Spectrum obtained by Yohannes H. Rezenom, Texas A&M University – Laboratory for Biological Mass Spectrometry.

Phenotype Assays in HEK293T Cells

Viability Assay (MTS)

HEK293T cells were plated in 96-well plates at 2000 cells/well. After 24 h of growth, cells were treated with varied concentrations of auranofin for 24, 48, and 72 hours. Cells were then treated with MTS reagent (Promega) according to manufacturer protocol for 1, 2, 3, and 4 hours. Optimal signal and response was obtained after 72 h of auranofin treatment with 4 h MTS reagent incubation. (n=5, all data corrected for background absorbance of compound + media).

Colony Formation Assays

For 3-D colony formation assays, HEK293T cells were plated in full media at 1000 cells/well in the top layer of 0.4%(top)/1%(bottom) agarose (6-well plates). The top layer of agarose contained 0, 0.5, 1, and 2.5 μM of auranofin (0.5% DMSO). After 11 days of growth, cells were stained with 0.005% crystal violet, imaged, and colonies were manually counted on ImageJ (Fiji) software.

To assess 2-D colony growth, HEK293T cells plated at 500 cells/well in full media in 6-well plates. After 24 h, cells were dosed in triplicate with 0, 0.5, 1, or 5 μM auranofin with 0.5% DMSO (final). After 8 days of exposure the cells were fixed in 1.3% paraformaldehyde for 30 min and stained with 0.2% crystal violet. Colonies were counted using OpenCFU with a threshold of Regular/4 and a radius filter of 3-200 pixels. Colony radii in pixels were converted to mm using ImageJ (Fiji) to determine scaling of 42.6 $\mu\text{m}/\text{pixel}$.

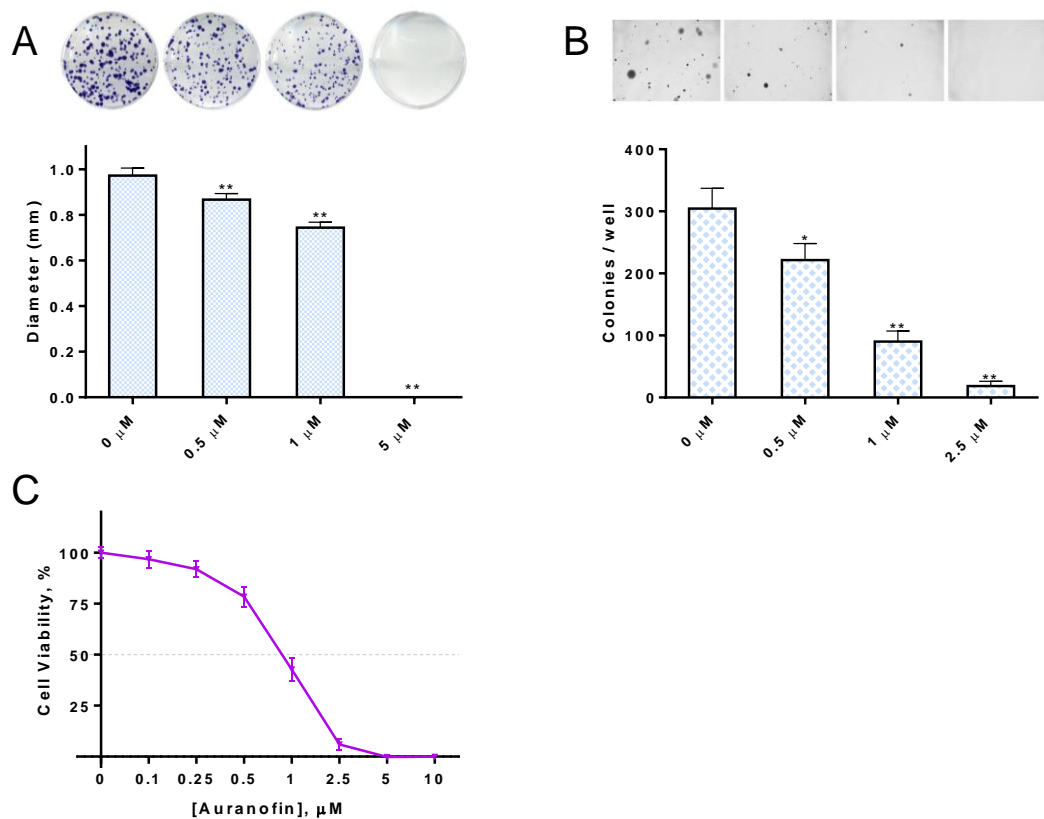


Figure B12. Auranofin inhibits proliferation and survival in HEK293T cells.

Auranofin inhibited two-dimensional clonogenic growth (A) and anchorage independent colony formation (B) of HEK293T cells in 6-well plates (500 cells/well; ** $p < 0.0001$, * $p < 0.05$; 3-D error bars = SD; 2-D error bars = 95% CI; 3-D FOV = 18.5 x 13.8 mm). (C) Auranofin additionally inhibited cell proliferation in a dose dependent manner by MTS assay ($EC_{50} = 0.7 \pm 0.2 \mu\text{M}$ for 3 days incubation).

APPENDIX C: SUPPLEMENTARY INFORMATION FOR CHAPTER 3

Combinatorial Library Screening Optimization

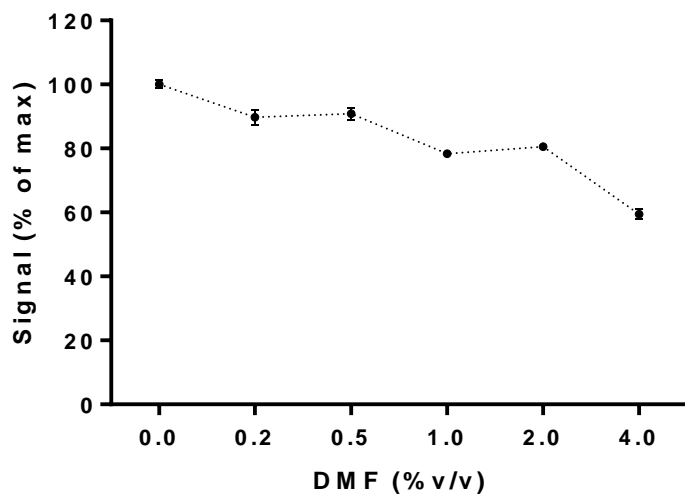


Figure C1. Dependence of maximum anisotropy signal on DMF % (v/v).

ERK2 at 1 μ M was incubated with 10 nM FITC-X-Lig-D at room temperature in the presence of 0-4 % (v/v) DMF for 1 hour. Anisotropy was measured and normalized to the maximum signal at 0 % (v/v) DMF. All subsequent screening conditions utilized 0.5 % (v/v) DMF.

Fluorescence intensity			
	Average (RFU)	St. Dev.	CV (%)
(-)	35.34	14.42	40.82
(+)	6684.63	212.71	3.18
Z = 0.90			

Parallel intensity component			
	Average (RFU)	St. Dev.	CV (%)
(-)	336.38	10.89	3.24
(+)	38583.29	816.29	2.12
Z = 0.94			

Perpendicular intensity component			
	Average (RFU)	St. Dev.	CV (%)
(-)	180.27	7.91	4.39
(+)	32821.19	649.40	1.98
Z = 0.94			

Table C1. Validation of manual screening plate preparation.

A 384-well plate containing samples with (+) and without (-) 10 nM FITC-X-Lig-D was prepared by hand-pipetting (+) and (-) samples into alternating rows. Average fluorescence values \pm standard deviation (st. dev.) were used to calculate coefficient of variation (CV) and Z-factor (Z) for the plate. See Chapter 3 Materials and Methods. Parallel and perpendicular intensity components account for polarized emission measurements that are used to calculate anisotropy.

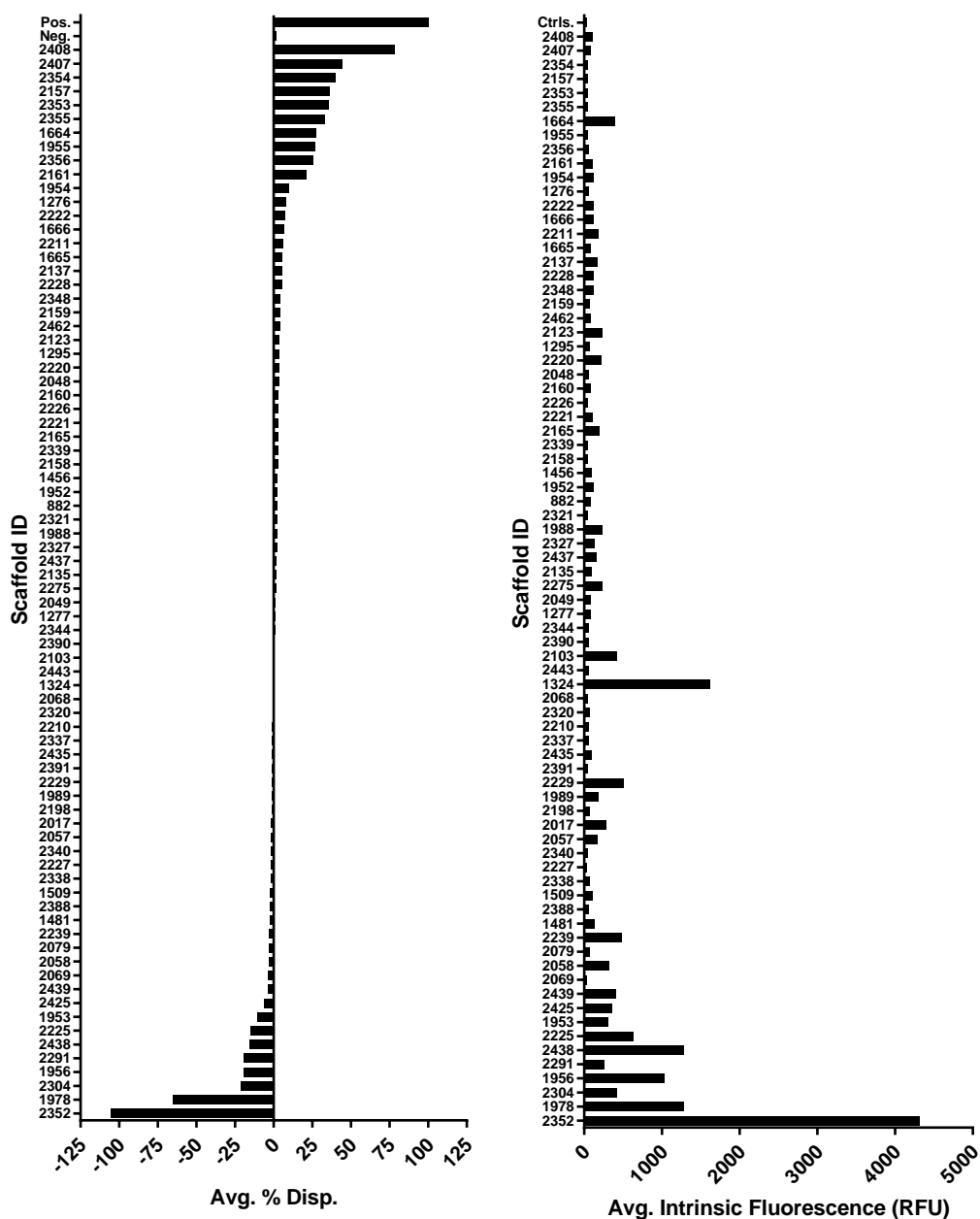


Figure C2. Screening Phase I – scaffold mixtures at 50 $\mu\text{g/mL}$.

Scaffold mixtures were ranked by their average % displacement of the FITC-X-Lig-D probe from the DRS of ERK2. Intrinsic fluorescence of each mixture is shown adjacent to its average % displacement. Controls for probe displacement data were FITC-X-Lig-D fully bound to ERK2 (neg.) and free FITC-X-Lig-D in solution (pos.). Intrinsic fluorescence controls (ctrls.) included the average fluorescence of all samples with no scaffolds present (pos. and neg.). Samples were screened in duplicate.

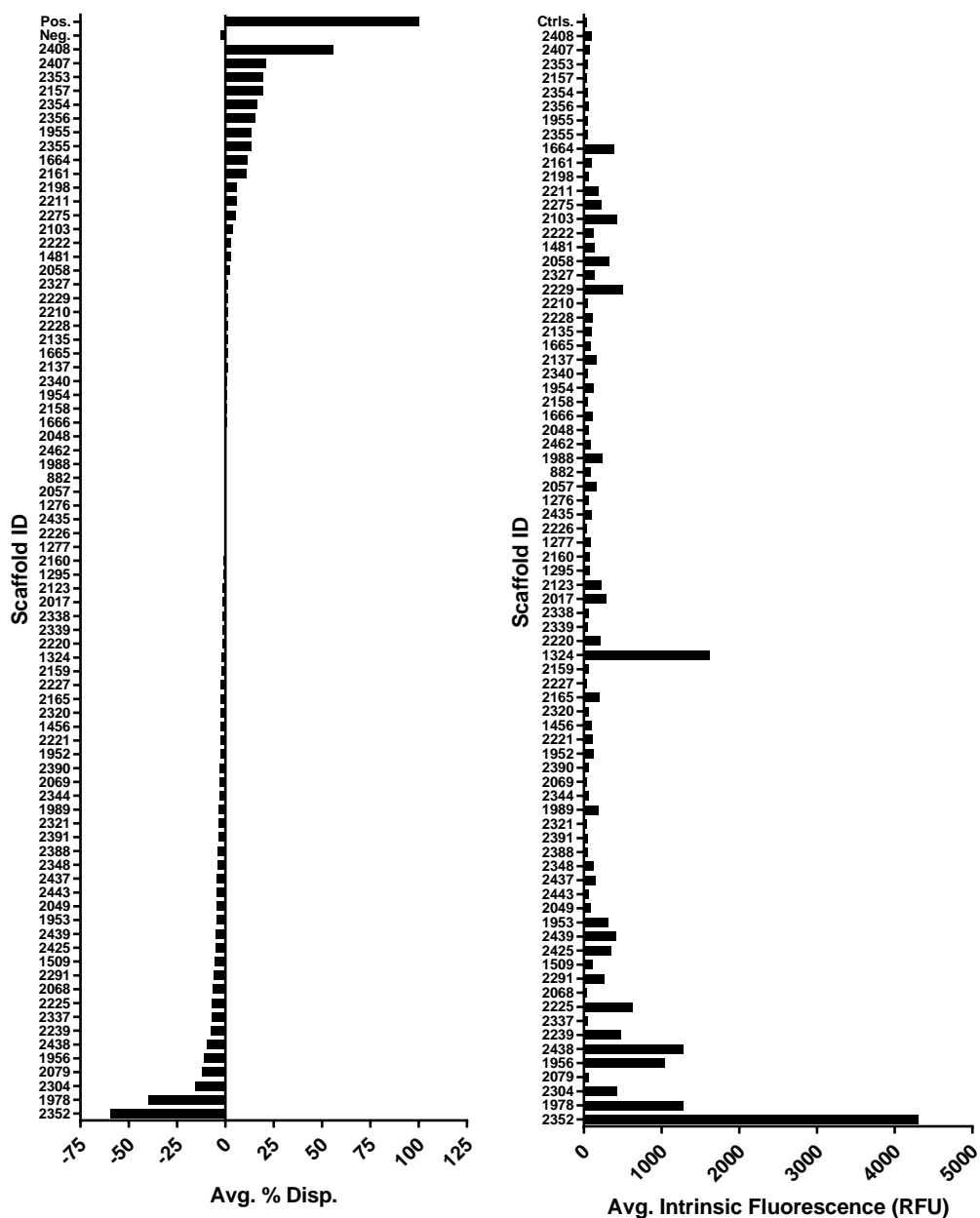


Figure C3. Screening Phase I – scaffold mixtures at 25 $\mu\text{g/mL}$.

Scaffold mixtures were ranked by their average % displacement of the FITC-X-Lig-D probe from the DRS of ERK2. Intrinsic fluorescence of each mixture is shown adjacent to its average % displacement. Controls for probe displacement data were FITC-X-Lig-D fully bound to ERK2 (neg.) and free FITC-X-Lig-D in solution (pos.). Intrinsic fluorescence controls (ctrls.) included the average fluorescence of all samples with no scaffolds present (pos. and neg.). Samples were screened in duplicate.

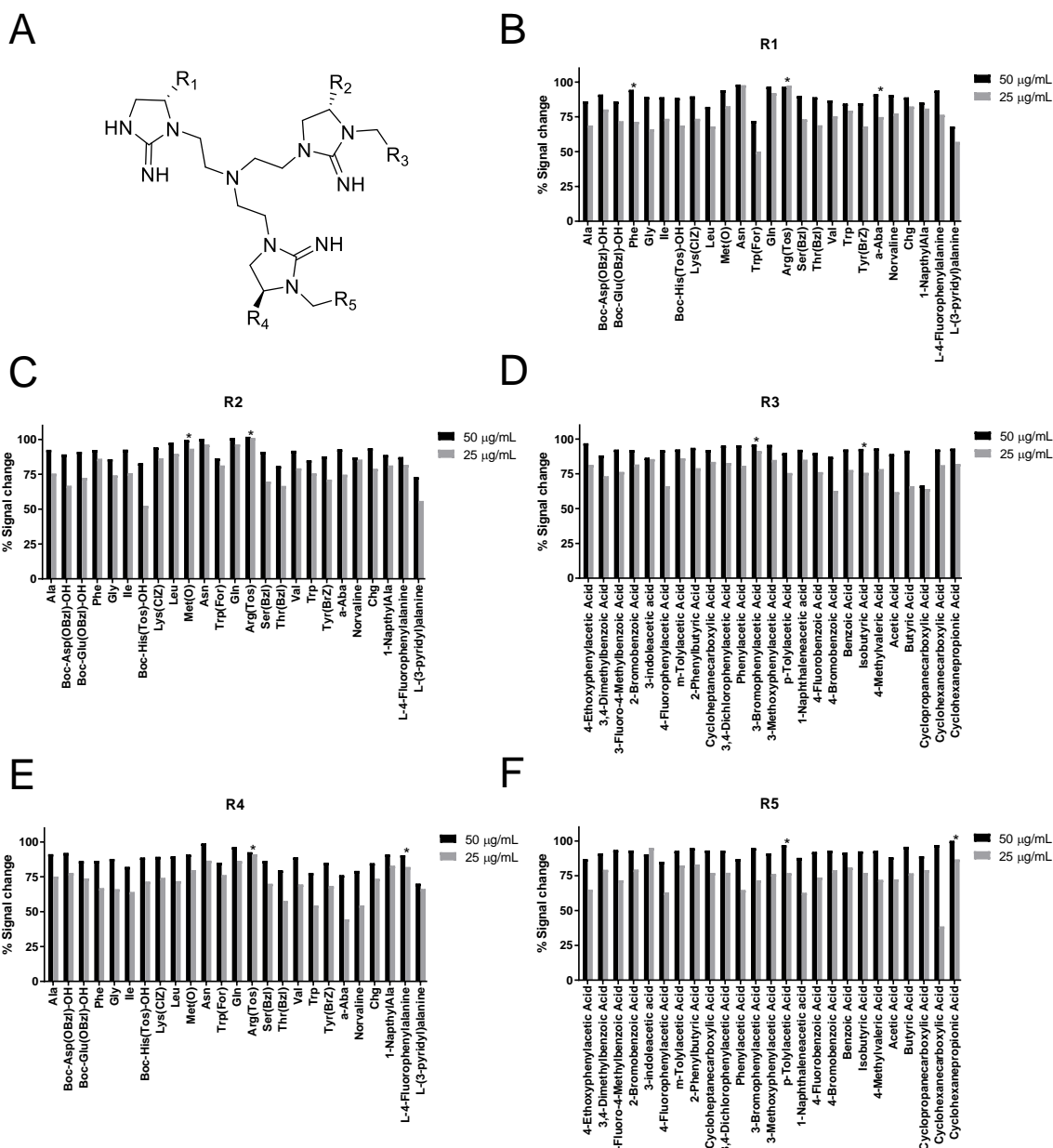


Figure C4. Positional scanning of library 2408 mixtures at 25 and 50 µg/mL.

Mixtures derived from the top hit scaffold 2408 (A) were re-screened for binding of ERK2 as described. (B)-(F) show results for varied moieties at R1-R5, respectively. *Moieties selected to advance to the next screening phase. Samples at each dose were screened in duplicate; average % displacement values are shown as determined from anisotropy measurements.

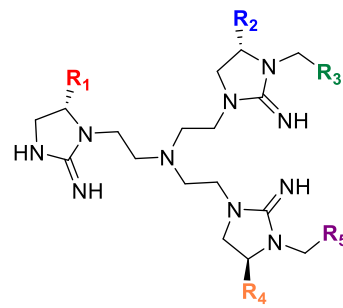
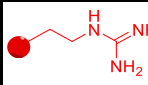
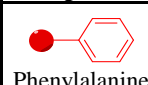
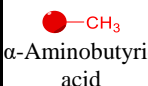
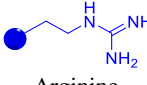
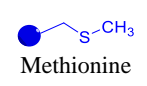
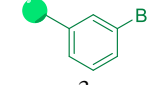
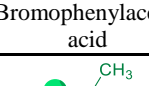
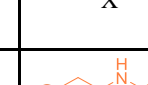
Mixture #						% Signal Change
	R1	R2	R3	R4	R5	
14	 Arginine	X	X	X	X	97.2
4	 Phenylalanine	X	X	X	X	71.5
20	 α-Aminobutyric acid	X	X	X	X	74.9
39	X	 Arginine	X	X	X	100.9
35	X	 Methionine	X	X	X	93.2
62	X	X	 3-Bromophenylacetic acid	X	X	91.2
69	X	X	 Isobutyric acid	X	X	75.6
89	X	X	X	 Arginine	X	90.9

Table C2. Top mixtures derived from scaffold 2408 in screening Phase II.

The functional groups that were held constant for each mixture are shown, while functional groups that were varied at random are denoted by ‘X’. The control (labeled ‘C’) is the bare scaffold where every R-group is fixed as –H. These results were used to generate 48 compounds for the next screening phase.


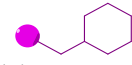

99	X	X	X	 L-4-fluorophenyl- alanine	X	82.0
125	X	X	X	X	 cyclohexanepropionic acid	86.7
114	X	X	X	X	 p-Tolylacetic acid	76.8
C	H	H	H	H	H	62.3

Table C2, continued.

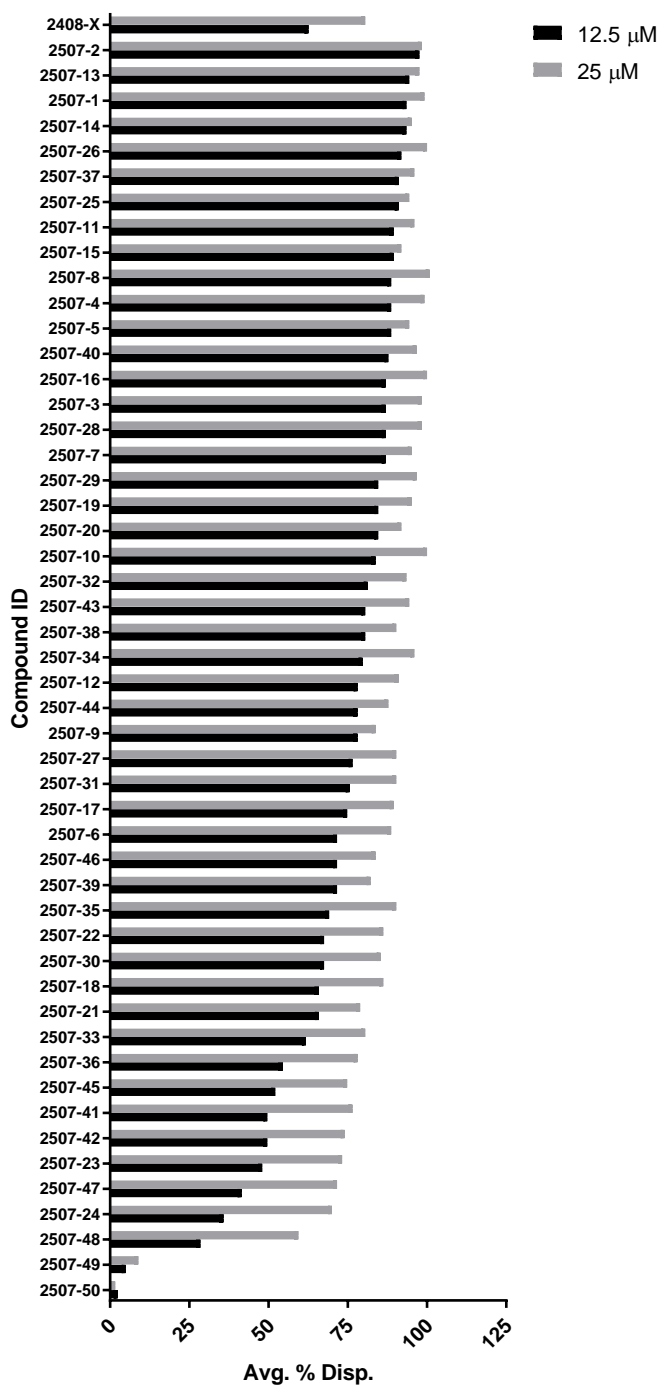


Figure C5. Screening of crude individual compounds at 12.5 and 25 μM.

The top 50 hits from the second screening phase were synthesized (70%< purity) and screened at 12.5 and 25 μM. 2408-X is a control where all R-groups are –H.

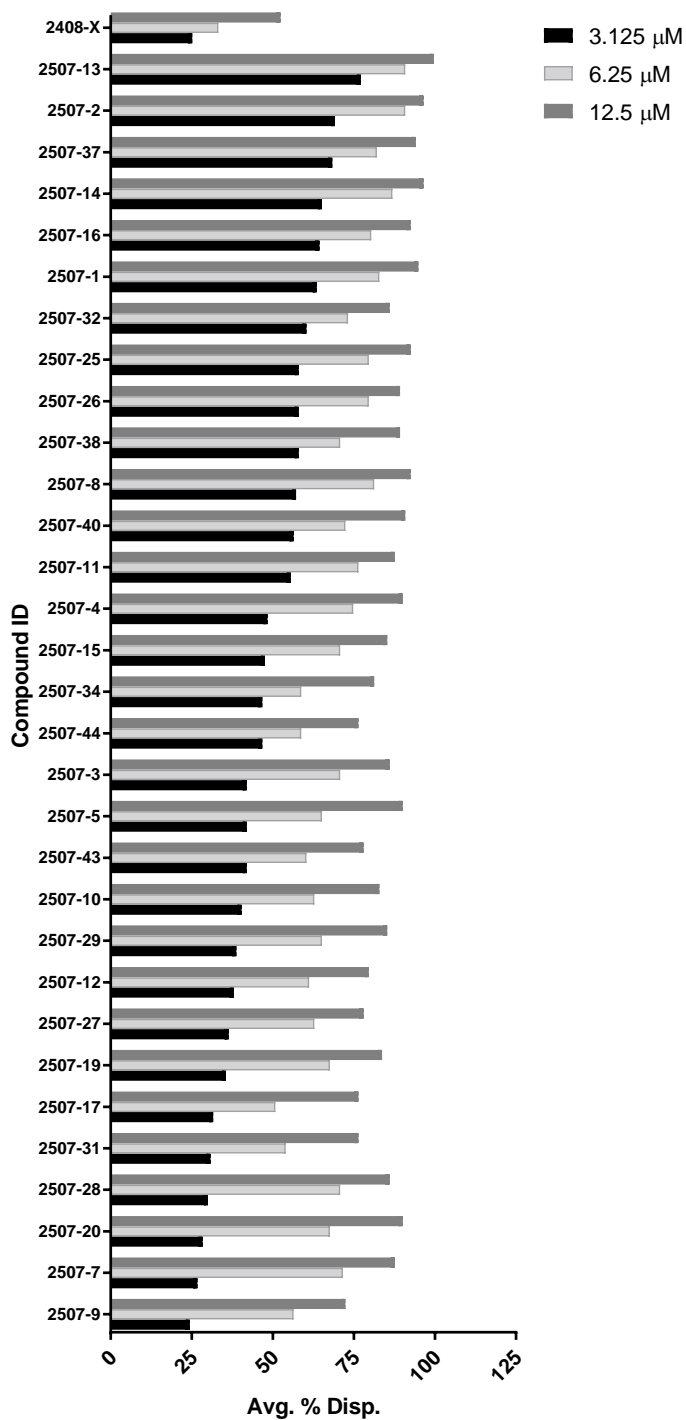


Figure C6. Screening of crude individual compounds at 12.5, 6.25, and 3.125 μM .

The top 30 compounds were rescreened at lower concentrations of 3.125, 6.25, and 12.5 μM . 2408-X is a control where all R-groups are -H.

Dose-Response Curves

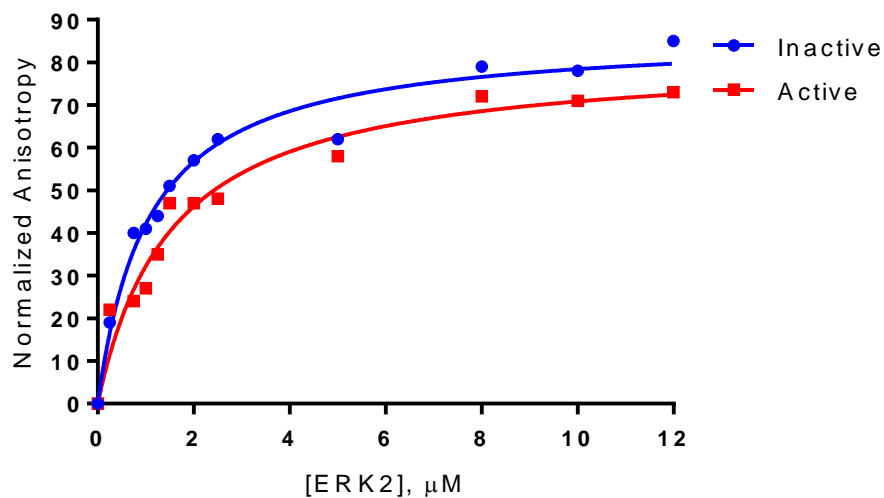


Figure C7. Binding affinities of FITC-X-Lig-D for active and inactive ERK2.

K_d curves fit using equation for tight binding from [67, 68] (with $R= 0.94$). K_d (inactive ERK2) = $1.0 \pm 0.1 \mu\text{M}$ and K_d (active ERK2) = $1.4 \pm 0.2 \mu\text{M}$. These K_d values were used in the anisotropy model (Appendix B) to calculate K_i for each inhibitor in Table 3.3.

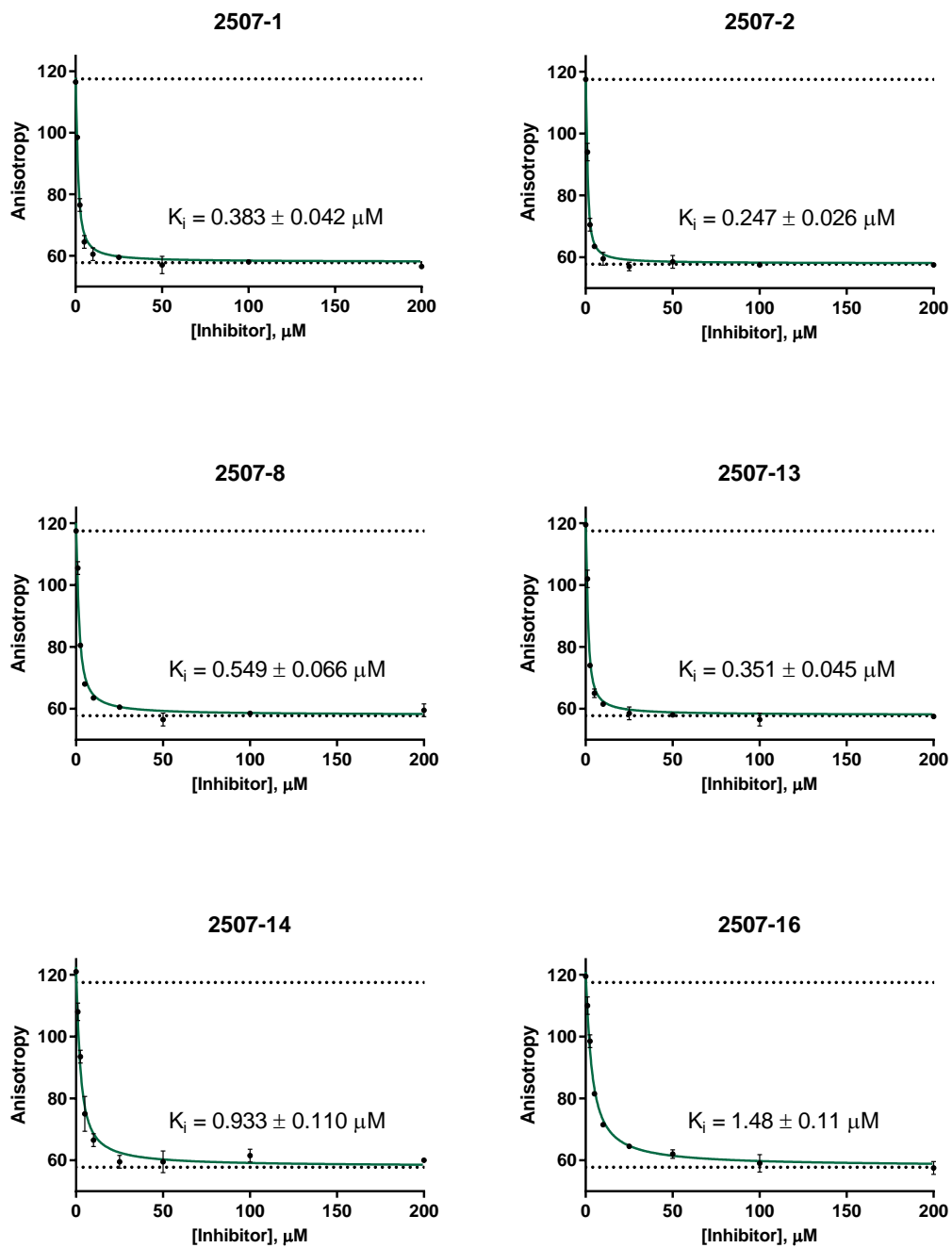


Figure C8. K_i curves for inactive ERK2 inhibition, part 1.

Boundary dotted lines indicate the average values of minimum and maximum anisotropy signal for positive and negative controls, respectively. K_i values were fit using the parameter $R = 0.94$ and the K_d value from Figure C7 (see model in Appendix B).

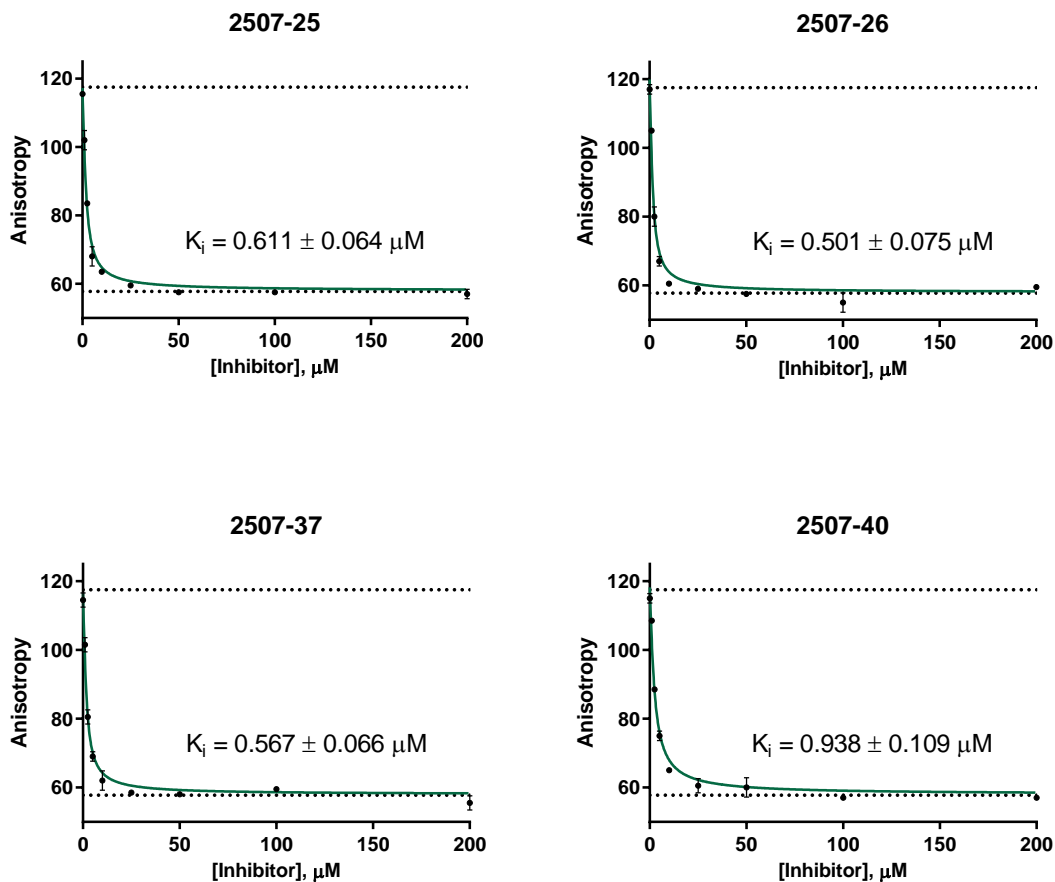


Figure C9. K_i curves for inactive ERK2 inhibition, part 2.

Boundary dotted lines indicate the average values of minimum and maximum anisotropy signal for positive and negative controls, respectively. K_i values were fit using the parameter $R = 0.94$ and the K_d value from Figure C7 (see model in Appendix B).

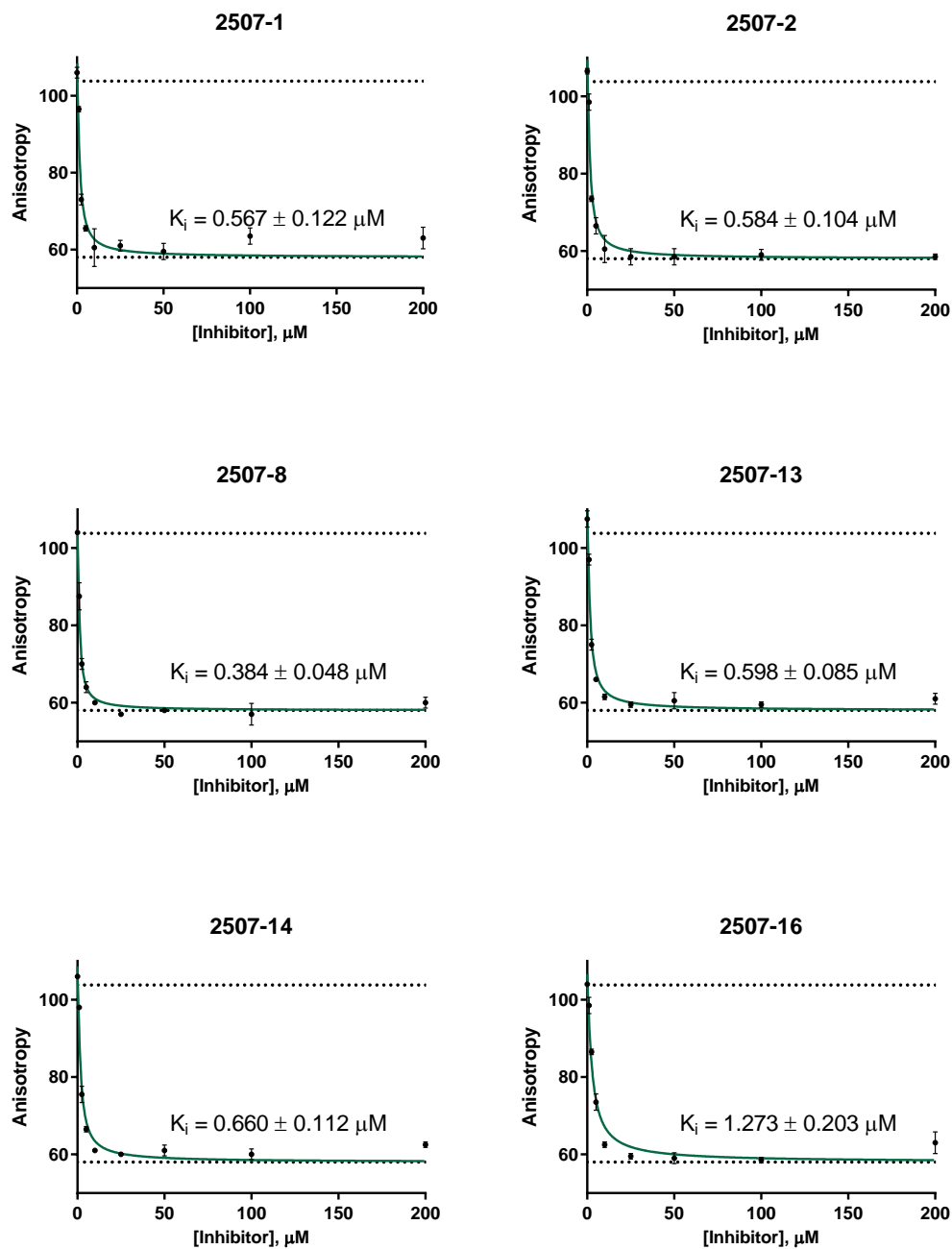


Figure C10. K_i curves for active ERK2 inhibition, part 1.

Boundary dotted lines indicate the average values of minimum and maximum anisotropy signal for positive and negative controls, respectively. K_i values were fit using the parameter $R = 0.94$ and the K_d value from Figure C7 (see model in Appendix B).

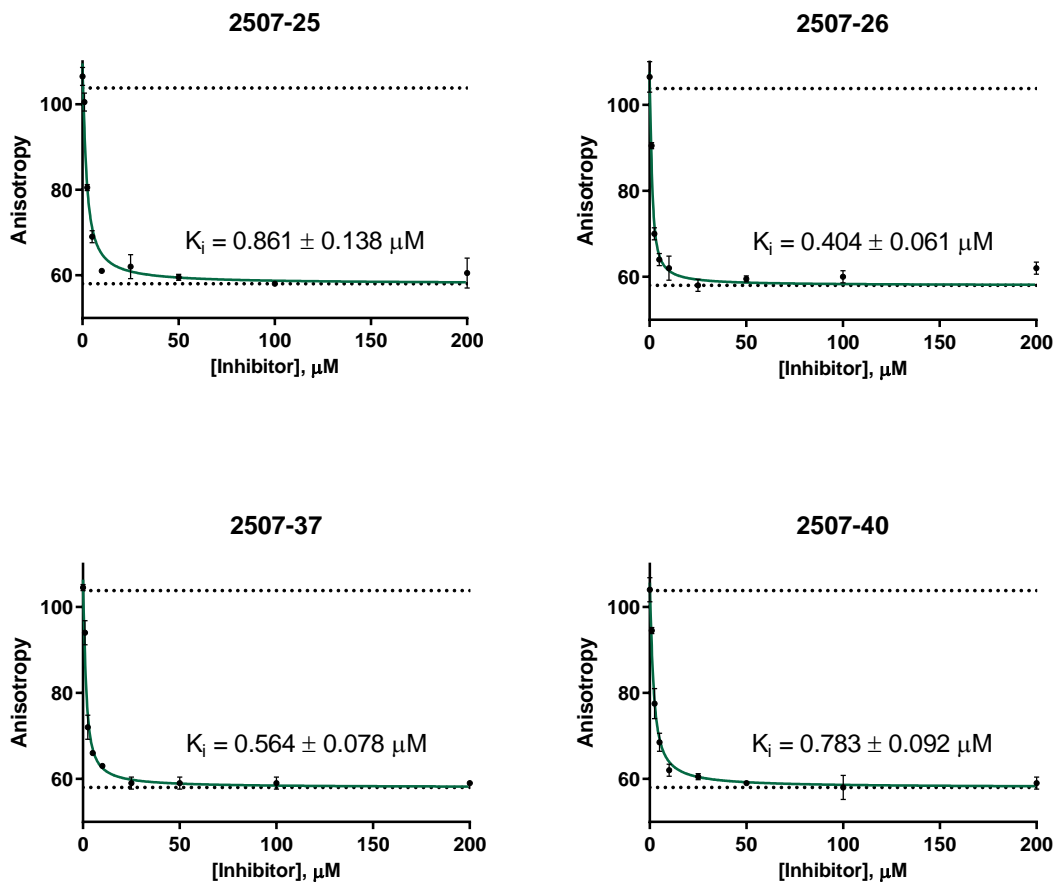


Figure C11. K_i curves for active ERK2 inhibition, part 2.

Boundary dotted lines indicate the average values of minimum and maximum anisotropy signal for positive and negative controls, respectively. K_i values were fit using the parameter $R = 0.94$ and the K_d value from Figure C7 (see model in Appendix B).

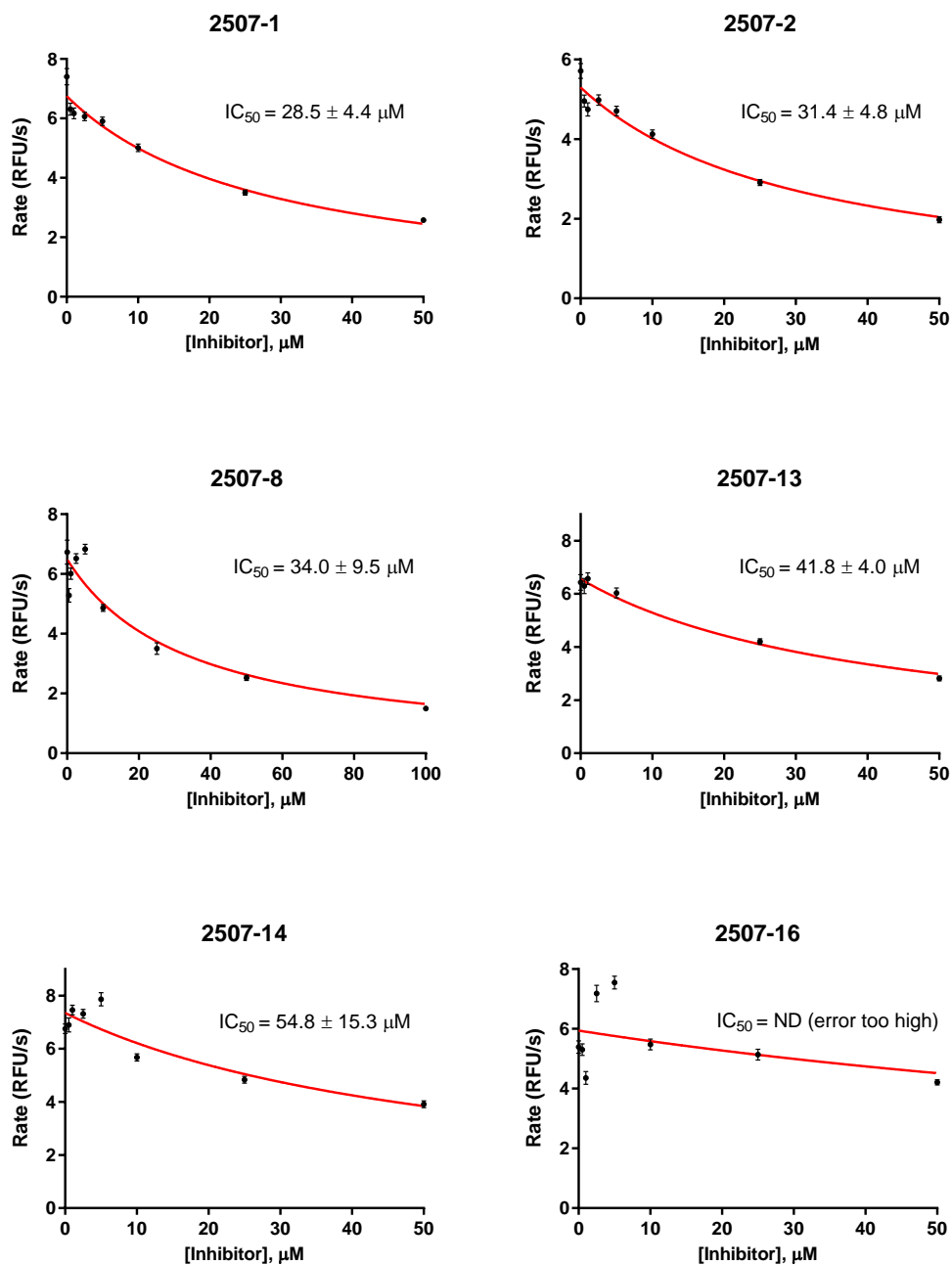


Figure C12. IC_{50} curves for top 10 compounds, part 1.

ERK2 phosphorylation of sox-Sub-D peptide was measured in the presence of 0-100 μM of each compound by change in sox-Sub-D fluorescence over time (RFU/s). IC_{50} curves and fit values are shown for 2507-1, 2507-2, 2507-8, 2507-13, 2507-14, and 2507-16.

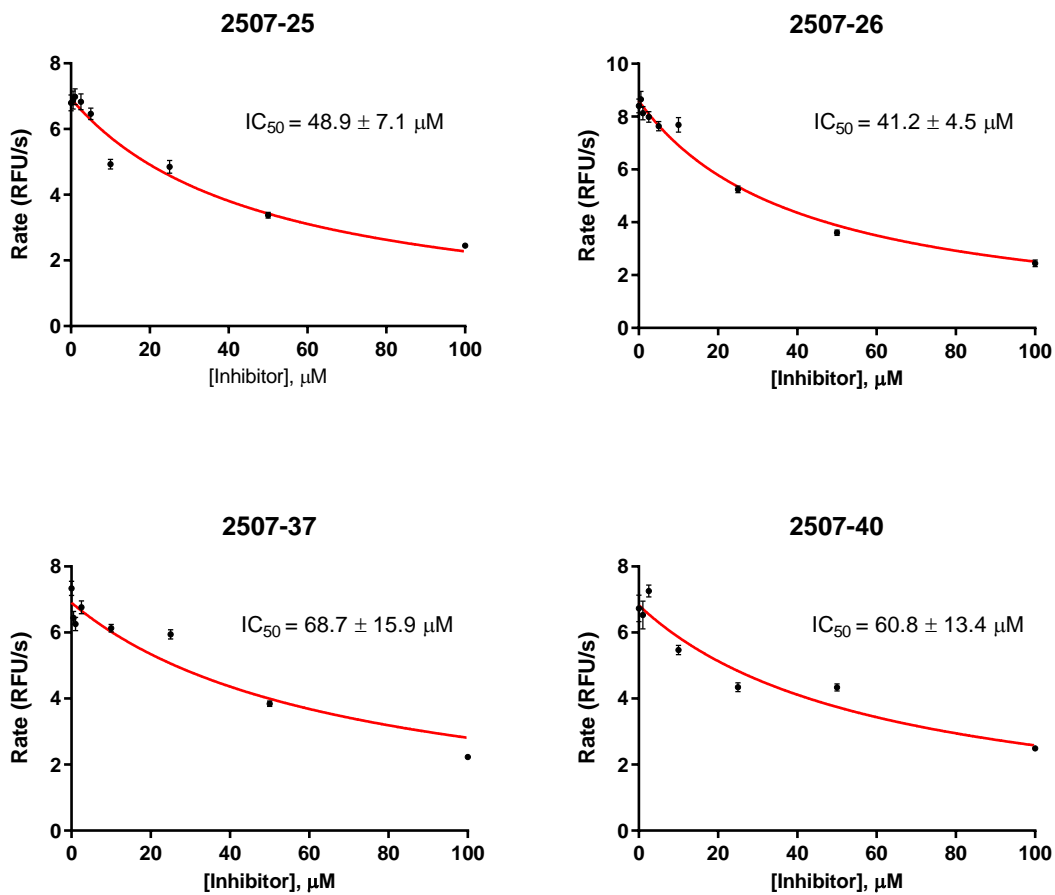


Figure C13. IC₅₀ curves for top 10 compounds, part 2.

ERK2 phosphorylation of sox-Sub-D peptide was measured in the presence of 0-100 μM of each compound by change in sox-Sub-D fluorescence over time (RFU/s). IC₅₀ curves and fit values are shown for 2507-25, 2507-26, 2507-37, and 2507-40.

Structural Studies

Residue code	Residue number	$\Delta\delta$ (CSP)	1.5*STDev	n*STDev	2D struct./other
Y	314	--			
T	158	--			ED
C	159	--			DRS cysteine
D	122	--			
L	155	0.3642	1.5stdev	3stdev	hydrophobic
H	123	0.2521	1.5stdev	3stdev	hydrophobic
I	124	0.2386	1.5stdev	3stdev	
Q	313	0.1681	1.5stdev	3stdev	
I	322	0.1591	1.5stdev	3stdev	
D	319	0.1572	1.5stdev	3stdev	CD
E	320	0.1422	1.5stdev	3stdev	
Y	315	0.1382	1.5stdev	3stdev	
D	42	0.0999	1.5stdev	3stdev	
D	316	0.0981	1.5stdev	3stdev	CD
N	156	0.089	1.5stdev	3stdev	
A	323	0.0887	1.5stdev	3stdev	
A	325	0.0778	1.5stdev	3stdev	
E	79	0.0688	1.5stdev	3stdev	
Y	126	0.0673	1.5stdev	3stdev	hydrophobic
E	348	0.0585	1.5stdev	3stdev	
S	120	0.0515	1.5stdev	3stdev	
T	116	0.0513	1.5stdev	3stdev	
V	143	0.0424	1.5stdev	3stdev	
D	109	0.04	1.5stdev	3stdev	
T	66	0.0393	1.5stdev	3stdev	
E	303	0.0374	1.5stdev	3stdev	
N	222	0.0371	1.5stdev	3stdev	
C	125	0.0342	1.5stdev	3stdev	
A	33	0.0331	1.5stdev	3stdev	
R	77	0.0314	1.5stdev	3stdev	
S	318	0.031	1.5stdev	2stdev	
D	104	0.0309	1.5stdev	2stdev	
H	78	0.0295	1.5stdev	2stdev	

Table C3. Chemical shift perturbations for ERK2 residues in the presence of compound 2507-8.

The single-letter amino acid codes for the residues with chemical shift changes that were greater than 1 standard deviation (1stdev) of the mean, calculated over a set of CSP values [56], are listed and numbered according to PDB entry 3ERK. Key DRS residues are marked in red and their secondary structural elements noted as either: hydrophobic, ED domain, CD (common docking) domain, or solvent-exposed cysteine.

Residue code	Residue number	$\Delta\delta$ (CSP)	1.5*STDev	n*STDev	2D struct./other
I	87	0.0292	1.5stdev	2stdev	
A	284	0.029	1.5stdev	2stdev	
E	324	0.0289	1.5stdev	2stdev	
A	141	0.0281	1.5stdev	2stdev	
D	86	0.0276	1.5stdev	2stdev	
S	140	0.0268	1.5stdev	2stdev	
E	10	0.0259	1.5stdev	2stdev	
A	172	0.0256	1.5stdev	2stdev	
K	112	0.0238	1.5stdev	2stdev	
L	119	0.0234	1.5stdev	2stdev	hydrophobic
I	345	0.0233	1.5stdev	2stdev	
Q	304	0.0229	1.5stdev	2stdev	
K	97	0.0193	1.5stdev	1stdev	
K	115	0.0193	1.5stdev	1stdev	
C	164	0.0191	1.5stdev	1stdev	active site cysteine
S	221	0.0191	1.5stdev	1stdev	
C	63	0.0189	1.5stdev	1stdev	
N	251	0.0183	1.5stdev	1stdev	
Q	103	0.0182	1.5stdev	1stdev	
Y	23	0.0179	1.5stdev	1stdev	
F	76	0.0173	1.5stdev	1stdev	
R	65	0.0168	1.5stdev	1stdev	
I	81	0.0165	1.5stdev	1stdev	
T	108	0.0161	1.5stdev	1stdev	
S	151	0.0155		1stdev	
R	351	0.0155		1stdev	
L	44	0.0153		1stdev	
L	242	0.0153		1stdev	
R	299	0.0153		1stdev	
L	144	0.0151		1stdev	
L	154	0.0151		1stdev	
I	300	0.0151		1stdev	
I	84	0.015		1stdev	
C	252	0.0147		1stdev	
S	246	0.0141		1stdev	
N	45	0.0138		1stdev	
K	298	0.0136		1stdev	
V	302	0.0135		1stdev	

Table C3, continued.

Residue code	Residue number	$\Delta\delta$ (CSP)	1.5*STDev	n*STDev	2D struct./other
D	335	0.0128		1stdev	
L	341	0.0128		1stdev	
G	243	0.0127		1stdev	
L	276	0.0127		1stdev	
K	46	0.0124		1stdev	
H	118	0.0122		1stdev	
Y	261	0.0122		1stdev	
N	142	0.012		1stdev	
I	253	0.0116		1stdev	
D	281	0.0116		1stdev	
F	346	0.0114		1stdev	
K	340	0.0109		1stdev	
E	312	0.0106		1stdev	
R	68	0.0105		1stdev	

Table C3, continued.

ERK2
Inhibitor 2507-8

PDB accession code	(<i>in prep.</i>)
Data Collection and Processing^a	
Beamline	21-ID-F
Space groups	P2 ₁
Cell Dimensions: a, b, c (Å)	48.9, 71.2, 60.2
α, β, γ (degrees)	90, 109.4, 90
Resolution (Å)	37.2-1.90 (1.968-1.90)
Total Reflections	30,771
Unique Reflections	3,054
R _{sym} ^b (%)	0.102 (1.619)
R _{pim} ^c (%)	0.049 (0.791)
<I>/<σ>	20.09 (1.55)
Completeness (%)	99.9 (99.8)
Refinement Statistics	
R _{work} ^d (%)	16.9
R _{free} (%)	20.6
RMS deviations	
Bond (Å)	0.006
Angle (°)	0.80
Ramachandran statistics ^e	
Favored (%)	95.86
Allowed (%)	4.14
Outliers (%)	0.0

Table C4. Crystallographic data collection and refinement statistics.

^aNumbers in parentheses indicate statistics for the highest shell.

^b $R_{sym} = \sum |I_i - (I)| / \sum |I_i|$ where I is intensity, I_i is the i th measurement, and (I) is the weighted mean of I .

^c $R_{pim} = \sum_{hkl} \sqrt{[1/(N-1)] \sum_i |I_i(hkl) - \overline{I(hkl)}|} / \sum_{hkl} \sum_i I_i(hkl)$ where I is running over the number of independent observations of reflection hkl and N is representing the number of replicate observations.

^d $R_{work} = \sum ||Fo| - |Fc|| / \sum |Fo|$ where Fo and Fc are the observed and calculated structure factor amplitudes. R_{free} is the same as R_{work} for a set of data omitted from the refinement.

^eRamachandran analysis from MOLPROBITY [252]

Chemical Synthesis and Purification

Synthesis of Compounds

The compounds and libraries were synthesized by our collaborators at Torrey Pines Institute for Molecular Studies (Port St. Lucie, FL), who provided the protocols and purification data shown in this section.

The screening results indicated that the most active compounds consisted of a tripodal *tris*-(2-aminoethyl)amine scaffold appended with three imidazolidin-2-imines (denoted as 2507 group of compounds). These tripodal *tris*-(2-(2-iminoimidazolidin-1-yl)ethyl)amines are from the mixture-based positional scanning library 2408, which consists of 125 samples comprising a total of 9,765,625 individual *tris*-(2-(2-iminoimidazolidin-1-yl)ethyl)amines. The tripodal *tris*-(2-(2-iminoimidazolidin-1-yl)ethyl)amines were synthesized through a solid-phase synthetic approach shown in Figure C14. Briefly, a Boc-protected *L*-amino acid (Boc-AA₁-OH, R₁) was coupled to the 4-methylbenzhydrylamine (MBHA) resin (A), forming a resin-bound amino amide (B). The resin-bound amino amide was reacted with a bromoacetic acid to form a resin-bound (C) containing a reactive bromide, followed by reaction with a mono-Boc-protected ethylenediamine to form (D). The unprotected secondary amino group of (D) was coupled with an Fmoc-protected glycine to form a tripodal intermediate (E), containing Boc-protected and Fmoc-protected legs. After treatment of the intermediate (E) with 55% TFA to remove the Boc protective group, a second Boc-protected *L*-amino acid (Boc-AA₂-OH, R₂) was coupled to form (F). The Boc-protected amino group was then transformed to an acyl terminus through reaction with a carboxylic acid (R₃-COOH, R₃) (G).

Next, the Fmoc protective group was removed by the treatment of (G) with 20% piperidine and a third Boc-protected *L*-amino acid (Boc-AA₃-OH, R₄) was coupled to form (H). The Boc-protected amino group of (H) was then removed and a carboxylic acid (R₅-COOH, R₅) was coupled to cap the amino terminus, forming a tripodal peptide (I).

The resin-bound tripodal peptide (I) was then reduced to a tripodal polyamine (J) using an exhaustive borane reduction method [253]. The tripodal polyamine (J) was treated with cyanogen bromide to form a resin-bound, tripodal (K) containing the *tris*-(2-(2-iminoimidazolidin-1-yl)ethyl)amines. Following treatment of (K) with anhydrous HF, the final product, *tris*-(2-(2-iminoimidazolidin-1-yl)ethyl)amine (L), was released from the resin.

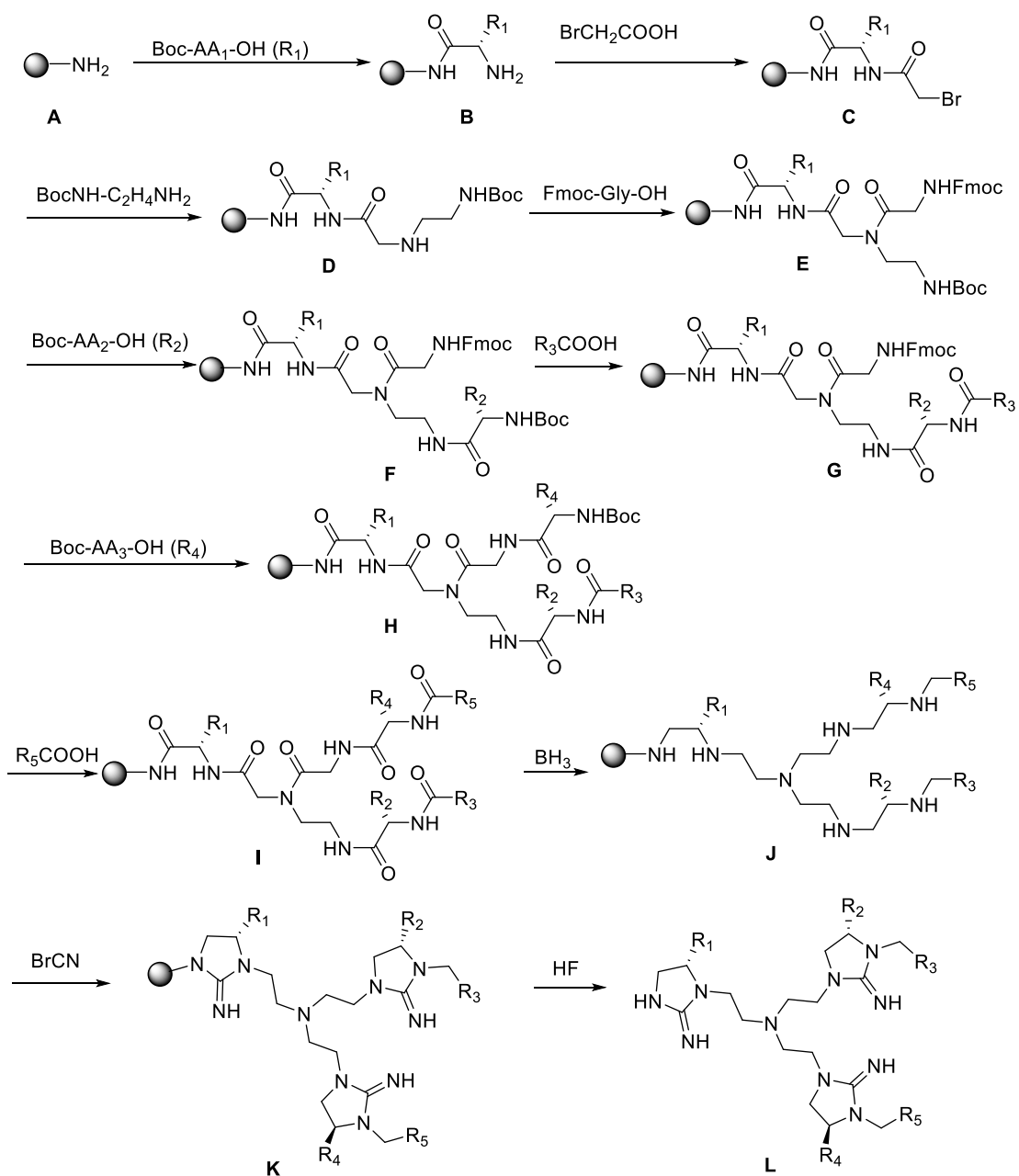
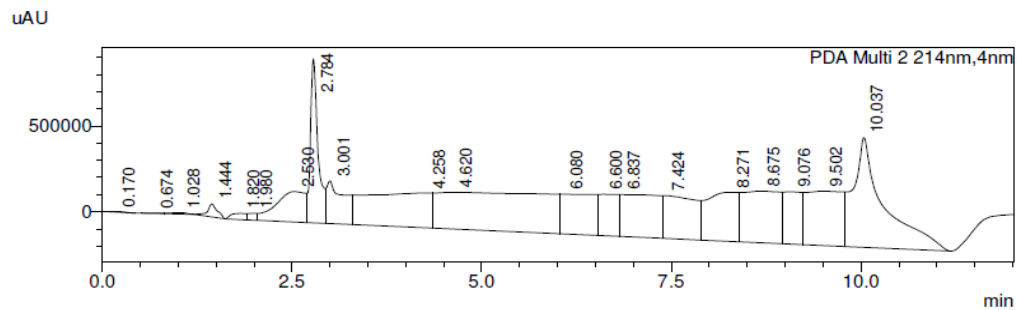


Figure C14. Synthetic approach for tris-(2-(2-iminoimidazolidin-1-yl)ethyl)amines.

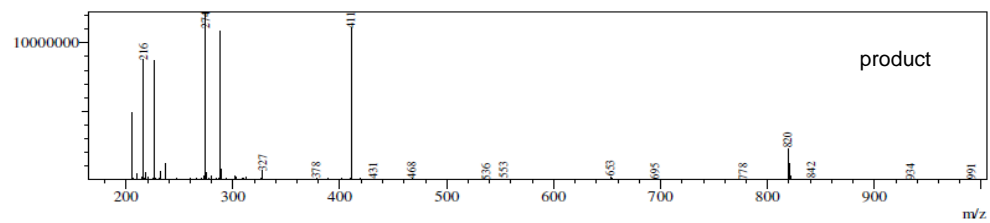
Synthesis of the Mixture-Based Tris-(2-(2-iminoimidazolidin-1-yl)ethyl)amine Library.

The mixture-based *tris*-(2-(2-iminoimidazolidin-1-yl)ethyl)amine library (2408) was constructed using the same method as for the synthesis of the individual compounds. The library was synthesized in a positional scanning format. The library was composed of 125 samples divided into 5 sub-libraries; each sub-library represents a position, R₁, R₂, R₃, R₄, or R₅ and each position was defined with either a single reagent or a mixture of the 25 reagents. For each of the 125 samples, one position was made up of a single reagent and the 4 remaining positions were a mixture of 25 reagents. Therefore, each sample contained 390,625 individual *tris*-(2-(2-iminoimidazolidin-1-yl)ethyl)amine compounds.

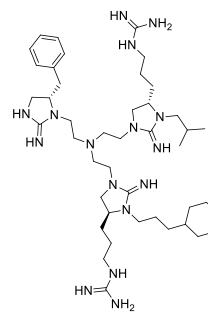
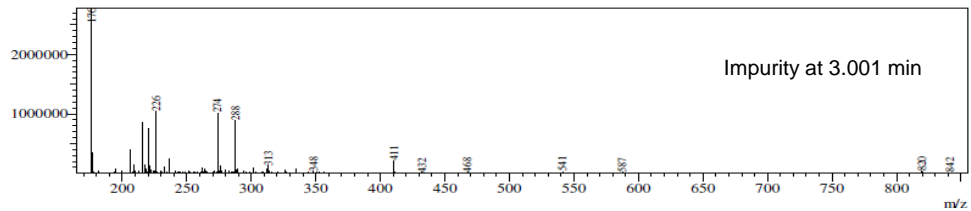
Compound 2507-8



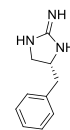
Peak#: 1 R.Time:2.844(Scan#:684)
 MassPeaks:168
 Spectrum Mode:Averaged 2.842-2.850(683-685)
 BG Mode:Calc Segment 1 - Event 1



R.Time:3.038(Scan#:730)
 MassPeaks:101
 Segment 1 - Event 1



Chemical Formula: C₄₃H₇₃N₁₆
 Molecular Weight: 819.19



Chemical Formula: C₁₀H₁₃N₃
 Molecular Weight: 175.23

Figure C16. LC-MS results for compound 2507-8 purification.

The compound 2507-8 was purified by HPLC. Under our HPLC conditions, a byproduct showing an m/z of 176 was not separable from the 2507-8, resulting in a purity of ~90% of the final product. This product was then examined by LC-MS (Figure C16) and its structure was characterized by 1D and 2D NMR spectroscopy.

NMR data of 2507-8:

H NMR (400 MHz, DMSO-d₆): δ 0.80-0.89 (8H), 1.14-1.20 (6H), 1.39-1.46 (7H), 1.58-1.73 (8H), 1.92 (1H), 2.69-2.84 (7H), 2.99-3.10 (7H), 3.25 - 3.45 (11H), 3.60-3.75 (3H), 3.88 (2H), 4.26 (1H), 7.26-7.30 (m, 5H), 8.24 (brs, 8H), 8.46 (s, 5H), 9.53 (brs, 6H)

C NMR (100 MHz, DMSO-d₆): δ 19.6, 20.0, 23.6, 23.7, 24.3, 26.2, 26.3, 26.6, 28.4, 28.7, 33.3, 33.9, 37.3, 37.7, 40.1, 40.7, 42.6, 43.3, 45.7, 48.7, 50.6, 50.9, 51.1, 56.0, 56.1, 59.0, 127.2, 129.0, 129.9, 136.9, 157.2, 157.3, 158.3, 159.5, 167.6

H NMR data of 8.46 ppm (s, 5H) and C NMR of 167.6 ppm are from formic acid.

APPENDIX D: SUPPLEMENTARY INFORMATION FOR CHAPTER 4

Michaelis-Menten Kinetics

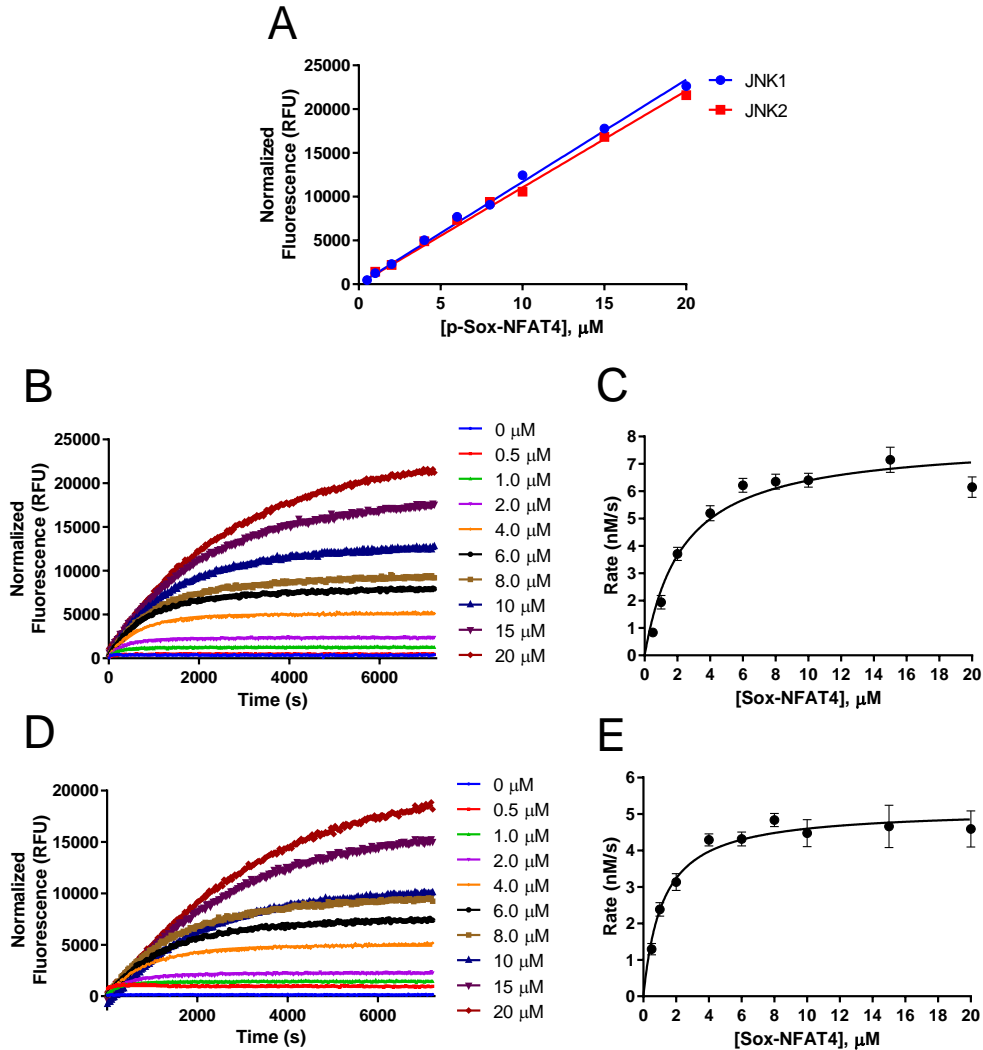


Figure D1. Michaelis-Menten kinetics for JNK phosphorylation of sox-NFAT4.

ATP concentration was fixed at 100 μM. (A) Fluorescence signal was directly proportional to amount of phosphorylated sox-NFAT4. Reaction progress curves (B) for phosphorylation of varied amounts of sox-NFAT4, and initial rates (C) fit to the Michaelis-Menten equation, were used to determine $K_{m,S}$ and $k_{cat,S}$ for JNK1. The reaction progress curves (D) and initial rate analysis (E) for JNK2 were conducted in the same manner.

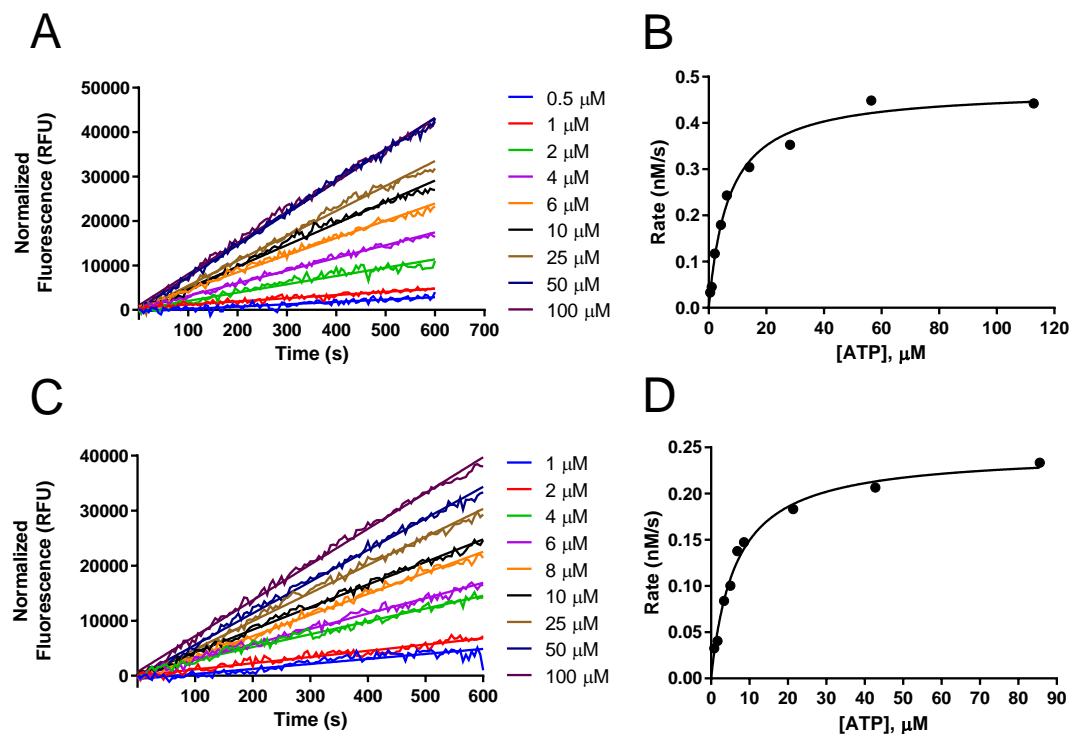


Figure D2. Michaelis-Menten kinetics for JNK with respect to ATP.

Michaelis-Menten kinetics with respect to ATP. Fluorescence measurements for (A) JNK1 and (C) JNK2 phosphorylation of 4 μM sox-NFAT4 in the presence of varied concentrations of ATP (0.5-100 μM). Initial rates were fit to Michaelis-Menten model for (B) JNK1 and (D) JNK2.

Global Fitting of JNK1/2 Inactivation in GraphPad Prism

The following equations were entered as a model for nonlinear regression analysis of the data sets (Y = rate of fluorescence or rate of substrate phosphorylation, X = time). Note that the parameter 'Ki' here is the apparent K_I^* , but K_I can be evaluated using ATP concentration and $K_{m,A}$ for ATP as describe in Chapter 4, Materials and Methods. This can be done in Prism by applying a transform to the output 'Ki'.

Equation set for inhibition model:

$$k_{obs} = k_{inact} * I / (K_i + I)$$

$$Y = v / k_{obs} * (1 - \exp(-k_{obs} * X))$$

(or $Y = v * X$ for $I = 0$)

<u>Parameter</u>	<u>Constraint</u>	<u>Value</u>
kinact	Shared and must be >0	0
I	Data set constant (=column title)	
Ki	Shared and must be >0	0
v	No constraint	

The inhibitor concentration (I) constraint is drawn from the numerical column title of the input data in Prism. The 'shared' constraint specifies that all inhibitor concentrations are fit globally.

Kinetics of THZ-3-60-1 Inhibition

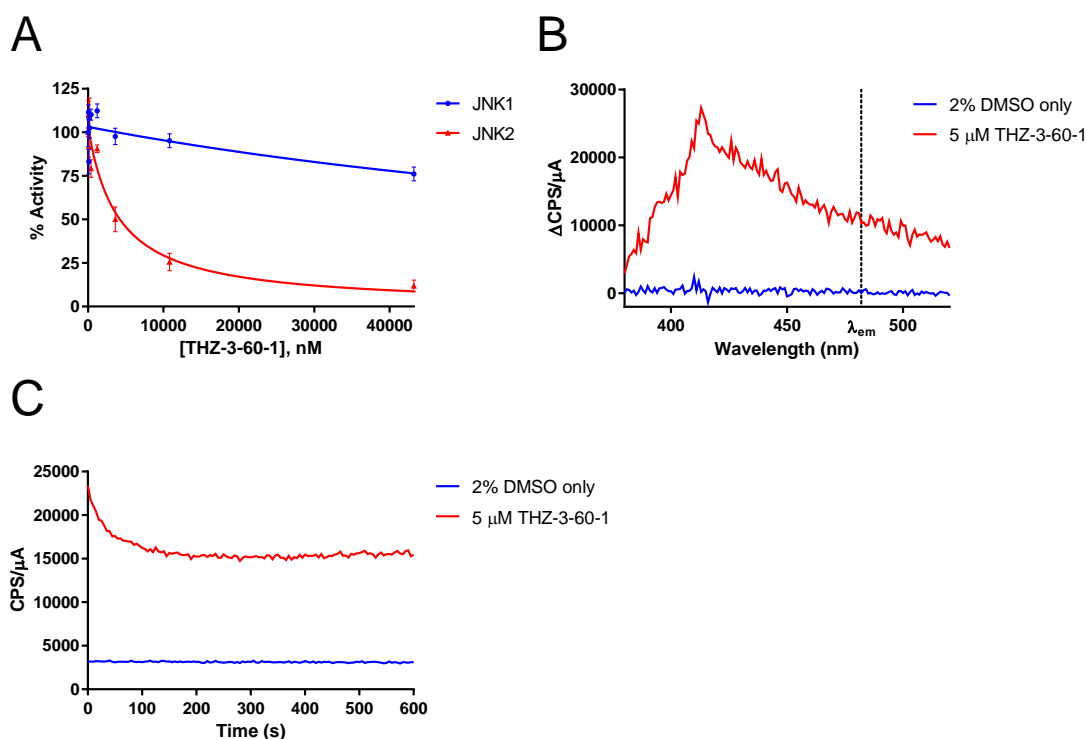


Figure D3. Characterization of THZ-3-60-1.

(A) IC₅₀ curves for THZ-3-60-1 inhibition of JNK1 and JNK2 by ³²P assay. (B) Normalized fluorescence emission spectra for 5 μ M THZ-3-60-1 and 2% (v/v) DMSO control in assay buffer. λ_{em} as indicated by the dotted line marks the fluorescence assay emission wavelength of 482 nm. (C) Time-dependent fluorescence of 5 μ M THZ-3-60-1 compared to 2% (v/v) DMSO control at the emission wavelength of 482 nm. Relative fluorescence units (RFU) here are expressed as CPS/ μ A.

Evaluation of IC₅₀ Values for THZ-3-60-1

To evaluate the IC₅₀ values for THZ-3-60-1 inhibition of JNK1 and JNK2, THZ-3-60-1 (0-43.2 μ M) was incubated with 20 nM JNK1 or JNK2 for 30 minutes at room temperature. Reactions were initiated by addition of 10 μ M ATF-2 substrate and 100 μ M [γ -³²P] MgATP and carried out at 30°C. Initial reaction rates were determined for each condition as previously described, and the rates as a function of inhibitor concentration

were used to evaluate the IC_{50} . For JNK1, $IC_{50} > 100 \mu\text{M}$, and for JNK2, $IC_{50} = 4.0 \pm 1.1 \mu\text{M}$. These IC_{50} curves were determined for 0, 60, 120, and 240 minutes of incubation of JNK1/2 with inhibitor with no significant change in IC_{50} . Therefore, we assumed that THZ-3-60-1 exhibited no time-dependent inhibition.

References

1. Manning, G., et al., *The protein kinase complement of the human genome*. Science, 2002. 298(5600): p. 1912-34.
2. Avruch, J., *MAP kinase pathways: the first twenty years*. Biochim Biophys Acta, 2007. 1773(8): p. 1150-60.
3. Plotnikov, A., et al., *The MAPK cascades: signaling components, nuclear roles and mechanisms of nuclear translocation*. Biochim Biophys Acta, 2011. 1813(9): p. 1619-33.
4. Wortzel, I. and R. Seger, *The ERK Cascade: Distinct Functions within Various Subcellular Organelles*. Genes Cancer, 2011. 2(3): p. 195-209.
5. Roskoski, R., Jr., *ERK1/2 MAP kinases: structure, function, and regulation*. Pharmacol Res, 2012. 66(2): p. 105-43.
6. Raman, M., W. Chen, and M.H. Cobb, *Differential regulation and properties of MAPKs*. Oncogene, 2007. 26(22): p. 3100-12.
7. Pylayeva-Gupta, Y., E. Grabocka, and D. Bar-Sagi, *RAS oncogenes: weaving a tumorigenic web*. Nat Rev Cancer, 2011. 11(11): p. 761-74.
8. Roskoski, R., Jr., *RAF protein-serine/threonine kinases: structure and regulation*. Biochem Biophys Res Commun, 2010. 399(3): p. 313-7.
9. Yoon, S. and R. Seger, *The extracellular signal-regulated kinase: multiple substrates regulate diverse cellular functions*. Growth Factors, 2006. 24(1): p. 21-44.
10. Saba-El-Leil, M.K., et al., *An essential function of the mitogen-activated protein kinase Erk2 in mouse trophoblast development*. EMBO Rep, 2003. 4(10): p. 964-8.
11. Bos, J.L., *ras oncogenes in human cancer: a review*. Cancer Res, 1989. 49(17): p. 4682-9.
12. Davies, H., et al., *Mutations of the BRAF gene in human cancer*. Nature, 2002. 417(6892): p. 949-54.
13. Garnett, M.J. and R. Marais, *Guilty as charged: B-RAF is a human oncogene*. Cancer Cell, 2004. 6(4): p. 313-9.
14. Muslin, A.J., *MAPK signalling in cardiovascular health and disease: molecular mechanisms and therapeutic targets*. Clin Sci (Lond), 2008. 115(7): p. 203-18.
15. Chico, L.K., L.J. Van Eldik, and D.M. Watterson, *Targeting protein kinases in central nervous system disorders*. Nat Rev Drug Discov, 2009. 8(11): p. 892-909.

16. Tanti, J.F. and J. Jager, *Cellular mechanisms of insulin resistance: role of stress-regulated serine kinases and insulin receptor substrates (IRS) serine phosphorylation*. *Curr Opin Pharmacol*, 2009. 9(6): p. 753-62.
17. Kim, E.K. and E.J. Choi, *Pathological roles of MAPK signaling pathways in human diseases*. *Biochim Biophys Acta*, 2010. 1802(4): p. 396-405.
18. Gupta, S., et al., *Selective interaction of JNK protein kinase isoforms with transcription factors*. *EMBO J*, 1996. 15(11): p. 2760-70.
19. Davis, R.J., *Signal transduction by the JNK group of MAP kinases*. *Cell*, 2000. 103(2): p. 239-52.
20. Kyriakis, J.M. and J. Avruch, *pp54 microtubule-associated protein 2 kinase. A novel serine/threonine protein kinase regulated by phosphorylation and stimulated by poly-L-lysine*. *J Biol Chem*, 1990. 265(28): p. 17355-63.
21. Pulverer, B.J., et al., *Phosphorylation of c-jun mediated by MAP kinases*. *Nature*, 1991. 353(6345): p. 670-4.
22. Derijard, B., et al., *JNK1: a protein kinase stimulated by UV light and Ha-Ras that binds and phosphorylates the c-Jun activation domain*. *Cell*, 1994. 76(6): p. 1025-37.
23. Bogoyevitch, M.A. and B. Kobe, *Uses for JNK: the many and varied substrates of the c-Jun N-terminal kinases*. *Microbiol Mol Biol Rev*, 2006. 70(4): p. 1061-95.
24. Hunot, S., et al., *JNK-mediated induction of cyclooxygenase 2 is required for neurodegeneration in a mouse model of Parkinson's disease*. *Proc Natl Acad Sci U S A*, 2004. 101(2): p. 665-70.
25. Yarza, R., et al., *c-Jun N-terminal Kinase (JNK) Signaling as a Therapeutic Target for Alzheimer's Disease*. *Front Pharmacol*, 2015. 6: p. 321.
26. Hirosumi, J., et al., *A central role for JNK in obesity and insulin resistance*. *Nature*, 2002. 420(6913): p. 333-6.
27. Roy, P.K., et al., *Role of the JNK signal transduction pathway in inflammatory bowel disease*. *World J Gastroenterol*, 2008. 14(2): p. 200-2.
28. Bubici, C. and S. Papa, *JNK signalling in cancer: in need of new, smarter therapeutic targets*. *Br J Pharmacol*, 2014. 171(1): p. 24-37.
29. Tournier, C., *The 2 Faces of JNK Signaling in Cancer*. *Genes Cancer*, 2013. 4(9-10): p. 397-400.
30. Xie, X., et al., *c-Jun N-terminal kinase promotes stem cell phenotype in triple-negative breast cancer through upregulation of Notch1 via activation of c-Jun*. *Oncogene*, 2017. 36(18): p. 2599-2608.

31. Hubner, A., et al., *JNK and PTEN cooperatively control the development of invasive adenocarcinoma of the prostate*. Proc Natl Acad Sci U S A, 2012. 109(30): p. 12046-51.
32. Kaoud, T.S., et al., *Development of JNK2-selective peptide inhibitors that inhibit breast cancer cell migration*. ACS Chem Biol, 2011. 6(6): p. 658-66.
33. Cui, J., et al., *c-Jun NH(2)-terminal kinase 2 α 2 promotes the tumorigenicity of human glioblastoma cells*. Cancer Res, 2006. 66(20): p. 10024-31.
34. Shibata, W., et al., *c-Jun NH2-terminal kinase 1 is a critical regulator for the development of gastric cancer in mice*. Cancer Res, 2008. 68(13): p. 5031-9.
35. Hui, L., et al., *Proliferation of human HCC cells and chemically induced mouse liver cancers requires JNK1-dependent p21 downregulation*. J Clin Invest, 2008. 118(12): p. 3943-53.
36. Chang, Q., et al., *JNK1 activation predicts the prognostic outcome of the human hepatocellular carcinoma*. Mol Cancer, 2009. 8: p. 64.
37. Das, M., et al., *The role of JNK in the development of hepatocellular carcinoma*. Genes Dev, 2011. 25(6): p. 634-45.
38. Chapman, P.B., et al., *Improved survival with vemurafenib in melanoma with BRAF V600E mutation*. N Engl J Med, 2011. 364(26): p. 2507-16.
39. Hauschild, A., et al., *Dabrafenib in BRAF-mutated metastatic melanoma: a multicentre, open-label, phase 3 randomised controlled trial*. Lancet, 2012. 380(9839): p. 358-65.
40. Little, A.S., P.D. Smith, and S.J. Cook, *Mechanisms of acquired resistance to ERK1/2 pathway inhibitors*. Oncogene, 2013. 32(10): p. 1207-15.
41. Wagle, N., et al., *Dissecting therapeutic resistance to RAF inhibition in melanoma by tumor genomic profiling*. J Clin Oncol, 2011. 29(22): p. 3085-96.
42. Zhao, Y. and A.A. Adjei, *The clinical development of MEK inhibitors*. Nat Rev Clin Oncol, 2014. 11(7): p. 385-400.
43. Fallahi-Sichani, M., et al., *Systematic analysis of BRAF(V600E) melanomas reveals a role for JNK/c-Jun pathway in adaptive resistance to drug-induced apoptosis*. Mol Syst Biol, 2015. 11(3): p. 797.
44. Lopez-Bergami, P., et al., *Rewired ERK-JNK signaling pathways in melanoma*. Cancer Cell, 2007. 11(5): p. 447-60.
45. Roskoski, R., Jr., *Classification of small molecule protein kinase inhibitors based upon the structures of their drug-enzyme complexes*. Pharmacol Res, 2016. 103: p. 26-48.

46. Dar, A.C. and K.M. Shokat, *The evolution of protein kinase inhibitors from antagonists to agonists of cellular signaling*. *Annu Rev Biochem*, 2011. 80: p. 769-95.
47. Foda, Z.H. and M.A. Seeliger, *Kinase inhibitors: an allosteric add-on*. *Nat Chem Biol*, 2014. 10(10): p. 796-7.
48. Simard, J.R., et al., *A new screening assay for allosteric inhibitors of cSrc*. *Nat Chem Biol*, 2009. 5(6): p. 394-6.
49. Liu, Y. and N.S. Gray, *Rational design of inhibitors that bind to inactive kinase conformations*. *Nat Chem Biol*, 2006. 2(7): p. 358-64.
50. Scapin, G., *Protein kinase inhibition: different approaches to selective inhibitor design*. *Curr Drug Targets*, 2006. 7(11): p. 1443-54.
51. Knight, Z.A. and K.M. Shokat, *Features of selective kinase inhibitors*. *Chem Biol*, 2005. 12(6): p. 621-37.
52. Vulpetti, A. and R. Bosotti, *Sequence and structural analysis of kinase ATP pocket residues*. *Farmaco*, 2004. 59(10): p. 759-65.
53. Garai, A., et al., *Specificity of linear motifs that bind to a common mitogen-activated protein kinase docking groove*. *Sci Signal*, 2012. 5(245): p. ra74.
54. Zeke, A., et al., *Systematic discovery of linear binding motifs targeting an ancient protein interaction surface on MAP kinases*. *Mol Syst Biol*, 2015. 11(11): p. 837.
55. Tompa, P., et al., *A million peptide motifs for the molecular biologist*. *Mol Cell*, 2014. 55(2): p. 161-9.
56. Piserchio, A., et al., *Local destabilization, rigid body, and fuzzy docking facilitate the phosphorylation of the transcription factor Ets-1 by the mitogen-activated protein kinase ERK2*. *Proc Natl Acad Sci U S A*, 2017. 114(31): p. E6287-E6296.
57. Callaway, K.A., et al., *Properties and regulation of a transiently assembled ERK2.Ets-1 signaling complex*. *Biochemistry*, 2006. 45(46): p. 13719-33.
58. Graves, L.M., et al., *The dynamic nature of the kinome*. *Biochem J*, 2013. 450(1): p. 1-8.
59. Akella, R., T.M. Moon, and E.J. Goldsmith, *Unique MAP Kinase binding sites*. *Biochim Biophys Acta*, 2008. 1784(1): p. 48-55.
60. Tanoue, T., et al., *Identification of a docking groove on ERK and p38 MAP kinases that regulates the specificity of docking interactions*. *EMBO J*, 2001. 20(3): p. 466-79.
61. Tanoue, T. and E. Nishida, *Molecular recognitions in the MAP kinase cascades*. *Cell Signal*, 2003. 15(5): p. 455-62.

62. Burkhard, K.A., F. Chen, and P. Shapiro, *Quantitative analysis of ERK2 interactions with substrate proteins: roles for kinase docking domains and activity in determining binding affinity*. J Biol Chem, 2011. 286(4): p. 2477-85.
63. Dimitri, C.A., et al., *Spatially separate docking sites on ERK2 regulate distinct signaling events in vivo*. Curr Biol, 2005. 15(14): p. 1319-24.
64. Piserchio, A., et al., *Docking interactions of hematopoietic tyrosine phosphatase with MAP kinases ERK2 and p38alpha*. Biochemistry, 2012. 51(41): p. 8047-9.
65. Martin, M.C., et al., *The docking interaction of caspase-9 with ERK2 provides a mechanism for the selective inhibitory phosphorylation of caspase-9 at threonine 125*. J Biol Chem, 2008. 283(7): p. 3854-65.
66. Bardwell, A.J., et al., *A conserved docking site in MEKs mediates high-affinity binding to MAP kinases and cooperates with a scaffold protein to enhance signal transmission*. J Biol Chem, 2001. 276(13): p. 10374-86.
67. Callaway, K., et al., *The anti-apoptotic protein PEA-15 is a tight binding inhibitor of ERK1 and ERK2, which blocks docking interactions at the D-recruitment site*. Biochemistry, 2007. 46(32): p. 9187-98.
68. Callaway, K., M.A. Rainey, and K.N. Dalby, *Quantifying ERK2-protein interactions by fluorescence anisotropy: PEA-15 inhibits ERK2 by blocking the binding of DEJL domains*. Biochim Biophys Acta, 2005. 1754(1-2): p. 316-23.
69. Mace, P.D., et al., *Structure of ERK2 bound to PEA-15 reveals a mechanism for rapid release of activated MAPK*. Nat Commun, 2013. 4: p. 1681.
70. Formstecher, E., et al., *PEA-15 mediates cytoplasmic sequestration of ERK MAP kinase*. Dev Cell, 2001. 1(2): p. 239-50.
71. Adachi, M., M. Fukuda, and E. Nishida, *Nuclear export of MAP kinase (ERK) involves a MAP kinase kinase (MEK)-dependent active transport mechanism*. J Cell Biol, 2000. 148(5): p. 849-56.
72. Zheng, C.F. and K.L. Guan, *Cytoplasmic localization of the mitogen-activated protein kinase activator MEK*. J Biol Chem, 1994. 269(31): p. 19947-52.
73. Zeke, A., et al., *JNK Signaling: Regulation and Functions Based on Complex Protein-Protein Partnerships*. Microbiol Mol Biol Rev, 2016. 80(3): p. 793-835.
74. Hancock, C.N., et al., *Identification of novel extracellular signal-regulated kinase docking domain inhibitors*. J Med Chem, 2005. 48(14): p. 4586-95.
75. Schnieders, M.J., et al., *Computational insights for the discovery of non-ATP competitive inhibitors of MAP kinases*. Curr Pharm Des, 2012. 18(9): p. 1173-85.
76. Chen, F., et al., *Characterization of ATP-independent ERK inhibitors identified through in silico analysis of the active ERK2 structure*. Bioorg Med Chem Lett, 2006. 16(24): p. 6281-7.

77. Boston, S.R., et al., *Characterization of ERK docking domain inhibitors that induce apoptosis by targeting Rsk-1 and caspase-9*. BMC Cancer, 2011. 11: p. 7.
78. Li, Q., et al., *Structure-activity relationship (SAR) studies of 3-(2-amino-ethyl)-5-(4-ethoxy-benzylidene)-thiazolidine-2,4-dione: development of potential substrate-specific ERK1/2 inhibitors*. Bioorg Med Chem Lett, 2009. 19(21): p. 6042-6.
79. Kinoshita, T., et al., *Identification of allosteric ERK2 inhibitors through in silico biased screening and competitive binding assay*. Bioorg Med Chem Lett, 2016. 26(3): p. 955-958.
80. Heo, Y.S., et al., *Structural basis for the selective inhibition of JNK1 by the scaffolding protein JIP1 and SP600125*. EMBO J, 2004. 23(11): p. 2185-95.
81. Borsello, T., et al., *A peptide inhibitor of c-Jun N-terminal kinase protects against excitotoxicity and cerebral ischemia*. Nat Med, 2003. 9(9): p. 1180-6.
82. Bonny, C., et al., *Cell-permeable peptide inhibitors of JNK: novel blockers of beta-cell death*. Diabetes, 2001. 50(1): p. 77-82.
83. Bogoyevitch, M.A., et al., *c-Jun N-terminal kinase (JNK) signaling: recent advances and challenges*. Biochim Biophys Acta, 2010. 1804(3): p. 463-75.
84. Ngoei, K.R., et al., *A novel retro-inverso peptide is a preferential JNK substrate-competitive inhibitor*. Int J Biochem Cell Biol, 2013. 45(8): p. 1939-50.
85. Stebbins, J.L., et al., *Identification of a new JNK inhibitor targeting the JNK-JIP interaction site*. Proc Natl Acad Sci U S A, 2008. 105(43): p. 16809-13.
86. De, S.K., et al., *Discovery of 2-(5-nitrothiazol-2-ylthio)benzo[d]thiazoles as novel c-Jun N-terminal kinase inhibitors*. Bioorg Med Chem, 2009. 17(7): p. 2712-7.
87. De, S.K., et al., *Design, synthesis, and structure-activity relationship of substrate competitive, selective, and in vivo active triazole and thiadiazole inhibitors of the c-Jun N-terminal kinase*. J Med Chem, 2009. 52(7): p. 1943-52.
88. De, S.K., et al., *Synthesis and optimization of thiadiazole derivatives as a novel class of substrate competitive c-Jun N-terminal kinase inhibitors*. Bioorg Med Chem, 2010. 18(2): p. 590-6.
89. Borhani, D.W., *Covalent JNK inhibitors?* Proc Natl Acad Sci U S A, 2009. 106(8): p. E18; author reply E19.
90. Kaoud, T.S., et al., *From in Silico Discovery to intra-Cellular Activity: Targeting JNK-Protein Interactions with Small Molecules*. ACS Med Chem Lett, 2012. 3(9): p. 721-725.
91. Kaoud, T.S., et al., *Manipulating JNK signaling with (–)-zuonin A*. ACS Chem Biol, 2012. 7(11): p. 1873-83.

92. Galanis, A., S.H. Yang, and A.D. Sharrocks, *Selective targeting of MAPKs to the ETS domain transcription factor SAP-1*. J Biol Chem, 2001. 276(2): p. 965-73.
93. Tzarum, N., et al., *DEF pocket in p38alpha facilitates substrate selectivity and mediates autophosphorylation*. J Biol Chem, 2013. 288(27): p. 19537-47.
94. Elkins, J.M., et al., *X-ray crystal structure of ERK5 (MAPK7) in complex with a specific inhibitor*. J Med Chem, 2013. 56(11): p. 4413-21.
95. Lee, T., et al., *Docking motif interactions in MAP kinases revealed by hydrogen exchange mass spectrometry*. Mol Cell, 2004. 14(1): p. 43-55.
96. Jacobs, D., et al., *Multiple docking sites on substrate proteins form a modular system that mediates recognition by ERK MAP kinase*. Genes Dev, 1999. 13(2): p. 163-75.
97. Lee, S., et al., *A model of a MAPK*substrate complex in an active conformation: a computational and experimental approach*. PLoS One, 2011. 6(4): p. e18594.
98. Sheridan, D.L., et al., *Substrate discrimination among mitogen-activated protein kinases through distinct docking sequence motifs*. J Biol Chem, 2008. 283(28): p. 19511-20.
99. Fernandes, N., et al., *Use of docking peptides to design modular substrates with high efficiency for mitogen-activated protein kinase extracellular signal-regulated kinase*. ACS Chem Biol, 2007. 2(10): p. 665-73.
100. Liu, X., et al., *A conserved motif in JNK/p38-specific MAPK phosphatases as a determinant for JNK1 recognition and inactivation*. Nat Commun, 2016. 7: p. 10879.
101. Comess, K.M., et al., *Discovery and characterization of non-ATP site inhibitors of the mitogen activated protein (MAP) kinases*. ACS Chem Biol, 2011. 6(3): p. 234-44.
102. Samadani, R., et al., *Small-molecule inhibitors of ERK-mediated immediate early gene expression and proliferation of melanoma cells expressing mutated BRAf*. Biochem J, 2015. 467(3): p. 425-38.
103. Miller, C.J., Y. Muftuoglu, and B.E. Turk, *A high throughput assay to identify substrate-selective inhibitors of the ERK protein kinases*. Biochem Pharmacol, 2017. 142: p. 39-45.
104. Yang, S.H., et al., *Differential targeting of MAP kinases to the ETS-domain transcription factor Elk-1*. EMBO J, 1998. 17(6): p. 1740-9.
105. Lee, S., et al., *Examining docking interactions on ERK2 with modular peptide substrates*. Biochemistry, 2011. 50(44): p. 9500-10.
106. Piserchio, A., et al., *Structural and Dynamic Features of F-recruitment Site Driven Substrate Phosphorylation by ERK2*. Sci Rep, 2015. 5: p. 11127.

107. Canagarajah, B.J., et al., *Activation mechanism of the MAP kinase ERK2 by dual phosphorylation*. Cell, 1997. 90(5): p. 859-69.
108. Wilsbacher, J.L., et al., *Characterization of mitogen-activated protein kinase (MAPK) dimers*. Biochemistry, 2006. 45(44): p. 13175-13182.
109. Herrero, A., et al., *Small Molecule Inhibition of ERK Dimerization Prevents Tumorigenesis by RAS-ERK Pathway Oncogenes*. Cancer Cell, 2015. 28(2): p. 170-82.
110. Amor-Mahjoub, M., et al., *The effect of the hexahistidine-tag in the oligomerization of HSC70 constructs*. J Chromatogr B Analyt Technol Biomed Life Sci, 2006. 844(2): p. 328-34.
111. Wu, J. and M. Filutowicz, *Hexahistidine (His6)-tag dependent protein dimerization: a cautionary tale*. Acta Biochim Pol, 1999. 46(3): p. 591-9.
112. Kaoud, T.S., et al., *Activated ERK2 is a monomer in vitro with or without divalent cations and when complexed to the cytoplasmic scaffold PEA-15*. Biochemistry, 2011. 50(21): p. 4568-78.
113. Morris, E.J., et al., *Discovery of a novel ERK inhibitor with activity in models of acquired resistance to BRAF and MEK inhibitors*. Cancer Discov, 2013. 3(7): p. 742-50.
114. Chaikuad, A., et al., *A unique inhibitor binding site in ERK1/2 is associated with slow binding kinetics*. Nat Chem Biol, 2014. 10(10): p. 853-60.
115. Kummer, L., et al., *Structural and functional analysis of phosphorylation-specific binders of the kinase ERK from designed ankyrin repeat protein libraries*. Proc Natl Acad Sci U S A, 2012. 109(34): p. E2248-57.
116. Parizek, P., et al., *Designed ankyrin repeat proteins (DARPin) as novel isoform-specific intracellular inhibitors of c-Jun N-terminal kinases*. ACS Chem Biol, 2012. 7(8): p. 1356-66.
117. Wu, Y., et al., *Structural Basis for the Selective Inhibition of c-Jun N-Terminal Kinase 1 Determined by Rigid DARPin-DARPin Fusions*. J Mol Biol, 2017.
118. Johnson, D.S., E. Weerapana, and B.F. Cravatt, *Strategies for discovering and derisking covalent, irreversible enzyme inhibitors*. Future Med Chem, 2010. 2(6): p. 949-64.
119. Barf, T. and A. Kaptein, *Irreversible protein kinase inhibitors: balancing the benefits and risks*. J Med Chem, 2012. 55(14): p. 6243-62.
120. Liu, Q., et al., *Developing irreversible inhibitors of the protein kinase cysteinome*. Chem Biol, 2013. 20(2): p. 146-59.
121. Garuti, L., M. Roberti, and G. Bottegoni, *Irreversible protein kinase inhibitors*. Curr Med Chem, 2011. 18(20): p. 2981-94.

122. Singh, J., et al., *The resurgence of covalent drugs*. Nat Rev Drug Discov, 2011. 10(4): p. 307-17.
123. Kwak, E.L., et al., *Irreversible inhibitors of the EGF receptor may circumvent acquired resistance to gefitinib*. Proc Natl Acad Sci U S A, 2005. 102(21): p. 7665-70.
124. Kobayashi, S., et al., *An alternative inhibitor overcomes resistance caused by a mutation of the epidermal growth factor receptor*. Cancer Res, 2005. 65(16): p. 7096-101.
125. Schirmer, A., et al., *Targeted covalent inactivation of protein kinases by resorcylic acid lactone polyketides*. Proc Natl Acad Sci U S A, 2006. 103(11): p. 4234-9.
126. Ohori, M., et al., *Role of a cysteine residue in the active site of ERK and the MAPKK family*. Biochem Biophys Res Commun, 2007. 353(3): p. 633-7.
127. Ward, R.A., et al., *Structure-Guided Design of Highly Selective and Potent Covalent Inhibitors of ERK1/2*. J Med Chem, 2015. 58(11): p. 4790-801.
128. Zhang, T., et al., *Discovery of potent and selective covalent inhibitors of JNK*. Chem Biol, 2012. 19(1): p. 140-54.
129. Gross, S., et al., *Targeting cancer with kinase inhibitors*. J Clin Invest, 2015. 125(5): p. 1780-9.
130. Hopkins, A.L., J.S. Mason, and J.P. Overington, *Can we rationally design promiscuous drugs?* Curr Opin Struct Biol, 2006. 16(1): p. 127-36.
131. Bilanges, B., N. Torbett, and B. Vanhaesebroeck, *Killing two kinase families with one stone*. Nat Chem Biol, 2008. 4(11): p. 648-9.
132. Petrelli, A. and S. Giordano, *From single- to multi-target drugs in cancer therapy: when aspecificity becomes an advantage*. Curr Med Chem, 2008. 15(5): p. 422-32.
133. Lechtenberg, B.C., et al., *Structure-Guided Strategy for the Development of Potent Bivalent ERK Inhibitors*. ACS Med Chem Lett, 2017. 8(7): p. 726-731.
134. Ngoei, K.R., et al., *Identification and characterization of bi-thiazole-2,2'-diamines as kinase inhibitory scaffolds*. Biochim Biophys Acta, 2013. 1834(6): p. 1077-88.
135. Chen, T., et al., *Identification of small-molecule inhibitors of the JIP-JNK interaction*. Biochem J, 2009. 420(2): p. 283-94.
136. Stebbins, J.L., et al., *Design and characterization of a potent and selective dual ATP- and substrate-competitive subnanomolar bidentate c-Jun N-terminal kinase (JNK) inhibitor*. J Med Chem, 2011. 54(18): p. 6206-14.

137. De, S.K., et al., *Design, synthesis, and structure-activity relationship studies of thiophene-3-carboxamide derivatives as dual inhibitors of the c-Jun N-terminal kinase*. *Bioorg Med Chem*, 2011. 19(8): p. 2582-8.
138. Balko, J.M., et al., *Activation of MAPK pathways due to DUSP4 loss promotes cancer stem cell-like phenotypes in basal-like breast cancer*. *Cancer Res*, 2013. 73(20): p. 6346-58.
139. Jiang, T., C.Q. Pan, and B.C. Low, *BPGAP1 spatially integrates JNK/ERK signaling crosstalk in oncogenesis*. *Oncogene*, 2017. 36(22): p. 3178-3192.
140. Kang, B.S., Y.J. Hwang, and Z. Dong, *ERK1 Directly Interacts With JNK1 Leading to Regulation of JNK1/c-Jun Activity and Cell Transformation*. *J Cell Biochem*, 2017. 118(8): p. 2357-2370.
141. Ritt, D.A., et al., *Inhibition of Ras/Raf/MEK/ERK Pathway Signaling by a Stress-Induced Phospho-Regulatory Circuit*. *Mol Cell*, 2016. 64(5): p. 875-887.
142. Hughes, P.E., S. Caenepeel, and L.C. Wu, *Targeted Therapy and Checkpoint Immunotherapy Combinations for the Treatment of Cancer*. *Trends Immunol*, 2016. 37(7): p. 462-76.
143. Holohan, C., et al., *Cancer drug resistance: an evolving paradigm*. *Nat Rev Cancer*, 2013. 13(10): p. 714-26.
144. Logue, J.S. and D.K. Morrison, *Complexity in the signaling network: insights from the use of targeted inhibitors in cancer therapy*. *Genes Dev*, 2012. 26(7): p. 641-50.
145. Niederst, M.J. and J.A. Engelman, *Bypass mechanisms of resistance to receptor tyrosine kinase inhibition in lung cancer*. *Sci Signal*, 2013. 6(294): p. re6.
146. Chandarlapaty, S., *Negative feedback and adaptive resistance to the targeted therapy of cancer*. *Cancer Discov*, 2012. 2(4): p. 311-9.
147. Neel, D.S. and T.G. Bivona, *Resistance is futile: overcoming resistance to targeted therapies in lung adenocarcinoma*. *npj Precision Oncology*, 2017. 1(1): p. 3.
148. Tam, W.L. and R.A. Weinberg, *The epigenetics of epithelial-mesenchymal plasticity in cancer*. *Nat Med*, 2013. 19(11): p. 1438-49.
149. Stuhlmiller, T.J., et al., *Inhibition of Lapatinib-Induced Kinome Reprogramming in ERBB2-Positive Breast Cancer by Targeting BET Family Bromodomains*. *Cell Rep*, 2015. 11(3): p. 390-404.
150. Angus, S.P., J.S. Zawistowski, and G.L. Johnson, *Epigenetic Mechanisms Regulating Adaptive Responses to Targeted Kinase Inhibitors in Cancer*. *Annu Rev Pharmacol Toxicol*, 2017.

151. Rizos, H., et al., *BRAF inhibitor resistance mechanisms in metastatic melanoma: spectrum and clinical impact*. Clin Cancer Res, 2014. 20(7): p. 1965-77.
152. Van Allen, E.M., et al., *The genetic landscape of clinical resistance to RAF inhibition in metastatic melanoma*. Cancer Discov, 2014. 4(1): p. 94-109.
153. Shi, H., et al., *Melanoma whole-exome sequencing identifies (V600E)B-RAF amplification-mediated acquired B-RAF inhibitor resistance*. Nat Commun, 2012. 3: p. 724.
154. Duncan, J.S., et al., *Dynamic reprogramming of the kinome in response to targeted MEK inhibition in triple-negative breast cancer*. Cell, 2012. 149(2): p. 307-21.
155. Devkota, A.K., et al., *High-throughput screens for eEF-2 kinase*. J Biomol Screen, 2014. 19(3): p. 445-52.
156. Nissan, M.H., N. Rosen, and D.B. Solit, *ERK pathway inhibitors: how low should we go?* Cancer Discov, 2013. 3(7): p. 719-21.
157. Hirata, E., et al., *Intravital imaging reveals how BRAF inhibition generates drug-tolerant microenvironments with high integrin beta1/FAK signaling*. Cancer Cell, 2015. 27(4): p. 574-88.
158. Sweeney, S.E. and G.S. Firestein, *Mitogen activated protein kinase inhibitors: where are we now and where are we going?* Ann Rheum Dis, 2006. 65 Suppl 3: p. iii83-8.
159. Schlesinger, T.K., et al., *The TAO of MEKK*. Front Biosci, 1998. 3: p. D1181-6.
160. Chen, Z., et al., *MAP kinases*. Chem Rev, 2001. 101(8): p. 2449-76.
161. Forbes, S.A., et al., *COSMIC: mining complete cancer genomes in the Catalogue of Somatic Mutations in Cancer*. Nucleic Acids Res, 2011. 39(Database issue): p. D945-50.
162. Davis, M.I., et al., *Comprehensive analysis of kinase inhibitor selectivity*. Nat Biotechnol, 2011. 29(11): p. 1046-51.
163. Aronov, A.M., et al., *Structure-guided design of potent and selective pyrimidylpyrrole inhibitors of extracellular signal-regulated kinase (ERK) using conformational control*. J Med Chem, 2009. 52(20): p. 6362-8.
164. Krishnamurty, R. and D.J. Maly, *Biochemical mechanisms of resistance to small-molecule protein kinase inhibitors*. ACS Chem Biol, 2010. 5(1): p. 121-38.
165. Daub, H., K. Specht, and A. Ullrich, *Strategies to overcome resistance to targeted protein kinase inhibitors*. Nat Rev Drug Discov, 2004. 3(12): p. 1001-10.
166. Hatzivassiliou, G., et al., *ERK inhibition overcomes acquired resistance to MEK inhibitors*. Mol Cancer Ther, 2012. 11(5): p. 1143-54.

167. Bauer, R.A., *Covalent inhibitors in drug discovery: from accidental discoveries to avoided liabilities and designed therapies*. Drug Discov Today, 2015. 20(9): p. 1061-73.
168. Yun, C.H., et al., *The T790M mutation in EGFR kinase causes drug resistance by increasing the affinity for ATP*. Proc Natl Acad Sci U S A, 2008. 105(6): p. 2070-5.
169. Miller, C.J., Y. Muftuoglu, and B.E. Turk, *A high throughput assay to identify substrate-selective inhibitors of the ERK protein kinases*. Biochem Pharmacol, 2017.
170. Yan, C., et al., *Understanding the specificity of a docking interaction between JNK1 and the scaffolding protein JIP1*. J Phys Chem B, 2011. 115(6): p. 1491-502.
171. Waas, W.F. and K.N. Dalby, *Transient protein-protein interactions and a random-ordered kinetic mechanism for the phosphorylation of a transcription factor by extracellular-regulated protein kinase 2*. J Biol Chem, 2002. 277(15): p. 12532-40.
172. Abramczyk, O., et al., *Expanding the repertoire of an ERK2 recruitment site: cysteine footprinting identifies the D-recruitment site as a mediator of Ets-1 binding*. Biochemistry, 2007. 46(32): p. 9174-86.
173. Madsen, J.A., et al., *193-nm photodissociation of singly and multiply charged peptide anions for acidic proteome characterization*. Proteomics, 2011. 11(7): p. 1329-34.
174. Zamora-Olivares, D., et al., *Differential sensing of MAP kinases using SOX-peptides*. Angew Chem Int Ed Engl, 2014. 53(51): p. 14064-8.
175. Shults, M.D., D.A. Pearce, and B. Imperiali, *Modular and tunable chemosensor scaffold for divalent zinc*. J Am Chem Soc, 2003. 125(35): p. 10591-7.
176. Hastie, C.J., H.J. McLauchlan, and P. Cohen, *Assay of protein kinases using radiolabeled ATP: a protocol*. Nat Protoc, 2006. 1(2): p. 968-71.
177. Devkota, A.K., et al., *Fluorescent peptide assays for protein kinases*. Curr Protoc Mol Biol, 2010. Chapter 18: p. Unit 18 17.
178. Zhang, J.H., T.D. Chung, and K.R. Oldenburg, *A Simple Statistical Parameter for Use in Evaluation and Validation of High Throughput Screening Assays*. J Biomol Screen, 1999. 4(2): p. 67-73.
179. Feng, B.Y. and B.K. Shoichet, *A detergent-based assay for the detection of promiscuous inhibitors*. Nat Protoc, 2006. 1(2): p. 550-3.

180. Jadhav, A., et al., *Quantitative analyses of aggregation, autofluorescence, and reactivity artifacts in a screen for inhibitors of a thiol protease*. J Med Chem, 2010. 53(1): p. 37-51.
181. Baell, J. and M.A. Walters, *Chemistry: Chemical con artists foil drug discovery*. Nature, 2014. 513(7519): p. 481-3.
182. Baell, J.B. and G.A. Holloway, *New substructure filters for removal of pan assay interference compounds (PAINS) from screening libraries and for their exclusion in bioassays*. J Med Chem, 2010. 53(7): p. 2719-40.
183. Senger, M.R., et al., *Filtering promiscuous compounds in early drug discovery: is it a good idea?* Drug Discov Today, 2016. 21(6): p. 868-72.
184. Chai, C.L. and P. Matyus, *One size does not fit all: Challenging some dogmas and taboos in drug discovery*. Future Med Chem, 2016. 8(1): p. 29-38.
185. Capuzzi, S.J., E.N. Muratov, and A. Tropsha, *Phantom PAINS: Problems with the Utility of Alerts for Pan-Assay Interference CompoundS*. J Chem Inf Model, 2017. 57(3): p. 417-427.
186. Roder, C. and M.J. Thomson, *Auranofin: repurposing an old drug for a golden new age*. Drugs R D, 2015. 15(1): p. 13-20.
187. Gottlieb, N.L., *Pharmacology of auranofin: overview and update*. Scand J Rheumatol Suppl, 1986. 63: p. 19-28.
188. Piserchio, A., et al., *Solution NMR insights into docking interactions involving inactive ERK2*. Biochemistry, 2011. 50(18): p. 3660-72.
189. Zhou, T., et al., *Docking interactions induce exposure of activation loop in the MAP kinase ERK2*. Structure, 2006. 14(6): p. 1011-9.
190. Casini, A. and L. Messori, *Molecular Mechanisms and Proposed Targets for Selected Anticancer Gold Compounds*. Current Topics in Medicinal Chemistry, 2011. 11(21): p. 2647-2660.
191. Pessetto, Z.Y., et al., *Drug Repurposing for Gastrointestinal Stromal Tumor*. Molecular Cancer Therapeutics, 2013. 12(7): p. 1299-1309.
192. Marzano, C., et al., *Inhibition of thioredoxin reductase by auranofin induces apoptosis in cisplatin-resistant human ovarian cancer cells*. Free Radic Biol Med, 2007. 42(6): p. 872-81.
193. Harbut, M.B., et al., *Auranofin exerts broad-spectrum bactericidal activities by targeting thiol-redox homeostasis*. Proc Natl Acad Sci U S A, 2015. 112(14): p. 4453-8.
194. Nakaya, A., et al., *The gold compound auranofin induces apoptosis of human multiple myeloma cells through both down-regulation of STAT3 and inhibition of NF-kappaB activity*. Leuk Res, 2011. 35(2): p. 243-9.

195. Jeon, K.I., J.Y. Jeong, and D.M. Jue, *Thiol-reactive metal compounds inhibit NF-kappa B activation by blocking I kappa B kinase*. J Immunol, 2000. 164(11): p. 5981-9.
196. Froscio, M., A.W. Murray, and N.P. Hurst, *Inhibition of protein kinase C activity by the antirheumatic drug auranofin*. Biochem Pharmacol, 1989. 38(13): p. 2087-9.
197. Han, S., et al., *Auranofin inhibits overproduction of pro-inflammatory cytokines, cyclooxygenase expression and PGE2 production in macrophages*. Arch Pharm Res, 2008. 31(1): p. 67-74.
198. Pessetto, Z.Y., et al., *Drug repurposing for gastrointestinal stromal tumor*. Mol Cancer Ther, 2013. 12(7): p. 1299-309.
199. Johnson, G.L., et al., *Molecular pathways: adaptive kinome reprogramming in response to targeted inhibition of the BRAF-MEK-ERK pathway in cancer*. Clin Cancer Res, 2014. 20(10): p. 2516-22.
200. Albeck, J.G., G.B. Mills, and J.S. Brugge, *Frequency-modulated pulses of ERK activity transmit quantitative proliferation signals*. Mol Cell, 2013. 49(2): p. 249-61.
201. Fantz, D.A., et al., *Docking sites on substrate proteins direct extracellular signal-regulated kinase to phosphorylate specific residues*. J Biol Chem, 2001. 276(29): p. 27256-65.
202. Callaway, K., et al., *Phosphorylation of the transcription factor Ets-1 by ERK2: rapid dissociation of ADP and phospho-Ets-1*. Biochemistry, 2010. 49(17): p. 3619-30.
203. Rainey, M.A., et al., *Proximity-induced catalysis by the protein kinase ERK2*. J Am Chem Soc, 2005. 127(30): p. 10494-5.
204. Lawrence, D.S. and J. Niu, *Protein kinase inhibitors: the tyrosine-specific protein kinases*. Pharmacol Ther, 1998. 77(2): p. 81-114.
205. Breen, M.E. and M.B. Soellner, *Small molecule substrate phosphorylation site inhibitors of protein kinases: approaches and challenges*. ACS Chem Biol, 2015. 10(1): p. 175-89.
206. Roberts, P.J. and C.J. Der, *Targeting the Raf-MEK-ERK mitogen-activated protein kinase cascade for the treatment of cancer*. Oncogene, 2007. 26(22): p. 3291-310.
207. Liu, Q.H., et al., *Role of the ERK1/2 pathway in tumor chemoresistance and tumor therapy*. Bioorg Med Chem Lett, 2015. 25(2): p. 192-7.
208. Burkhard, K., et al., *Development of extracellular signal-regulated kinase inhibitors*. Curr Top Med Chem, 2009. 9(8): p. 678-89.

209. Cerchietti, L.C., et al., *A small-molecule inhibitor of BCL6 kills DLBCL cells in vitro and in vivo*. *Cancer Cell*, 2010. 17(4): p. 400-11.
210. Arkin, M.R., Y. Tang, and J.A. Wells, *Small-molecule inhibitors of protein-protein interactions: progressing toward the reality*. *Chem Biol*, 2014. 21(9): p. 1102-14.
211. Tanoue, T., et al., *A conserved docking motif in MAP kinases common to substrates, activators and regulators*. *Nat Cell Biol*, 2000. 2(2): p. 110-6.
212. Bardwell, L. and J. Thorner, *A conserved motif at the amino termini of MEKs might mediate high-affinity interaction with the cognate MAPKs*. *Trends Biochem Sci*, 1996. 21(10): p. 373-4.
213. Xu, B., et al., *The N-terminal ERK-binding site of MEK1 is required for efficient feedback phosphorylation by ERK2 in vitro and ERK activation in vivo*. *J Biol Chem*, 1999. 274(48): p. 34029-35.
214. Camps, M., et al., *Catalytic activation of the phosphatase MKP-3 by ERK2 mitogen-activated protein kinase*. *Science*, 1998. 280(5367): p. 1262-5.
215. Smith, J.A., et al., *Identification of an extracellular signal-regulated kinase (ERK) docking site in ribosomal S6 kinase, a sequence critical for activation by ERK in vivo*. *J Biol Chem*, 1999. 274(5): p. 2893-8.
216. Bott, C.M., S.G. Thorneycroft, and C.J. Marshall, *The sevenmaker gain-of-function mutation in p42 MAP kinase leads to enhanced signalling and reduced sensitivity to dual specificity phosphatase action*. *FEBS Lett*, 1994. 352(2): p. 201-5.
217. Goetz, E.M., et al., *ERK mutations confer resistance to mitogen-activated protein kinase pathway inhibitors*. *Cancer Res*, 2014. 74(23): p. 7079-89.
218. Waas, W.F. and K.N. Dalby, *Purification of a model substrate for transcription factor phosphorylation by ERK2*. *Protein Expr Purif*, 2001. 23(1): p. 191-7.
219. Pervushin, K., et al., *Attenuated T2 relaxation by mutual cancellation of dipole-dipole coupling and chemical shift anisotropy indicates an avenue to NMR structures of very large biological macromolecules in solution*. *Proc Natl Acad Sci U S A*, 1997. 94(23): p. 12366-71.
220. Delaglio, F., et al., *NMRPipe: a multidimensional spectral processing system based on UNIX pipes*. *J Biomol NMR*, 1995. 6(3): p. 277-93.
221. Goddard, T.G.K., D.G., *SPARKY3*. 2008, University of California: San Francisco.
222. Otwinowski, Z. and W. Minor, *Processing of X-ray Diffraction Data Collected in Oscillation Mode*. 1997, Academic Press: *Methods in Enzymology*. p. p.307-326.
223. McCoy, A.J., et al., *Phaser crystallographic software*. *Journal of Applied Crystallography*, 2007. 40(4): p. 658-674.

224. Adams, P.D., et al., *PHENIX: a comprehensive Python-based system for macromolecular structure solution*. Acta Crystallographica Section D, 2010. 66(2): p. 213-221.
225. Zhang, F., et al., *Atomic structure of the MAP kinase ERK2 at 2.3 Å resolution*. Nature, 1994. 367(6465): p. 704-711.
226. Emsley, P., Lohkamp, B., Scott, W.G. and Cowtan, K., *Features and Development of Coot*. 2010. p. 486-501.
227. Wallace, A.C., R.A. Laskowski, and J.M. Thornton, *LIGPLOT: a program to generate schematic diagrams of protein-ligand interactions*. Protein Eng, 1995. 8(2): p. 127-34.
228. Houghten, R.A., *Combinatorial libraries. Finding the needle in the haystack*. Curr Biol, 1994. 4(6): p. 564-7.
229. Ostresh, J.M., et al., *"Libraries from libraries": chemical transformation of combinatorial libraries to extend the range and repertoire of chemical diversity*. Proc Natl Acad Sci U S A, 1994. 91(23): p. 11138-42.
230. Figuera-Losada, M. and P.V. LoGrasso, *Enzyme kinetics and interaction studies for human JNK1beta1 and substrates activating transcription factor 2 (ATF2) and c-Jun N-terminal kinase (c-Jun)*. J Biol Chem, 2012. 287(16): p. 13291-302.
231. Szafranska, A.E. and K.N. Dalby, *Kinetic mechanism for p38 MAP kinase alpha. A partial rapid-equilibrium random-order ternary-complex mechanism for the phosphorylation of a protein substrate*. FEBS J, 2005. 272(18): p. 4631-45.
232. Manning, A.M. and R.J. Davis, *Targeting JNK for therapeutic benefit: from junk to gold?* Nat Rev Drug Discov, 2003. 2(7): p. 554-65.
233. Barr, R.K. and M.A. Bogoyevitch, *The c-Jun N-terminal protein kinase family of mitogen-activated protein kinases (JNK MAPKs)*. Int J Biochem Cell Biol, 2001. 33(11): p. 1047-63.
234. Bogoyevitch, M.A., *The isoform-specific functions of the c-Jun N-terminal kinases (JNKs): differences revealed by gene targeting*. Bioessays, 2006. 28(9): p. 923-934.
235. Bogoyevitch, M.A., *Therapeutic promise of JNK ATP-noncompetitive inhibitors*. Trends Mol Med, 2005. 11(5): p. 232-9.
236. Graczyk, P.P., *JNK inhibitors as anti-inflammatory and neuroprotective agents*. Future Med Chem, 2013. 5(5): p. 539-51.
237. Kyriakis, J.M. and J. Avruch, *Mammalian mitogen-activated protein kinase signal transduction pathways activated by stress and inflammation*. Physiol Rev, 2001. 81(2): p. 807-69.

238. Genova, C., et al., *Afatinib for the treatment of advanced non-small-cell lung cancer*. *Expert Opin Pharmacother*, 2014. 15(6): p. 889-903.
239. Sanderson, K., *Irreversible kinase inhibitors gain traction*. *Nat Rev Drug Discov*, 2013. 12(9): p. 649-51.
240. Szafranska, A.E., X. Luo, and K.N. Dalby, *Following in vitro activation of mitogen-activated protein kinases by mass spectrometry and tryptic peptide analysis: purifying fully activated p38 mitogen-activated protein kinase alpha*. *Anal Biochem*, 2005. 336(1): p. 1-10.
241. Copeland, R.A., *Enzymes : a practical introduction to structure, mechanism, and data analysis*. 2nd ed. 2000, New York: J. Wiley. xvi, 397 p.
242. Ebelt, N.D., et al., *A c-Jun N-terminal kinase inhibitor, JNK-IN-8, sensitizes triple negative breast cancer cells to lapatinib*. *Oncotarget*, 2017. 8(62): p. 104894-104912.
243. Schwartz, P.A., et al., *Covalent EGFR inhibitor analysis reveals importance of reversible interactions to potency and mechanisms of drug resistance*. *Proc Natl Acad Sci U S A*, 2014. 111(1): p. 173-8.
244. Krippendorff, B.F., et al., *Mechanism-based inhibition: deriving $K(I)$ and $k(inact)$ directly from time-dependent $IC(50)$ values*. *J Biomol Screen*, 2009. 14(8): p. 913-23.
245. Silverman, R.B., *Mechanism-based enzyme inactivators*. *Methods Enzymol*, 1995. 249: p. 240-83.
246. Chen, P., et al., *Jnk2 effects on tumor development, genetic instability and replicative stress in an oncogene-driven mouse mammary tumor model*. *PLoS One*, 2010. 5(5): p. e10443.
247. Alessi, D.R., et al., *PD 098059 is a specific inhibitor of the activation of mitogen-activated protein kinase kinase in vitro and in vivo*. *J Biol Chem*, 1995. 270(46): p. 27489-94.
248. Singh, J., et al., *Structure-based design of a potent, selective, and irreversible inhibitor of the catalytic domain of the erbB receptor subfamily of protein tyrosine kinases*. *J Med Chem*, 1997. 40(7): p. 1130-5.
249. Wang, B., et al., *Structure-activity relationship investigation for benzonaphthyridinone derivatives as novel potent Bruton's tyrosine kinase (BTK) irreversible inhibitors*. *Eur J Med Chem*, 2017. 137: p. 545-557.
250. Liu, Y., et al., *Development of the First Generation of Disulfide-Based Subtype-Selective and Potent Covalent Pyruvate Dehydrogenase Kinase 1 (PDK1) Inhibitors*. *J Med Chem*, 2017. 60(6): p. 2227-2244.

251. Roberts, J.R., et al., *Kinetics and Mechanism of the Reaction between Serum Albumin and Auranofin (and Its Isopropyl Analogue) in Vitro*. *Inorg Chem*, 1996. 35(2): p. 424-433.
252. Chen, V.B., et al., *MolProbity: all-atom structure validation for macromolecular crystallography*. *Acta Crystallogr D Biol Crystallogr*, 2010. 66(Pt 1): p. 12-21.
253. Ostresh, J.M.S., C.C.; Hamashin, V.T.; Nefzi, A.; Meyer, J.-P.; Houghten, R.A., *Solid-phase synthesis of trisubstituted bicyclic guanidines via cyclization of reduced N-acetylated dipeptides*. *J. Org. Chem.*, 1998. 63: p. 8622-8623.